

# **Multi Level Monte Carlo Methods for Uncertainty Quantification and Robust Design Optimization in Aerodynamics**

THÈSE N° 8082 (2017)

PRÉSENTÉE LE 15 DÉCEMBRE 2017  
À LA FACULTÉ DES SCIENCES ET TECHNIQUES DE L'INGÉNIEUR  
GROUPE DE SCIENTIFIQUES IGM  
PROGRAMME DOCTORAL EN MÉCANIQUE

ÉCOLE POLYTECHNIQUE FÉDÉRALE DE LAUSANNE

POUR L'OBTENTION DU GRADE DE DOCTEUR ÈS SCIENCES

PAR

**Michele PISARONI**

acceptée sur proposition du jury:

Prof. C. Ancey, président du jury  
Dr P. Leyland, Prof. F. Nobile, directeurs de thèse  
Prof. F. Stern, rapporteur  
Dr D. Quagliarella, rapporteur  
Prof. J.-F. Molinari, rapporteur



ÉCOLE POLYTECHNIQUE  
FÉDÉRALE DE LAUSANNE

Suisse  
2017



# Acknowledgements

This accomplishment would not have been possible without the support of many people that I would like to thank here.

First of all, I would like to express my gratitude to my two supervisors Dr. Pénélope Leyland and Prof. Fabio Nobile for providing me the precious opportunity to work with them during my PhD. Thanks to your respective areas of expertise, I have been deeply influenced and positively guided with valuable technical and moral support whenever needed.

Next, I would like to thank Prof. Jean-François Molinari, Prof. Frederick Stern and Dr. Domenico Quagliarella for being part of my thesis jury and to Prof. Christophe Ancey for presiding it.

Over the years at EPFL, I shared great times with awesome colleagues in IGM and CSQI. Sebastian, Lorenzo, Angelo and Gaffu thanks for the friendly and patient valuable technical support. Mathieu for being such a diligent student when I teach you how to ski! Nikhil, Elise and Jermemy for the great laughs and awesome time we spent in DC. Andrea for the great times, laughs and polemic debates! Francesco and Eleonora thanks for being not only two bizarre and uncommon office mates but also awesome friends with who I shared memorable moments.

Thanks to my great house mates Benji, Luca, Chris, Emmi and Calmum that helped and supported me during my PhD but in particular because you friendly tolerated my Italian nature (in particular in the kitchen and during Inter matches) and for the great times we spent together.

Ninni and Giorgio deserve a special word of gratitude for their remarkable unconditional availability, positive influence and for the terrific experiences and adventures we shared in these years that strengthened our friendship and our characters.

A very special word of thanks goes to Noémie for her endless support, care and encouragement. You inspire and motivate me every day and I feel very lucky.

Lastly, I would like to thank from the bottom of my heart my parents Fabrizio and Lucia. This would have been impossible without your teachings, encouragement and support. I dedicate this thesis to you.

*Lausanne, November 2017*

M. P.

## **Acknowledgements**

---

This work has received funding from the European Union's Seventh Framework Programme for research, technological development and demonstration under grant agreement no ACP3-GA-2013-605036 (Uncertainty Management for Robust Industrial Design in Aeronautics - UMRIDA project).





# Abstract

The vast majority of problems that arise in aircraft production and operation require decisions to be made in the presence of uncertainty. An effective and accurate quantification and control of the level of uncertainty introduced in the design phase and during the manufacturing and operation of aircraft vehicles is imperative in order to design robust and risk tolerant systems. Indeed, the geometrical and operational parameters, that characterize aerodynamic systems, are naturally affected by aleatory uncertainties due to the intrinsic variability of the manufacturing processes and the surrounding environment. Reducing the geometrical uncertainties due to manufacturing tolerances can be prohibitively expensive while reducing the operational uncertainties due to atmospheric variability is simply impossible. The quantification of those two type of uncertainties should be available in reasonable time in order to be effective and practical in an industrial environment. The objective of this thesis is to develop efficient and accurate approaches for the study of aerodynamic systems affected by geometric and operating uncertainties. In order to treat this class of problems we first adapt the Multi Level Monte Carlo probabilistic approach to tackle aerodynamic problems modeled by Computational Fluid Dynamics simulations. Subsequently, we propose and discuss different strategies and extensions of the original technique to compute statistical moments, distributions and risk measures of random quantities of interest. We show on several numerical examples, relevant in compressible inviscid and viscous aerodynamics, the effectiveness and accuracy of the proposed approach. We also consider the problem of optimization under uncertainties. In this case we leverage the flexibility of our Multi Level Monte Carlo approach in computing different robust and reliable objective functions and probabilistic constraints. By combining our approach with single and multi objective evolutionary strategies, we show how to optimize the shape of transonic airfoils in order to obtain designs whose performances are as insensitive as possible to uncertain conditions.

Key words: Uncertainty Quantification; Multi Level Monte Carlo; Continuation Multi Level Monte Carlo; Robust Design Optimization; Reliability-based Design Optimization; Optimization Under Uncertainties; Aeronautics; Aerodynamics.



# Résumé

La grande majorité des problèmes qui surgissent dans le cycle de conception, production et opérations en aéronautique requiert une stratégie décisionnelle prenant en compte des paramètres d'incertitude. Une quantification précise et ciblée et un contrôle du niveau d'incertitude introduit dans la phase de conception et pendant les phases de fabrication de l'avion sont impératives pour concevoir systèmes robuste avec un niveau de risque contrôlé. Les paramètres géométriques et opérationnels, qui caractérisent des systèmes aérodynamiques, sont naturellement influencés par des incertitudes aléatoires en raison de la variabilité intrinsèque des procédés de fabrication et de l'environnement dans lequel ils évoluent. La réduction des incertitudes géométriques en raison des tolérances industrielles peut être conduire à un prix prohibitif. Pendant que la réduction des incertitudes opérationnelles en raison des variations atmosphériques locales par exemple, soit impossible. Ajouté à cela, sont les incertitudes de modèle associées aux paramètres qui apparaissent dans ces modèles. La quantification de ces incertitudes devrait être disponible dans le temps raisonnable pour être efficace et pragmatique dans un environnement industriel. L'objectif de cette thèse est de développer des approches efficaces et précises pour l'étude de la conception des systèmes en aéronautiques soumis à des incertitudes géométriques et opérationnelles. Pour aboutir à de telles méthodologies nous adaptons d'abord des techniques probabiliste de Multi-Niveaux Monte-Carlo dans des simulations de problèmes types de l'aérodynamique. Ensuite, nous avons proposé, vérifié et validé des stratégies et des extensions différentes de la technique originale avec aussi l'estimation des moments statistiques, des distributions de probabilité et des mesures de risque des quantités aléatoires d'intérêt, démontrés par des simulations des exemples pertinents des écoulements compressibles et l'optimisation des formes des tuyères, des écoulements aérodynamiques autour des profils d'ailes, en régime complexe (transsonique), avec l'impact de l'optimisation des paramètres aérodynamiques en tenant compte des changements induits par la prise en compte des incertitudes quantifiés. Enfin, les techniques sont appliquées à des cas industriels, avec des données expérimentales complètes, dont un rotor et la réduction de traînée autour d'un avion complète. Nous considérons aussi l'incorporation de la quantification des incertitudes dans les processus d'optimisation avec des algorithmes évolutionnaires, d'abord en mono-objectif et ensuite en multi-objectif. La flexibilité de notre approche Multi-Niveaux Monte-Carlo dans le calcul des différentes fonctions objectives robustes et fiables et les contraintes probabilistes, prouve d'être une méthode fiable et convergente. En combinant notre approche avec des méthodes d'optimisation évolutionnaire à objectifs simples ou multiples, nous montrons comment optimiser la forme des

## **Acknowledgements**

---

profils d'ailes transsoniques pour obtenir des conceptions dont les performances sont aussi imperturbables que possibles aux conditions incertaines.

Mots clefs : Quantification d'Incertitude ; Multi Niveaux Monte Carlo ; Continuation Multi Niveaux Monte Carlo ; Optimisation Robuste et Conception ; Optimisation avec fiabilité ; Aéronautique ; Aérodynamique.

# Contents

<b>Acknowledgements</b>	<b>i</b>
<b>Abstract</b>	<b>iii</b>
<b>List of figures</b>	<b>xi</b>
<b>List of tables</b>	<b>xix</b>
<b>List of Symbols</b>	<b>xxi</b>
<b>Acronyms</b>	<b>xxiii</b>
<b>1 Introduction</b>	<b>3</b>
1.1 The Need for Effective Uncertainty Management in Aeronautics . . . . .	3
1.2 Forward Propagation of Uncertainties . . . . .	4
1.3 Optimization Under Uncertainties . . . . .	5
1.4 Aim . . . . .	6
1.5 Thesis Outline . . . . .	6
<b>2 Uncertainty Management in Aerodynamic Design</b>	<b>9</b>
2.1 Flow Models and Aerodynamic Coefficients . . . . .	9
2.1.1 Navier Stokes Equations . . . . .	10
2.1.2 Euler Equations . . . . .	11
2.1.3 Finite Volume Approximation . . . . .	12
2.1.4 Aerodynamic Quantities of Interest . . . . .	16
2.2 Uncertainties in Aerodynamics . . . . .	18
2.3 Epistemic Uncertainties in Aerodynamic Design . . . . .	19
2.4 A Taxonomy of Aleatory Uncertainties in Aerodynamic Design . . . . .	20
2.4.1 Operating Uncertainties . . . . .	20
2.4.2 Geometric Uncertainties . . . . .	23
2.4.3 Treatment of Geometric Uncertainties . . . . .	26
<b>3 Uncertainty Propagation</b>	<b>33</b>
3.1 Probabilistic Framework . . . . .	33
3.2 Intrusive approaches . . . . .	35

## Contents

---

3.3	Non-intrusive approaches . . . . .	36
3.3.1	Polynomial/Collocation-based approaches . . . . .	36
3.3.2	Monte Carlo based Methods . . . . .	40
<b>4</b>	<b>Multi Level Monte Carlo Method</b>	<b>45</b>
4.1	Multi Level Monte Carlo . . . . .	46
4.1.1	MLMC Complexity Analysis . . . . .	46
4.1.2	Practical Aspects of MLMC . . . . .	48
4.1.3	MLMC for scalar field QoI . . . . .	49
4.1.4	MLMC Algorithm . . . . .	50
4.2	MLMC for UQ in Inviscid Aerodynamics . . . . .	52
4.2.1	Euler Equations . . . . .	52
4.2.2	MLMC Grid Hierarchy . . . . .	53
4.2.3	Inviscid transonic test cases: NACA 0012 and NASA SC(2)-0012 . . . . .	54
4.3	Disadvantages of Standard MLMC . . . . .	59
<b>5</b>	<b>Continuation Multi Level Monte Carlo</b>	<b>61</b>
5.1	The C-MLMC Method . . . . .	61
5.1.1	C-MLMC Iterative Procedure . . . . .	61
5.1.2	Practical Aspect of C-MLMC . . . . .	63
5.1.3	Bayesian Update . . . . .	63
5.1.4	C-MLMC Algorithm . . . . .	65
5.2	C-MLMC for UQ in Inviscid Aerodynamics . . . . .	66
5.2.1	Quasi-1D Model Problem: Flow in a Laval nozzle . . . . .	66
5.2.2	2D Model Problem: Flow around RAE 2822 airfoil . . . . .	77
5.3	Extension to Turbulent Problems . . . . .	85
5.3.1	Transonic Airfoil Model Problem: RAE2822 . . . . .	86
5.4	Summary . . . . .	90
<b>6</b>	<b>MLMC for Central Statistical Moments</b>	<b>93</b>
6.1	Introduction: Central Moments . . . . .	93
6.2	Monte Carlo estimation of central moments . . . . .	95
6.2.1	Classic ensemble based Monte Carlo estimator . . . . .	96
6.3	Multilevel Monte Carlo estimation of central moments. . . . .	99
6.3.1	Practical aspect: MSE and unbiased level-wise variance estimation . . . . .	103
6.3.2	From mean squared errors to confidence intervals . . . . .	104
6.4	Implementation details and complete algorithm . . . . .	105
6.5	Numerical Experiments . . . . .	108
6.5.1	Stochastic differential equation model: a financial option . . . . .	108
6.5.2	Elliptic PDE in two spatial dimensions . . . . .	109
6.5.3	Transonic Airfoil: 2d . . . . .	113
6.6	Summary . . . . .	117

<b>7</b>	<b>MLMC for Distributions and Risk Measures</b>	<b>119</b>
7.1	Multi Level Monte Carlo approximation of parametric expectations . . . . .	120
7.1.1	Practical aspects: computation of the MSE and optimal hierarchy . . . . .	123
7.2	Multi Level Monte Carlo approximation of derivatives . . . . .	126
7.2.1	Practical aspects: computation of the MSE and optimal hierarchy . . . . .	127
7.3	MLMC estimators for Distributions and Risk Functions . . . . .	128
7.3.1	MLMC estimator for the Cumulative Distribution Function . . . . .	129
7.3.2	MLMC estimator for the Characteristic function . . . . .	129
7.3.3	MLMC estimator for the simultaneous computation of VaR, CVar and CDF	130
7.4	Numerical Experiments . . . . .	132
7.4.1	Stochastic differential equation model: a financial option . . . . .	132
7.4.2	Elliptic PDE in two spatial dimensions . . . . .	134
7.5	Summary . . . . .	136
<b>8</b>	<b>C-MLMC Application to Industrial Problems</b>	<b>139</b>
8.1	Turbomachinery Model Problem: NASA ROTOR-37 . . . . .	139
8.1.1	Deterministic results . . . . .	139
8.1.2	Stochastic Results using C-MLMC . . . . .	143
8.2	NASA Common Research Model . . . . .	146
8.2.1	Deterministic results . . . . .	146
8.2.2	Stochastic Results using C-MLMC . . . . .	150
8.3	Conclusion and Recommendations . . . . .	151
<b>9</b>	<b>Airfoil Design Optimization Under Uncertainty</b>	<b>155</b>
9.1	Transonic Airfoil Design . . . . .	155
9.2	Deterministic Shape Optimization . . . . .	158
9.3	Shape Optimization Under Uncertainties . . . . .	160
9.4	Continuation Multilevel Monte Carlo Evolutionary Algorithm . . . . .	162
9.4.1	Covariance Matrix Adaptation Evolutionary Strategies (CMA-ES) . . . . .	163
9.4.2	Practical aspects: Evolution meets C-MLMC . . . . .	163
9.4.3	C-MLMC CMA-ES Algorithm . . . . .	166
9.5	Application to Single-Objective Optimization Under Uncertainties . . . . .	166
9.5.1	Maximization of Lift-Drag Ratio . . . . .	167
9.5.2	Minimization of Drag Coefficient . . . . .	171
9.6	Application to Multi-Objective Optimization Under Uncertainties . . . . .	178
9.6.1	Optimization of Lift and Drag . . . . .	178
9.7	Conclusions . . . . .	182
<b>10</b>	<b>Conclusions and Perspectives</b>	<b>183</b>
10.1	Conclusions . . . . .	183
10.2	Perspectives . . . . .	184

## Contents

---

<b>A Appendix</b>	<b>187</b>
A.1 Unbiased variance estimator for $p = 4$ for MC method . . . . .	187
A.2 Unbiased variance estimator on level $\ell$ for $p = 3$ . . . . .	188
<b>Bibliography</b>	<b>202</b>
<b>Curriculum Vitae</b>	<b>203</b>



# List of Figures

2.1	Aerodynamic forces and moments. . . . .	17
2.2	Real atmosphere temperature obtained from the ERA5 climate reanalysis dataset. . . . .	21
2.3	Real atmosphere instantaneous U and V wind component obtained from the ERA5 climate reanalysis dataset. . . . .	21
2.4	Comparison of the Standard Atmosphere (ISA) model with the real atmosphere temperature obtained from the ERA5 climate reanalysis dataset in three locations of the globe. . . . .	22
2.5	Overview of design, production and operation aspect that can have impact on the shape of aerodynamic systems. . . . .	25
2.6	Leading edge deformation with random Hicks-Henne bumps. . . . .	27
2.7	Deformation of an airfoil with FFD methodology. . . . .	28
2.8	PARSEC parameters for a RAE 2822 airfoil. . . . .	29
2.9	Random geometrical airfoil shapes (scale magnified) and corresponding grid deformation. . . . .	30
3.1	Graphical interpretation of propagation of uncertainties. . . . .	34
3.2	Pseudo random, LHS and Quasi Random (Halton's sequence) sample sets (512 points). . . . .	37
3.3	Tensor and Sparse grid based on Fejer nested quadrature points. . . . .	38
4.1	Difference between MC and MLMC. . . . .	45
4.2	Primal mesh (black) and control volumes in the dual mesh (blue). . . . .	52
4.3	Nested computational grids; close up view of the leading edge of an airfoil. . . . .	53
4.4	Grids adapted around the airfoil boundary. . . . .	53
4.5	Deterministic solutions for the NACA 0012 and NASA SC(2)-0012 airfoils at $M = 0.8$ . . . . .	55
4.6	Grids and realizations for the first three levels in the MLMC hierarchy for the NACA 0012 airfoil. . . . .	56
4.7	Mean $C_p$ profile and a band of uncertainty that corresponds to one standard deviation (68.27%) for the NACA 0012 and NASA SC(2)-0012 airfoils affected by 10 geometric uncertainties ( $R_p, R_S, X_P, X_S, Y_P, Y_S, C_P, C_S, \theta_P, \theta_S$ ). . . . .	57

**List of Figures**

---

4.8 Mean  $C_p$  profile and a band of uncertainty that corresponds to one standard deviation (68.27%) for the NACA 0012 and NASA SC(2)-0012 airfoils affected by 4 operating ( $M, \alpha, T_\infty, p_\infty$ ) and 10 geometric uncertainties ( $R_p, R_S, X_P, X_S, Y_P, Y_S, C_P, C_S, \theta_P, \theta_S$ ). . . . . 58

4.9 Levels and samples per level  $N_\ell$  required to achieve a relative tolerance of 0.01 on the total error for the  $C_p$  profile for the three NACA 0012 uncertainty scenarios. 59

5.1 Geometry and discretization of the convergent-divergent nozzle. . . . . 66

5.2 Deterministic solution (2051 uniform grid nodes) of the Laval nozzle with a normal shock in the diverging section ( $X_S = 0.8481$ ). . . . . 68

5.3 Mach number inside the nozzle (black line),  $X_{dM_+}$  (blue circle, maximum of the blue line ( $M(x_i) - M(x_{i+1})$ ),  $X_{dM_-}$  (red circle, minimum of the red line ( $M(x_i) - M(x_{i-1})$ ) and approximate shock position  $X_S$  (green square) for different levels. 70

5.4 C-MLMC iterations (0, 10, 13 and the final 14) for the estimation of  $\mathbb{E}[X_S]$  (3 operating uncertainties, final relative tolerance  $\varepsilon_r = 0.001$ ). The columns represent, from left to right, the bias, variance of  $Y_\ell$  and cost per level. . . . . 70

5.5 C-MLMC levels and samples per level for iterations 0, 10, 13 and the final 14 for the estimation of  $\mathbb{E}[X_S]$ . . . . . 71

5.6 Decay of  $\text{Var}[Y_\ell]$  for the C-MLMC (computed with Eq.(5.12) red solid line and LS fit blue dashed line) and  $\text{Var}[Q_\ell]$  for MC (black dashed line) for three different sets of uncertain parameters (final relative tolerance  $\varepsilon_r = 0.001$ ); lower row:  $N_\ell$  for different iterations of the C-MLMC . . . . . 72

5.7 Sensitivity of the number of levels and samples per level (left plot) and the accuracy of the final results of the C-MLMC simulation (right plot) on the choice of  $k_0$  and  $k_1$ . . . . . 73

5.8 C-MLMC iterations (0, 11, 12 and the final 13) for the estimation of  $\mathbb{E}[M(x)]$  (3 operational uncertainties and 2 geometrical, final relative tolerance  $\varepsilon_r = 0.01$ ). The columns represent, from left to right, the bias, variance of  $Y_\ell$  and the cost per level. . . . . 74

5.9 C-MLMC levels and samples per level for iterations 0, 11, 12 and the final 13 for the estimation of  $\mathbb{E}[M(x)]$ . . . . . 74

5.10 Decay of  $\|\text{Var}[\mathcal{Y}_\ell]\|_{L^1(D)}$  for the C-MLMC (computed with Eq.(5.12) red solid line and LS fit blue dashed line) and  $\|\text{Var}[\mathcal{Q}_\ell]\|_{L^1(D)}$  for MC (black dashed line) for three different sets of uncertain parameters (final relative tolerance  $\varepsilon_r = 0.001$ ); lower row:  $N_\ell$  for different iterations of the C-MLMC. . . . . 75

5.11 Mean Mach profile inside the nozzle (red solid line), *cloud* of uncertainty corresponding to one standard deviation (grey area) and deterministic solution (black solid line) for three different sets of uncertain parameters. . . . . 75

5.12 Cost (left plot) and accuracy (right plot) of MLMC with screening and C-MLMC for the computation of the scalar QoI  $X_S$  (shock position in the nozzle) with relative tolerance  $\varepsilon_r = 0.005$ . The lower bars in light green, blue and magenta in the left plot represent the cost of the screening phase. . . . . 76

5.13	Cost (left plot) and accuracy (right plot) of MLMC with screening and C-MLMC for the computation of the scalar QoI $X_s$ (shock position in the nozzle) with relative tolerance $\varepsilon_r = 0.001$ . The lower bars in light green, blue and magenta in the left plot represent the cost of the screening phase. . . . .	77
5.14	Cost required to achieve the prescribed tolerance requirements for C-MLMC (blue line) an MC (black line). The red dashed line represents the cost for a deterministic simulation achieving an error on the QoI of size $\varepsilon$ . . . . .	77
5.15	Geometry of the RAE 2822 transonic airfoil and PARSEC parameters. . . . .	78
5.16	Grids, Mach contour and $C_p$ profile around the RAE2822 airfoil for the first four levels in the MLMC hierarchy. . . . .	80
5.17	C-MLMC iterations (0, 11, 14 and the final 15) for the estimation of $\mathbb{E}[C_L]$ (2 operational uncertainties and 6 geometrical, final relative tolerance $\varepsilon_r = 0.003$ ). The columns represent, from left to right, the bias, variance of $Y_\ell$ , cost and number of samples per level. . . . .	81
5.18	C-MLMC levels and samples per level for iterations 0, 11, 14 and the final 15 for the estimation of $\mathbb{E}[C_L]$ . . . . .	82
5.19	Decay of $\text{Var}[Y_\ell]$ for the C-MLMC (computed with Eq.(5.12) red solid line and LS fit blue dashed line) and MC (black dashed line) for three different sets of uncertain parameters (final relative tolerance $\varepsilon_r = 0.003$ ); lower row: $N_\ell$ for different iterations of the C-MLMC . . . . .	82
5.20	Mean $C_p$ profile around the RAE2822 airfoil (red solid line) affected by increasing number of uncertainties, <i>cloud</i> of uncertainty corresponding to one standard deviation and deterministic solution. . . . .	83
5.21	Decay of $\ \text{Var}[\mathcal{Y}_\ell]\ _{L^1(D)}$ for the C-MLMC (computed with Eq.(5.12) red solid line and LS fit blue dashed line) and MC (black dashed line) for three different sets of uncertain parameters (final relative tolerance $\varepsilon_r = 0.05$ ); lower row: $N_\ell$ for different iterations of the C-MLMC . . . . .	84
5.22	Cost required to achieve prescribed tolerance requirements for C-MLMC (blue line) an MC (black line). The red dashed line represents the cost for a deterministic simulation at the finest level. . . . .	84
5.23	Cost required to achieve prescribed tolerance requirements for C-MLMC an MC for different sets of uncertainties. . . . .	85
5.24	Geometry of the RAE 2822 transonic airfoil and PARSEC parameters that define the geometry of the airfoil. . . . .	86
5.25	Details for the structured RAE-2822 grid setting. . . . .	88
5.26	Leading edge closeup view of level 0 and 1 grids for the RAE2822 problem. . . . .	88
5.27	Deterministic results for the RAE2822 airfoil. . . . .	89
5.28	Grid deformation to accommodate the geometric uncertainty. . . . .	89
5.29	Probability density functions of the operating (red) and geometric (blue suction side and green pressure side) parameters for the RAE2822 stochastic analysis. . . . .	90

## List of Figures

---

5.30	UQ analysis results for the RAE2822 presenting the mean pressure coefficient profile around the airfoil and its standard deviation. Experimental data from [VA79]. . . . .	91
5.31	C-MLMC hierarchies for two different sets of uncertain parameters (left) and aggregate computational cost compared with MC (right). The solid lines in the cost plot are an extrapolated model based on the rates and constants ( $\alpha, c_\alpha, \beta, c_\beta, \gamma, c_\gamma$ ) fitted in C-MLMC. The red and blue squares are the actual computed cost and error in the C-MLMC simulations. . . . .	92
6.1	Computed values of 100 repetitions of the MLMC algorithm compared with the reference solution (first row) and MLMC hierarchies (number of levels and sample size per level) required to achieve prescribed relative tolerance requirements when estimating the expectation and various central moments of the QoI $Q$ (second row) for the SDE problem. . . . .	110
6.2	Decay rates for the bias and variances of MLMC estimator with increasing $p$ for the SDE problem. . . . .	110
6.3	Computed values of 100 repetitions of the MLMC algorithm compared with the reference solution (first row) and MLMC hierarchies (number of levels and sample size per level) required to achieve prescribed relative tolerance requirements when estimating the expectation and various central moments of the QoI $Q$ (second row) for the Elliptic PDE problem. . . . .	112
6.4	Decay rates for the bias and variances of MLMC estimator with increasing $p$ for the Elliptic PDE problem. . . . .	112
6.5	Exemplary probability density functions of two uncertain operating input parameters for the random RAE-2822. . . . .	113
6.6	Airfoil LD PDFs. . . . .	116
6.7	Pressure coefficients $C_p$ of the RAE 2822 airfoil in the different conditions and uncertainty scenarios and the reconstructed lift-drag ratio $L/D$ distributions. . . . .	117
6.8	Computational complexity of MC and MLMC (in CPU hours) required to achieve a certain tolerance requirement for the first central moments. . . . .	118
7.1	CDF of $Q$ for the SDE problem showing an atom in $\{0\}$ . . . . .	133
7.2	Error vs. tolerance demand for different value of $\tau$ for the SDE problem. . . . .	133
7.3	MLMC hierarchies (number of levels and sample size per level) required to achieve prescribed relative tolerance requirements when estimating simultaneously VaR, CVaR and CDF of $Q$ for different value of $\tau$ for the SDE problem. . . . .	134
7.4	Decay rates for the bias and variances of MLMC estimator $P_H^{\text{MLMC}}(\vartheta)$ of $H_Q(\vartheta)$ for different value of $\tau$ for the SDE problem. . . . .	134
7.5	CDF of $Q$ for the Elliptic PDE problem. . . . .	135
7.6	MLMC hierarchies (number of levels and sample size per level) required to achieve prescribed relative tolerance requirements when estimating simultaneously VaR, CVaR and CDF of $Q$ for different value of $\tau$ for the Elliptic PDE problem. . . . .	136

7.7	Decay rates for the bias and variances of MLMC estimator $P_H^{MLMC}(\vartheta)$ of $H_Q(\vartheta)$ for different value of $\tau$ for the Elliptic PDE problem. . . . .	136
8.1	(a) NASA Rotor 37 and (b) computational model. . . . .	140
8.2	Experimental and computational compressor maps of the ROTOR-37. The green circles indicate the design parameters presented in the previous table. . . . .	141
8.3	Deterministic results for the ROTOR-37. Left: suction side; right: pressure side. . . . .	142
8.4	Uncertain total pressure and total temperature inlet profiles. The blue line represents the mean profile ( $\mu$ ), the shaded gray area is one standard deviation ( $\pm\sigma$ ) and the red lines are the upper and lower boundaries of the uncertain range ( $X_{LOW}, X_{UP}$ ). . . . .	143
8.5	Experimental, deterministic and stochastic results for the compressor map of the ROTOR-37. Each red interval correspond to mean $\pm$ standard deviation. . . . .	145
8.6	NASA CRM (WBT: wing body tail) geometry. . . . .	146
8.7	NASA CRM computational domain and details of the hybrid unstructured grid. . . . .	147
8.8	Comparison of CFD results obtained with the hybrid unstructured grids used in this study (black line), other CFD results obtained during the 5th AIAA DPW (pink region representative of mean $\pm$ standard deviation) and experimental measurements performed at the NASA Langley National Transonic Facility (NTF Test 197, green region) and the NASA Ames 11-ft transonic wind tunnel (Ames Test 216, blue region). On the right we report the moment coefficient obtained with our gird hierarchy. . . . .	148
8.9	Surface pressure and skin friction coefficient of the NASA CRM at $M = 0.85$ , $C_L = 0.5$ (upper and lower views). . . . .	149
8.10	Surface pressure and skin friction coefficient of the NASA CRM at $M = 0.85$ , $C_L = 0.5$ (upper and lower views). . . . .	150
8.11	Cumulative density function (CDF) of total drag $C_D^T$ , inviscid drag $C_D^I$ (pressure drag components), viscous drag (skin friction drag component) $C_D^V$ and moment coefficient $C_M$ for four different lift conditions $C_L = 0.3, 0.4, 0.5, 0.55$ for the NASA CRM under operating uncertainties. . . . .	151
8.12	Total drag $C_D^T$ , inviscid drag $C_D^I$ (pressure drag components), viscous drag (skin friction drag component) $C_D^V$ and moment coefficient $C_M$ mean $\pm$ 2 standard deviation for four different lift conditions $C_L = 0.3, 0.4, 0.5, 0.55$ for the NASA CRM under operating uncertainties. The total drag coefficient is compared with the experimental results performed at the NASA Langley National Transonic Facility (NTF Run 44, black circles). . . . .	152
9.1	Transonic flow features and comparison of conventional and supercritical airfoils. . . . .	156
9.2	Pressure profile at Mach 0.7 (left image) with center of pressure about 30% of the chord and pressure profile at Mach 0.875 (right image) with a center of pressure about 40% of the chord (from Boeing Airliner July 1959). . . . .	156

## List of Figures

---

9.3	NASA-Langley Whitcomb integral supercritical airfoil and RAE 2882 transonic airfoil shapes and drag coefficients for different Mach number at fixed lift ( $C_L = 0.5$ ). . . . .	157
9.4	Graphical interpretation of robust design optimization (RDO) and reliability-based design optimization (RBDO). . . . .	161
9.5	Geometrical trapezoid box constraint. . . . .	168
9.6	Performances of the SO-RDO1 and SO-DO1 airfoil compared with the original RAE-2822. The upper plots present the uncertain $C_p$ profile of the airfoils under operating and geometric uncertainties. The lower plots present the $L/D$ variation (mean $\pm$ two standard deviations). The diamond symbol represents the performance of the airfoil at design condition (airfoil operating at $M_\infty = 0.730$ , $\alpha_\infty = 2.31$ ). . . . .	170
9.7	Single Point optimization of the RAE 2822 airfoil for different cruise Mach number and fixed $C_L^* = 0.5$ . The thickness of the airfoils is constrained to be the same as the original RAE 2822 airfoil, while the other PARSEC geometrical parameters are free. . . . .	172
9.8	Multi Point optimization of the RAE 2822 airfoil for different choices of cruise Mach number and weights (fixed $C_L^* = 0.5$ ). The thickness of the airfoils is constrained to be the same as the original RAE 2822 airfoil, while the other PARSEC geometrical parameters are free. . . . .	173
9.9	Pressure coefficient $C_p$ (mean $\pm$ two standard deviations) and shape of the RAE 2822 (in black), the deterministic optimized shapes (SP in red and MP in magenta) and robust/reliable shapes obtained with different probabilistic loss functions (in green) under operating uncertainties. . . . .	176
9.10	CDF of the drag coefficient $C_D$ of the RAE 2822 (in black), the deterministic optimized shapes (SP in red and MP in magenta) and robust/reliable shape obtained with different probabilistic loss functions (in green) under operating uncertainties. . . . .	177
9.11	15 nodes FFD box for the RAE2822. . . . .	178
9.12	Deterministic and Robust Pareto fronts obtained by solving respectively the MO-DO1 and the MO-RDO1. The central plot is a blow-up view of the full Pareto. The red squares are the mean of $C_L$ and $C_D$ when the airfoils are operated in the uncertain environment, while the red ellipses are the dispersion around such mean values (two standard deviations). The green squares are the mean values of the robust optimal points and the green ellipses are their dispersion around such mean values (two standard deviations). Finally the black point and grey ellipse correspond to the RAE-2822 airfoil. . . . .	180

9.13 Deterministic and Robust Pareto fronts obtained by solving respectively the MO-DO1 (using PARSEC as design parameters) and the MO-RDO2. The central plot is a blow-up view of the full Pareto. The red squares are the mean of  $C_L$  and  $C_D$  when the airfoils are operated in the uncertain environment, while the red ellipses are the dispersion around such mean values (two standard deviations). The green squares are the mean values of the robust optimal points and the green ellipses are their dispersion around such mean values (two standard deviations). 181





# List of Tables

2.1	Parsec parameters and definitions (LE= leading edge; TE= trailing edge). . . . .	28
4.1	Operational and Geometrical parameters and uncertainties for the NACA 0012 and NASA SC(2)-0012 problems. . . . .	56
4.2	MLMC grid hierarchy for the NACA 0012 and NASA SC(2)-0012 cases. . . . .	57
4.3	MLMC computed rates and constants for the weak error, strong error and computational cost and theoretical cost models for MLMC and MC methods (obtained with a screening of 100 samples on 4 levels) for the airfoil problem with increasing number of uncertain parameters. . . . .	58
5.1	Operational and Geometrical parameters and uncertainties for the Laval nozzle problem. . . . .	67
5.2	MLMC 7-levels grid hierarchy for the nozzle problem. . . . .	68
5.3	Setting for the C-MLMC algorithm for the computation of the scalar QoI $X_s$ and the scalar field QoI $M(x)$ in the Laval nozzle test case. . . . .	69
5.4	Operational and Geometrical parameters and uncertainties for the RAE 2822 airfoil problem. . . . .	78
5.5	MLMC 5-levels grid hierarchy for the RAE2822 problem. . . . .	79
5.6	Settings for the C-MLMC algorithm for the computation of the scalar QoI $C_L$ and the scalar field QoI $C_p$ . . . . .	81
5.7	Geometric and Operating reference parameters for the RAE2822 problem. . . . .	86
5.8	MLMC 4-levels grid hierarchy for the RAE2822 problem. $CTime[s]$ is the real time in seconds required to compute one deterministic simulation on the prescribed number of cpus. . . . .	87
5.9	Operating and geometric uncertainties for the RAE2822 stochastic analysis. . . . .	90
6.1	Closed-form expressions of the unbiased estimators $\hat{V}_p/N$ for $\text{Var}[h_p(Q_{N,M})] = V_p/N$ , $p = 2, 3$ , as polynomial functions of the power sums $S_a \equiv S_a(Q_{N,M})$ . . . . .	99
6.2	Reference values for the expected value $\mathbb{E}[Q]$ and various central moments $\mu_p(Q)$ for the QoI $Q$ derived from the geometric Brownian motion SDE. . . . .	108
6.3	Sample estimate of relative root MSE based on 100 repetitions of the MLMC algorithm for computing $m_p^{\text{MLMC}}$ for different relative tolerance requirements. . . . .	109
6.4	Reference values for the expected value $\mathbb{E}[Q]$ and the first three central moments $\mu_p(Q)$ for the QoI $Q$ derived from the random Poisson problem. . . . .	111

## List of Tables

---

6.5	Sample estimate of relative root MSE of 100 repetitions of the MLMC estimators $m_p^{\text{MLMC}}$ for different relative tolerance requirements. . . . .	111
6.6	Operational and geometrical parameters as well as uncertainties for the RAE-2822 airfoil. . . . .	114
6.7	MLMC 5-levels grid hierarchy for the RAE2822 problem. . . . .	115
7.1	Quantiles and conditional values at risk for the quantity of interest associated with the geometric Brownian motion SDE. . . . .	133
7.2	Quantiles and conditional values at risk for the quantity of interest associated with random Poisson equation. . . . .	135
8.1	Design values for the NASA ROTOR-37 problem. . . . .	139
8.2	MLMC 4-levels grid hierarchy for the ROTOR-37 problem. $C\text{Time}[s]$ is the real time in seconds required to compute one deterministic simulation on the prescribed number of cpus. . . . .	140
8.3	Operating uncertainties for the ROTOR-37 stochastic analysis. . . . .	143
8.4	Deterministic and stochastic results for the ROTOR-37. . . . .	144
8.5	NASA CRM geometrical parameters. . . . .	146
8.6	Flow conditions and lift coefficient for the validation of the NASA CRM deterministic simulations. . . . .	148
8.7	MLMC 3-levels grid hierarchy for the NASA CRM. $C\text{Time}[s]$ is the real time required to compute one deterministic simulation on 280 CPUs. . . . .	148
8.8	Operating uncertainties and lift conditions for the NASA CRM stochastic analysis. . . . .	150
9.1	Deterministic loss functions and constraints for airfoil shape optimization problems. ( $SP$ ) indicate deterministic single point optimization problems solved for a single flight Mach number condition, while ( $MP$ ) indicates multi point deterministic optimization problems. . . . .	160
9.2	MLMC 5-levels grid hierarchy for the RAE2822 problem. . . . .	167
9.3	Operating parameters and uncertainties for the RAE2822 problem. . . . .	169
9.4	PARSEC parameters of the RAE2822 airfoil, and geometric uncertainties applied on the shape and design range for the geometric parameters. . . . .	169
9.5	Performances and variabilities (mean $\pm$ two standard deviations) of the SO-DO2 and SO-RDO2 airfoil compared with the original RAE-2822 at design conditions and when they operate in an uncertain environment. . . . .	170
9.6	Flight conditions and weight for deterministic multi point optimization. . . . .	173
9.7	Operating parameters and uncertainties for the RAE2822 problem. . . . .	174
9.8	PARSEC parameters of the RAE2822 airfoil and feasible design space range for the geometric parameters. . . . .	174
9.9	Probabilistic loss functions for problem SO-RDO2. . . . .	175

# List of Symbols

$\mathbf{u} = (u, v, w)$	velocity
$\rho$	density
$p$	static pressure
$\tau_{ij}$	viscous shear stress tensor component
$\mu$	dynamic viscosity
$\nu$	kinematic viscosity
$\kappa$	thermal conductivity
$\gamma_h$	ratio of specific heats
$E$	total energy
$H$	total enthalpy
$T$	Temperature
$\delta_{ij}$	Kronecker delta
$q_x, q_y, q_z$	heat flux components
$M, M_\infty$	Mach number
$Re, Re_c$	Reynolds number
$C_L$	lift coefficient
$C_D$	drag coefficient
$C_M$	moment coefficient
$C_p$	pressure coefficient
$C_F$	friction coefficient
$\omega$	random input data
$Q$	quantity of interest
$\mathcal{N}$	Normal distribution
$\mathcal{NG}$	Normal-Gamma distribution
$\mathcal{TN}$	Truncated Normal distribution
$\mathcal{B}$	Beta distribution
$\mathcal{U}$	Uniform distribution





## Acronyms

<b>UQ</b>	Uncertainty Quantification
<b>VVUQ</b>	Verification, Validation, and Uncertainty Quantification
<b>OUU</b>	Optimization Under Uncertainty
<b>QoI</b>	Quantity of Interest
<b>CFD</b>	Computational Fluid Dynamics
<b>CSM</b>	Computational Structural Mechanics
<b>M&amp;S</b>	Modeling and Simulation
<b>TRL</b>	Technology Readiness Level
<b>MC</b>	Monte Carlo
<b>MLMC</b>	Multi Level Monte Carlo
<b>C-MLMC</b>	Continuation Multi Level Monte Carlo
<b>RANS</b>	Reynolds-Averaged Navier-Stokes
<b>DOF</b>	Degrees of Freedom
<b>CLT</b>	Central Limit Theorem
<b>CPU</b>	Central Processing Unit
<b>VaR</b>	Value at Risk
<b>CVaR</b>	Conditional Value at Risk
<b>CRM</b>	Common Research Model
<b>RDO</b>	Robust Design Optimization
<b>SP</b>	Single Point
<b>MP</b>	Multi Point
<b>DO</b>	Deterministic Optimization
<b>RBDO</b>	Reliability Based Design Optimization
<b>CMA-ES</b>	Covariance Matrix Adaptation Evolutionary Strategy



*Nemo est tam fortis, quin rei novitate perturbetur*  
*(No one is so brave that he is not disturbed by something unexpected)*

*J. Caesar*





# 1 Introduction

## 1.1 The Need for Effective Uncertainty Management in Aeronautics

The increasing availability of computational resources, technological challenges and the *need for speed*<sup>1</sup> in product development fueled, in the last decades, the wide spread use of Modeling and Simulation (M&S) tools in design and decision making in the aerospace and defense industry.

The application of Computational Fluid Dynamics (CFD) simulations can effectively reduce the Time To Market, reduce the overall product development costs of disruptive technologies, and provide a better understanding of the operating behavior of aerospace systems. Nowadays, CFD, together with wind tunnel and flight tests, is definitely an essential tool in aerodynamic design [Rub94] [JTY05]. Additionally, the use of numerical methods for aerodynamic and structural design of transport aircraft configurations allows for an appropriate integration of relevant operational and safety-related features already in the early stage of the development process [Tin07].

An effective and accurate quantification and control of the level of uncertainty introduced in the M&S analysis, manufacturing and operation is imperative in order to design robust and risk tolerant systems. Such quantification should be available in reasonable time in order to timely respond to the military challenges, reducing the environmental impact of aeronautic transportation and the fierce industrial competition.

Several scientific, industrial and public institutions have sponsored round-robin studies to address the issue of accurate and timely effective uncertainty quantification and optimization under uncertainties in the aeronautic sector. Amongst them is the European Union 7th Framework Programme project UMRIDA (Uncertainty Management for Robust Industrial Design in Aeronautics) and the NATO Applied Vehicle Technology (AVT) group AVT-252 (Stochastic

---

<sup>1</sup>citing Rob Weiss, executive vice president and general manager of advanced development programs with Lockheed Martin Aeronautics (June 5th, opening plenary session - 2017 AIAA AVIATION Forum, Denver, USA) when it comes to war-fighting programs and military systems development.

Design Optimization for Naval and Aero Military Vehicles) which have both motivated (and funded) the study presented in this thesis. UMRIDA involves a consortium of 21 partners from the industrial aeronautics sector, research institutes, universities and small and medium-sized enterprises (SMEs) and aims at providing guidelines and improve the technology readiness level (TRL) of uncertainty quantification and robust based design methodologies in aeronautical industrial design. NATO AVT-252 is willing to promote and demonstrate the capabilities of stochastic design optimization approaches for real-world fluid, thermal and structural military system design affected by geometric and operating uncertainties. The aim of this program is to design configurations that are less sensitive to environmental variability and geometry imperfections due to manufacturing and aging.

### 1.2 Forward Propagation of Uncertainties

A possible way to describe and quantify the geometric and operating uncertainties is within a probabilistic framework. In such a setting, the uncertainties are characterized as random variables and propagated (forward propagation of uncertainties) into a computational model in order to quantify their effects onto relevant output quantities of interests such as the performances of an aerodynamics system.

Among the several forward uncertainty propagation approaches proposed in literature for fluid dynamics problems, we can distinguish between intrusive and non-intrusive approaches. The former involve the formulation and solution of a stochastic version of the original deterministic model, and hence usually require rewriting the simulation code, which is often impractical for large industrial CFD codes. For this reason, non-intrusive uncertainty propagation techniques are often preferred as they simply require multiple solutions of the original model and can use CFD flow solvers as black box.

Within non-intrusive approaches we can discern polynomial/collocation strategies and Monte Carlo sampling based methodologies. The former class includes methods based on local or global basis functions that are appropriately employed to approximate the uncertain system response. Such approaches have been successfully applied to propagate uncertainties in aerodynamics simulation, see e.g. [HW10] for regression type methods or [LB08] [LWB07] for stochastic collocation (interpolation) techniques. Although extremely efficient for smooth response functions and moderate number of uncertain parameters, they typically suffer the so called curse of dimensionality, i.e. the exponential increase of the cost with the number of uncertain variables. Moreover, they are not particularly efficient for problems whose solutions exhibit sharp gradients or discontinuities due to the development of shock waves and contact discontinuities as in hyperbolic systems of conservation laws (Euler and Navier-Stokes equations). Such discontinuities propagate into the stochastic space and inhibit the use of data compression techniques which are based on the regularity of the response function. Promising alternatives are given by adaptive multi-element [WK05], [FK10], multi wavelet [LMNP<sup>+</sup>07] and simplex stochastic collocation methods [WI13]. However so far these methods

have been applied to problems with non-smooth response functions with discontinuities not aligned with the coordinate axes only with few uncertain parameters and their extensions to moderate number of uncertain variables is still open. The same can be said to Padé type rational approximation proposed in [CDI09].

On the other hand, Monte Carlo (MC) sampling based methodologies have a dimension independent convergence rate, which is not affected by the presence of possible discontinuities in the parameter space, however, they are known to have a very slow convergence rate. For this reason they are generally impractical in complex applications that require the solution of accurate large scale CFD simulations. One way to improve the efficiency of MC simulations is the Multi Level Monte Carlo (MLMC) approach that has been introduced by Heinrich [Hei98, HS99] in the context of parametric integration and thereupon extended by Giles [Gil08] to approximate stochastic differential equations (SDEs) in financial mathematics. The key idea of MLMC is that one can draw MC samples simultaneously and independently on several approximations of the problem under investigation on a hierarchy of computational meshes (levels). By this way, most of the computational effort is transported from the finest level (as in a standard Monte Carlo approach) to the coarsest one, leading to substantial computational saving.

In this thesis we consider the Multi Level Monte Carlo approach and propose different extension of the original methodology in order to compute accurate statistics of quantities of interest of aerodynamic systems affected by uncertainties. In particular the extension we propose are effective methodologies for the accurate estimation of central statistical moments, cumulative distribution function and risk functions that involve Value at Risk (VaR) and Conditional Value at Risk (CVaR). These approaches are tested on benchmark problems and applied on industrial test cases relevant to turbo machinery and external aerodynamics.

### 1.3 Optimization Under Uncertainties

From the dawn of aviation, optimization always had a integral part in the aircraft design process. Aircraft producers are constantly operating and improving their systems in an industrial environment characterized by compromises between many competing factors and constraints. Designs are endlessly modernized and upgraded in order to meet the market requirements, customers and manufacturer demands, safety protocols and economic constraints.

Additionally, nowadays the ever-increasing demand for aircrafts with better performance, higher reliability and robustness at lower cost requires optimization techniques seeking optimality under uncertain conditions that may arise during design, manufacture and operation of the vehicle. The geometric and operating parameters, that characterize aerodynamic systems, are naturally affected by uncertainties due to the intrinsic variability of the manufacturing processes and the surrounding environment. Reducing the geometric uncertainties due to manufacturing tolerances can be prohibitively expensive while reducing the operating uncertainties due to atmospheric turbulence, for example in external aerodynamics, is simply

impossible.

Optimization under uncertainty refers to a broad class of methodologies that address the problem of improving the performance of a system while reducing its variability (robust design optimization) or increasing its reliability (reliability-based design optimization) under uncertain conditions.

In this thesis we first extend the MLMC concept to accurately compute central statistical moments and risk measures in order to efficiently compute robust and reliable objective functions and probabilistic constraints. Afterwards we propose a complete algorithm based on MLMC and (single and multi objective) evolutionary strategy to effectively design transonic airfoils whose performances are as much insensitive as possible to uncertainties.

### 1.4 Aim

The overall aim of this thesis is to extend the Multi Level Monte Carlo approach in order to perform accurate uncertainty quantification and optimization of the performances of aerodynamics systems modeled by Computational Fluid Dynamics (CFD) simulations. In order to be relevant for industrial problems, our endeavor is to present an accurate and robust methodology that can be efficiently employed to treat compressible viscous aerodynamic problems. Additionally, we wish to reduction of the overall computational cost required to set up and perform an uncertainty analysis in view of time effective decision making and optimization under uncertainties.

### 1.5 Thesis Outline

**Chapter 2** introduces the problem of uncertainty management in aerodynamic design, defines different types of geometric and operating uncertainties and justifies the assumptions and computational models employed in this work.

**Chapter 3** introduces the probabilistic framework and presents a review of relevant approaches for forward propagation of uncertainties.

**Chapter 4** presents the Multi Level Monte Carlo method, describes practical aspects and extensions of the original methodology, that are required in order to effectively perform the propagation of geometric and operating uncertainties in compressible inviscid aerodynamic problems.

**Chapter 5** describes the Continuation Multi Level Monte Carlo, presents a complete algorithm and different numerical experiments that show the reliability, robustness and efficiency of the continuation algorithm with respect to standard Multi Level Monte Carlo and Monte Carlo approaches. In the second part of the chapter, the Continuation Multi Level Monte Carlo method is applied in the specific setting of viscous compressible aerodynamics simulations.

Recommendations are provided in order to build effective Multi Level grid hierarchies for this class of problems.

**Chapter 6** presents an extension of the Multi Level Monte Carlo approach to compute central statistical moments required to effectively study important features of a random variable distribution.

**Chapter 7** provides a description of a Multi Level approach for the efficient approximation of parametric expectations. Specifically, this extension of the Multi Level Monte Carlo method allows an accurate and robust computation of an uncertain system output's cumulative distribution function, quantiles and conditional value at risk (CVaR).

**Chapter 8** presents the application of Multi Level Monte Carlo methodologies presented in the previous chapters to large scale industrial problems relevant in turbo machinery and external aerodynamics.

**Chapter 9** concentrates on airfoil design optimization under uncertainties. An effective algorithm based on the Continuation Multi Level Monte Carlo and Evolutionary Strategies for single and multi objective robust and reliability based design optimization is introduced and described. Detailed numerical studies relevant in transonic airfoil design under uncertainties are presented and discussed.

**Chapter 10** concludes the thesis, underlines the addition to state of the art knowledge of the topic and proposes future research opportunities.

*What we observe is not nature itself, but nature exposed to our method of questioning.*

*Werner Karl Heisenberg*

## 2 Uncertainty Management in Aerodynamic Design

The large majority of problems in aircraft production and operation require decisions made in the presence of uncertainty. Uncertainty Management (UM) is a branch of Risk Management that focuses on the evaluation of risk as the possibility of not matching the design and performance targets, suffering damage, failure and occurrence of any non-desirable event by considering all uncertainties affecting the design, development and operation of the system. UM includes Uncertainty Quantification (UQ) and Robust/Reliability-based Design Optimization (RDO/RBDO) techniques.

Deterministic optimization has always been an integral part in aerodynamic design. Nowadays the ever-increasing demand for aircrafts with better performance, higher reliability and robustness at lower cost requires RDO/RBDO techniques capable of seeking optimality under uncertain conditions that may arise during the conceptualization and the entire lifetime of the vehicle.

Additionally, in spite of the considerable success and prediction capabilities of Modeling and Simulation (M&S) tools, their use in high-impact decisions require a rigorous quantification of the errors and uncertainties introduced to establish objectively their predictive capabilities [Iac11].

### 2.1 Flow Models and Aerodynamic Coefficients

In this work we treat the problem of uncertainty propagation in aerodynamic systems operating in viscous and inviscid flows. We recall hereafter the main models used in this context.

### 2.1.1 Navier Stokes Equations

The dynamics of compressible viscous flows in a Cartesian coordinate system  $(x, y, z)$  can be described by the Navier Stokes equations in conservative form as:

$$\frac{\partial}{\partial t} W + \frac{\partial}{\partial x} (f_I - f_V) + \frac{\partial}{\partial y} (g_I - g_V) + \frac{\partial}{\partial z} (h_I - h_V) = 0, \quad (2.1)$$

where  $W$  is the vector of state variables:

$$W = \begin{bmatrix} \rho \\ \rho u \\ \rho v \\ \rho w \\ \rho E \end{bmatrix}, \quad (2.2)$$

$f_I, g_I, h_I$  are the convective inviscid fluxes:

$$f_I = \begin{bmatrix} \rho u \\ \rho u^2 + p \\ \rho uv \\ \rho uw \\ u(\rho E + p) \end{bmatrix}, \quad g_I = \begin{bmatrix} \rho u \\ \rho uv \\ \rho v^2 + p \\ \rho vw \\ v(\rho E + p) \end{bmatrix}, \quad h_I = \begin{bmatrix} \rho w \\ \rho wu \\ \rho wv \\ \rho w^2 + p \\ w(\rho E + p) \end{bmatrix} \quad (2.3)$$

with  $(u, v, w)$  denoting Cartesian components of the velocity vector  $\mathbf{u}$ .  $p$  denotes the pressure,  $\rho$  the density and  $E$  the total energy.

The viscous fluxes  $f_V, g_V, h_V$  are defined as:

$$f_V = \begin{bmatrix} 0 \\ \tau_{xx} \\ \tau_{xy} \\ \tau_{xz} \\ (\tau \mathbf{u})_x - q_x \end{bmatrix}, \quad g_V = \begin{bmatrix} 0 \\ \tau_{yx} \\ \tau_{yy} \\ \tau_{yz} \\ (\tau \mathbf{u})_y - q_y \end{bmatrix}, \quad h_V = \begin{bmatrix} 0 \\ \tau_{zx} \\ \tau_{zy} \\ \tau_{zz} \\ (\tau \mathbf{u})_z - q_z \end{bmatrix}. \quad (2.4)$$

In case of Newtonian fluids in local thermodynamic equilibrium the shear stress tensor  $\tau$  is defined as:

$$\tau_{ij} = \mu \left[ \left( \frac{\partial u_j}{\partial x_i} + \frac{\partial u_i}{\partial x_j} \right) - \frac{2}{3} (\nabla \cdot \mathbf{u}) \delta_{ij} \right] \quad (2.5)$$

with  $\mu$  denoting the dynamic viscosity of the fluid and  $\delta_{ij}$  the Kronecker delta.



## 2.1. Flow Models and Aerodynamic Coefficients

For a caloric perfect gas,  $\mu$  is computed from the Sutherland's law:

$$\frac{\mu}{\mu_{\infty}} = \left( \frac{T}{T_{\infty}} \right)^{3/2} \frac{T_{\infty} + S_1}{T + S_1} \quad (2.6)$$

where  $\mu_{\infty}$  is the viscosity at the reference temperature  $T_{\infty}$  and the constant  $S_1 = 110.3 [K]$  for air.

The heat flux components due to conduction  $q_x, q_y, q_z$  are given by the Fourier's law:

$$q_x = -k \frac{\partial T}{\partial x}, \quad q_y = -k \frac{\partial T}{\partial y}, \quad q_z = -k \frac{\partial T}{\partial z} \quad (2.7)$$

where  $T$  is the temperature and  $k$  the heat conductivity. Under the assumption of constant Prandtl number (defined as the ratio of momentum diffusivity to thermal diffusivity, for air  $Pr = 0.72$ ), the heat conductivity can be computed as:

$$k = \frac{\mu c_p}{Pr} \quad (2.8)$$

where  $c_p$  is the specific heat at constant pressure<sup>1</sup>.

Finally to close the system, the pressure  $p$  for a caloric perfect gas is obtained as:

$$p = \rho RT \quad \text{with } R = 287.0 [J/kgK] \quad \text{for air} \quad (2.9)$$

### 2.1.2 Euler Equations

When viscous forces are neglected, such as in inviscid flow, the Navier-Stokes equation in (2.1) can be simplified and the properties of the flow are described by the Euler equations:

$$\frac{\partial}{\partial t} W + \frac{\partial}{\partial x} f_I + \frac{\partial}{\partial y} g_I + \frac{\partial}{\partial z} h_I = 0. \quad (2.10)$$

In this work we consider as benchmark problems for inviscid flows mainly 2D and quasi-1D problems.

### 2D Euler Equations

In the case of 2D problems (2.10) reduce to:

$$\frac{\partial}{\partial t} W + \frac{\partial}{\partial x} f_I + \frac{\partial}{\partial y} g_I = 0 \quad (2.11)$$

---

<sup>1</sup>The specific heats at constant volume and constant pressure for a caloric perfect gas are obtained from  $c_v = \frac{R}{\gamma-1}$  and  $c_p = \gamma c_v$  respectively.  $\gamma = 1.4$  and  $R = 287.0 [J/kgK]$  for air

and the fluxes are defined as:

$$W = \begin{bmatrix} \rho \\ \rho u \\ \rho v \\ \rho E \end{bmatrix}, \quad f_I = \begin{bmatrix} \rho u \\ \rho v^2 + p \\ \rho uv \\ u(\rho E + p) \end{bmatrix}, \quad g_I = \begin{bmatrix} \rho v \\ \rho vu \\ \rho v^2 + p \\ v(\rho E + p) \end{bmatrix}, \quad (2.12)$$

### Quasi-1D Euler Equations

In the case of quasi-1D problems (2.10) reduce to:

$$\frac{\partial}{\partial t} W + \frac{\partial}{\partial x} f = Q \quad (2.13)$$

and with  $W$ ,  $f_I$  and  $Q$  defined as:

$$W = \begin{bmatrix} \rho A \\ \rho u A \\ \rho E A \end{bmatrix}, \quad f_I = \begin{bmatrix} \rho u A \\ (\rho u^2 + p) A \\ u(\rho E + p) A \end{bmatrix}, \quad Q = \begin{bmatrix} 0 \\ p \frac{dA}{dx_1} \\ 0 \end{bmatrix} \quad (2.14)$$

In quasi-1D problem, each grid node in the computational grid is associated with a certain area, denoted with  $A$ .

### 2.1.3 Finite Volume Approximation

In order to solve the above presented non-linear systems of conservation laws (Euler and Navier-Stokes) we employ in this work different Finite Volume (FV) methods. Since the probabilistic framework presented hereafter is completely black-box, different techniques such as Finite Element and Finite Difference methods can be also employed in the same fashion.

The pivotal feature of numerical methods to approximate compressible flow problems is the appropriate treatment of discontinuities or sharp gradients that naturally develop due to shock waves, contact discontinuities and rarefaction waves.

The numerical schemes should hence provide accurate solutions and avoid the creation of spurious oscillations or the smearing of those discontinuities over a large number of grid cells. Godunov [God59] showed that, in order to guarantee the monotonicity of the solution at discontinuities, a numerical scheme can not be of order higher than one (of accuracy). This implies that, the computational approach should be able to switch from high order of accuracy in large parts of the domain where the flow field is smooth, to first order in the vicinity of the discontinuities.

In order to ensures that the discretized equations capture discontinuities it is of primary

importance that the discretization of Navier Stokes and Euler equations satisfies the discrete version of the conservation laws. The integration of (2.1.1) over a domain  $\mathcal{D}$  yields to:

$$\int_{\mathcal{D}} \frac{\partial}{\partial t} W dV + \int_{\mathcal{D}} \nabla \cdot F dV = 0 \quad (2.15)$$

where  $F = (f_I - f_V, g_I - g_V, h_I - h_V)$  denotes the flux tensor. The application of the divergence theorem gives:

$$\int_{\mathcal{D}} \frac{\partial}{\partial t} W dV + \oint_{\partial \mathcal{D}} F \cdot \mathbf{n} dV = 0 \quad (2.16)$$

where  $\mathbf{n}$  is the unit normal pointing in the outward direction of the boundary  $\partial \mathcal{D}$  of the domain  $\mathcal{D}$ . The time rate of change of  $W$  in the domain  $\mathcal{D}$  is balanced by the fluxes entering and leaving at the boundaries  $\partial \mathcal{D}$ .

The conservation laws are discretized in this work on structured or unstructured grid depending on the application, the complexity of the geometry and the efficiency of a CFD solver in approximating the flow problem under investigation. For the sake of explanation, we restrict ourself in this section to structured grids and solvers, but the same concept can be applied to unstructured ones. Considering a discrete volume cell denoted with  $\mathcal{D}_{i,j,k}$  (with  $i, j, k \in \mathcal{I} \subset \mathbb{Z}^3$  denoting the address space in the structured grid) then (2.16) is approximated as:

$$\frac{d}{dt} (W^{i,j,k} V^{i,j,k}) + F^{i,j,k} = 0 \quad \forall i, j, k \in \mathcal{I} \quad (2.17)$$

with  $W^{i,j,k}$  denoting an approximation of the average value of the state vector in the cell (in the cell center),  $V^{i,j,k}$  the volume of the cell and  $F^{i,j,k}$  the net flux leaving the cell. In order to discriminate the inviscid and viscous fluxes contributions we write  $F^{i,j,k} = F_I^{i,j,k} + F_V^{i,j,k}$ .

As (2.17) suggests, the Euler and the Navier Stokes equations can be solved by employing a separate discretization in space and time (method of lines [RM94]). In a first step the flux integrals are evaluated on control volumes defined in a computational grid, afterwards the resulting system of ordinary differential equations are advanced in time, starting from a specified initial condition. On the other hand, if flow properties do not change in time, a steady-state solution is obtained by solving the governing equations by means of an iterative process.

In order to approximate the convective flux  $F_I$ , we employ in this work the second order central scheme of Jameson Schmidt Turkel (JST) (see [JST81] for more details). Compared to other more advanced approaches (Roe, HLLC see [Yee89]), the JST combines a satisfactory capability in capturing shock waves, a fairly rapid convergence to steady state and robustness also on coarse grids to approximate the convective flux. The latter is a pivotal feature, in order to apply our probabilistic uncertainty propagation framework, that strongly relies on the convergence of the flow quantities of interest on a hierarchy of computational grids.

### Turbulence Modeling

Despite the performance and the wide availability of large high performance computers (HPC), the direct simulation of the Navier Stokes equations (Direct Numerical Simulations, DNS) for turbulent flows is only limited to simple problems at very low Reynolds number. This is due to the excessive number of grid points required to achieve an appropriate spatial/temporal resolution in order to capture the chaotic fluctuations of the flow variables. For this reason, large scale complex aerodynamic problems at high Reynolds numbers can nowadays only be treated with turbulence models of different level of complexity; in this work we apply Favre-Reynolds Averaged Navier Stokes (F-RANS) models to approximate the turbulent viscous flow around aerodynamic systems.

By rewriting (2.1) in differential coordinate invariant form, using Einstein notation, we obtain:

$$\begin{aligned}
 \frac{\partial \rho}{\partial t} + \frac{\partial}{\partial x_i} (\rho u_i) &= 0 \\
 \frac{\partial}{\partial t} (\rho u_i) + \frac{\partial}{\partial x_j} (\rho u_i u_j) &= -\frac{\partial p}{\partial x_i} + \frac{\partial \tau_{ij}}{\partial x_j} \\
 \frac{\partial}{\partial t} (\rho E) + \frac{\partial}{\partial x_j} (\rho u_j H) &= \frac{\partial}{\partial x_j} (u_i \tau_{ij}) + \frac{\partial}{\partial x_j} \left( k \frac{\partial T}{\partial x_j} \right)
 \end{aligned} \tag{2.18}$$

with  $u_i$  denoting a velocity component of  $\mathbf{u} = (u_1, u_2, u_3)$ ,  $x_i$  a coordinate direction and  $H = E + \frac{p}{\rho} = h + \frac{1}{2} u_i u_i$  the total enthalpy.

In order to approximate turbulent viscous flows and solve (2.18) for the mean value of the flow quantities we apply the Reynolds averaging and the Favre averaging. Both methodologies are based on the intuitive decomposition of variables into mean and fluctuating part.

For a general flow quantity  $q$ , the Reynolds averaging [Rey94] procedure leads to a decomposition in mean and turbulent fluctuating part  $q = \bar{q} + q'$ . The mean part is obtained as:

$$\bar{q}(t) = \lim_{\Delta t \rightarrow \infty} \frac{1}{\Delta t} \int_t^{t+\Delta t} q(s) ds \tag{2.19}$$

As we are treating compressible flows, where density is not constant, we also apply Favre density weighted decomposition  $q = \tilde{q} + q''$ . The mean Favre average [Fav65] is obtained as:

$$\tilde{q}(t) = \frac{1}{\bar{\rho}} \lim_{\Delta t \rightarrow \infty} \frac{1}{\Delta t} \int_t^{t+\Delta t} \rho(s) q(s) ds \tag{2.20}$$

where  $\bar{\rho}$  is the Reynolds averaged density.

By applying the Reynolds average to velocity and pressure and the Favre average to the other

remaining flow quantities we obtain [Bla15]:

$$\begin{aligned}
 \frac{\partial \bar{\rho}}{\partial t} + \frac{\partial}{\partial x_i} (\bar{\rho} \tilde{u}_i) &= 0 \\
 \frac{\partial}{\partial t} (\bar{\rho} \tilde{u}_i) + \frac{\partial}{\partial x_j} (\bar{\rho} \tilde{u}_i \tilde{u}_j) &= -\frac{\partial \bar{p}}{\partial x_i} + \frac{\partial}{\partial x_j} (\tilde{\tau}_{ij} + \tau_{ij}^F) \\
 \frac{\partial}{\partial t} (\bar{\rho} \tilde{E}) + \frac{\partial}{\partial x_j} (\bar{\rho} \tilde{u}_j \tilde{H}) &= \frac{\partial}{\partial x_j} \left( k \frac{\partial \tilde{T}}{\partial x_j} - \bar{\rho} \widetilde{u_i'' h''} + \widetilde{\tau_{ij} u_i''} - \bar{\rho} \widetilde{u_j'' K} \right) + \frac{\partial}{\partial x_j} \left[ \tilde{u}_i (\tilde{\tau}_{ij} + \tau_{ij}^F) \right]
 \end{aligned} \tag{2.21}$$

where we denote with  $\tau_{ij}^F$  the Favre averaged Reynolds stress tensor defined as:

$$\tau_{ij}^F = -\bar{\rho} \widetilde{u_i'' u_j''} \tag{2.22}$$

and the Favre-averaged turbulent kinetic energy

$$\bar{\rho} \tilde{K} = \frac{1}{2} \bar{\rho} \widetilde{u_i'' u_j''}. \tag{2.23}$$

Following the Bussinesq eddy-viscosity hypothesis that assume that the turbulent shear stress is linearly related to the mean rate of strain (as in laminar flows), we can write:

$$\tau_{ij}^F = -\bar{\rho} \widetilde{u_i'' u_j''} = 2\mu_T \tilde{S}_{ij} - \left( \frac{2\mu_T}{3} \right) \frac{\partial \tilde{u}_k}{\partial x_k} \delta_{ij} - \frac{2}{3} \bar{\rho} \tilde{K} \delta_{ij} \tag{2.24}$$

with  $\tilde{S}_{ij}$  denoting the averaged strain rate. Thanks to this simplifying assumption, it is now only required to compute the turbulent viscosity  $\mu_T$  in order to close the system of equations.

In this work we employ the Spalart-Allmaras one-equation turbulence model [SA<sup>+</sup>94] to compute  $\mu_T$ . Based on empiricism, arguments of dimensional analysis, Galilean invariance, and calibrated using experimental measurements on flat-plate boundary layers and mixing layers, the Spalart-Allmaras turbulence model employs a transport equation for an eddy-viscosity quantity  $\tilde{\nu}$ :

$$\begin{aligned}
 \frac{\partial \tilde{\nu}}{\partial t} + \frac{\partial}{\partial x_j} (\tilde{\nu} u_j) &= C_{b1} (1 - f_{t2}) \tilde{S} \tilde{\nu} + \frac{1}{\sigma} \left\{ \frac{\partial}{\partial x_j} \left[ (\nu_L + \tilde{\nu}) \frac{\partial \tilde{\nu}}{\partial x_j} \right] + C_{b2} \frac{\partial \tilde{\nu}}{\partial x_j} \frac{\partial \tilde{\nu}}{\partial x_j} \right\} \\
 &\quad - \left[ C_{w1} f_w - \frac{C_{b1}}{\kappa^2} f_{t2} \right] \left( \frac{\tilde{\nu}}{d} \right)^2 + f_{t1} \|\Delta \mathbf{u}\|_2^2
 \end{aligned} \tag{2.25}$$

where  $\nu_L = \frac{\mu_i}{\rho}$  denotes the laminar kinetic viscosity and  $d$  the distance to the closest wall. The

production, destruction and laminar-turbulent transition terms are obtained from:

$$\begin{aligned}
 \tilde{S} &= f_{v3}S + \frac{\tilde{\nu}}{\kappa^2 d^2} f_{v2}, \\
 f_{v1} &= \frac{\chi^3}{\chi^3 + C_{v1}^3}, \quad f_{v2} = \left(1 + \frac{\chi}{C_{v2}}\right)^{-3}, \quad f_{v3} = \frac{(1 + \chi f_{v1})(1 - f_{v2})}{\max(\chi, 0.001)}, \\
 \chi &= \frac{\tilde{\nu}}{\nu_L}, \\
 f_w &= g \left( \frac{1 + C_{w3}^6}{g^6 + C_{w3}^6} \right)^{1/6}, \quad g = r + C_{w2}(r^6 - r), \quad r = \frac{\tilde{\nu}}{\tilde{S}\kappa^2 d^2}, \\
 f_{t1} &= C_{t1} g_t \exp\left(-C_{t2} \frac{\omega_t^2}{\Delta U^2} (d^2 + g_t^2 d_t^2)\right) \quad f_{t2} = C_{t3} \exp(-C_{t4} \chi^2), \\
 g_t &= \min\left[0.1, \frac{\|\Delta \mathbf{u}\|_2}{\omega_t \Delta x_t}\right].
 \end{aligned} \tag{2.26}$$

$\omega_t$  denotes the vorticity at the wall at a trip point,  $\|\Delta \mathbf{u}\|_2$  the 2-norm of the difference between the velocity at the trip and the actual point,  $d_t$  the distance to the nearest trip point and  $\Delta x_t$  the spacing along the wall at the trip point.

The constants are generally set to:

$$\begin{aligned}
 C_{b1} &= 0.1355, \quad C_{b2} = 0.622, \quad C_{v1} = 7.1, \quad C_{v2} = 5, \quad \sigma = \frac{2}{3}, \quad \kappa = 0.41 \\
 C_{w1} &= \frac{C_{b1}}{\kappa^2} + \frac{1 + C_{b2}}{\sigma}, \quad C_{w2} = 0.3, \quad C_{w3} = 2, \quad C_{t1} = 1, \quad C_{t2} = 2, \quad C_{t3} = 1.3, \quad C_{t4} = 0.5
 \end{aligned} \tag{2.27}$$

Finally, the turbulent eddy viscosity is obtained from  $\tilde{\nu}$  as

$$\mu_T = f_{v1} \rho \tilde{\nu} \tag{2.28}$$

We decided to employ this turbulence model, instead of more complex and accurate approaches, for the same reason presented above for the approximation of convective fluxes. The Spalart Allmaras provide reasonably accurate prediction of turbulent flows, and in particular has fast and robust convergence to steady state solutions with moderate wall grid resolutions.

### 2.1.4 Aerodynamic Quantities of Interest

In this work we concentrate on the effect of uncertainties on the performances of aerodynamic system. It is worth defining here the most relevant aerodynamic quantities of interest that will be considered in the following chapters.

First we introduce the dimensionless numbers that have an essential role in defining the

behaviour of fluids.

**Definition 1.** *Mach Number* is the ratio of the flow velocity and the local speed of sound

$$M = \frac{u}{c} \quad (2.29)$$

In a perfect gas the speed of sound is given by:

$$c = \sqrt{\gamma \frac{p}{\rho}} \quad (2.30)$$

**Definition 2.** *Reynolds Number* is the ratio of inertial forces to viscous forces within a fluid:

$$Re = \frac{\rho u L_{ref}}{\mu} \quad (2.31)$$

$L_{ref}$  is a characteristic length scale. For the applications presented hereafter  $L_{ref}$  corresponds to the chord length of a 2D airfoil or the mean chord length in case of an aircraft wing.

The fluid flowing around an aerodynamic shape generates a local force on each point of the body. The normal and tangential components of such force are the pressure  $p$  and the shear stress  $\tau$ . By integrating the force/stress distribution around the surface of the shape under investigation we obtain a total force  $F$  and a moment  $F_M$  about a reference point (center of pressure).

The parallel and perpendicular component of  $F$  with respect to the free-stream direction  $M_\infty$  are the lift  $F_L$  and drag  $F_D$  forces respectively (See Figure 2.1).

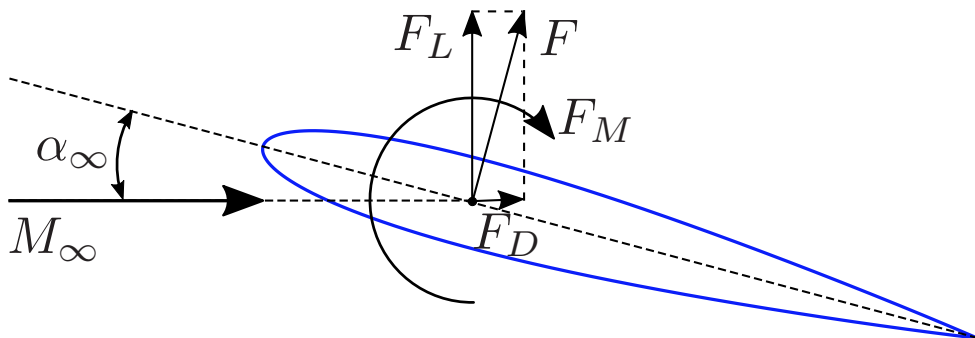


Figure 2.1 – Aerodynamic forces and moments.

For an aerodynamic shape with surface  $S$  we define the following lift, drag and moment

dimensionless coefficients:

$$C_L = \frac{F_L}{q_\infty S}, \quad C_D = \frac{F_D}{q_\infty S}, \quad C_M = \frac{F_M}{q_\infty S L_{ref}}. \quad (2.32)$$

with  $q_\infty = \frac{1}{2} M_\infty^2 \gamma p_\infty$  denoting the dynamic pressure.

Additionally in our simulations we also consider the pressure and skin friction coefficients defined as:

$$C_p = \frac{p - p_\infty}{q_\infty}, \quad C_F = \frac{\tau}{q_\infty}. \quad (2.33)$$

Here the subscript  $\infty$  refers to values far away from the shape where the fluid is assumed undisturbed.

## 2.2 Uncertainties in Aerodynamics

In this work we follow the definition of errors and uncertainties proposed by Oberkampf and Trucano in the SANDIA report on Verification and Validation in Computational Fluid Dynamics [OT02].

**Definition 3. Error** is a recognizable deficiency in any phase or activity of modeling and simulation that is not due to lack of knowledge.

Unacknowledged error are blunders or mistakes, such as programming errors, input data errors, and compiler errors. Acknowledged error are characterized by knowledge of divergence from an approach or ideal condition that is considered to be a baseline for accuracy such as finite precision arithmetic in a computer and conversion of PDEs into discrete equations. The estimation and control of the former is not straightforward while the latter can be measured as their origins are fully identified.

**Definition 4. Uncertainty** is a potential deficiency in any phase or activity of the modeling process that is due to lack of knowledge.

The term uncertainty can be used to identify the estimated amount or percentage by which an observed or calculated value may differ from the true value but also in term of prediction of future events and the estimation of the reliability of systems.

In order to establish the quality and validity of decisions made in presence of errors and uncertainties, Verification and Validation (V&V) procedures have been organized and proposed by authorities and institutions in different engineering fields [Ste16] [DoD08], [OT07], [TDH<sup>+</sup>04], [SK00], [ASM09], [ASM06].



**Definition 5. Verification** is the process of determining that a model implementation accurately represents the developer's conceptual description of the model and the solution to the model.

**Definition 6. Validation** is the process of determining the degree to which a model is an accurate representation of the real world from the perspective of the intended uses of the model.

Uncertainties are generally classified into two categories: epistemic and aleatory.

**Definition 7. Epistemic uncertainties**, also known as reducible or model uncertainties, originate from some level of ignorance or lack of knowledge and can be reduced with an increase in knowledge, additional experimental data or understanding of complex physical processes. Examples are turbulence model or chemical gas/fluid assumptions.

**Definition 8. Aleatory uncertainties**, also known as variability or irreducible uncertainties, describe the natural inherent variations associated with the physical system or the surrounding environment and cannot be reduced. Examples are the material properties, the operating conditions, manufacturing tolerances, etc.

## 2.3 Epistemic Uncertainties in Aerodynamic Design

The mathematical and numerical models employed to predict the performances of aerodynamic systems inherently introduce some sort of assumptions and simplifications in order to reduce the computational efforts and provide converged numerical results for the CFD simulations. The effect of such simplifications on the accuracy of predicted quantities can be generally controlled but sometimes can lead to unexpected large discrepancies.

Due to their reasonable computational cost, compared to Large Eddy Simulations (LES) and Direct Numerical Simulation (DNS), Reynolds-Averaged Navier-Stokes (RANS) turbulence models are nowadays the only viable option to predict viscous flows around large scale complex aerodynamic shapes. In addition to the Reynolds averaging of the full Navier Stokes equations, all RANS models introduce some sort of semi-empirical turbulent closure [W<sup>+</sup>98] for the transport equations. Hence, the effect of modeling uncertainties and the empiricism of RANS model due to their flow specific calibration from experimental data should be controlled and appropriately accounted for simulations used for high impact decisions. The misspecification of the turbulence model constants, that have been derived and designed to fit a specific set of experimental data, which in turn are affected by uncertainties, for a given range of applications, can lead to large errors. The effect of surface curvature, can also play an important role in defining the range of validity of a set of model constants or turbulence models. Additionally the results of RANS simulations are generally very sensitive to grid and simulation setup parameters. In order to reduce the dependency of RANS simulation results with respect to all these above mentioned factors Best Practice Guidelines (BPG) [CW00] [MCM03] and Verification and Validation (V&V) methodologies [OTH04] [SWCP99], [SWCP01] have been proposed since the introduction of RANS in industrial design.

A common practice in aerodynamics simulations is the fixing of transition at a set of locations in order to compare the results with experimental data, where a trip at a fixed location has been used. Obviously the location and the eventuality that transition might likely to occur naturally, could lead to difficulties of interpretation and discrepancies in experimental and computational results. [ETD07]

Such epistemic uncertainties, whose distributions are generally not available, are usually treated with interval analysis [Kea96] or with membership functions in a fuzzy logic framework [MV02, WA03].

### 2.4 A Taxonomy of Aleatory Uncertainties in Aerodynamic Design

In this work we concentrate on UQ and Optimization under Uncertainty (OUU) of aerodynamic systems affected by aleatory uncertainties. These uncertainties have to be taken into account to achieve and guarantee the highest safety standards and to design aerodynamic systems whose performance is unchanged when exposed to variabilities. Indeed, the geometric and operating parameters, that characterize aerodynamic systems, are naturally affected by aleatory uncertainties due to the intrinsic variability of the manufacturing processes and the surrounding environment. Reducing the geometrical uncertainties due to manufacturing tolerances can be prohibitively expensive while reducing the operational uncertainties due to atmospheric turbulence is simply impossible.

We believe it is useful to distinguish these two sources of uncertainties in order to provide an appropriate description and methodology to treat them in a computational probabilistic framework.

#### 2.4.1 Operating Uncertainties

With *operating uncertainties* we denote the natural environmental variability of the flow surrounding an aerodynamic system.

In external aerodynamic problems the inherent atmospheric fluctuations, the mission flight profile deviation from design scenarios and transition strip location are the main factors affecting the flow surrounding an aircraft. For example, the non homogeneous properties of the atmosphere with respect to location (see Figure 2.2 and Figure 2.3), time and wind directions, are often neglected and the preliminary design of an aircraft is performed using simplified model such as the standard atmospheres.

In Figure 2.4 we compare the air temperature obtained from the International Standard Atmosphere (ISA) model [Atm75] and the real atmosphere temperature obtained from the ERA5 climate reanalysis dataset [Gib97]. We choose three locations on the globe representative of a international transatlantic flight from Geneva to Miami and compare the temperature fluctuations the 1st of January 2015 and the 1st of July 2015. As it is possible to observe, up

## 2.4. A Taxonomy of Aleatory Uncertainties in Aerodynamic Design

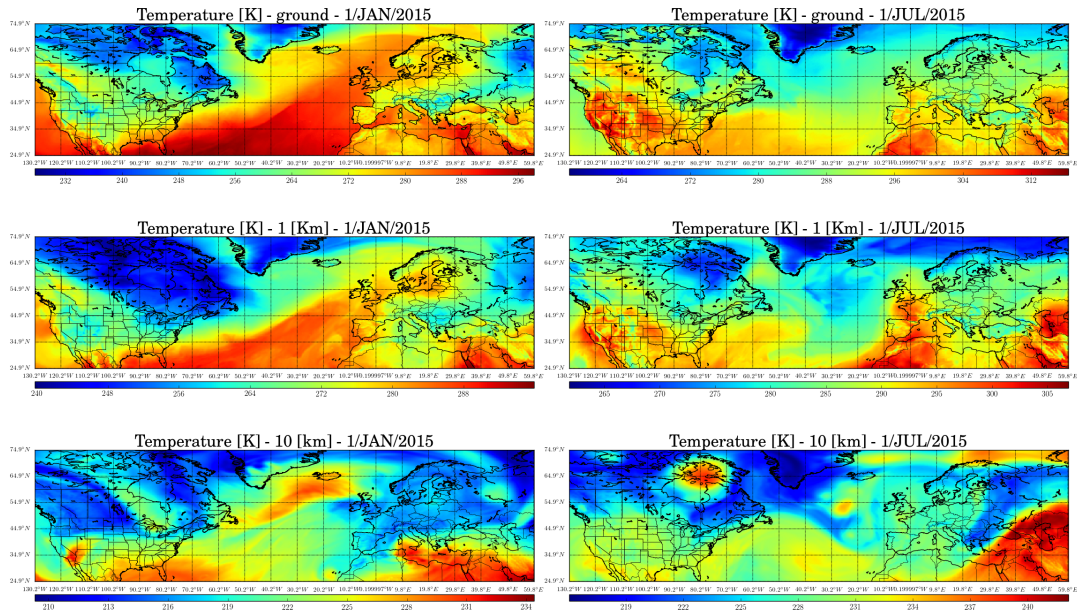


**Figure 2.2** – Real atmosphere temperature obtained from the ERA5 climate reanalysis dataset.

to 30 degrees Kelvin deviations are present between the model and the real reanalysis data. Additionally it is worth underline, in particular in Geneva and Greenland, a sensitive seasonal variation in temperature below 10 km of altitude.

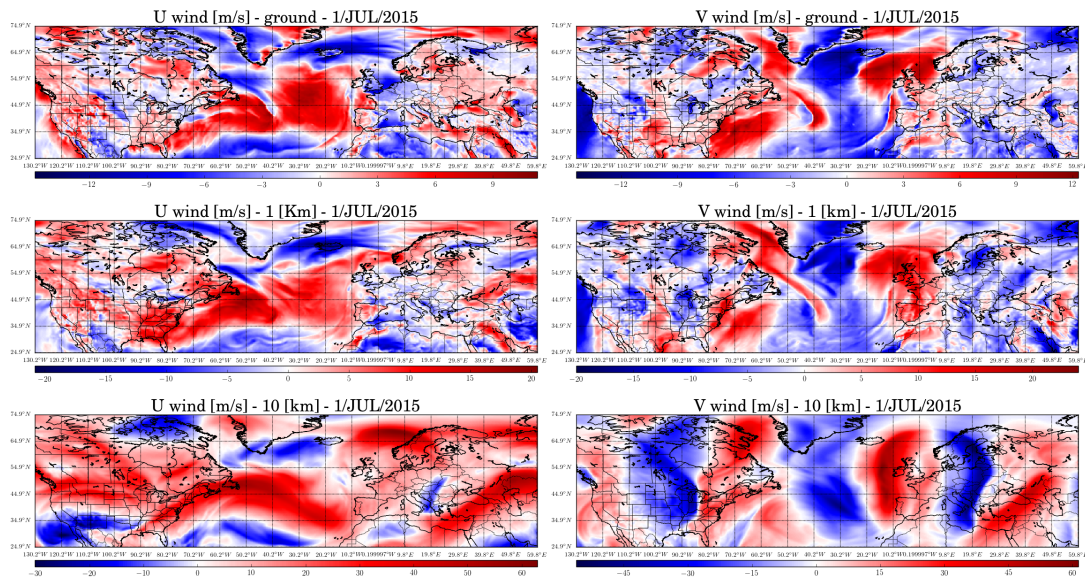


**Figure 2.3** – Real atmosphere instantaneous U and V wind component obtained from the ERA5 climate reanalysis dataset.

On the other hand, in internal aerodynamic problems, the inlet flow profile, inflow/outflow

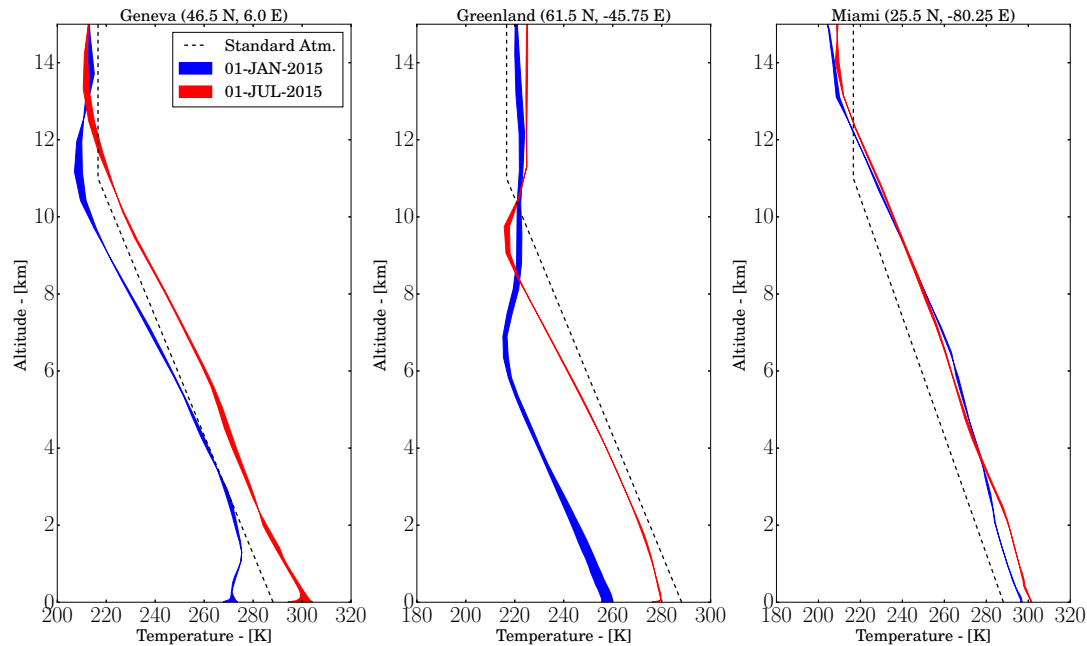


**Figure 2.4** – Comparison of the Standard Atmosphere (ISA) model with the real atmosphere temperature obtained from the ERA5 climate reanalysis dataset in three locations of the globe.

boundary conditions and combustion instabilities are generally the main sources of variability in aircraft engines. Uniform characteristic profiles are generally considered in absence of appropriate experimental data, but only for few discrete operating points and atmospheric conditions.

In order to account for those uncertainties in our computational probabilistic framework we consider the following flow parameters as uncertain:

- **Mach number**
- **Reynolds number**
- **Angle of Incidence**
- **Total and Static Temperature**
- **Total and Static Pressure**

Depending on the type of analysis and the goal of a specific set of simulations we prescribe probability distributions for the above mentioned parameters. Once the distributions are defined we propagate the input uncertain parameters into the computational model in order to measure their effects on specific performance indexes or quantity of interest (QoI) relevant for the problem.

## 2.4. A Taxonomy of Aleatory Uncertainties in Aerodynamic Design

---

Even small variations of such parameters during an extended cruise phase can have large impact on the fuel consumption and the performances of an aircraft during a mission.

### 2.4.2 Geometric Uncertainties

With *geometric uncertainties* we denote the variabilities related to the geometry of the aerodynamic system. The factors that can affect the external shape of an aircraft or the internal geometry of an engine are multiple and may appear in different time frames during their entire lifetime.

Starting from the initial design, a generic parametrization (e.g. Parsec or Bezier parametrization of an airfoil) of an aerodynamic shape is generally converted to Computer-Aided Design (CAD) models using appropriate geometrical surface model such as Non-Uniform Rational Basis Spline (NURBS). Aircraft wings and turbine/compressor blades are complex 3D shapes obtained by stacking together many elementary 2D profiles. Some sort of smoothing is required in order to obtain a final continuous shape.

The CAD model is then imported into Computer-Aided Manufacturing (CAM) environments and the aerodynamic parts are actually produced and machined through complex manufacturing chains in different factories and even countries as in the case of large multinational aircraft producers. The final parts that fulfill tolerance and quality requirements are then assembled together.

Alternative machining and manufacturing techniques that differ in terms of cost and accuracy are applied in order to fulfill the pivotal trade-off in aircraft industrial production between precision, reliability and manufacturing cost. A detailed study on the influence of tolerances on aerodynamic surfaces and operating costs can be found in [CKRM02] and [CKR<sup>+</sup>03].

During their actual lifetime the shape and surface roughness of aircraft wings and turbine/compressor blades can change dramatically due to:

- Temporary factors: wing twist under different loadings (aeroelastic), icing.
- Permanent/degrading factors: wear and tear, corrosion, erosion, fouling, impacts with particle and animals (e.g. hail and birds impacts), maintenance processes (panels, rivets and hatches).

Figure 2.5 provides an overview of the geometrical aspects that can affect the shape of an aircraft during design, production and operation.

Practically speaking there will always be uncertainties associated with the location of every point on the surface of an aerodynamic object designed with parameterized models, produced, assembled and operating in an inherently uncertain environment.

As the number of possible shape deviations is unlimited and some sort of assumptions are

## **Chapter 2. Uncertainty Management in Aerodynamic Design**

---

needed in order to account for geometric uncertainties in a computational framework, we consider in this work only a limited set of parameters.

It is worth underline that the range of variability used for the simulations presented in the following chapters have been derived during the UMRIDA European FP7 collaborative project thanks to the inputs of industrial aeronautics partners and are representative of manufacturing/assembling tolerances and temporary factors that take place during the operation of an aircraft.

In order to account for those uncertainties in our computational probabilistic framework we consider the following geometrical parameters as uncertain:

- **Leading edge radius**
  
- **Leading and trailing edge sweeps**
  
- **Airfoil/Wing thickness**
  
- **Pressure/Suction curvature**
  
- **Surface Roughness**

Small variations of such parameters can have large impact on the fuel consumption and the performances of an aircraft during its entire lifetime.

## 2.4. A Taxonomy of Aleatory Uncertainties in Aerodynamic Design

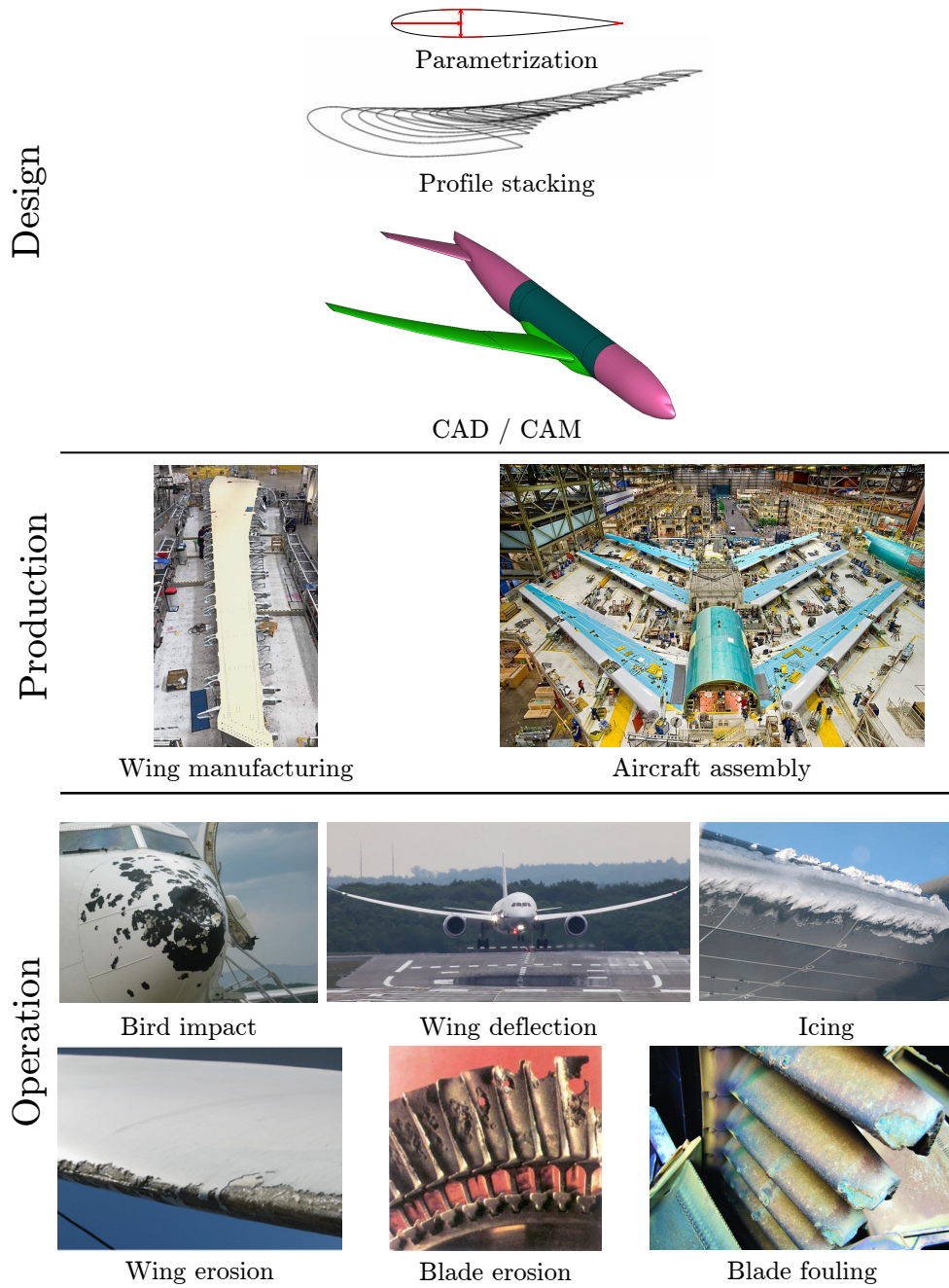


**Figure 2.5** – Overview of design, production and operation aspect that can have impact on the shape of aerodynamic systems.



### 2.4.3 Treatment of Geometric Uncertainties

In this work we treat airfoils and aircraft wings affected by geometrical uncertainties due to manufacturing tolerances, icing, impacts, erosion and wing deflections. Such uncertainties can be local (as in case of icing) or affect the the entire geometry (as in manufacturing and deflections due to differential loadings). Depending on the type of uncertainties, the amplitude of the defects and the problem under investigation, we considered in this work different methodologies in order to include and integrate the above mentioned geometric uncertainties in a computational probabilistic framework.

The purpose of a geometric parametrization is to provide an effective and efficient approach to manipulate the shape of aerodynamic systems using a limited number of coefficients. Masters et al. [MTR<sup>+</sup>15] categorize aerodynamic shape parameterizations and distinguish between constructive and deformative approaches.

The **constructive** class include methodologies that define airfoil and wing shapes from a set of parameters and includes splines [BF84], Class-Shape function Transformation (CST) [KB<sup>+</sup>06] and the Parameterized Sections (PARSEC) approach [Sob99].

**Deformative** approaches on the other hand, need an initial airfoil shape and deform it into a new shape. Examples are the discrete approach of Jameson [Jam88], Hicks-Henne bump functions [HH78] and the free-form deformation (FFD) [SP86] [Sam04] methods.

In the UQ computational framework presented in this work we apply the Hicks-Henne bumps to treat local perturbations that arises due to icing, impacts and erosion, the FFD to treat mainly deformation due to wing deflections and constructive methodologies such as the PARSEC parametrization to propagate uncertainties due to manufacturing tolerances.

**Hicks-Henne** From a initial "nominal" airfoil shape (defined as  $y_0 = \pm S(x_0)$  coordinates), the Hicks-Henne bump approach add/subtract a linear combination of  $n$  basis functions to its contour to generate a new deformed shape  $(x_0, y_D)$ :

$$y_D = y_0 \pm \sum_{i=0}^n c_i \psi_i(x_0). \quad (2.34)$$

$c_i$  are weighting coefficients and  $\psi_i$  are the sine basis functions defined as:

$$\psi_i(x_0) = \sin^{t_i}(\pi x_0^{m_i}) \quad \text{with} \quad m_i = \frac{\ln(0.5)}{\ln(x_{MAX_i})} \quad (2.35)$$

where  $x_{MAX_i}$  is the location of the maximum/minimum of the  $i$ -th bump and  $t_i$  its width.

Even for local perturbations, this approach provides smooth local modifications to the original airfoil shape (see Figure 2.6) and can be effectively used to propagate uncertainties (such as geometrical uncertainties due to icing) but also in an optimization framework to design



radical new shapes.

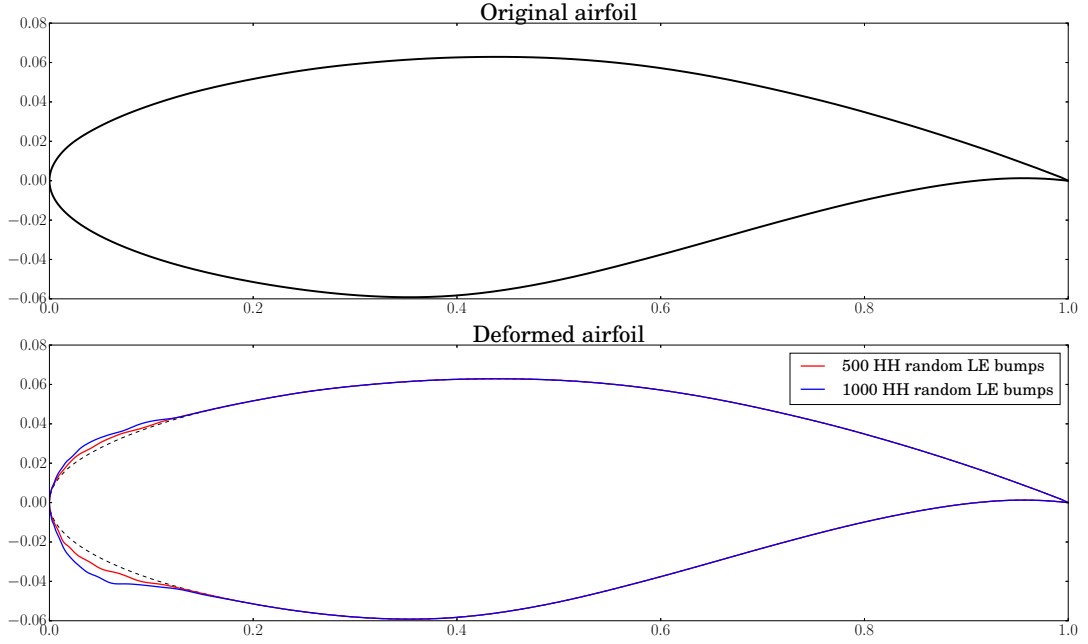


**Figure 2.6** – Leading edge deformation with random Hicks-Henne bumps.

**Free-Form Deformation (FFD)** The FFD methodology have been first introduced as computer graphics 3D morphing technique [SP86] and afterwards proposed in the context of aerodynamic optimization [PBL98]. The approach is based on the intuitive idea of expressing the deformation from an initial nominal shape by the displacement of an embedding control box. The competitive advantage of this approach is that as the external box is deformed, the embedded objects are deformed too with the same degree of flexibility. This is particularly appealing when the FFD approach is applied on CFD grid boundaries. The airfoil/wing shape and the computational grid surrounding it can be smoothly deformed in just one step.

Considering the local curvilinear coordinates  $\mathbf{x} = (s, t, u)$  mapped into the control box (lattice coordinates), the displacement  $\delta(\mathbf{x})$  of any point inside the control box is defined as:

$$\mathbf{x} + \delta(\mathbf{x}) = \sum_{i=1}^l \sum_{j=1}^m \sum_{k=1}^n \mathbf{B}_{l-1}^{i-1}(s) \mathbf{B}_{m-1}^{j-1}(t) \mathbf{B}_{n-1}^{k-1}(u) (\mathbf{P}_{i,j,k} + \mathbf{D}_{i,j,k}) \quad (2.36)$$

where  $\mathbf{B}_{l-1}^{i-1}(s)$  is the  $(i-1)$ -th Bernstein polynomial of degree  $l-1$  [YMC08].  $\mathbf{P}_{i,j,k}$  and  $\mathbf{D}_{i,j,k}$  are the matrices of original coordinates and displacements for the node points  $(i, j, k)$  of the control box defined by  $n_{cp} = l \cdot m \cdot n$  control points.

Starting from the local curvilinear coordinates of the points embedded by the control box and

the blending functions  $B$ , once the external box is deformed (update of  $D_{i,j,k}$  see Figure 2.7), the location of all nodes inside it are obtained from (2.36).

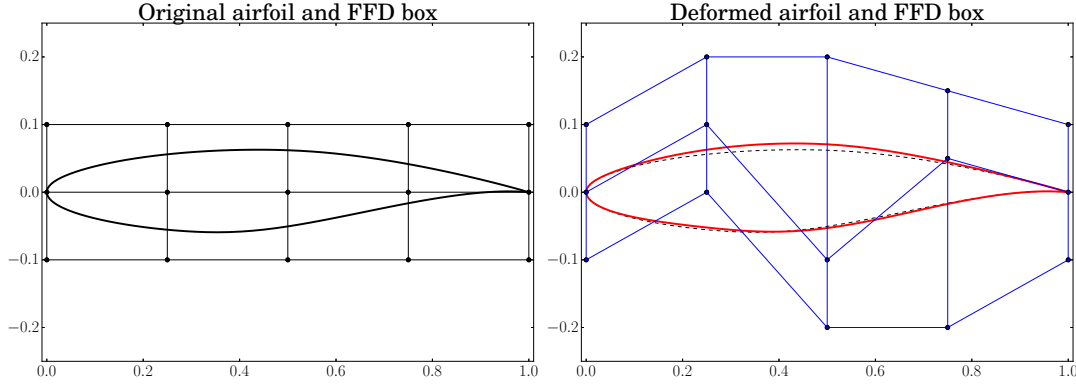


Figure 2.7 – Deformation of an airfoil with FFD methodology.

**PARSEC** The PARSEC approach is a constructive parametrization methodology proposed by Sobieczky [Sob99] to introduce more engineering relevant and geometrically intuitive airfoil parameters in the design process. The suction ( $x, y_s$ ) and pressure ( $x, y_p$ ) side of an airfoil shape is defined by 6th order polynomials:

$$y_s(x) = \sum_{i=0}^6 s_i x^{i-0.5}, \quad y_p(x) = \sum_{i=0}^6 p_i x^{i-0.5}, \quad (2.37)$$

The free parameters are the PARSEC parameters presented in Table 2.1. The shape of the airfoil (2.37) is determined by solving the set of 12 (nonlinear) equations for the coefficients  $s_i$  and  $p_i$ ,  $i = 1, \dots, 6$  given the PARSEC parameters (see right column Table 2.1).

Parameter	Symbol	Definition
Pressure LE radius	$R_p$	$p_1$
Suction LE radius	$R_s$	$s_1$
Pressure Crest position	$X_p$	$y'_p(X_p) = 0$
Suction Crest position	$X_s$	$y'_s(X_s) = 0$
Pressure Crest hight	$Y_p$	$y_p(X_p)$
Suction Crest hight	$Y_s$	$y_s(X_s)$
Pressure Crest curvature	$C_p$	$y''_p(X_p)$
Suction Crest curvature	$C_s$	$y''_s(X_s)$
TE angle	$\theta_s$	$y'_s(x_s = 1) = -\tan(\theta_s + \frac{\theta_p}{2})$
Boat-tail angle	$\theta_p$	$y'_p(x_p = 1) = -\tan(\theta_s - \frac{\theta_p}{2})$
TE offset	$Y_{TE}$	$y_p(x_p = 1)$
TE thickness	$\Delta Y_{TE}$	$y_s(x_s = 1) - y_p(x_p = 1)$

Table 2.1 – Parsec parameters and definitions (LE= leading edge; TE= trailing edge).

## 2.4. A Taxonomy of Aleatory Uncertainties in Aerodynamic Design

It is worth underlying that in our framework we set the trailing edge offset  $Y_{TE}$  and the trailing edge thickness  $\Delta Y_{TE}$  to zero. Hence the airfoil shapes are identified by 10 parameters as presented in figure 2.8.

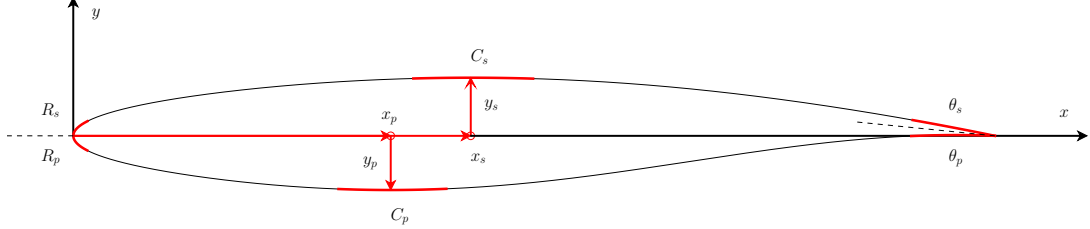


**Figure 2.8** – PARSEC parameters for a RAE 2822 airfoil.

Thanks to the intuitive nature of such parametrization and the direct link between parameters and airfoil geometry we are able to prescribe appropriate uncertainties due to manufacturing tolerances directly to the PARSEC parameters.

### Mesh Deformation

For each random geometrical realization obtained by sampling the appropriate coefficients of the parametrizations presented above we need to perform a CFD simulation in order to compute the performances or QoI of the aerodynamic shape. In order to avoid computationally demanding and sometimes inappropriate grid re-generation for each realization of the random shape, we deform an existing "nominal grid" by solving a linear elasticity problem. The elasticity problem is solved on the volume grid to accommodate the new boundary definition.

Each edge of the mesh is replaced by a spring with stiffness inversely proportional to the edge length [Bat90]. By applying Hook's law, the displacement of node (denoted  $\delta_i$ ), surrounded by  $n_i$  neighbors nodes, is computed iteratively as:

$$\delta_i^{k+1} = \frac{\sum_{j=1}^{n_i} \kappa_{ij} \delta_j^k}{\sum_{j=1}^{n_i} \kappa_{ij}} \quad (2.38)$$

and applying the known displacements at the boundaries (see Figure 2.9) resulting from the difference between the deterministic (reference) shape and a random realization.  $\kappa_{ij}$  denotes the stiffness of the spring between node  $i$  and  $j$ .

In case of geometrical uncertainties due to manufacturing tolerances we don't expect large displacements in the volume grid. Other types of geometrical uncertainties (e.g. due to icing) may promote larger displacements in the volume grid and the edges may cross each other, leading to negative grid volumes. To overcome such eventuality it is required to include torsional

springs at the corner between adjacent edges [FDKL98] to prohibit the inter-penetration of neighboring grid triangles.

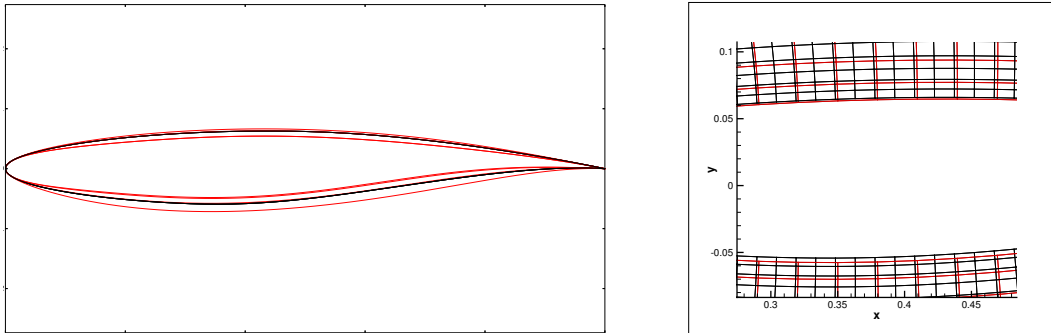


**Figure 2.9** – Random geometrical airfoil shapes (scale magnified) and corresponding grid deformation.

*What we observe is not nature itself, but nature exposed to our method of questioning.*

*Werner Karl Heisenberg*



# 3 Uncertainty Propagation

In this chapter we introduce the notation and the main ideas of propagation of uncertainties in aerodynamics simulations followed by a brief overview of polynomial and sampling based methodologies.

## 3.1 Probabilistic Framework

As presented in the previous chapter, the geometric and operating parameters that define the shape of an aerodynamic system and the surrounding environment cannot be defined deterministically, therefore we treat them as random quantities. Hereafter we characterize such random quantities by a complete probability space  $(\Omega, \Sigma, P)$ , with  $\Omega \subset \mathbb{R}^n$ .

**Definition 9.** *A complete probability space is a mathematical framework that models processes or experiments that occur randomly.  $\Omega$  is called sample space and is the set of all possible outcomes of an experiment,  $\Sigma$  is a non-empty collection of subsets of  $\Omega$  called events ( $\sigma$ -algebra) and the probability measure  $P : \Sigma \rightarrow [0, 1]$  assigns a probability to each event.*

Hence the random quantities are characterized as a random vector  $\omega \in \mathbb{R}^n$  taking values in  $\Omega$  and for which the probability  $P(\omega \in B)$  of any event  $B \in \Sigma$  is given.

It is worth underlining once and for all that the existence of the above mentioned probability space will be implicitly assumed without loss of generality and that the probability measure of the random vector  $\omega$  is known. We also assume to be able to generate independent samples from such probability measure.

In this work we mainly consider aerodynamic problems modeled by partial differential equations (PDEs) defined on a generic physical space  $D \subset \mathbb{R}^d$  (i.e. Euler, Navier-Stokes equations). We denote with  $\mathbf{x} = (x, y, z, t)$  the set of space/time variables and with  $p$  the set of system parameters. We assume, regardless of the nature of the problem, the availability of a numerical method capable of computing space/time dependent approximations  $u_M(\mathbf{x}, p)$  of the response  $u(\mathbf{x}, p)$  of the physical system  $\mathcal{S}(p)$  in finite computational time given a set of input

parameters  $p$ :

$$u_M(\mathbf{x}, p) \approx u(\mathbf{x}, p) = \mathcal{S}(p) \quad (3.1)$$

where  $M$  denotes the discretization parameter corresponding to the number of spatial/temporal degrees of freedom (DOF).

**Definition 10.** *Mathematical and computational models are characterized by dependent and independent variables. The former represent the output while the latter represent the inputs. Depending on the context, the dependent variables of mechanical/physical systems are often called **response** variables, response functions, response surfaces or simply response.*

Within a probabilistic uncertainty propagation framework we seek to compute statistics of the response  $u(\mathbf{x}, p, \boldsymbol{\omega}) = \mathcal{S}(p, \boldsymbol{\omega})$  of the system induced by the randomness in the input data  $\boldsymbol{\omega}$ .

In other words, the problem of uncertainty propagation consist in quantifying the probability law of the response  $u$  or of a quantity of interest (QoI)  $Q = f(u)$  given the distribution of the random input parameters  $\boldsymbol{\omega}$  (see Fig. 3.1).

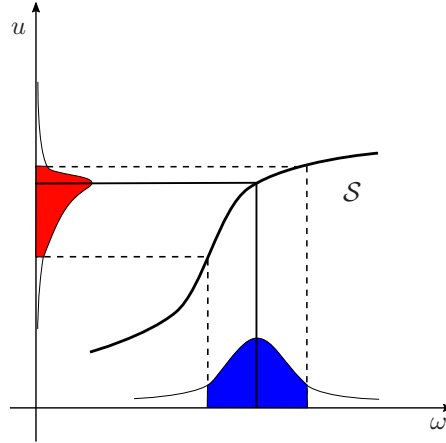


**Figure 3.1** – Graphical interpretation of propagation of uncertainties.

In this work we mainly consider finite-volume (FV) solvers for the solution of the Euler and Navier-Stokes equations that models flows surrounding aerodynamic systems, hence  $u_M(x, \boldsymbol{\omega})$  is generally the result of complex CFD simulations.

As mentioned above, the primary objective of uncertainty propagation is the computation of the probability law or some statistics of the QoI. For a general random variable  $X : \Omega \rightarrow \mathbb{R}$ ,  $X = X(\boldsymbol{\omega})$  defined on the probability space  $(\Omega, \Sigma, P)$  we denote with  $\mathbb{E}[X]$  or  $\mu_X$  the **expected value** of  $X$ :

$$\mu_X = \mathbb{E}[X] = \int_{\Omega} X(\boldsymbol{\omega}) dP(\boldsymbol{\omega}) \quad (3.2)$$



Provided the above integral exist and is finite ( $\int_{\Omega} |X(\boldsymbol{\omega})| dP(\boldsymbol{\omega}) < \infty$ ), the expectation operator has the following proprieties; if  $Y$  is another random variable defined on  $(\Omega, \Sigma, P)$ :

- $X \geq 0 \Rightarrow \mathbb{E}[X]$
- $Y \leq X \Rightarrow \mathbb{E}[Y] \leq \mathbb{E}[X]$
- $|\mathbb{E}[X]| \leq \mathbb{E}[|X|]$
- $\mathbb{E}[aX + bY] = a\mathbb{E}[X] + b\mathbb{E}[Y]$  (Linearity)

We denote with  $\text{Var}[X]$  or  $\sigma_X^2$  the **variance** of  $X$ ; provided it exist:

$$\sigma_X^2 = \text{Var}[X] = \int_{\Omega} (X(\boldsymbol{\omega}) - \mu_X)^2 dP(\boldsymbol{\omega}) = \int_{\Omega} X(\boldsymbol{\omega})^2 dP(\boldsymbol{\omega}) - \mu_X^2 \quad (3.3)$$

Among the several methodologies proposed in the literature for UQ in fluid dynamics problems, we can distinguish between **intrusive** and **non-intrusive** UQ approaches.

### 3.2 Intrusive approaches

The Galerkin polynomial chaos (PC) [GS03] [TLMNE10] [PDL09] is probably the most well known intrusive approach. The method relies on the assumption that the response of the system can be written as a combination of polynomial functions of the uncertain parameters  $\phi_i(\boldsymbol{\omega})$  with deterministic coefficients  $c_{i,M}(\mathbf{x}, p)$  that depend only on the input variables  $\mathbf{x}$  and parameters  $p$ :

$$u(\mathbf{x}, p, \boldsymbol{\omega}) \approx u_M^N(\mathbf{x}, p, \boldsymbol{\omega}) = \sum_{i=1}^N c_{i,M}(\mathbf{x}, p) \phi_i(\boldsymbol{\omega}). \quad (3.4)$$

By replacing the polynomial representation in the governing equations of the problem and projecting onto the space spanned by the basis functions we obtain a system of equations that can be solved for the uncertain response. The accuracy and efficiency of the approximation strongly rely on the regularity of the response function and the appropriate choice of the basis functions. Additionally such approach requires the formulation and solution of the stochastic version of the original deterministic model and hence rewriting the simulation code which is often impractical for large industrial CFD codes.

The basis functions are derived from the Askey scheme family of hypergeometric orthogonal polynomials [XK02]. Based on the type of the probability distribution of the input parameters it is possible to choose appropriate sets of basis functions. The optimality of a specific set of basis with respect to the others originates from their orthogonality with respect to weighting functions that correspond to the probability density function of the underlying input random

variables [EB09]. The Hermite polynomials are optimal for normal, Legendre for uniform and Jacobi for beta distributions. Nonlinear variable transformations to the Askey basis [DKL86] or numerically generated orthogonal polynomials can be employed in order to treat problems with correlated input variables or with more complex distributions [WB06].

Considering the complexity of industrial flow solvers, non-intrusive uncertainty propagation techniques are often preferred as they simply require multiple solutions of the original model for several values of  $\omega$  and can use CFD flow solvers as black box.

### 3.3 Non-intrusive approaches

Non-intrusive uncertainty propagation approaches are designed and conceived to overcome the above mentioned limitation of intrusive approaches. Instead of solving a stochastic version of the original model they treat the deterministic solver as a black-box and simply require a set of simulations for different realizations of the uncertain parameters. Depending on the choice of inputs and reconstruction of the response of the uncertain system we discriminate between polynomial/collocation-based and Monte Carlo-based approaches.

#### 3.3.1 Polynomial/Collocation-based approaches

**Non-intrusive polynomial chaos** (NIPC) approaches rely on the same assumption of intrusive PC method that the response of a system can be described as a combination of polynomial functions with random coefficients:

$$u(\mathbf{x}, p, \omega) \approx u_M^N(\mathbf{x}, p, \omega) = \sum_{i=1}^N c_{i,M}(\mathbf{x}, p) \phi_i(\omega). \quad (3.5)$$

$c_{i,M}(\mathbf{x}, p)$  are the deterministic coefficients and  $\phi_i(\omega)$  the polynomial basis functions orthonormal with respect to the underlying probability measure, i.e.  $\int_{\Omega} \phi_i(\omega) \phi_j(\omega) dP(\omega) = \delta_{ij}$ . The number of coefficients  $N$  required to build a polynomial representation of order  $k$  for a system with  $d$  random parameters is  $N = \frac{(d+k)!}{d!k!}$ .

Once the coefficients are obtained, the statistics of the system response are simply computed as:

$$\begin{aligned} \mathbb{E}[u(\mathbf{x}, p, \omega)] &\approx c_0 \\ \text{Var}[u(\mathbf{x}, p, \omega)] &\approx \sum_{i=1}^p [c_i^2 \langle \phi_i^2 \rangle] \end{aligned} \quad (3.6)$$

It is worth underlying that the expectation of the response is simply the zero-th mode of the expansion.

Following the polynomial orthogonality properties of the basis and projecting the response against each basis function using the  $L^2$  inner product, it is possible to compute the unknown polynomial coefficients in (3.5) as:

$$c_{i,M} = \frac{\langle u_M, \phi_i \rangle}{\langle \phi_i^2 \rangle} = \frac{\mathbb{E}[u_M \phi_i]}{\mathbb{E}[\phi_i^2]} \quad (3.7)$$

$\langle \phi_i^2 \rangle$  is simply the norm squared of multivariate polynomials and can be computed analytically, while the multidimensional integral over the support of the weighting function  $\langle u_M, \phi_i \rangle$  should be evaluated numerically through sampling, tensor-product quadrature or sparse grid approaches.

In the sampling approach the integral in (3.7) is estimated by computing the expectation of  $(u, \phi_i)$  with a large number of random samples. The accuracy will depend, as in the Monte Carlo (MC) method, on the number of samples used to approximate the expectation. MC quadrature is appealing for high-dimensional problems, since the convergence rate of the expectation will be independent of the number of random dimensions [IRG98], [DNP<sup>+</sup>04]. Considering the large number of samples required (error goes to zero asymptotically as  $1/\sqrt{N_s}$ ,  $N_s$  being the number of samples) to obtain accurate estimations, this approach is unfeasible for problems that require the solution of computationally demanding CFD simulations. In order to reduce the number of samples required to achieve a prescribed tolerance it is possible to employ more efficient sampling strategies such as Latin Hypercube Sampling (LHS) [MBC79] and Quasi Monte Carlo (QMC) sampling [MC95]. The former sampling strategy tries to force the sampler to draw realizations within equiprobable bins in the parameter range in order to cover the domain more uniformly. In QMC, low discrepancy deterministic sequences are generated in order to maximize the uniformity (maximize the space-filling) of points in the parameter domain (i.e. Halton, Sobol sequences). LHS perform better in terms of sample distribution but also lead to the same asymptotic convergence rate  $O(1/\sqrt{N_s})$  of MC, QMC sample are more uniformly distributed as one can see in Figure 3.2, and can lead to slightly better asymptotic convergence rate  $O(\ln(N_s^d)/N_s)$  than MC.

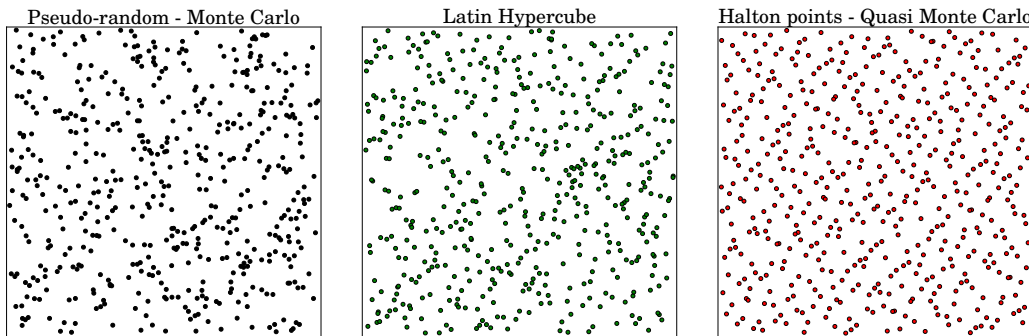


Figure 3.2 – Pseudo random, LHS and Quasi Random (Halton’s sequence) sample sets (512 points).

The integral in (3.7) can also be computed using numerical tensor-product quadrature. Gauss

quadrature points, which are the zeros of orthogonal polynomials chosen for the given input parameters, yield the highest degree of exactness but have the drawback of being not nested, meaning that the simulations performed to build a specific tensor grid cannot be re-used if the grid is refined or coarsened. Nested quadrature points such as Clenshaw-Curtis and Fejer rules overcome this drawback.

If  $N_p$  points are used in each random variable, Gaussian quadrature can achieve fast rates  $N_p^r$  where  $r$  relates to the smoothness of the response function (e.g.  $e^r$ ). However the total number of points in the grid is  $N_s = N_p^d$ . Hence the effective rate will be  $N_s^{-r/d}$  which strongly degrades as  $d$  gets large.

In order to alleviate the so called *curse of dimensionality*, the multidimensional integrals can be computed more efficiently using sparse tensor products [Smo63] [XH05] instead of full-tensor products of quadrature points (See Figure 3.3).

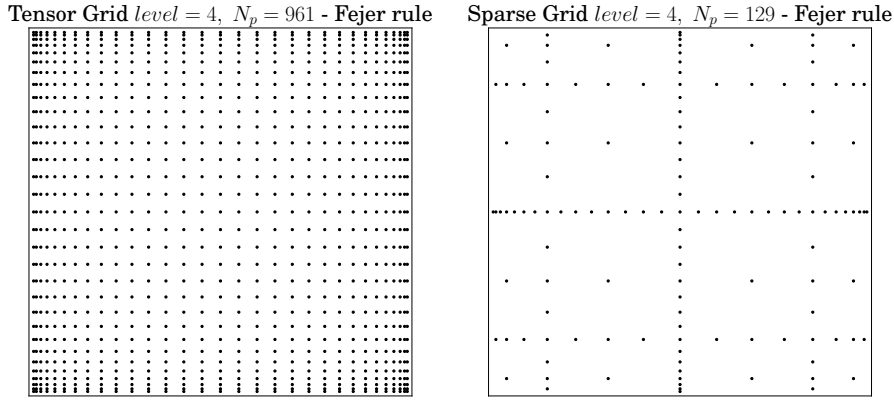


Figure 3.3 – Tensor and Sparse grid based on Fejer nested quadrature points.

The unknown coefficients can be efficiently computed also by solving the linear least squares (LS) regression problem:

$$\Phi^T \Phi \mathbf{c} = \Phi^T \mathbf{u} \tag{3.8}$$

in order to find a vector of polynomial coefficients  $\mathbf{c}$  that best match (in a least square sense) a set of response evaluation  $\mathbf{u}$  with random inputs [HWB07].  $\Phi$  denotes a matrix that contains  $N$  multivariate polynomial terms  $\phi_i$  evaluated at the sample  $\omega^{(j)}$ . The LS problem is over-determined as it is generally recommended to perform a random oversampling of response evaluations. Instead of performing a random over-sampling, such approach can be further improved in accuracy and efficiency by selecting an appropriate set of minimization points (similar idea of QMC) and by 'enriching' the regression equations with derivative information [LWB07].

Instead of computing the coefficients by quadrature (3.7) or regression (3.8), **stochastic collo-**

**caution** (SC) approaches try to build interpolation polynomials on structured grids of collocation points derived from tensor-products or sparse grids [BNT07]. Essentially, instead of trying to determine the projection of the system response on a pre-defined polynomial subspace, SC approaches rely on interpolation and build the approximation and the subspace implicitly from a set of response evaluations. The objective of SC is to find an approximation  $u_M^{N_c}(\mathbf{x}, \boldsymbol{\omega})$  such that:

$$u_M^{N_c}(\mathbf{x}, p, \boldsymbol{\omega}^{(i)}) = u(\mathbf{x}, p, \boldsymbol{\omega}^{(i)}) \quad 1 \leq i \leq N_c \quad (3.9)$$

meaning that the approximation is exact at the  $N_c$  collocation points.

In order to build an expansion

$$u_M^N(\mathbf{x}, p, \boldsymbol{\omega}) = \sum_{i=1}^N c_i(\mathbf{x}, p) \phi_i(\boldsymbol{\omega}). \quad (3.10)$$

and fulfilling (3.9), the most natural choice is to consider a vector space of basis functions, like Lagrange polynomials, that have the propriety:

$$\phi_i(\boldsymbol{\omega}) = L_i(\boldsymbol{\omega}) = \prod_{\substack{k=1 \\ k \neq j}}^m \frac{\xi - \xi_k}{\xi_j - \xi_k} = \begin{cases} 1 & \text{if } \xi = \xi_j \\ 0 & \text{if } \xi \neq \xi_j \end{cases} \quad (3.11)$$

$L_i(\boldsymbol{\omega})$  denotes the Lagrange polynomial at the  $i$ -th collocation point. By doing so (3.10) can be rewritten as:

$$u_M^N(\mathbf{x}, p, \boldsymbol{\omega}) = \sum_{i=1}^N u_M(\mathbf{x}, p, \boldsymbol{\omega}^{(i)}) L_i(\boldsymbol{\omega}). \quad (3.12)$$

Thanks to this propriety of the Lagrange polynomials, the coefficients of the expansion  $u_M(\mathbf{x}, p, \boldsymbol{\omega}^{(i)})$  are simply the response values of the system evaluated at each of the collocation points  $\boldsymbol{\omega}^{(i)}$ . The latter are defined on tensor product or Smolyak sparse grids build as combinations of 1D Clenshaw-Curtis nodes.

Both intrusive and non-intrusive (PC and SC) approaches based on global functions that span the entire random domain have been successfully applied to propagate input uncertainties in aerodynamic simulations, see e.g. [HW10] for regression type methods or [LB08, LWB07] for stochastic collocation (interpolation) techniques. Although extremely efficient for smooth response functions and moderate number of uncertainty parameters, they typically suffer the so called **curse of dimensionality**, i.e. the exponential increase of the cost with the number of uncertain variables. Moreover, they are not particularly efficient for problems whose solutions exhibit **sharp gradients or discontinuities** such as shock waves and contact discontinuities in hyperbolic systems of conservation laws (Euler and Navier-Stokes equations). Such discontinuities propagate into the stochastic space and inhibit the use of data compression techniques which are based on the regularity of the response function. Promising alternatives are given

by adaptive multi-element [WK05, FK10], multi wavelet [LMNP<sup>+</sup>07] and simplex stochastic collocation methods [WI13, EDC16]. However so far these methods have been applied to problems with non-smooth response functions with discontinuities not aligned with the coordinate axes only with few uncertain parameters and their extensions to moderate number of uncertain variables is still open. The same can be said to Padé type rational approximation proposed in [CDI09]. This is the main reason to focus in this work on Monte Carlo (MC) type methods as we are interested in CFD problems with discontinuous response functions and several uncertain parameters (of the order of 10 or more).

### 3.3.2 Monte Carlo based Methods

Monte Carlo (MC) methods are a broad class of approaches that rely on the idea of approximating statistics of the response variables of a system by simulation. Because of its simplicity, robustness and dimension independent convergence rate, MC methods can be used to characterize, in principle, any system that has a probabilistic interpretation and are often the easiest way (sometimes the only feasible one) to solve a wide range of high-dimensional (in terms of number uncertain parameters) problems.

**Definition 11.** *The MC estimator  $E^{\text{MC}}[Q]$  for the expectation  $\mathbb{E}[Q]$  of a QoI  $Q(\omega) = Q(u(\cdot, \omega))$  is defined as:*

$$E^{\text{MC}}[Q] := \frac{1}{N} \sum_{i=1}^N Q(\omega^{(i)}) = \frac{1}{N} \sum_{i=1}^N Q^{(i)}, \quad (3.13)$$

where  $\omega^{(i)}$  are independent and identically distributed (iid) samples drawn from the probability measure  $P$  and  $N$  is the number of samples.

Thanks to the Strong Law of Large Numbers [Rob04], the approximation of  $E^{\text{MC}}[Q]$  converges with probability one (converges almost surely) to  $\mathbb{E}[Q]$  as  $N \rightarrow \infty$  as long as  $Q$  is integrable.

Moreover,  $E^{\text{MC}}[Q]$  is an unbiased estimator:

$$\mathbb{E}[E^{\text{MC}}[Q]] = \mathbb{E}[Q] \quad (3.14)$$

where the expectation on the left is with respect to the random sample  $\{\omega^{(1)}, \dots, \omega^{(N)}\}$ .

The rate of convergence of MC methods can be described by the Central Limit Theorem (CLT) using the concept of convergence in distribution (weak convergence, size of the error with some probability). If the variance of  $Q$ , denoted with  $\mathbb{V}ar[Q]$ , is finite then the CLT asserts that

$$\sqrt{N}(E^{\text{MC}}[Q] - \mathbb{E}[Q]) \Rightarrow \sqrt{\mathbb{V}ar[Q]} \mathcal{N}(0, 1) \quad (3.15)$$

as  $N \rightarrow \infty$ , where  $\mathcal{N}(0, 1)$  is a normal random variable with mean zero and unit variance and  $\Rightarrow$  means convergence in distribution.

From (3.15), for  $N$  large enough, we can derive confidence intervals for the estimator  $E^{\text{MC}}[Q]$ :

$$|E^{\text{MC}}[Q] - E[Q]| \leq C_\alpha \frac{\sqrt{\text{Var}[Q]}}{\sqrt{N}} \quad \text{with probability } 1 - \alpha \quad (3.16)$$

where  $C_\alpha$  satisfies  $\Phi(C_\alpha) = 1 - \frac{\alpha}{2}$  with  $\Phi$  the cumulative distribution function of a standard normal random variable .

From Eqn. (3.16) we can draw three conclusions:

- the rate of convergence of MC is  $O(N^{-1/2})$ ,
- for large  $N$  the error is normally distributed,
- the complexity of the computation depends solely on  $\text{Var}[Q]$ .

For many practical applications we usually cannot access the exact evaluation of the QoI and we generally rely on a numerical approximation with a discretization parameter  $M$  (e.g. number of spatial degrees of freedom). Then  $Q$  will be approximated by  $Q_M = f(u_M)$  and the Monte Carlo estimator for  $E[Q]$  is:

$$E^{\text{MC}}[Q_M] := \frac{1}{N} \sum_{i=1}^N Q_M(\omega^{(i)}), \quad (3.17)$$

#### MC Complexity Analysis

The accuracy in estimating  $E[Q]$  by  $E^{\text{MC}}[Q_M]$  can be quantified by considering the mean square error (MSE) of the estimator hereafter denoted by  $MSE[\cdot]$ :

$$MSE[E^{\text{MC}}[Q_M]] := \mathbb{E}[(E^{\text{MC}}[Q_M] - E[Q])^2] = \underbrace{\mathbb{E}[Q_M - Q]^2}_{(\text{B-}E^{\text{MC}})} + \underbrace{\frac{\text{Var}[Q_M]}{N}}_{(\text{SE-}E^{\text{MC}})}. \quad (3.18)$$

On the right hand side in (3.18) we can isolate two distinct contributions. The first term, the discretization error or bias (B- $E^{\text{MC}}$ ), is the squared error in mean between  $Q_M$  and  $Q$  and depends solely on the space discretization parameter  $M$ . The second term, the statistical error (SE- $E^{\text{MC}}$ ), represents the variance of the estimator and decays inversely with the number of samples  $N$ .

Concerning the space discretization, we assume that we can build a sequence of (converging) discretizations, indexed by  $M$ , for which the error decreases as  $M$  increases and the cost for computing  $Q_M$  increases as  $M$  increases with algebraic rates in  $M$ .

### Chapter 3. Uncertainty Propagation

---

**A1.** There exist  $c_\gamma, \gamma > 0$  such that the cost to compute one realization  $Q_M(\omega^{(i)})$  is:

$$C(Q_M(\omega^{(i)})) \leq c_\gamma M^\gamma, \quad (3.19)$$

**A2.** There exist  $c_\alpha, \alpha > 0$  such that:

$$|\mathbb{E}[Q_M - Q]| \leq c_\alpha M^{-\alpha} \quad (3.20)$$

**A3.**  $\text{Var}(Q_M)$  is approximately constant w.r.t.  $M$

The actual rates  $\alpha, \gamma$  will heavily depend on the specific problem and QoI considered, the specific discretization and solvers used.

For instance, for a FV discretization and explicit time integrator of the Euler equations on a uniform structured mesh with spatial mesh size  $h = M^{-1/d}$  ( $M$  being the number of degrees of freedom) and time step  $\Delta t \approx h = M^{-1/d}$ , one typically has  $C(Q_M) \lesssim h^{-d} \Delta t^{-1} = M^{1+1/d}$ . Similarly, for a steady state solution obtained by pseudo time stepping, we expect the number of iterations needed to reach convergence to be proportional to some power of  $M$  leading to  $C(Q_M) \lesssim M^\gamma$  with  $\gamma > 1$ .

Although theoretical rates might be available for certain classes of problems, in this work  $\alpha$  will always be estimated from calculations.

A sufficient condition to achieve a root mean squared error (RMSE) of order  $\varepsilon$  for the MC estimator (3.13) is that both terms in the right hand side of (3.18) are less than  $\frac{\varepsilon^2}{2}$ . Hence by choosing:

$$N \approx \varepsilon^{-2}, \quad M \approx \varepsilon^{-1/\alpha}, \quad (3.21)$$

the total cost, hereafter denoted by  $\mathbf{C}$ , of achieving a RMSE of  $\varepsilon$  is:

$$\mathbf{C}_{\text{MC}} = \sum_{i=1}^N C(Q_M(\omega^{(i)})) \lesssim \varepsilon^{-2-\gamma/\alpha} = \varepsilon^{-2} \varepsilon^{-\gamma/\alpha} \quad (3.22)$$

The two factors in (3.22) can be interpreted as follows:  $\varepsilon^{-2}$  is the cost to achieve a prescribed MC error tolerance for a unitary cost per sample and  $\varepsilon^{-\gamma/\alpha}$  is the cost of each deterministic solve on a discretization level that achieves the prescribed tolerance.

MC methods have been proven to be robust and accurate for non smooth problems, nevertheless their very slow convergence rate  $O(N^{-1/2})$  prevents to achieve reasonable estimations in acceptable time for large scale problems that require the solution of computationally expensive CFD simulations.

Different strategies have been investigated in the last decades to accelerate MC methods either by reducing the constant  $\sqrt{\text{Var}[Q]}$  in Eq. (3.16) (**variance reduction techniques**) or by



improving the rate  $1/\sqrt{N}$  (**improved sampling techniques**).

The latter class of approaches includes (low-discrepancy) sequences, stratified sampling or Latin Hypercube Sampling rather than pseudo-random numbers.

Variance Reduction techniques: reduce the numerator term  $\text{Var}[Q]$  by suitably modifying the quantity  $Q$  in a consistent way (i.e. without changing the expectation).

In the following chapter we will present the Multi Level Monte Carlo variance reduction technique and detail its application in aerodynamic problems affected by uncertainties.

*If one has really technically penetrated a subject, things that previously seemed in complete contrast, might be purely mathematical transformations of each other.*

*John von Neumann*

## 4 Multi Level Monte Carlo Method

As presented in the previous chapter traditional Monte Carlo (MC) type sampling methods have a dimension independent convergence rate which is not affected by the presence of possible discontinuities in the parameter space. The very slow convergence rate of MC methods however makes them impractical in complex applications that require accurate solutions.

The Multi Level Monte Carlo (MLMC) method has been introduced by Heinrich [Hei98, HS99] in the context of parametric integration and thereupon extended by Giles [Gil08] to approximate stochastic differential equations (SDEs) in financial mathematics, as a way to improve the efficiency of MC simulations. Applications to PDE models with random parameters can be found in [BLS13, BSZ11, CST13, CGST11, CHAN<sup>+</sup>14, TSGU13].

The key idea of MLMC is that one can draw MC samples simultaneously and independently on several approximations of the problem under investigation on a hierarchy of computational meshes (levels). The expectation of an QoI is computed as a sample average of coarse solutions corrected by averages of the differences of solutions computed on two consecutive levels in a hierarchy of computational grids. By this way, most of the computational effort can be transported from the finest level (as in a standard MC approach) to the coarsest one (Fig.4.1).

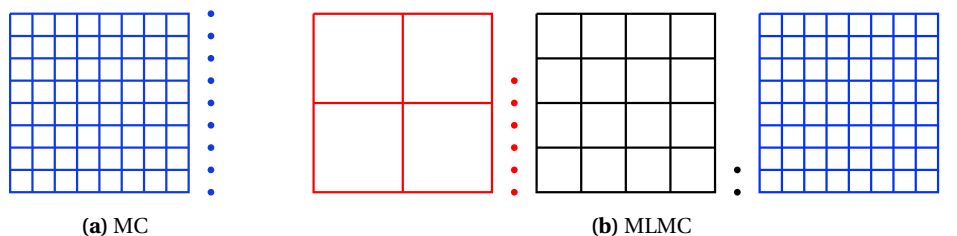


**Figure 4.1** – Difference between MC and MLMC.

Hereafter we review the Multi Level Monte Carlo (MLMC) method, provide a detailed description on its application on inviscid aerodynamic problems and compare with the MC method,

on a benchmark airfoil problem affected by operating and geometric uncertainties, in terms of accuracy and computational complexity.

## 4.1 Multi Level Monte Carlo

The key idea of MLMC algorithms is that one can draw MC samples simultaneously and independently on several approximations of the problem under investigation on a hierarchy of computational grids, called levels, with corresponding number of DOFs  $M_0 < M_1 < \dots < M_L = M$ .

The linearity of the expectation operator suggests that the expectation of the QoI on the finest level can be written as a telescopic sum of the expectation of the QoI on the coarsest level plus a sum of correction terms adding the difference in expectation between evaluations on consecutive levels:

$$\mathbb{E}[Q_{M_L}] = \mathbb{E}[Q_{M_0}] + \sum_{\ell=1}^L \mathbb{E}[Q_{M_\ell} - Q_{M_{\ell-1}}] = \sum_{\ell=0}^L \mathbb{E}[Y_\ell] \quad (4.1)$$

with  $Y_\ell = Q_{M_\ell} - Q_{M_{\ell-1}}$  and  $Y_0 = Q_{M_0}$ .

**Definition 12.** *The MLMC estimator for  $\mathbb{E}[Q]$  is:*

$$\mathbb{E}^{\text{MLMC}}[Q_M] := \sum_{\ell=0}^L \frac{1}{N_\ell} \sum_{i=1}^{N_\ell} Y_\ell(\omega^{(i,\ell)}) = \sum_{\ell=0}^L \mathbb{E}^{\text{MC}}[Q_{M_\ell} - Q_{M_{\ell-1}}] \text{ with } Q_{M_{-1}} = 0 \quad (4.2)$$

It is important to underline that the correction terms  $Y_\ell = Q_{M_\ell} - Q_{M_{\ell-1}}$  are computed using the same sample on both levels whereas corrections on different levels are sampled independently.

### 4.1.1 MLMC Complexity Analysis

The MSE of the MLMC estimator  $\mathbb{E}^{\text{MLMC}}[Q_M]$  is given by:

$$e_{\text{MLMC}}^2 := \mathbb{E}[(\mathbb{E}^{\text{MLMC}}[Q_M] - \mathbb{E}[Q])^2] = \underbrace{(\mathbb{E}[Q_M - Q])^2}_{(\text{B-E}^{\text{MLMC}})} + \underbrace{\sum_{\ell=0}^L \frac{\text{Var}[Y_\ell]}{N_\ell}}_{(\text{SE-E}^{\text{MLMC}})} \quad (4.3)$$

As for the MC case the MLMC error presents two contributions: the discretization error or bias  $\text{B-E}^{\text{MLMC}}$  that is the same as in the MC case and the statistical error  $\text{SE-E}^{\text{MLMC}}$  (variance of the estimator).

Again, we assume that the sequence of discretizations with parameters  $M_0 < M_1 < \dots < M_L = M$  provides errors that decrease algebraically with  $M_\ell$  and costs that increase algebraically in  $M_\ell$ . More precisely **(A1)** and **(A2)** are the same as in MC, whereas **(A3)** is replaced by **(A3)**:

**A1.** There exist  $c_\gamma, \gamma > 0$  such that the cost  $C_\ell$  to compute one sample  $Q_{M_\ell}$  at level  $l$  is:

$$C_\ell = C(Q_{M_\ell}(\omega^{(i)})) \leq c_\gamma M_\ell^\gamma, \quad (4.4)$$

**A2.** There exist  $c_\alpha, \alpha > 0$  such that:

$$|\mathbb{E}[Q_{M_\ell} - Q]| \leq c_\alpha M_\ell^{-\alpha} \quad (4.5)$$

**$\tilde{\text{A3}}$ .** There exist  $c_\beta, \beta > 0$ , with  $\alpha \geq \min(\beta, \gamma)$  such that:

$$\text{Var}[Y_\ell] \leq c_\beta M_\ell^{-\beta}, \quad (4.6)$$

It can be shown [Gil08, TSGU13] that under these assumptions, for any  $\varepsilon > 0$ , there exist  $L = L(\varepsilon)$ ,  $M_L = M$  and  $\{N_\ell\}_{\ell=0}^L$  such that

$$e_{\text{MLMC}}^2 < \varepsilon^2 \quad (4.7)$$

and the cost to achieve a RMSE of  $\varepsilon$  is:

$$\mathbf{C}_{\text{MLMC}} = \sum_{\ell=0}^L N_\ell C_\ell \lesssim \begin{cases} \varepsilon^{-2} & \beta > \gamma, \\ \varepsilon^{-2} (\log \varepsilon)^2 & \beta = \gamma, \\ \varepsilon^{-2 - (\gamma - \beta)/\alpha} & \beta < \gamma. \end{cases} \quad (4.8)$$

This result clearly shows the importance of the parameter  $\beta$ , that defines the convergence of the variance of the consecutive differences, in reducing the overall computational cost of the MLMC with respect to standard MC approach. Comparing (3.22) and (4.8) we immediately see that for  $\beta > \gamma$  the computation effort will be primarily on the coarsest levels (the overall complexity is dominated by the MC sampling on the coarse level and does not "see" the cost of fine discretization), whereas for  $\beta < \gamma$  the primary cost will be on the finest levels and for  $\beta = \gamma$  it will be spread across all levels. Observe that, even in the worst case  $\beta < \gamma$ , the complexity of the MLMC method  $\mathbf{C}_{\text{MLMC}} \lesssim \varepsilon^{-2 - (\gamma - \beta)/\alpha}$  improves that of MC method  $\mathbf{C}_{\text{MC}} \lesssim \varepsilon^{-2 - \gamma/\alpha}$ . Moreover, it is quite common in applications involving PDEs with random coefficients to have  $\beta = 2\alpha$ . In such case, the cost of a MLMC simulation for  $\beta < \gamma$  reduces to  $\mathbf{C}_{\text{MLMC}} \lesssim \varepsilon^{-\gamma/\alpha}$ , i.e. it compares to the cost of a single deterministic simulation on the finest grid and does not "see" the cost of the MC sampling.

The result (4.8) is not only a theoretical bound on the best complexity achievable with a MLMC method, but does also provide recipes to select the maximum level  $L$  and the number of samples per level  $\{N_\ell\}_{\ell=0}^L$  to achieve a given tolerance  $\varepsilon$ . We review hereafter one such recipe from [CHAN<sup>+</sup>14].

### 4.1.2 Practical Aspects of MLMC

Instead of looking at the MSE, we can alternatively require that the MLMC estimator  $E^{\text{MLMC}}[Q_M]$  achieves the desired tolerance  $\varepsilon$  with high probability, with a confidence  $(1 - \phi)$ :

$$\mathbb{P} \left[ |E^{\text{MLMC}}[Q_M] - \mathbb{E}[Q]| > \varepsilon \right] \leq \phi, \quad \phi \ll 1. \quad (4.9)$$

This will give, hopefully, a more robust estimator. Exploiting the asymptotic normality of the estimator  $E^{\text{MLMC}}[Q_M]$  (see [CHAN<sup>+</sup>14]) we have asymptotically as  $\varepsilon \rightarrow 0$  and with probability  $(1 - \phi)$  that:

$$|E^{\text{MLMC}}[Q_M] - \mathbb{E}[Q_M]| \leq \mathcal{C}_\phi \sqrt{\text{Var}[E^{\text{MLMC}}[Q_M]]} \quad (4.10)$$

where  $\mathcal{C}_\chi = \Phi^{-1}(1 - \frac{\chi}{2})$  and  $\Phi$  is the cumulative distribution function (CDF) of a standard normal random variable. Therefore, with probability  $(1 - \chi)$ , the total error can be bounded by:

$$\begin{aligned} \text{TErr} &:= |E^{\text{MLMC}}[Q_M] - \mathbb{E}[Q]| \leq |\mathbb{E}[Q - Q_M]| + |E^{\text{MLMC}}[Q_M] - \mathbb{E}[Q_M]| \\ &\leq \underbrace{|\mathbb{E}[Q] - \mathbb{E}[Q_M]|}_{\mathbf{B}} + \mathcal{C}_\chi \sqrt{\underbrace{\text{Var}[E^{\text{MLMC}}[Q_M]]}_{\text{SE}}} \end{aligned} \quad (4.11)$$

Following [CHAN<sup>+</sup>14] we introduce a splitting parameter  $\theta \in (0, 1)$  and require in our simulations that:

$$\text{Bias: } \mathbf{B} := |\mathbb{E}[Q] - \mathbb{E}[Q_M]| \leq (1 - \theta)\varepsilon, \quad (4.12a)$$

$$\text{Statistical Error: } \mathbf{SE} := \text{Var}[E^{\text{MLMC}}[Q_M]] = \sum_{\ell=0}^L \frac{\text{Var}[Y_\ell]}{N_\ell} \leq \left( \frac{\theta\varepsilon}{\mathcal{C}_\phi} \right)^2 \quad (4.12b)$$

so that (4.9) is satisfied (at least asymptotically). From (4.5), the bias constraint (4.12a) is satisfied for:

$$L: M_L \geq \left( \frac{(1 - \theta)\varepsilon}{c_\alpha} \right)^{-\frac{1}{\alpha}} \quad (4.13)$$

On the other hand, following the optimization argument in [Gil08] (see also [CHAN<sup>+</sup>14]) and the Lindeberg Central Limit Theorem in the limit  $\varepsilon \rightarrow 0$ , the statistical error constraint (4.12b) is satisfied by choosing:

$$N_\ell = \left[ \left( \frac{\mathcal{C}_\phi}{\theta\varepsilon} \right)^2 \sqrt{\frac{\text{Var}[Y_\ell]}{C_\ell}} \sum_{k=0}^L \sqrt{C_k \text{Var}[Y_k]} \right] \quad l = 0, 1, \dots, L. \quad (4.14)$$

In practice, the bias contribution  $\mathbf{B}$ , in absence of an exact solution  $\mathbb{E}[Q]$  of the problem under

consideration, is approximated as:

$$\mathbf{B} \approx |\mathbb{E}^{\text{MC}}[Q_L - Q_{L-1}]|. \quad (4.15)$$

that is a reasonable estimate of the discretization error for sufficiently fine grids. In the simulations presented hereafter we have chosen hierarchies of grids for which we could observe a grid convergence over all levels of discretization (meaning that even the coarsest mesh resolves the main features of the flow, see e.g. Fig. 4.6).

On the other hand, the statistical error  $\mathbf{SE}$  (variance of the MLMC estimator  $\text{Var}[\mathbb{E}^{\text{MLMC}}[Q_M]]$ ) is estimated using the level sample variance hereafter denoted as  $V^{\text{MC}}[Y_\ell]$ :

$$\text{Var}[Y_\ell] \approx V^{\text{MC}}[Y_\ell] = \frac{1}{N_\ell - 1} \sum_{n=1}^{N_\ell} \left( Y_\ell(\omega^{(n,\ell)}) - \mathbb{E}^{\text{MC}}[Y_\ell] \right)^2 \quad (4.16)$$

as:

$$\mathbf{SE} \approx \sum_{\ell=0}^L \frac{V^{\text{MC}}[Y_\ell]}{N_\ell}. \quad (4.17)$$

### 4.1.3 MLMC for scalar field QoI

In practical aerodynamics applications we are generally interested in computing QoI  $\mathcal{Q}(x, \omega)$  that are scalar fields defined on a certain domain  $D$  (e.g. pressure coefficient around an airfoil). We can rewrite (4.3) for a scalar field, in which case we measure the spatial error in the  $L^2$  norm (mean-square sense):

$$\begin{aligned} e(\mathbb{E}^{\text{MLMC}}[\mathcal{Q}_M])^2 &:= \mathbb{E}[\|\mathbb{E}^{\text{MLMC}}[\mathcal{Q}_M] - \mathbb{E}[\mathcal{Q}]\|_{L^2(D)}^2] \\ &= \underbrace{\|\mathbb{E}[\mathcal{Q}_M - \mathcal{Q}]\|_{L^2(D)}^2}_{(\mathbf{B}\text{-}\mathbb{E}^{\text{MLMC}})} + \underbrace{\sum_{\ell=0}^L \frac{1}{N_\ell} \|\text{Var}[\mathcal{Y}_\ell]\|_{L^1(D)}}_{(\mathbf{SE}\text{-}\mathbb{E}^{\text{MLMC}})}. \end{aligned} \quad (4.18)$$

with  $\mathcal{Y}_\ell = \mathcal{Q}_{M_\ell}(x, \omega) - \mathcal{Q}_{M_{\ell-1}}(x, \omega)$ .

By doing so we require that:

$$\text{Bias: } \mathbf{B} := \|\mathbb{E}[\mathcal{Q}_M - \mathcal{Q}]\|_{L^2(D)} \leq (1 - \theta)\varepsilon, \quad (4.19a)$$

$$\text{Statistical Error: } \mathbf{SE} := \text{Var}[\mathbb{E}^{\text{MLMC}}[\mathcal{Q}_M]] = \sum_{\ell=0}^L \frac{\|\text{Var}[\mathcal{Y}_\ell]\|_{L^1(D)}}{N_\ell} \leq \theta(2 - \theta)\varepsilon^2, \quad (4.19b)$$

so that the  $\text{MSE} \leq \varepsilon^2$ . The parameter  $\theta$  prescribe the splitting between bias and the statistical error contributions in the total error. In our applications we choose to prescribe the same importance to both contributions, hence  $\theta = 0.5$ .

## Chapter 4. Multi Level Monte Carlo Method

---

Following the same optimization argument used for scalar QoI, it is possible to compute the optimal number of samples per level as:

$$N_\ell = \left[ \left( \frac{1}{\theta(2-\theta)\varepsilon^2} \right) \sqrt{\frac{\|\text{Var}[\mathcal{Y}_\ell]\|_{L^1(D)}}{C_\ell}} \sum_{k=0}^L \sqrt{C_k \|\text{Var}[\mathcal{Y}_k]\|_{L^1(D)}} \right] \quad (4.20)$$

and the cost of the algorithm with optimal choice of  $\{N_\ell\}_{\ell=0}^L$  becomes:

$$\mathbf{C}(\varepsilon_i, \theta, L) = \left( \frac{1}{\theta(2-\theta)\varepsilon^2} \right) \left( \sum_{\ell=0}^L \sqrt{C_\ell \|\text{Var}[\mathcal{Y}_\ell]\|_{L^1(D)}} \right)^2. \quad (4.21)$$

### 4.1.4 MLMC Algorithm

Given a hierarchy of discretizations with  $M_0 < M_1 < \dots$ , from the practical point of view the standard MLMC algorithm is generally composed of four steps:

1. Theoretical or computational estimation of the problem dependent rates and constants  $\mathcal{P} = \{c_\alpha, \alpha, c_\beta, \beta, c_\gamma, \gamma\}$
2. Estimation of  $\text{Var}[Y_\ell]$ .
3. Estimation of the optimal number of levels  $L$  from (4.13) and samples per level  $N_\ell$  from (4.14)
4. Run the hierarchy  $\{0, \dots, L\}$  with  $\{N_\ell\}_{\ell=0}^L$

The splitting parameter is usually taken as  $\theta = \frac{1}{2}$ .

Theoretical estimates for the parameters  $\alpha$  and  $\beta$  exist for certain classes of PDEs with random parameters [BSZ11, CGST11, BLS13, CST13] and depend on the smoothness of the data of the problem as well as the smoothing proprieties of the differential operator. Conversely the parameter  $\gamma$  depends on the efficiency of the deterministic solver. For CFD applications as those addressed in this work, which may feature flows with shocks and for which theoretical rates might be difficult to establish or might not be available, the rates  $\alpha$ ,  $\beta$ ,  $\gamma$  can always be estimated numerically. It is worth underlying the importance of estimating numerically also the constants  $c_\alpha$ ,  $c_\beta$ ,  $c_\gamma$  as they enter in the choice of the optimal parameters  $L$ ,  $\{N_\ell\}_{\ell=0}^L$ , and affect the total cost of the MLMC algorithm.

The common practice is to compute the rates and the constants by performing an initial *screening* over the first few levels  $\{0, \dots, \bar{L}\}$  with a predefined number of samples and fit the rates and constants via a least squares procedure. Here the bias  $\mathbb{E}[Q - Q_{M_\ell}]$ ,  $l = 1, \dots$ , can be estimated e.g. by  $\mathbb{E}^{\text{MC}}[Q_{M_\ell} - Q_{M_{\ell-1}}]$  and the variance of the differences  $\text{Var}[Y_\ell]$  by the sample variance formula on  $Q_{M_\ell} - Q_{M_{\ell-1}}$ .



Once the set of parameters  $\mathcal{P}$  is determined from this screening phase, the number of levels  $L$  and the number of samples per level  $N_\ell$  can be computed from (4.13) and (4.14) and the MLMC algorithm on the whole hierarchy  $0, \dots, L$  can be run and should provide an error smaller than  $\varepsilon$  with probability at least  $1 - \phi$ .

Hereafter we present a modular MLMC algorithm (Algorithm 1) capable of efficiently propagate operating and geometric uncertainties in internal and external aerodynamics problems.

---

**Algorithm 1:** Multi Level Monte Carlo with Screening.
 

---

**SCREENING** ( $\bar{N}, \bar{L}$ )

```

for  $\ell = 0 : \bar{L}$  do
    for  $i = 0 : \bar{N}$  do
        Generate random samples:  $\mathbf{O}(\omega^{(i,\ell)}), \mathbf{G}(\omega^{(i,\ell)})$ 
         $Q_{M_\ell}^{(i)} \leftarrow \text{PROBLEM}_\ell(\mathbf{O}(\omega^{(i,\ell)}), \mathbf{G}(\omega^{(i,\ell)}))$ 
         $Q_{M_{\ell-1}}^{(i)} \leftarrow \text{PROBLEM}_{\ell-1}(\mathbf{O}(\omega^{(i,\ell)}), \mathbf{G}(\omega^{(i,\ell)}))$ 
         $Y_\ell^{(i)} = Q_{M_\ell}^{(i)} - Q_{M_{\ell-1}}^{(i)}$ 
    estimate  $\{C_\ell\}, \{E[Y_\ell]\}, \{\text{Var}[Y_\ell]\}$  using (4.16)
    compute  $\mathcal{P} = \{c_\alpha, c_\beta, c_\gamma, \alpha, \beta, \gamma\}$  using least squares fit
    compute  $L$  using (4.13) and  $N_\ell$  using (4.14)
    return  $L, \{N_\ell\}_{\ell=0}^L$ 
    
```

**MLMC** ( $L, \{N_\ell\}_{\ell=0}^L$ )

```

for  $l = 0 : L$  do
    for  $i = 0 : N_\ell$  do
        Generate random samples:  $\mathbf{O}(\omega^{(i,\ell)}), \mathbf{G}(\omega^{(i,\ell)})$ 
         $Q_{M_\ell}^{(i)} \leftarrow \text{PROBLEM}_\ell(\mathbf{O}(\omega^{(i,\ell)}), \mathbf{G}(\omega^{(i,\ell)}))$ 
         $Q_{M_{\ell-1}}^{(i)} \leftarrow \text{PROBLEM}_{\ell-1}(\mathbf{O}(\omega^{(i,\ell)}), \mathbf{G}(\omega^{(i,\ell)}))$ 
         $Y_\ell^{(i)} = Q_{M_\ell}^{(i)} - Q_{M_{\ell-1}}^{(i)}$ 
    compute  $E^{\text{MC}}[Y_\ell]$ 
    estimate  $\{E[Y_\ell]\}, \{\text{Var}[Y_\ell]\}$  using (4.16) and  $\mathbf{B}$  using (4.15)
    compute  $\text{TErr} = \mathbf{B} + \mathcal{C}_\chi \sqrt{\sum_{\ell=0}^L \frac{\text{Var}[Y_\ell]}{N_\ell}}$ 
    return  $E^{\text{MLMC}}[Q_M] = \sum_{\ell=0}^L E^{\text{MC}}[Y_\ell], \text{TErr}$ 
    
```

---

Algorithm 1 returns the MLMC estimation  $E^{\text{MLMC}}[Q_M]$  of the expected value of the QoI as well as an estimation of the associated error  $\text{TErr} = \mathbf{B} + \mathcal{C}_\chi \sqrt{\mathbf{SE}}$ .

The notation  $\text{PROBLEM}_\ell$  denotes a general 'black-box' solver that computes the QoI of the problem under investigation given a set of input values at the grid discretization level  $l$ . We denote with  $\mathbf{O}(\omega^{(i,\ell)})$  and  $\mathbf{G}(\omega^{(i,\ell)})$  respectively, the sets of operating and geometric random input parameters that are provided to the black-box solver. These two sets of input parameters require a different treatment when we consider CFD problems solved using finite volumes (FV) methods. The operating  $\mathbf{O}(\omega^{(i,\ell)})$  uncertainties are simply input values for boundary condition (e.g. far-field Mach number, turbulence intensity, angle of attack), while the geometric ones

$\mathbf{G}(\omega^{(i,\ell)})$  require a grid deformation procedure to adapt the deformation of the boundary affected by uncertainty.

## 4.2 MLMC for UQ in Inviscid Aerodynamics

### 4.2.1 Euler Equations

In this section we consider compressible inviscid flows modeled by the 2D Euler equations in conservative form as presented in Chapter 2.1.2. The 2D Euler equations are discretized on an unstructured grid using dual grid (cell-vertex scheme) based finite volume method (Fig.4.2).

The discretized equations are advanced in time using explicit multistage scheme (Runge-Kutta). Local time-stepping and geometric multi-grid are used for convergence acceleration to the steady-state solution.

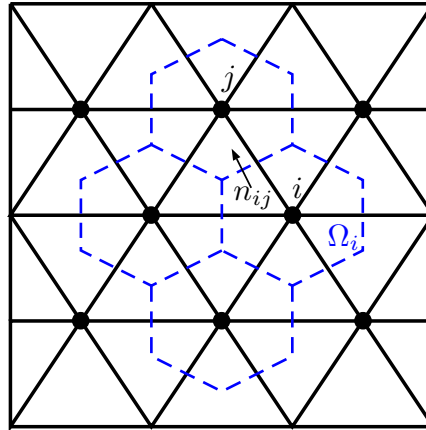


Figure 4.2 – Primal mesh (black) and control volumes in the dual mesh (blue).

For the purpose of this study, the convective flux will be calculated using a second-order JST [JST81] scheme for its satisfactory capability in capturing shock waves, a fairly rapid convergence to steady state and robustness also on coarse grids. The latter is a substantial feature required for a black box solver to be employed in combination with MLMC. The efficiency and accuracy of the entire algorithm rely on the hypothesis that the deterministic error monotonically decays when refining the grid (Eq. (4.5)). It is worth underlining that, in this chapter, we deliberately choose flow problems modeled by Euler equations because we can assume, without loss of generality, that the deterministic error in approximating the QoI under investigation and the variance of  $\mathcal{Y}_\ell = \mathcal{Q}_{M_\ell} - \mathcal{Q}_{M_{\ell-1}}$  decay while refining the computational grid. The former assumptions can also be applied to flow problems modeled by Navier-Stokes equations in turbulence regimes, however it is more difficult to ensure a decay in  $\text{Var}[\mathcal{Y}_\ell]$  and we postpone this discussion in the following section.

As black box solver for our simulations we use the Stanford University Unstructured (SU2)

[PEA<sup>+</sup> 14, PCA<sup>+</sup> 13] computational environment because of its flexibility and capability of being interfaced with the MLMC algorithm libraries we implemented in Python<sup>TM</sup>.

In the following sections we apply the above presented methodology to propagate operating and geometric uncertainties on 2D transonic airfoils. We consider the symmetric NACA 0012 airfoil and the NASA SC(2)-0012 affected by operating uncertainties due to atmospheric variability of the surrounding flow and geometric uncertainties due to manufacturing tolerances and fatigue.

### 4.2.2 MLMC Grid Hierarchy

As previously stated the MLMC methodology is based on the idea of drawing MC samples on a hierarchy of computational grids (levels). For inviscid problems, there are no restrictions on the type of grids or the strategy used to refine them. The only requirement is a grid convergence over all levels of discretization (meaning that even the coarsest mesh resolves the main features of the flow affecting the QoI under investigation, see e.g. Fig. 5.16).

Depending on the type of application and the QoI under investigation we might build a hierarchy of nested computational grids (Fig. 4.3) or refine only a specific boundary (Fig. 4.4) and re-mesh the domain to economize the total number of grid nodes and at the same time increase the accuracy in approximating the solution and hence the QoI.

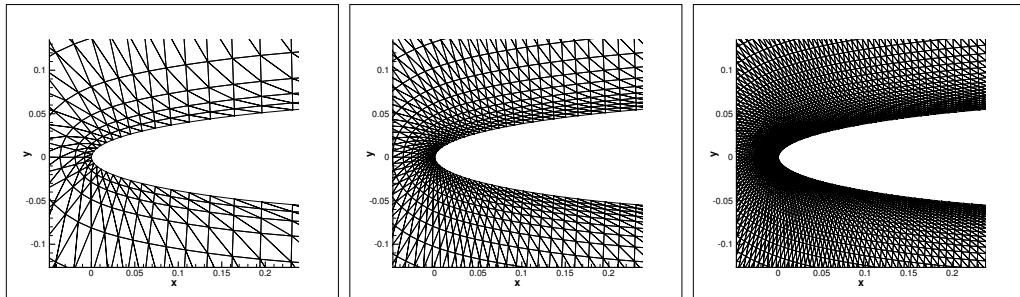


Figure 4.3 – Nested computational grids; close up view of the leading edge of an airfoil.

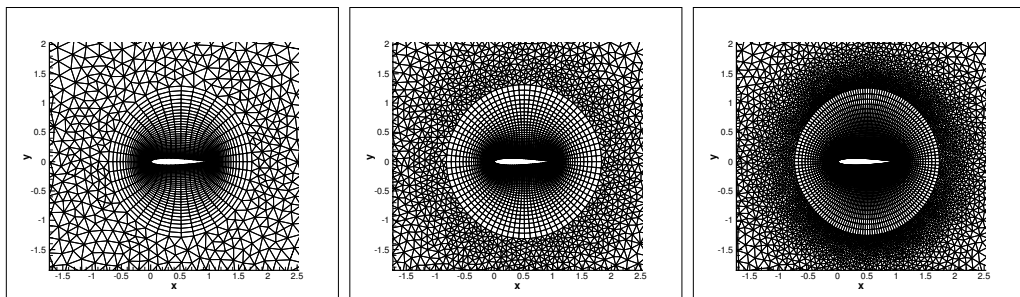


Figure 4.4 – Grids adapted around the airfoil boundary.

### 4.2.3 Inviscid transonic test cases: NACA 0012 and NASA SC(2)-0012

In this section we consider the two-dimensional NACA 0012 and the supercritical NASA SC(2)-0012 airfoils in transonic (Mach  $M = 0.8$ ) inviscid flow affected by operating and geometric uncertainties. The former airfoil is known to present a strong shock on the suction side and a weaker shock on the pressure one, while the latter was designed to delay and alleviate the effect of wave drag in the transonic speed range. With a flattened upper surface, highly cambered aft section and a larger leading edge radius, compared to the NACA 0012 airfoil, the NASA SC(2)-0012 is able to reduce the acceleration of the incoming flow around the surface of the airfoil and hence weaken the shock wave on the suction side and postpone the shock on the pressure side (Figure 4.5).

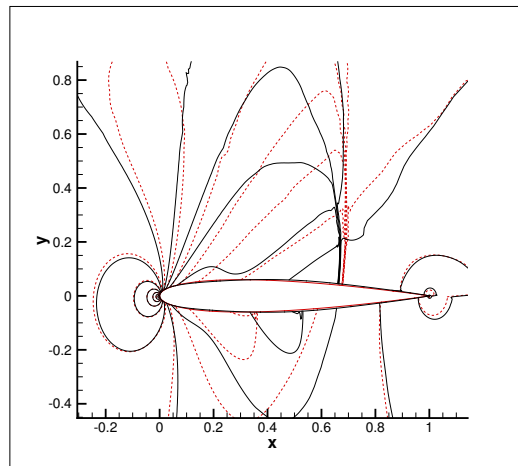
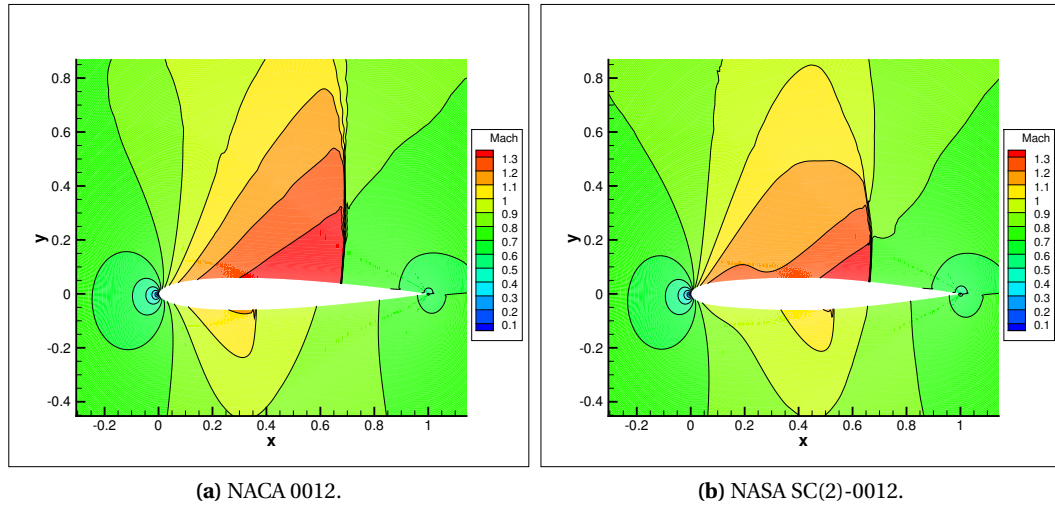
We investigate the effects of geometric and operating uncertainties on the pressure coefficient  $C_p$  profile around the two airfoils using the above introduced MLMC algorithm.

**Operational and Geometrical Uncertainties:** In the following simulations we consider a total of 14 uncertain parameters (4 operating and 10 geometric). The nominal values and the range of uncertainties considered are listed in Table 4.1. All parameters are described with truncated normal distributions that we identify with  $\mathcal{TN}(\mu, \sigma, a, b)$ , where  $\mu$  is the location or mean,  $\sigma$  is the standard deviation,  $a$  is the maximum allowed value and  $b$  is the minimum one (in percent with respect to the nominal value). The notation  $y \sim \mathcal{TN}(\mu, \sigma, a, b)$  denotes a r.v. with a density function:

$$p(y) = \begin{cases} 0 & y < a \\ \frac{1}{z} \frac{1}{\sqrt{2\pi}\sigma} e^{-\frac{(y-\mu)^2}{2\sigma^2}} & a \leq y \leq b \\ 0 & y > b. \end{cases} \quad \text{and} \quad z = \int_a^b \frac{1}{\sqrt{2\pi}\sigma} e^{-\frac{(y-\mu)^2}{2\sigma^2}} dy \quad (4.22)$$

The nominal geometric parameters correspond to the PARSEC [Sob98] coefficients of the NACA 0012 and NASA SC(2)-0012 respectively (see 2.4.3 for a detailed description of the PARSEC parametrization).

**Grid Hierarchy** Hereafter we employ a hierarchy composed of 6 hybrid-element O-grids that wraps around the surface of the airfoils. Quadrilaterals are used in the region adjacent to the airfoil surface and triangles in the remaining portion of the domain. The first three grid levels and corresponding deterministic solutions are presented in the following figures (Figure 4.6). We observe that the coarse solutions are only able to capture global flow features and cannot identify accurately the shock position but are monotonically converging to the exact solution while refining the grid. At each level we doubled the number of airfoil nodes and halved the distance of the first grid point from the airfoil surface.



(c) Mach isolines of the NACA 0012 (red dashed lines) compared with the NASA SC(2)-0012 (black solid lines).

**Figure 4.5** – Deterministic solutions for the NACA 0012 and NASA SC(2)-0012 airfoils at  $M = 0.8$ .

The number of cells of each grid level and the average computational time needed to achieve a reduction of the residual of six orders of magnitude in a single run are presented in the following Table 4.2. We used the same computational grid hierarchy for both airfoils and just adapted the inner boundary to accommodate the different airfoil shape.

**Propagation of Uncertainties** We consider three sets of simulations with an increasing number of uncertainties. First we propagate only operating uncertainties (4 uncertain parameters), then only the geometric (10 uncertain parameters) and finally all at the same time (14 uncertain parameters). As QoI for our simulations we consider the pressure coefficient  $C_p$  around the profile.

## Chapter 4. Multi Level Monte Carlo Method

	Name	Nominal value		Uncertainty
<b>Operational</b>	$T_\infty$	$T_n = 288.15 [K]$		$\mathcal{T}\mathcal{N}(T_n, 2\%, 110\%, 90\%)$
	$p_\infty$	$p_n = 101325 [N/m^2]$		$\mathcal{T}\mathcal{N}(p_n, 2\%, 110\%, 90\%)$
	$\alpha$	$\alpha_n = 1.25^\circ$		$\mathcal{T}\mathcal{N}(\alpha_n, 1\%, 110\%, 90\%)$
	$M$	$M_n = 0.8$		$\mathcal{T}\mathcal{N}(M_n, 2\%, 110\%, 90\%)$
<b>Geometrical</b>		<b>NACA 0012</b>	<b>NASA SC(2)-0012</b>	
	$R_p$	0.01458398	0.01710688	$\mathcal{T}\mathcal{N}(R_{P_n}, 2.5\%, 110\%, 90\%)$
	$R_s$	0.01458398	0.01710689	$\mathcal{T}\mathcal{N}(R_{S_n}, 2.5\%, 110\%, 90\%)$
	$X_p$	0.30049047	0.39738704	$\mathcal{T}\mathcal{N}(X_{P_n}, 2.5\%, 110\%, 90\%)$
	$X_s$	0.30049047	0.3973871	$\mathcal{T}\mathcal{N}(X_{S_n}, 2.5\%, 110\%, 90\%)$
	$Y_p$	-0.05994286	-0.06064754	$\mathcal{T}\mathcal{N}(Y_{P_n}, 2.5\%, 110\%, 90\%)$
	$Y_s$	0.05994286	0.06064754	$\mathcal{T}\mathcal{N}(Y_{S_n}, 2.5\%, 110\%, 90\%)$
	$C_p$	0.44213792	0.43927873	$\mathcal{T}\mathcal{N}(C_{P_n}, 2.5\%, 110\%, 90\%)$
	$C_s$	-0.44213792	-0.43927868	$\mathcal{T}\mathcal{N}(C_{S_n}, 2.5\%, 110\%, 90\%)$
	$\theta_p$	8.3763395	10.27242132	$\mathcal{T}\mathcal{N}(\theta_{P_n}, 2.5\%, 110\%, 90\%)$
$\theta_s$	-8.3763395	-10.27241363	$\mathcal{T}\mathcal{N}(\theta_{S_n}, 2.5\%, 110\%, 90\%)$	

**Table 4.1** – Operational and Geometrical parameters and uncertainties for the NACA 0012 and NASA SC(2)-0012 problems.

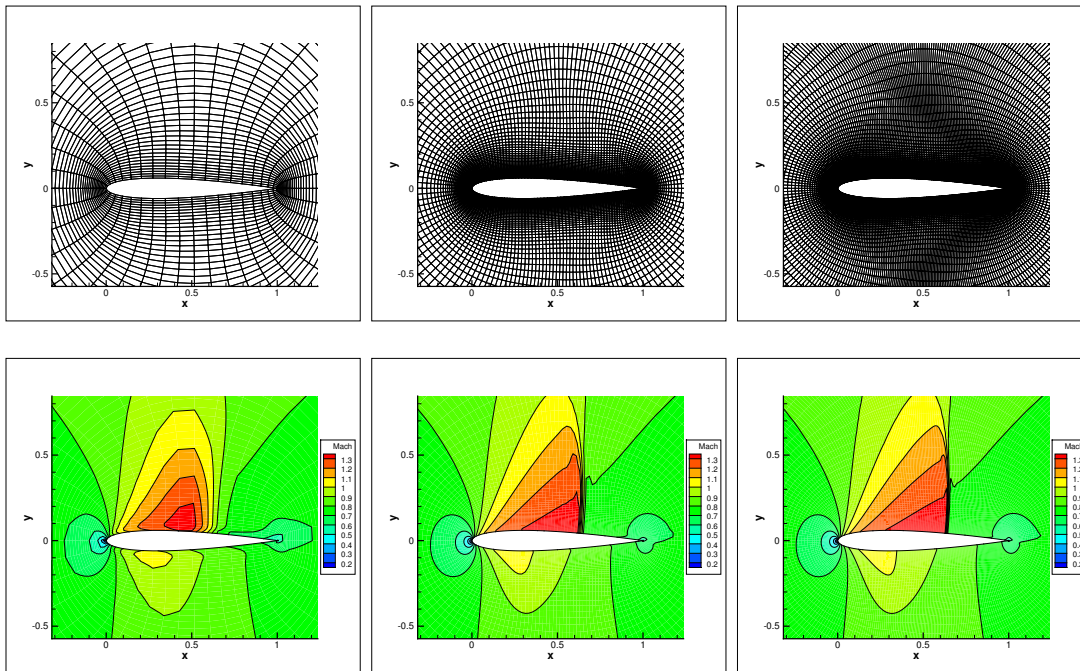


**Figure 4.6** – Grids and realizations for the first three levels in the MLMC hierarchy for the NACA 0012 airfoil.

In the following figures we present respectively the results with only geometric uncertainties (Figure 4.7) and with all uncertainties (Figure 4.8).

LEVEL	Airfoil nodes	Cells	Avg. Real Computational Time [s] (CPU)
$L_0$	41	6943	12.4 (32)
$L_1$	81	11115	20.9 (38)
$L_2$	161	19385	26.9 (44)
$L_3$	321	36251	71.1 (50)
$L_4$	641	71477	231.15 (56)
$L_5$	1281	145005	422.0 (64)

Table 4.2 – MLMC grid hierarchy for the NACA 0012 and NASA SC(2)-0012 cases.

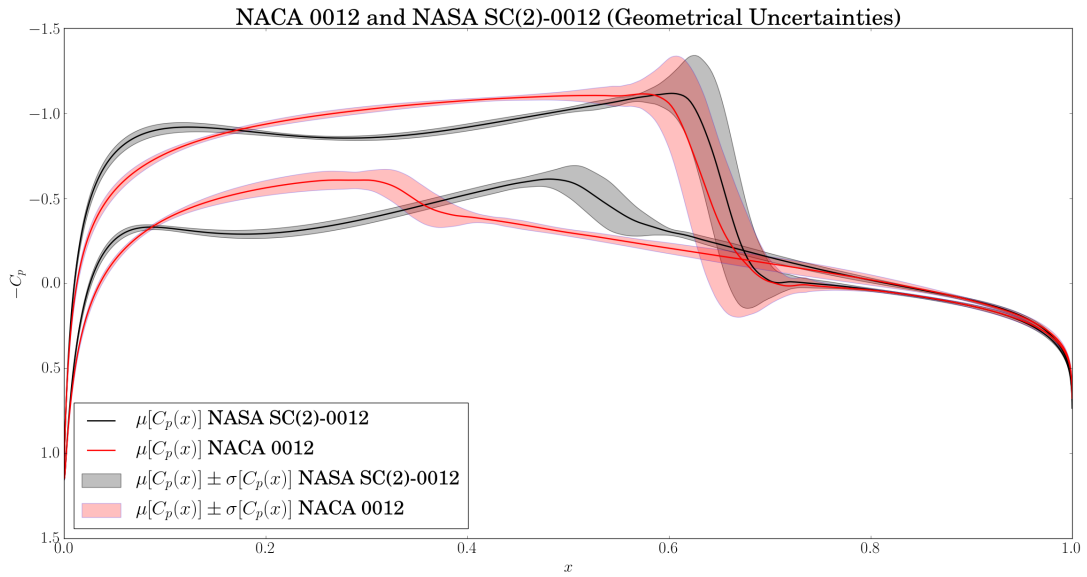
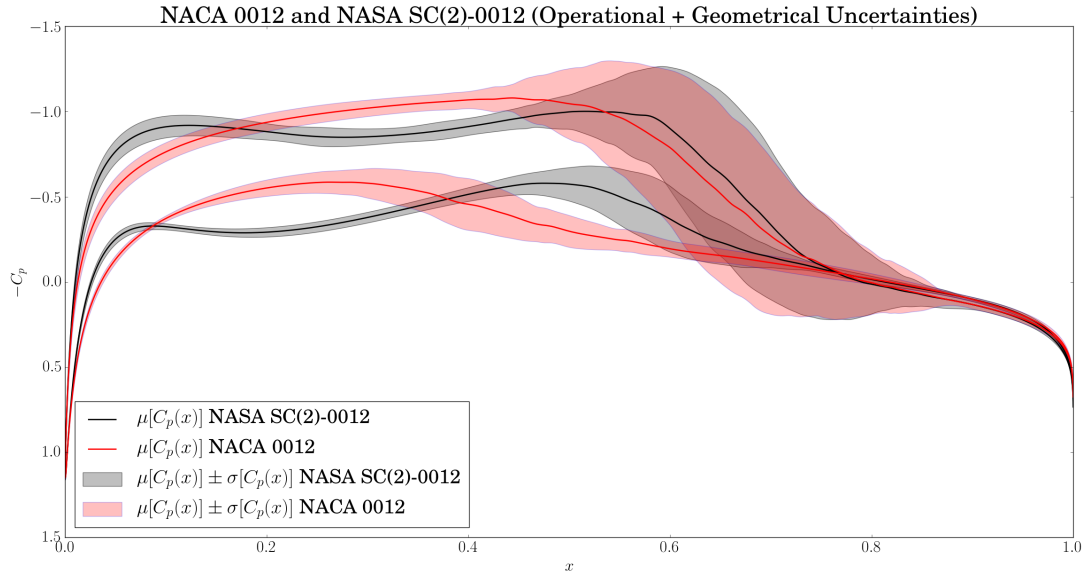


Figure 4.7 – Mean  $C_p$  profile and a band of uncertainty that corresponds to one standard deviation (68.27%) for the NACA 0012 and NASA SC(2)-0012 airfoils affected by 10 geometric uncertainties ( $R_p$ ,  $R_S$ ,  $X_p$ ,  $X_S$ ,  $Y_p$ ,  $Y_S$ ,  $C_p$ ,  $C_S$ ,  $\theta_p$ ,  $\theta_S$ ).

As one should expect, we witness a larger effect on the pressure profile when we consider all the uncertainties. It is interesting to observe a larger variability for the NACA 0012 in the shock position on the upper side to the airfoil.

The flattened upper surface together with a larger leading edge radius of the NASA SC(2)-0012, by reducing the acceleration of the incoming flow before the shock region, seems to reduce the effect of the operating and geometric uncertainties in affecting the shock position on the suction side.

In the case with operating and geometric uncertainties (Figure 4.8) we also recognize a beneficial effect of the shape of the supercritical airfoil in reducing the variability on the pressure side (Figure 4.8).



**Figure 4.8** – Mean  $C_p$  profile and a band of uncertainty that corresponds to one standard deviation (68.27%) for the NACA 0012 and NASA SC(2)-0012 airfoils affected by 4 operating ( $M, \alpha, T_\infty, p_\infty$ ) and 10 geometric uncertainties ( $R_p, R_S, X_p, X_S, Y_p, Y_S, C_p, C_S, \theta_p, \theta_S$ ).

**Computational Complexity of MLMC and MC** We now compare the computational cost required to achieve a prescribed tolerance using the MLMC algorithm presented above and the MC method.

First we report the set of rates and constants  $\mathcal{P} = \{c_\alpha, c_\beta, c_\gamma, \alpha, \beta, \gamma\}$  computed using least square fit during the screening phase of the MLMC algorithm for the three sets of simulations with an increasing number of uncertainties. In the last two rows of the table we provide a theoretical estimation (up to a constant  $C$ ) of the cost in function of the tolerance for MLMC (see Eq. (4.8)) and MC (see (3.22)).

	Operating (4)	Geometric (10)	Operating + Geometric (14)
$c_\alpha$	19.65	1652.07	344.91
$\alpha$	0.67	1.09	0.97
$c_\beta$	1474.09	8.27	16456.48
$\beta$	1.32	0.87	1.57
$c_\gamma$	0.001		
$\gamma$	1.49		
$\mathbf{C}_{MLMC}(\epsilon)$	$C \cdot \epsilon^{-2.25}$	$C \cdot \epsilon^{-2.56}$	$C \cdot \epsilon^{-1.91}$
$\mathbf{C}_{MC}(\epsilon)$	$C \cdot \epsilon^{-4.22}$	$C \cdot \epsilon^{-3.36}$	$C \cdot \epsilon^{-3.53}$

**Table 4.3** – MLMC computed rates and constants for the weak error, strong error and computational cost and theoretical cost models for MLMC and MC methods (obtained with a screening of 100 samples on 4 levels) for the airfoil problem with increasing number of uncertain parameters.



By looking at Table 4.3 and the left plot in Figure 4.9, we can observe a significant reduction in computational complexity of MLMC with respect to MC.

As theoretically predicted in Eq. (4.8), we observe that, for the MLMC method, the total cost required to achieve a RMSE of  $\varepsilon$  in the case of  $\beta < \gamma$  (rate of decay of  $\|\text{Var}[\mathcal{Y}_\ell]\|_{L^1(D)}$  smaller than the growth rate of the cost to compute one sample at level  $l$ ) is proportional to  $\varepsilon^{-2-(\gamma-\beta)/\alpha}$ ; on the other hand, for the MC method, as presented in Eq. (3.22), the total cost is proportional to  $\varepsilon^{-2-(\gamma/\alpha)}$ .

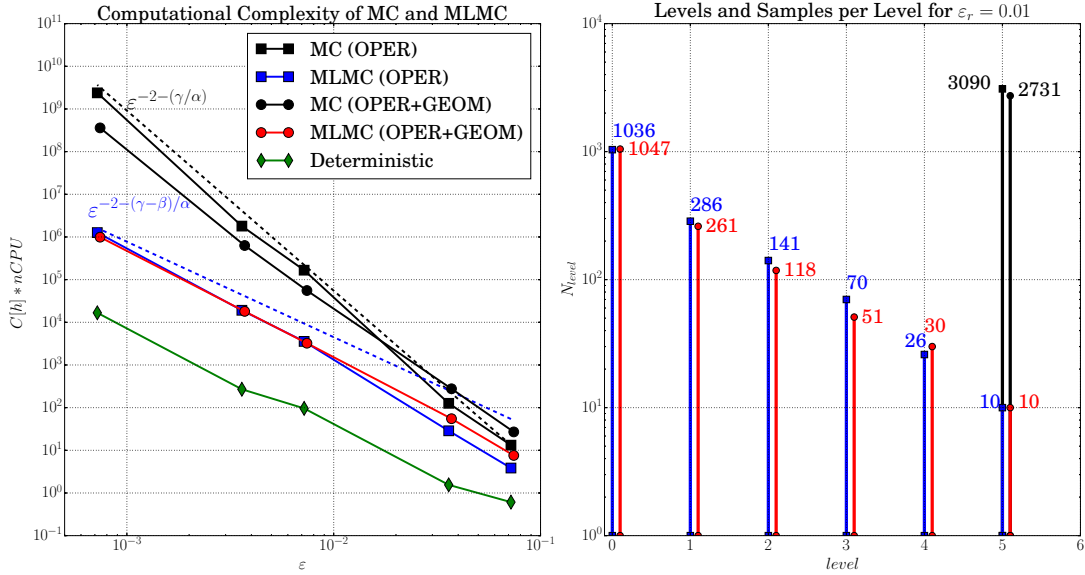


**Figure 4.9** – Levels and samples per level  $N_\ell$  required to achieve a relative tolerance of 0.01 on the total error for the  $C_p$  profile for the three NACA 0012 uncertainty scenarios.

The levels and number of samples per lever required to achieve a relative tolerance  $\varepsilon_r = 0.01$  for the case with 4 operating and 14 operating and geometric uncertain parameters are reported in the right plot on Figure 4.9 together with the number of MC samples required to achieve the same accuracy. By looking at the latter we can further appreciate the competitive advantage of MLMC with respect to the MC method: the largest number of simulations are performed on coarse grids and just few samples are drawn on the finest levels.

### 4.3 Disadvantages of Standard MLMC

In the previous sections we presented the MLMC approach and an efficient procedure to perform UQ in aerodynamics problems affected by operating and geometric uncertainties. The numerical example presented above provides clear indications of the computational reduction that can be achieved with MLMC with respect to MC.

The main disadvantage of the above presented procedure is that in order to compute the optimal number of levels and samples per levels required to achieve a prescribed tolerance we

## Chapter 4. Multi Level Monte Carlo Method

---

are required to perform a screening.

For computationally expensive problems, this screening phase, usually not accounted for in the literature in the total cost analysis of MLMC algorithm, can be quite time consuming. In particular, if  $\bar{L}$  and  $\bar{N}$  (number of screening levels and samples) are chosen too large the screening phase might turn out to be more expensive than the overall MLMC simulation on the optimal hierarchy  $\{0, \dots, L\}$ . On the other hand, if  $\bar{N}$  and  $\bar{L}$  are chosen too small, the extrapolation of the convergence rates  $\alpha$  and  $\beta$  might be quite unreliable leading to a hierarchy that is not appropriate to achieve a prescribed tolerance or that is far from optimal.

In the next chapter we present an adaptive version of the MLMC, named Continuation-MLMC that overcomes this problem.

# 5 Continuation Multi Level Monte Carlo

To overcome the limitations of the standard MLMC algorithm highlighted in the previous chapter concerning the *screening* phase and the estimation of the set of parameters  $\mathcal{P} = \{c_\alpha, c_\beta, c_\gamma, \alpha, \beta, \gamma\}$ , that directly affect the computational complexity and the accuracy of the method (through the appropriate choice of levels and samples per level required to achieve a prescribed tolerance), we consider here the Continuation Multi Level Monte Carlo (CMLMC) algorithm proposed in [CHAN<sup>+</sup>14] and we propose an extension to perform uncertainty quantification in inviscid and viscous aerodynamic problems affected by operating and geometric uncertain parameters.

## 5.1 The C-MLMC Method

The key idea of CMLMC is to solve for the QoI with a sequence of decreasing tolerances  $\varepsilon_0 > \varepsilon_1 > \varepsilon_2 > \dots > \varepsilon_M$  and progressively improve the estimation of the problem dependent parameters  $\mathcal{P}$  that directly control the number of levels and samples per level.

### 5.1.1 C-MLMC Iterative Procedure

The sequence of decreasing tolerances is constructed as:

$$\varepsilon_i = \begin{cases} (r_1^{i_E-i} r_2^{-1}) \varepsilon_M & i < i_E \\ (r_2^{i_E-i} r_2^{-1}) \varepsilon_M & i > i_E \end{cases} \quad (5.1)$$

where  $r_1, r_2 > 1$  are parameters that control the computational load and the tolerance decrease from the initial tolerance  $\varepsilon_0$  to the desired final one  $\varepsilon_M$ .

The first few iterations  $i < i_E$  are needed to obtain increasingly accurate estimates of the problem dependent parameters  $\mathcal{P}$  while the iterations  $i > i_E$  prevent redundant computations due to fluctuations in the estimates of  $\mathcal{P}$  by solving the problem for a slightly smaller tolerance than the desired one  $\varepsilon_M$ .

In (5.1)  $i_E$  is chosen as

$$i_E = \left\lfloor \frac{-\log(\boldsymbol{\varepsilon}_M) + \log(r_2) + \log(\boldsymbol{\varepsilon}_0)}{\log(r_1)} \right\rfloor \quad (5.2)$$

and corresponds to the iteration at which the problem is solved with tolerance  $\varepsilon_{i_E} = r_2^{-1} \boldsymbol{\varepsilon}_M$ .

At the  $i$ -th iteration of the C-MLMC algorithm, in the presence of an estimate of  $\mathcal{P} = \{c_\alpha, \alpha, c_\beta, \beta, c_\gamma, \gamma\}$ ,  $C_\ell$  and  $\text{Var}[Y_\ell]$ , we compute the optimal number of levels, with prescribed tolerance  $\varepsilon_i$ , by solving the following discrete optimization problem and by exhaustive search:

$$(L_i, \theta_i) = \underset{\substack{L \in [L_{i-1}, \dots, L_{MAX}], \theta \in (0,1) \\ \text{s.t. } c_\alpha M_L^{-\alpha} = (1-\theta)\varepsilon_i}}{\text{argmin}} \mathbf{C}_{\text{MLMC}}(\varepsilon_i, \theta, L) \quad (5.3)$$

using the cost model:

$$\mathbf{C}_{\text{MLMC}}(\varepsilon_i, \theta, L) = \left( \frac{\mathcal{C}_\phi}{\theta \varepsilon_i} \right)^2 \left( \sum_{\ell=0}^L \sqrt{C_\ell \text{Var}[Y_\ell]} \right)^2 \quad (5.4)$$

obtained with an optimal choice of  $N_\ell$ :

$$N_\ell = \left\lceil \left( \frac{\mathcal{C}_\phi}{\theta \varepsilon} \right)^2 \sqrt{\frac{\text{Var}[Y_\ell]}{C_\ell}} \sum_{k=0}^L \sqrt{C_k \text{Var}[Y_k]} \right\rceil \quad l = 0, 1, \dots, L. \quad (5.5)$$

It is worth underline that  $\mathcal{P} = \{c_\alpha, \alpha, c_\beta, \beta, c_\gamma, \gamma\}$  are obtained via a least square procedure using the samples computed at the previous iterations of the C-MLMC. On the other hand,  $C_\ell$  and  $\text{Var}[Y_\ell]$  are the actual computed average cost and variance of difference on the levels.

Notice that the constraint  $c_\alpha M_L^{-\alpha} = (1-\theta)\varepsilon_i$  in (5.3) represents the bias constrain and allows to determine  $\theta$  as a function of  $L$  (and  $\varepsilon_i$ ):

$$\theta(\varepsilon_i, L) = 1 - \frac{c_\alpha M_L^{-\alpha}}{\varepsilon_i} \quad (5.6)$$

Indeed, since  $c_\alpha M_L^{-\alpha}$  can take only discrete values, for each  $L$  that satisfies the bias constraint  $\mathbf{B} \leq \varepsilon_i$ , it is worth taking the largest possible  $\theta = 1 - \frac{\mathbf{B}}{\varepsilon_i}$  so as to relax as much as possible the statistical error constraint

$$\text{Var}[\mathbf{E}^{\text{MLMC}}[Q_M]] \leq \left( \frac{\theta \varepsilon_i}{\mathcal{C}_\phi} \right)^2 \quad (5.7)$$

and reduce the overall computational cost. Problem (5.3) is a discrete optimization problem and can be easily solved by an exhaustive search.

### 5.1.2 Practical Aspect of C-MLMC

The pivotal feature of the CMLMC with respect to standard MLMC algorithm is that the parameter set  $\mathcal{P}$  is computed on-the-fly and updated at each iteration of the algorithm. The estimation of the parameters that describe the cost  $(c_\gamma, \gamma)$  and the bias  $(c_\alpha, \alpha)$  is relatively straightforward since these quantities can be estimated with just few realizations per level. In practice, on each level, the cost  $C_\ell$  is estimated by averaging over the samples the time needed to obtain a single realization, and the discretization error is estimated as :

$$\mathbf{B}_\ell \approx |\mathbb{E}^{\text{MC}}[Q_\ell - Q_{\ell-1}]|. \quad (5.8)$$

Then a least squares fit over the levels is done to estimate  $(c_\gamma, \gamma)$  and  $(c_\alpha, \alpha)$ .

The estimation of the variances  $\mathbb{V}ar[Y_\ell]$ , on the other hand, can be quite inaccurate with a small sample size. In a standard MLMC such variances are usually computed using a sample variance estimator  $\mathbb{V}^{\text{MC}}[Y_\ell]$ :

$$\mathbb{V}ar[Y_\ell] \approx \mathbb{V}^{\text{MC}}[Y_\ell] = \frac{1}{N_\ell - 1} \sum_{n=1}^{N_\ell} \left( Y_\ell(\omega^{(n,l)}) - \mathbb{E}^{\text{MC}}[Y_\ell] \right)^2 \quad (5.9)$$

At the deepest levels usually we do not have enough realizations to accurately compute  $\mathbb{V}^{\text{MC}}[Y_\ell]$  (asymptotically accurate only as  $N_\ell \rightarrow \infty$ ) and estimate the sample sizes  $N_\ell$  for the next iteration, as well as the parameters  $(c_\beta, \beta)$  needed to extrapolate  $\mathbb{V}ar[Y_\ell]$  and hence  $N_\ell$  on new levels that are added at the next iteration.

### 5.1.3 Bayesian Update

Collier et al. [CHAN<sup>+</sup>14] presented an intuitive methodology based on Bayesian updates that use samples generated on all levels to locally improve the estimation of  $\mathbb{V}ar[Y_\ell]$  using the bias model  $\mathbb{E}[Y_\ell] \approx \hat{\mu}_\ell := c_\alpha M_\ell^{-\alpha}$  and variance model  $\mathbb{V}ar[Y_\ell] \approx \hat{\lambda}_\ell^{-1} := c_\beta M_\ell^{-\beta}$  with  $c_\alpha, \alpha, c_\beta, \beta$  estimated from the previous iteration of the CMLMC algorithm.

The intuitive idea is to describe  $Y_\ell$  as a Gaussian random variable  $\mathcal{N}(\mu_\ell, \lambda_\ell^{-1})$  and perform a Bayesian update of  $\mu_\ell$  and  $\lambda_\ell$  based on the collected values  $Y_\ell(\omega^{(n,l)})$  and a Normal-Gamma prior distribution  $\mathcal{N}^{\mathcal{G}}(\hat{\mu}_\ell, k_0, k_1 \hat{\lambda}_\ell + 1/2, k_1)$ <sup>1</sup> which has maximum in  $(\hat{\mu}_\ell, \hat{\lambda}_\ell)$ .  $k_0$  and  $k_1$  are two parameters that represent our "certainty" on  $\hat{\mu}_\ell$  and  $\hat{\lambda}_\ell^{-1}$ . Notice that  $k_0$  is non-dimensional while  $k_1$  has the dimension of  $\mathbb{V}ar[Q]$ . Therefore, it is convenient to express  $k_1$  in relative terms as  $k_1 = \tilde{k}_1 / \mathbb{V}ar[Q_M]$ , with  $\tilde{k}_1$  non-dimensional.

<sup>1</sup>The normal-gamma distribution is a bivariate four-parameter family of continuous probability distributions. It is the conjugate prior of a normal distribution with unknown mean and precision. Its joint probability density function is defined as:  $\mathcal{N}^{\mathcal{G}}(x, \tau | \mu, \lambda, \alpha, \beta) = \frac{\beta^\alpha \sqrt{\lambda}}{\Gamma(\alpha) \sqrt{2\pi}} \tau^{\alpha-1/2} e^{-\beta\tau} e^{-\frac{\lambda\tau(x-\mu)^2}{2}}$ .

The choice of a Normal distribution to model  $Y_\ell$  and a Normal-Gamma prior are for convenience. The Normal distribution depends only on the first two moments so we can rely on the mean and variance models estimated during the iterations of the algorithm. On the other hand, the Normal-Gamma prior is conjugate to the Normal distribution (with unknown mean and precision) and allows to obtain simple and closed formulas to update the parameters.

Indeed, the posterior is also a Normal-Gamma, with maximum at

$$\mu_\ell^{MAP} = \frac{N_\ell \mathbb{E}^{\text{MC}}[Y_\ell] + k_0 \widehat{\mu}_\ell}{k_0 + N_\ell} \quad \text{and} \quad \lambda_\ell^{MAP} = \frac{\Xi_{1,\ell} - \frac{1}{2}}{\Xi_{2,\ell}} \quad (5.10)$$

with:

$$\Xi_{1,\ell} = \frac{1}{2} + \widetilde{k}_1 \widehat{\lambda}_\ell + \frac{N_\ell}{2}, \quad (5.11a)$$

$$\Xi_{2,\ell} = \widetilde{k}_1 + \frac{N_\ell - 1}{2} \text{V}^{\text{MC}}[Y_\ell] + \frac{k_0 N_\ell (\mathbb{E}^{\text{MC}}[Y_\ell] - \widehat{\mu}_\ell)^2}{2(k_0 + N_\ell)}. \quad (5.11b)$$

The resulting update formula for  $\text{Var}[Y_\ell] \approx \lambda_\ell^{-1}$  is then:

$$\text{V}^{\text{C}}[Y_\ell] := \frac{\Xi_{2,\ell}}{\Xi_{1,\ell} - \frac{1}{2}} \quad l > 0 \quad (5.12)$$

We can easily show that:

$$N_\ell \rightarrow \infty \quad \Rightarrow \quad \text{V}^{\text{C}}[Y_\ell] \rightarrow \frac{1}{N_\ell - 1} \sum_{n=1}^{N_\ell} \left( Y_\ell(\omega^{(n,l)}) - \mathbb{E}^{\text{MC}}[Y_\ell] \right)^2 \quad (5.13)$$

thus recovering the sample variance estimator, whereas

$$N_\ell = 0 \quad \Rightarrow \quad \text{V}^{\text{C}}[Y_\ell] = \frac{1}{\widehat{\lambda}_\ell} = c_\beta M_\ell^{-\beta} \quad (5.14)$$

thus using just the prior model with fitted parameters  $(c_\beta, \beta)$ .

Thanks to the Bernstein–von Mises theorem [VdV00] the posterior distribution becomes effectively independent of the prior distribution once the amount of information supplied by a sample of data is large enough.

Finally, following the above arguments, we approximate the variance of the MLMC estimator as:

$$\text{Var}[\mathbb{E}^{\text{MLMC}}[Q_M]] = \sum_{\ell=0}^L \frac{\text{Var}[Y_\ell]}{N_\ell} \approx \sum_{\ell=0}^L \frac{\text{V}^{\text{C}}[Y_\ell]}{N_\ell} \quad (5.15)$$

and the total MSE as:

$$e(\mathbb{E}^{\text{MLMC}}[Q_M]) \approx \mathbb{E}^{\text{MC}}[Y_L]^2 + \sum_{\ell=0}^L \frac{\mathbb{V}^{\text{C}}[Y_\ell]}{N_\ell}. \quad (5.16)$$

### 5.1.4 C-MLMC Algorithm

The resulting algorithm is described in Algorithm 2.

---

**Algorithm 2:** Continuation Multi Level Monte Carlo.

---

CMLMC( $\bar{N}, \bar{L}, L_{MAX}, k_0, k_1, r_1, r_2, \varepsilon, \varepsilon_0$ )

```

for  $l = 0 : \bar{L}$  do
    for  $i = 0 : \bar{N}$  do
        Generate random samples:  $\mathbf{O}(\omega^{(i,\ell)}), \mathbf{G}(\omega^{(i,\ell)})$ 
         $Q_{M_\ell}^{(i)} \leftarrow \text{PROBLEM}_\ell(\mathbf{O}(\omega^{(i,\ell)}), \mathbf{G}(\omega^{(i,\ell)}))$ 
         $Q_{M_{\ell-1}}^{(i)} \leftarrow \text{PROBLEM}_{\ell-1}(\mathbf{O}(\omega^{(i,\ell)}), \mathbf{G}(\omega^{(i,\ell)}))$ 
         $Y_\ell^{(i)} = Q_{M_\ell}^{(i)} - Q_{M_{\ell-1}}^{(i)}$ 
    compute  $\{C_\ell\}, \{\mathbb{E}^{\text{MC}}[Y_\ell]\}, \{\mathbb{V}^{\text{MC}}[Y_\ell]\}$ 
    compute  $\mathcal{P} = \{c_\alpha, c_\beta, c_\gamma, \alpha, \beta, \gamma\}$  by least squares fit
    compute  $\mathbb{V}^{\text{C}}[Y_\ell]$  using (5.12) on all levels  $l = 0, \dots, L_{MAX}$ 
    compute  $\mathcal{I}_\varepsilon(\varepsilon, \varepsilon_0, r_1, r_2)$  using (5.2)
    while  $i < \mathcal{I}_\varepsilon$  or  $\text{TErr} > \varepsilon$  do
        update  $\varepsilon_i = \frac{\varepsilon_{i-1}}{r_1}$ 
        compute  $L_i(L_{MAX}, \varepsilon_i, c_\alpha, \alpha, \{\mathbb{V}^{\text{C}}[Y_\ell]\}, \{C_\ell\})$  using (5.3) and  $\theta_i = 1 - \frac{c_\alpha M_L^{-\alpha}}{\varepsilon_i}$ 
        for  $l = 0 : L_i$  do
            compute  $N_\ell(\varepsilon_i, \mathbb{V}^{\text{C}}[Y_\ell], \gamma, c_\gamma, \theta_i)$  using (5.5)
            for  $i = 0 : N_\ell$  do
                Generate random samples:  $\mathbf{O}(\omega^{(i,\ell)}), \mathbf{G}(\omega^{(i,\ell)})$ 
                 $Q_{M_\ell}^{(i)} \leftarrow \text{PROBLEM}_\ell(\mathbf{O}(\omega^{(i,\ell)}), \mathbf{G}(\omega^{(i,\ell)}))$ 
                 $Q_{M_{\ell-1}}^{(i)} \leftarrow \text{PROBLEM}_{\ell-1}(\mathbf{O}(\omega^{(i,\ell)}), \mathbf{G}(\omega^{(i,\ell)}))$ 
                 $Y_\ell^{(i)} = Q_{M_\ell}^{(i)} - Q_{M_{\ell-1}}^{(i)}$ 
            update  $\{C_\ell\}_{\ell=0}^{L_i}, \{\mathbb{E}^{\text{MC}}[Y_\ell]\}_{\ell=0}^{L_i}, \{\mathbb{V}^{\text{MC}}[Y_\ell]\}_{\ell=0}^{L_i}$ 
            update  $\mathbb{E}^{\text{MLMC}}[Q_M] = \sum_{\ell=0}^{L_i} \mathbb{E}^{\text{MC}}[Y_\ell]$ 
            compute  $(c_\alpha, \alpha) \leftarrow \{\mathbb{E}^{\text{MC}}[Y_\ell]\}_{\ell=0}^{L_i}$  using least squares fit
            compute  $(c_\gamma, \gamma) \leftarrow \{C_\ell\}_{\ell=0}^{L_i}$  using least squares fit
            compute  $(c_\beta, \beta) \leftarrow \{\mathbb{V}^{\text{MC}}[Y_\ell]\}_{\ell=0}^{L_i}$  using least squares fit
            update  $\mathcal{P} = \{c_\alpha, c_\beta, c_\gamma, \alpha, \beta, \gamma\}$  and  $\mathbb{V}^{\text{C}}[Y_\ell]$  using (5.12)
            estimate  $\mathbf{B}$  using (5.8) and  $\mathbb{V}ar[\mathbb{E}^{\text{MLMC}}[Q_M]]$  using (5.15)
            compute  $\text{TErr} = \mathbf{B} + \mathcal{E}_\phi \sqrt{\mathbb{V}ar[\mathbb{E}^{\text{MLMC}}[Q_M]]}$ 
        i = i+1
    return  $\mathbb{E}^{\text{MLMC}}[Q_M], \text{TErr}$ 

```

---

## 5.2 C-MLMC for UQ in Inviscid Aerodynamics

In this section we consider two relevant compressible aerodynamics model problems: a quasi 1D convergent-divergent Laval nozzle and the 2D transonic RAE-2822 airfoil affected by operating and geometric uncertainties.

### 5.2.1 Quasi-1D Model Problem: Flow in a Laval nozzle

For the Laval nozzle we employ the quasi-1D version of the Euler equations presented in Chapter 2.1.2. For the sake of explanation we report the vector of state variables  $\vec{W}$ , the convective flux  $\vec{F}$  and the source term  $\vec{Q}$ :

$$W = \begin{bmatrix} \rho A \\ \rho u A \\ \rho E A \end{bmatrix}, \quad f_I = \begin{bmatrix} \rho u A \\ (\rho u^2 + p) A \\ u(\rho E + p) A \end{bmatrix}, \quad Q = \begin{bmatrix} 0 \\ p \frac{dA}{dx_1} \\ 0 \end{bmatrix} \quad (5.17)$$

In (5.17),  $A$  denotes the area of the nozzle,  $\rho$ ,  $u$  and  $p$  the density, the velocity and the pressure of the fluid respectively and  $E$  is the total energy.

Since we are considering a quasi-1D problem, each grid node in the computational grid is associated with a certain area.

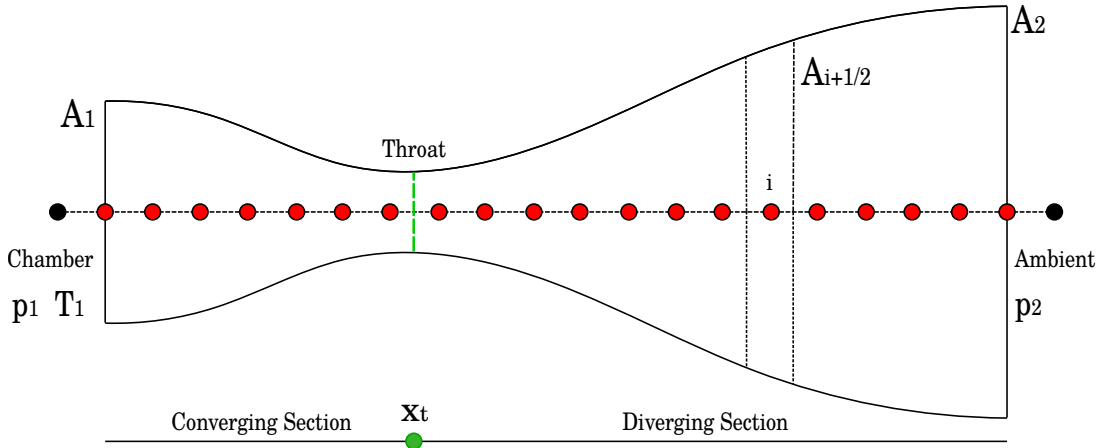


Figure 5.1 – Geometry and discretization of the convergent-divergent nozzle.

The area distribution over the x-axis corresponds to the Laval nozzle (Fig. 5.1) and it is



calculated using the relations:

$$\begin{aligned}
 A(x) &= 1 + \frac{1}{2}(A_1 - 1) \left\{ 1 + \cos\left(\frac{\pi x}{x_t}\right) \right\} \quad 0 \leq x \leq x_t \quad (\text{convergent section}) \\
 A(x) &= 1 + \frac{1}{2}(A_2 - 1) \left\{ 1 - \cos\left[\frac{\pi(x - x_t)}{1 - x_t}\right] \right\} \quad x_t \leq x \leq 1 \quad (\text{divergent section})
 \end{aligned} \tag{5.18}$$

We employ a central scheme with scalar artificial dissipation that computes the convective fluxes at a face of the control volume from the arithmetic average of the conservative variables on both sides of the face; to avoid overshoots at shocks, artificial dissipation, similar to the viscous fluxes, has to be added for stability [JST81]. We choose this simple but efficient approach, compared to other discretization methods, for its robustness also on coarse grids.

We specifically consider the case of a nozzle with a normal shock in the divergent section (*Laval nozzle flow*). The flow accelerates out of the chamber through the converging section and reaches its maximum subsonic speed at the throat ( $X_t$ ). After the throat the flow becomes supersonic, the Mach number increases and the pressure decrease as the area increases downstream. A normal shock forms in the duct, at  $X_s$ , and produces a near-instantaneous deceleration of the flow to subsonic speed. The subsonic flow then decelerates through the remainder of the diverging section, the Mach number decreases and pressure increases as the area increases, and exhausts as a subsonic jet.

**Operational and Geometrical Uncertainties:** Table 5.1 summarizes the physical and geometrical reference parameters and the uncertainties considered for the nozzle problem. The uncertainty on the different parameters is modeled as a truncated Gaussian random variable (see definition in Eq. (4.22)).

	Name	Nominal value	Uncertainty
<b>Operational</b>	$P_1$	$P_{1n} = 1.8e5 [Pa]$	$\mathcal{TN}(P_{1n}, 2\%, 110\%, 90\%)$
	$T_1$	$T_{1n} = 288 [K]$	$\mathcal{TN}(T_{1n}, 2\%, 110\%, 90\%)$
	$p_2$	$p_{2n} = 1.0e5 [Pa]$	$\mathcal{TN}(p_{2n}, 2\%, 110\%, 90\%)$
	$c_p$	$c_{pn} = 1005 [J/(kgK)]$	–
	$\gamma$	$\gamma_n = 1.4$	–
<b>Geometrical</b>	$A_1$	$A_{1n} = 1.5 [m^2]$	$\mathcal{TN}(P_{1n}, 2\%, 110\%, 90\%)$
	$A_2$	$A_{2n} = 2.0 [m^2]$	$\mathcal{TN}(P_{1n}, 2\%, 110\%, 90\%)$
	$X_t$	$X_{t2n} = 1/3 [m]$	–

**Table 5.1** – Operational and Geometrical parameters and uncertainties for the Laval nozzle problem.

**C-MLMC Settings and Grid Hierarchy:** In the following simulations we consider a scalar QoI, the shock location  $X_s$ , and a scalar field QoI, the Mach profile inside the nozzle  $M(x)$ .

Fig. 5.2 shows the Mach and pressure profile inside the Laval nozzle for the physical and geometrical deterministic reference conditions and the location of the shock ( $X_s$ ) in the divergent section.

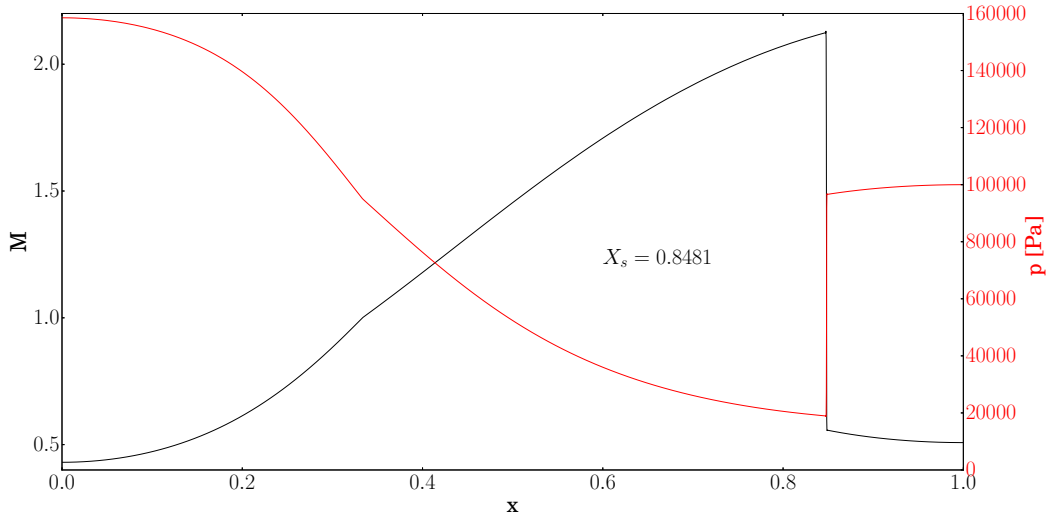


**Figure 5.2** – Deterministic solution (2051 uniform grid nodes) of the Laval nozzle with a normal shock in the diverging section ( $X_s = 0.8481$ ).

The hierarchy used for this problem is made up of 7 nested grid levels generated by doubling the number of nodes starting from the first level composed of 35 nodes:

$$N_\ell = N_0 * 2^\ell \quad \text{with} \quad N_0 = 35 \quad (5.19)$$

The number of nodes and the average computational time needed to achieve a reduction of the residual of six order of magnitude in a single run are presented in the following Table 5.2.

LEVEL	Nodes	CTime[s]
L0	35	0.025
L1	70	0.057
L2	140	0.19
L3	280	0.73
L4	560	2.94
L5	1120	11.5
L6	2240	49.1
L7	4480	147.4

**Table 5.2** – MLMC 7-levels grid hierarchy for the nozzle problem.

We prescribe a confidence of 10 % in the weak and strong error models with respect to the sampled ones (parameters  $k_0 = 0.1$  and  $k_1 = 0.1$ ). The parameters that define the computa-

tional load and the tolerance decrease from the initial to the final tolerance are presented in the following Table 5.3 for the two QoI considered in this test case.

Parameters	QoI $X_s$	QoI $M(x)$
$r_1$	1.5	1.5
$r_2$	1.15	1.15
$\varepsilon_0$	0.5	0.5
$\varepsilon_M$	0.001	0.01
$i_E$	15	9
$k_0$	0.1	0.1
$k_1$	0.1	0.1

**Table 5.3** – Setting for the C-MLMC algorithm for the computation of the scalar QoI  $X_s$  and the scalar field QoI  $M(x)$  in the Laval nozzle test case.

The parameter  $r_1 = 1.5$  has been chosen so that the cost of the MLMC increases of about 50% going from tolerance  $\varepsilon_i$  to  $\varepsilon_{i+1} < \varepsilon_M$ . The parameter  $r_2 = 1.15$  corresponds to a cost increase of about 15% at the final iteration.

**Propagation of Uncertainties with C-MLMC - scalar QoI** Hereafter we present the results using the C-MLMC method in computing the position of the shock in the divergent section of the nozzle.

The shock position  $X_s$  is computed as the mid-point between the location of the maximum positive and negative variation in the Mach number between two consecutive grid points (Figure 5.3):

$$X_s = \frac{1}{2} (X_{dM_+} + X_{dM_-}) \quad (5.20)$$

$$\begin{aligned} X_{dM_+} &= \arg \max_{x_i} (M(x_i) - M(x_{i+1})) \quad i = 0, \dots, n-1 \\ X_{dM_-} &= \arg \min_{x_i} (M(x_i) - M(x_{i-1})) \quad i = 1, \dots, n \end{aligned} \quad (5.21)$$

In Fig.5.4 and Fig.5.5 we present few iterations of the C-MLMC algorithm for the approximation of the expectation of the shock location in the nozzle with operating uncertainties ( $P_1$ ,  $T_1$  and  $p_2$ ). The first column in Fig.5.4 shows the estimated bias  $\mathbf{B}$  (Eq. (5.8)) of the estimator and the corresponding least squares (LS) fit model. In the second column we show the sample variance of  $Y_\ell$  (in red), its LS fit model (dashed blue line) and the Bayesian updated variance model

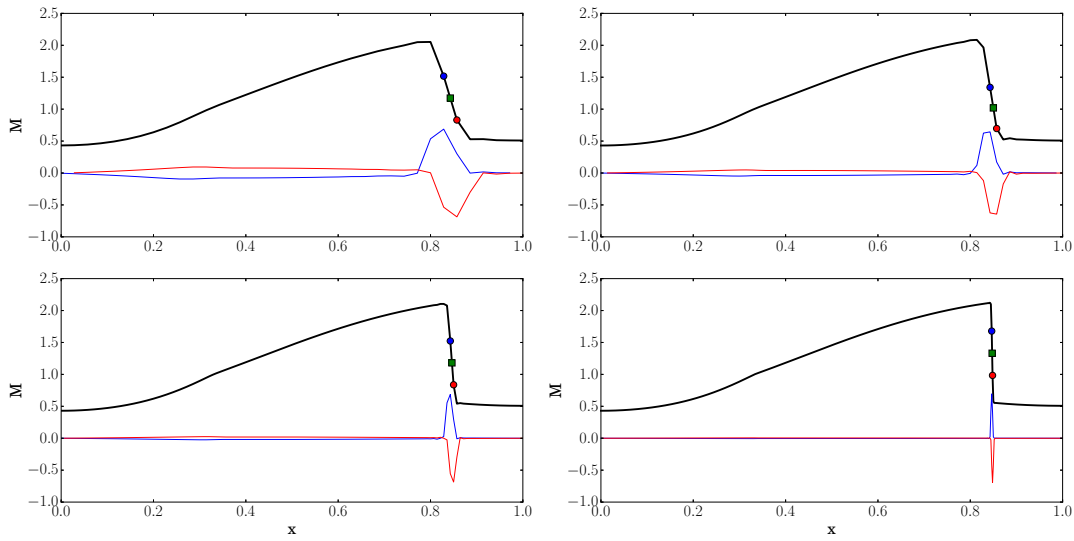


**Figure 5.3** – Mach number inside the nozzle (black line),  $X_{dM_+}$  (blue circle, maximum of the blue line ( $M(x_i) - M(x_{i+1}))$ ),  $X_{dM_-}$  (red circle, minimum of the red line ( $M(x_i) - M(x_{i-1}))$ ) and approximate shock position  $X_s$  (green square) for different levels.

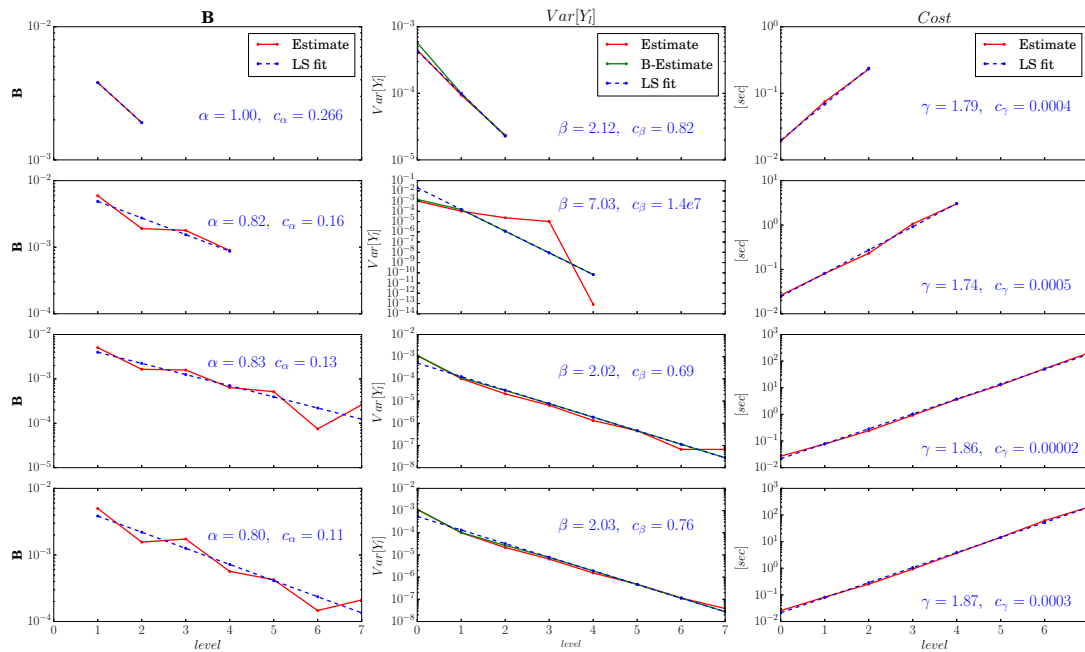


**Figure 5.4** – C-MLMC iterations (0, 10, 13 and the final 14) for the estimation of  $\mathbb{E}[X_s]$  (3 operating uncertainties, final relative tolerance  $\varepsilon_r = 0.001$ ). The columns represent, from left to right, the bias, variance of  $Y_\ell$  and cost per level.

$V^C[Y_\ell]$  (green line); the fitted asymptotic rate  $\beta \approx 2$  is consistent with a first order discretization scheme. The third column displays the cost required to compute one sample at a specific level. Fig.5.5 shows the number of samples per level prescribed at each iteration of the C-MLMC

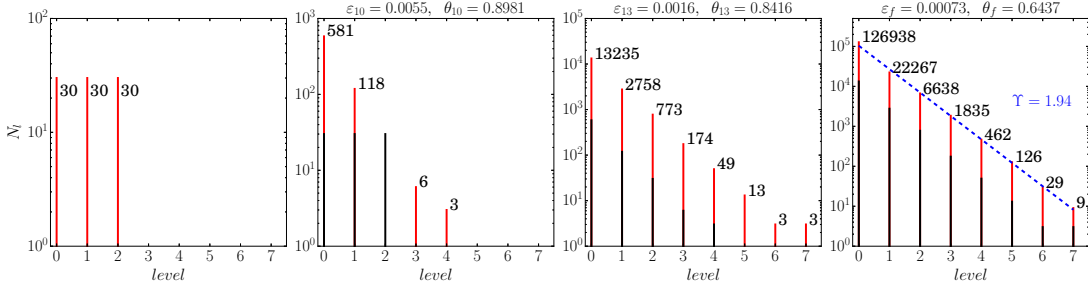


**Figure 5.5** – C-MLMC levels and samples per level for iterations 0, 10, 13 and the final 14 for the estimation of  $\mathbb{E}[X_s]$ .

algorithm with decreasing tolerance. At the final iteration we also compute the decay rate of the number of samples  $N_\ell$  with the level  $l$ ,  $N_\ell \approx C_\gamma l^\Upsilon$  and check that it corresponds to:

$$\Upsilon \approx \frac{1}{2}(\gamma + \beta) \tag{5.22}$$

The first remarkable feature that we can observe in Fig.5.4 is the robustness of the algorithm in predicting the variance of  $Y_\ell$  also with a small number of samples at the finest levels.

As already mentioned in the previous section, estimating  $\text{Var}[Y_\ell]$  using the sample variance can be quite inaccurate with a small number of samples. As a result of that, an over estimation of  $\beta$  and  $c_\beta$ , would result in a smaller number of samples per level than the ones needed to achieve a prescribed tolerance while an under estimation of them would imply a larger number of samples and hence a higher cost. The customary screening phase that precedes a standard MLMC can be the perilous step in the entire UQ analysis and can jeopardize the theoretical achievable speedup of MLMC with respect to MC or under-predict the final error thus failing to achieve prescribed tolerance requirements.

In Fig.5.6 we compare the decay rates of the  $\text{Var}[Y_\ell]$  (estimated by Eq.(5.12)) for the C-MLMC with the decay rate of  $\text{Var}[Q_\ell]$  which would influence the performance of simple MC algorithm for three different sets of uncertain parameters. In the first column we consider only the geometrical uncertainties, in the second one only the operating ones and in the last column all of them. The second line presents the number of samples  $N_\ell$  prescribed at each iteration of the C-MLMC and the final hierarchy obtained with the final prescribed relative tolerance on the QoI ( $\epsilon_r = 0.001$ ).

**Sensitivity of C-MLMC on the choice of parameters  $k_0$  and  $k_1$  of the Normal-Gamma prior**

In order to investigate the robustness of the C-MLMC method, we present here a sensitivity study of the cost required to achieve a prescribed relative tolerance  $\epsilon_r = 0.001$  and accuracy of C-MLMC simulations on the choice of  $k_0$  and  $k_1$ . We compare the C-MLMC results with a reference solution obtained with 100000 MC samples computed on the finest grid (L7).

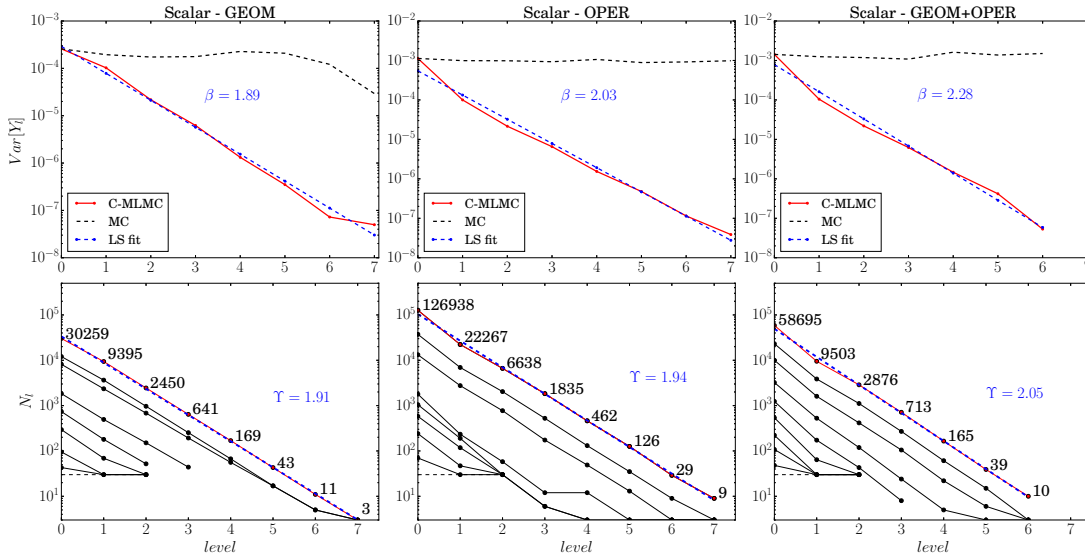


**Figure 5.6** – Decay of  $\text{Var}[Y_\ell]$  for the C-MLMC (computed with Eq.(5.12) red solid line and LS fit blue dashed line) and  $\text{Var}[Q_\ell]$  for MC (black dashed line) for three different sets of uncertain parameters (final relative tolerance  $\varepsilon_r = 0.001$ ); lower row:  $N_\ell$  for different iterations of the C-MLMC .

The left plot in Figure 5.7 compares the cost (number of levels and number of realizations per level) of C-MLMC simulations performed with different parameters values. The vertical bars show the variability in the obtained hierarchies over 10 repetitions of the whole algorithm with different seeds of the random number generator. They provide a good indicator of the variability in the cost of the C-MLMC. The simulations performed with  $k_0, k_1 = 0.001$  mainly rely on the sampled values of bias and variance of the MLMC estimator at the first iterations while simulations performed with  $k_0, k_1 = 1000$  strongly rely on the LS fit models. We observe that the simulations performed with high confidence in the weak and strong error models (large values of  $k_0$  and  $k_1$ ) appear to be overly conservative, in the sense that they provide errors much smaller than the prescribed tolerance, at a price of a much higher computational cost and, often, a higher number of simulations on the finest levels.

The right plot shows that all the simulations performed with different choices of  $k_0$  and  $k_1$  are within the prescribed tolerance. Based on this study we choose  $k_0 = 0.1$  and  $k_1 = 0.1$  in all our simulations.

**Propagation of Uncertainties with C-MLMC - scalar field QoI** As suggested in the previous chapter (see 4.1.3), the MLMC and hence the C-MLMC can be naturally extended to compute expectation of QoI that are scalar fields  $\mathcal{Q}(x, \omega)$ .

Here we consider the expected Mach number profile inside the Laval nozzle under operating and geometric uncertainties presented in Table 5.1. In Figure 5.8 we show few iterations of the C-MLMC algorithm for the computation of the Mach profile inside the nozzle for a final

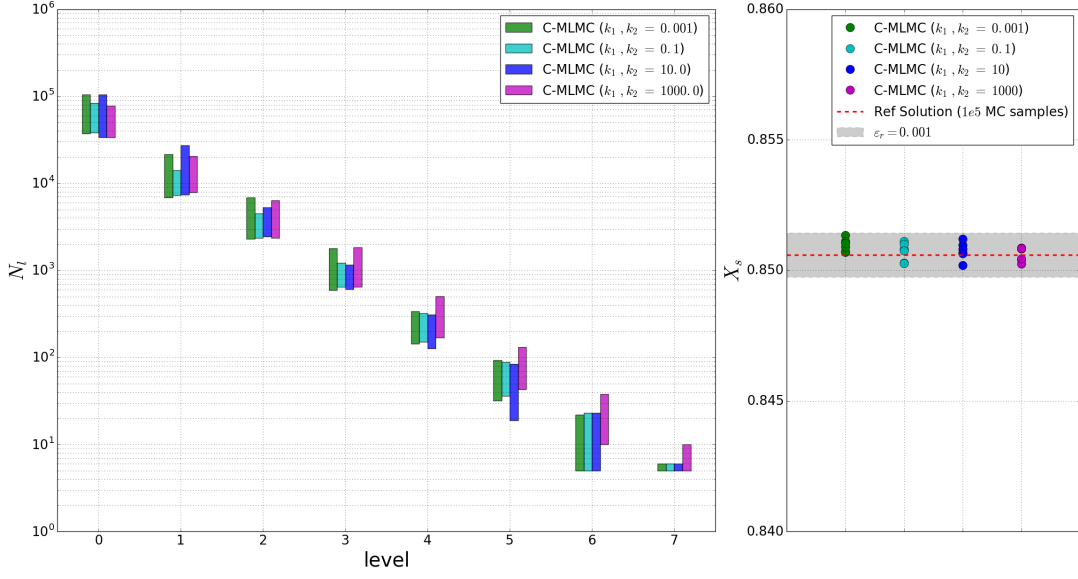


**Figure 5.7** – Sensitivity of the number of levels and samples per level (left plot) and the accuracy of the final results of the C-MLMC simulation (right plot) on the choice of  $k_0$  and  $k_1$ .

relative tolerance  $\varepsilon_r = 0.01$ .

Although the numerical scheme is the same as in the previous test case, here we are looking at the whole profile of Mach number, which is a discontinuous function due to the presence of the shock leading to a different optimization of the MLMC and different performances. This explains the reduced asymptotic rate  $\beta \approx 1.13$  observed, as well as the slower decay on  $N_\ell$  with  $l$ . Figure 5.10 shows the decay rates of  $\|\text{Var}[\mathcal{Q}_\ell]\|_{L^1(D)}$  (estimated by Eq.(5.12)) for the C-MLMC and  $\|\text{Var}[\mathcal{Q}_\ell]\|_{L^1(D)}$  for MC for three different sets of uncertain parameters and their respective hierarchies.

In Figure 5.11 we show the results obtained for the mean of the Mach number profile for the three different sets of uncertain parameters. It is important to underline that the standard deviation (gray area) has been computed during a post-process step using the samples obtained during the optimization of the hierarchy for the mean value of the Mach profile. We postpone to Chapter 6 the optimization of the MLMC hierarchy for accurate estimation of statistical moments and a better methodology to compute variances.

### Complexity, Reliability and Robustness of C-MLMC vs MC and MLMC

First we compare the cost and the accuracy of our implementation of C-MLMC with the classical MLMC with screening procedure (Algorithm 1 in Chapter 4). The screening phase requires the pivotal choice of the number of investigation levels and samples  $(\bar{L}, \bar{N})$  necessary to obtain an accurate estimation of the decay rates.

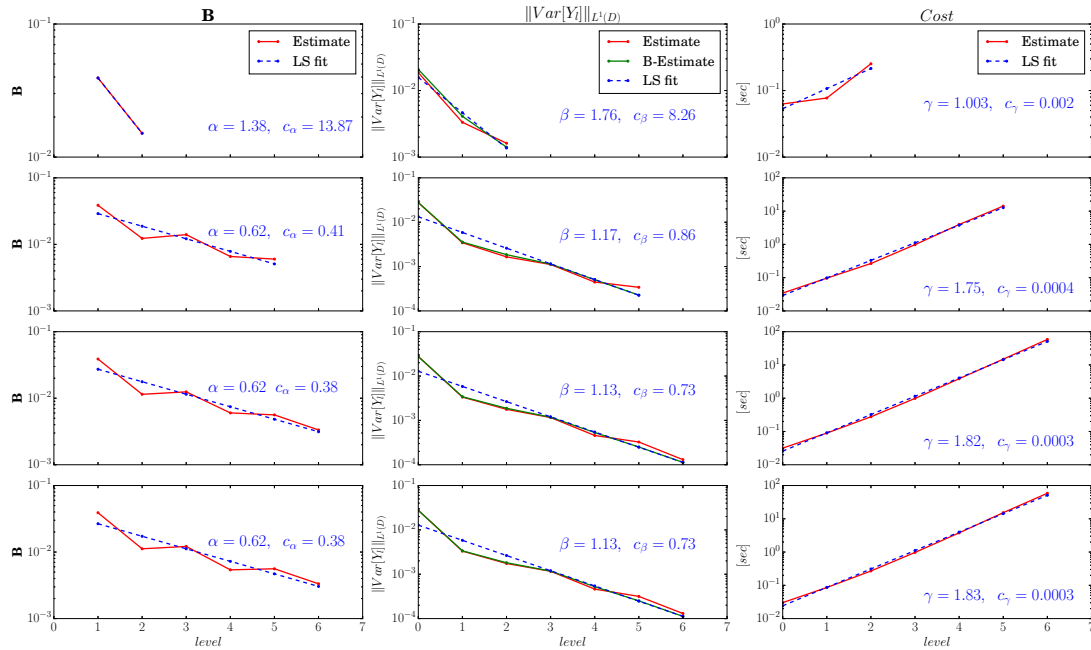


**Figure 5.8** – C-MLMC iterations (0, 11, 12 and the final 13) for the estimation of  $\mathbb{E}[M(x)]$  (3 operational uncertainties and 2 geometrical, final relative tolerance  $\varepsilon_r = 0.01$ ). The columns represent, from left to right, the bias, variance of  $Y_\ell$  and the cost per level.

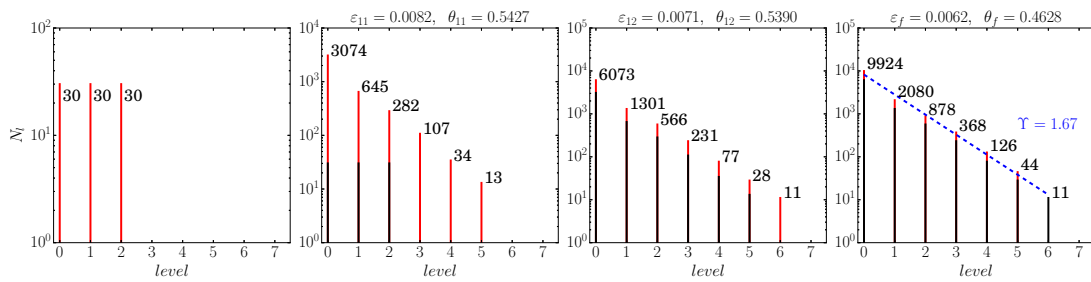


**Figure 5.9** – C-MLMC levels and samples per level for iterations 0, 11, 12 and the final 13 for the estimation of  $\mathbb{E}[M(x)]$ .

As already mentioned in the previous chapter, the rates are problem, solver and grid hierarchy dependent. Additionally the uncertainty range and flow regime (subsonic or supersonic in compressible flow problem) can dramatically influence those rates. Therefore one is generally required to perform the screening phase before the actual MLMC simulation each time the above mentioned features of the problem are modified.

In the existing literature on MLMC this aspect is generally ignored and the cost of the screening phase not included. We believe that in practical engineering applications, that require the solution of complex CFD models, this aspect cannot be neglected. A screening phase with a large number of investigation levels and samples per level is simply unfeasible and can be extremely computationally intensive. On the other hand, if the prediction of the rates is



## 5.2. C-MLMC for UQ in Inviscid Aerodynamics

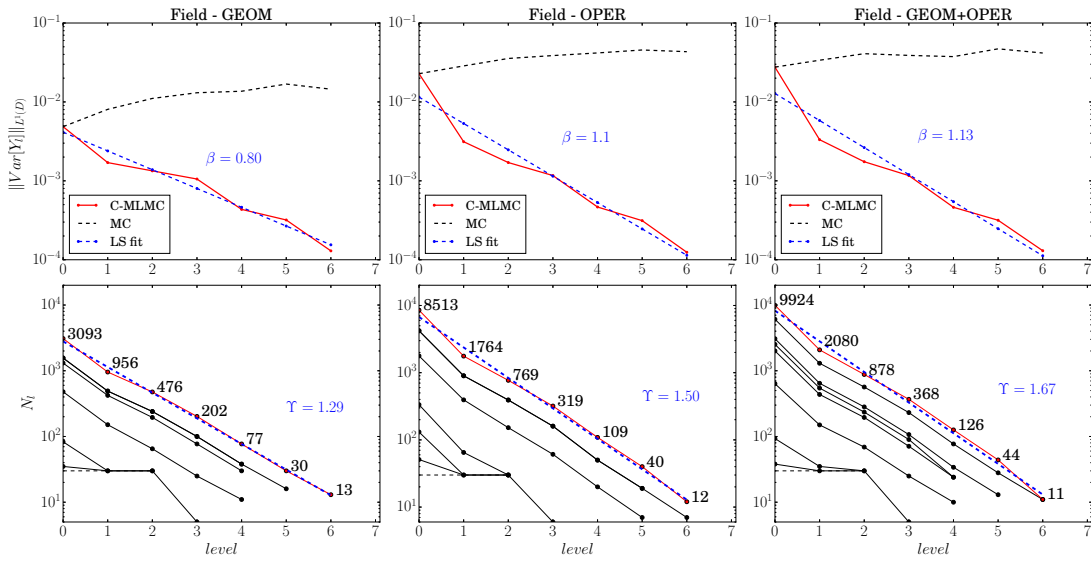


**Figure 5.10** – Decay of  $\|\text{Var}[\mathcal{Y}_\ell]\|_{L^1(D)}$  for the C-MLMC (computed with Eq.(5.12) red solid line and LS fit blue dashed line) and  $\|\text{Var}[\mathcal{Q}_\ell]\|_{L^1(D)}$  for MC (black dashed line) for three different sets of uncertain parameters (final relative tolerance  $\varepsilon_r = 0.001$ ); lower row:  $N_\ell$  for different iterations of the C-MLMC.

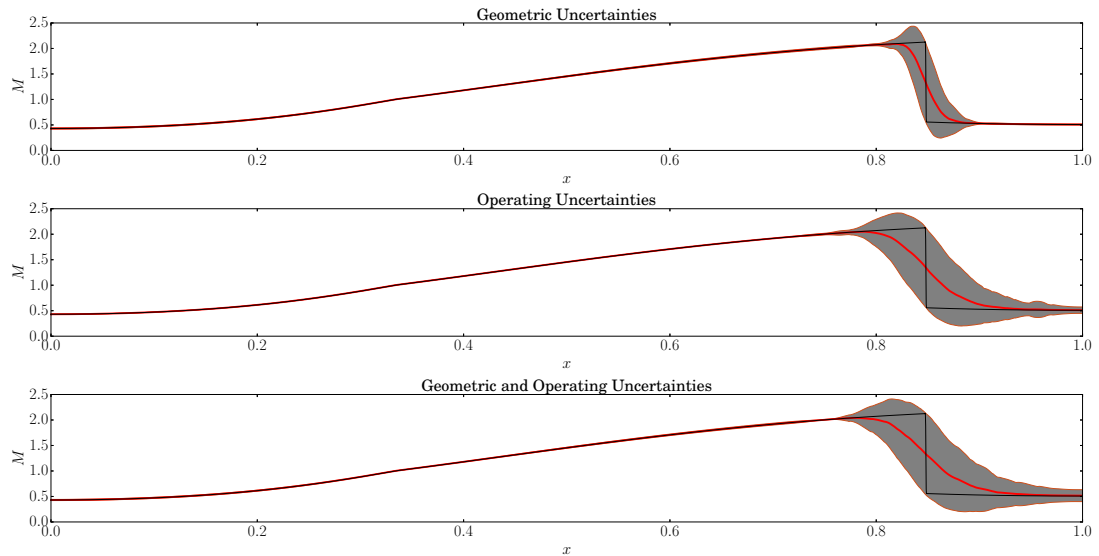


**Figure 5.11** – Mean Mach profile inside the nozzle (red solid line), *cloud* of uncertainty corresponding to one standard deviation (grey area) and deterministic solution (black solid line) for three different sets of uncertain parameters.

inaccurate, one can end up in the best case scenario with an overly conservative hierarchy that is much more expensive than the one needed to meet the tolerance requirements. In the worst case one might over-predict the rates and perform a MLMC simulation that does not meet the required tolerance.

In Figure 5.12 and Figure 5.13 we compare the cost of MLMC simulations with screening with our implementation of C-MLMC. We denote with S10x2, S20x3, S40x4 the screening procedures performed respectively with 10 samples on two levels, 20 samples on three levels and 40 samples on four levels. The left plots show, in particular for the lower tolerances (Figure 5.12,  $\varepsilon_r = 0.005$ ), the effect of the screening in the cost of the overall MLMC simulations with respect to the C-MLMC. The lower vertical bars in the plots represent the inevitable cost of the screening phases. Additionally we witness in the right plots of Figure 5.12 and Figure 5.13 that MLMC simulations can provide results that are not within the prescribed tolerance. This phenomenon is due to the inaccurate prediction of the decay rates. C-MLMC on the other hand, is able to provide accurate results with a cost that is comparable to the MLMC (with optimal hierarchy) without the screening phase.

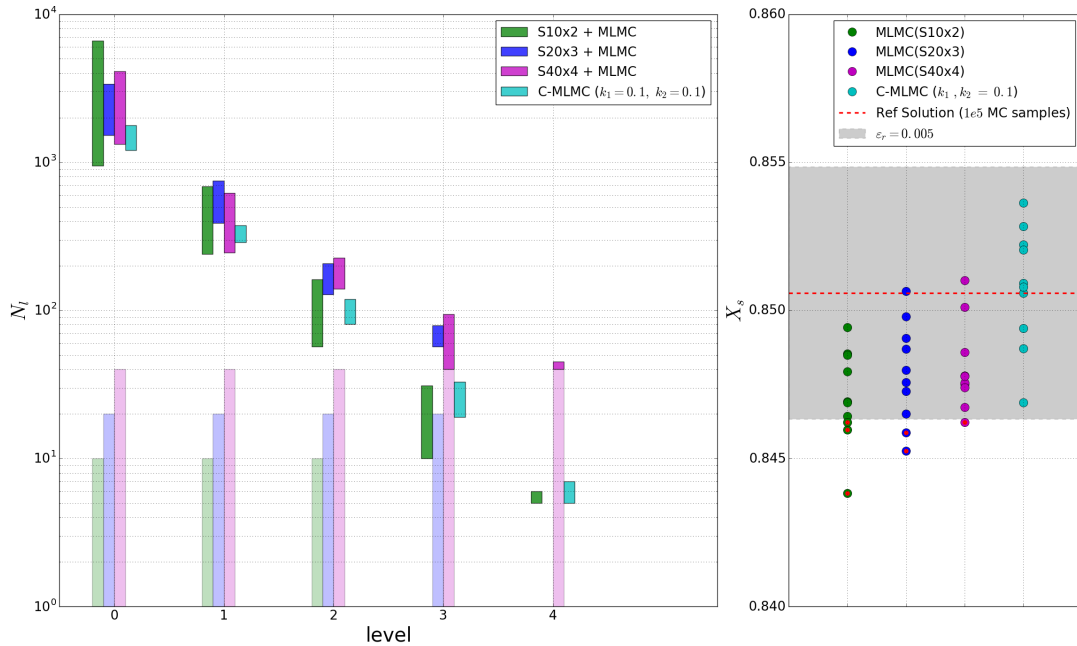


**Figure 5.12** – Cost (left plot) and accuracy (right plot) of MLMC with screening and C-MLMC for the computation of the scalar QoI  $X_s$  (shock position in the nozzle) with relative tolerance  $\varepsilon_r = 0.005$ . The lower bars in light green, blue and magenta in the left plot represent the cost of the screening phase.

Finally in Figure 5.14 we compare the cost required to achieve a prescribed tolerance with MC and with our implementation of C-MLMC. For the scalar QoI  $X_s$ , as theoretically predicted in Eq. (4.8), we observe that, for the MLMC method, the total cost required to achieve a RMSE of  $\varepsilon$  in the case of  $\beta > \gamma$  (rate of decay of  $\text{Var}[Y_\ell]$  greater than the growth rate of the cost to compute one sample at level  $l$ ) is proportional to  $\varepsilon^2$ ; on the other hand, for the MC method, as presented in Eq. (3.22), the total cost is proportional to  $\varepsilon^{-2-\gamma/\alpha}$ . For the scalar field QoI  $M(x)$ , we are in the case of  $\beta < \gamma$  and the total cost required to achieve a RMSE of  $\varepsilon$  for the MLMC method is proportional to  $\varepsilon^{2-(\gamma-\beta)/\alpha}$ . The results in Fig. 5.14 match nicely these theoretical estimates.

## 5.2. C-MLMC for UQ in Inviscid Aerodynamics

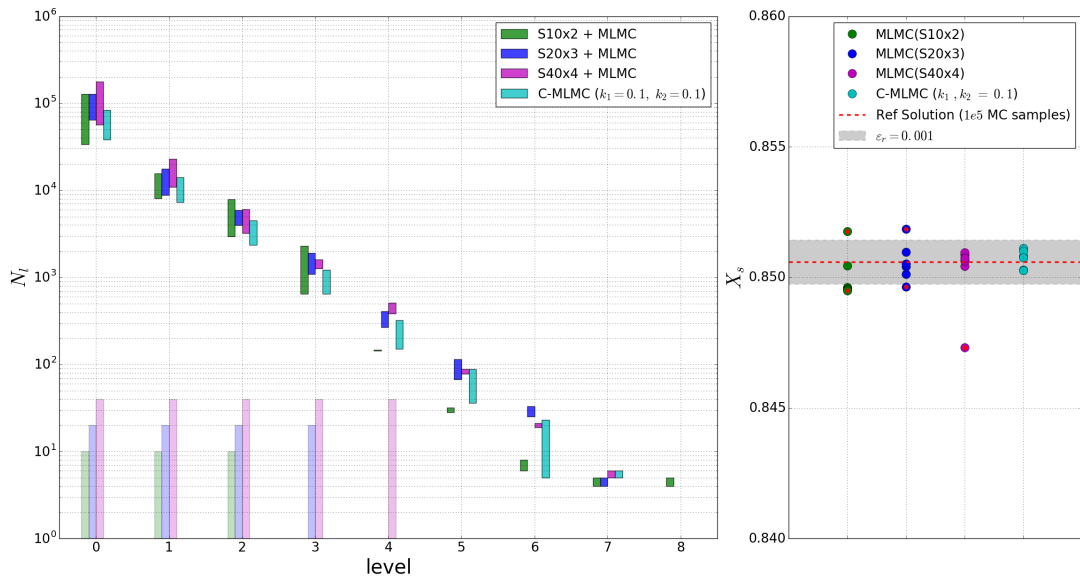


**Figure 5.13** – Cost (left plot) and accuracy (right plot) of MLMC with screening and C-MLMC for the computation of the scalar QoI  $X_s$  (shock position in the nozzle) with relative tolerance  $\epsilon_r = 0.001$ . The lower bars in light green, blue and magenta in the left plot represent the cost of the screening phase.

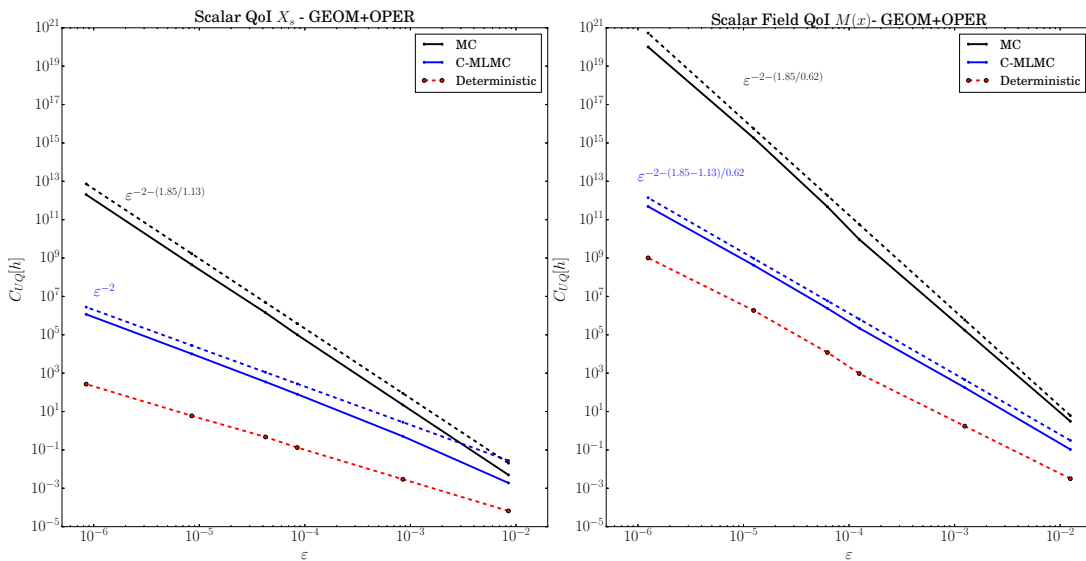


**Figure 5.14** – Cost required to achieve the prescribed tolerance requirements for C-MLMC (blue line) and MC (black line). The red dashed line represents the cost for a deterministic simulation achieving an error on the QoI of size  $\epsilon$ .

### 5.2.2 2D Model Problem: Flow around RAE 2822 airfoil

For the RAE 2822 airfoil problem we employ the 2D Euler equations presented in Chapter 2.1.2. Also for this problem, the convective flux is computed using a second-order JST [JST81] scheme.

For this specific problem as 'black-box' 2D Euler equations solver we choose the Stanford University Unstructured (SU2) [PEA<sup>+</sup>14, PCA<sup>+</sup>13] computational environment. The geometry that we consider here is the well known RAE 2822, a supercritical airfoil which has become a standard test case for transonic flows [V.A79].

**Operational and Geometrical Uncertainties:** Table 5.4 summarizes the physical and geometrical reference parameters and the uncertainties considered for the RAE 2822 airfoil problem. The uncertainty on the different parameters is modeled as a truncated Gaussian random variable (see definition in Eq. (4.22)).

	Name	Nominal value	Uncertainty
<b>Operational</b>	$\alpha_\infty$	2.31°	$\mathcal{TN}(T_n, 2\%, 110\%, 90\%)$
	$M_\infty$	0.729	$\mathcal{TN}(p_n, 2\%, 110\%, 90\%)$
	$p_\infty$	101325 [Pa]	–
	$T_\infty$	288.5 [K]	–
<b>Geometrical</b>	$R_p$	0.00853	$\mathcal{TN}(R_{p_n}, 2.5\%, 110\%, 90\%)$
	$R_s$	0.00839	$\mathcal{TN}(R_{s_n}, 2\%, 110\%, 90\%)$
	$X_p$	0.346	$\mathcal{TN}(X_{p_n}, 2\%, 110\%, 90\%)$
	$X_s$	0.431	$\mathcal{TN}(X_{s_n}, 2\%, 110\%, 90\%)$
	$Y_p$	-0.058	$\mathcal{TN}(Y_{p_n}, 2\%, 110\%, 90\%)$
	$Y_s$	0.063	$\mathcal{TN}(Y_{s_n}, 2\%, 110\%, 90\%)$
	$C_p$	0.699	$\mathcal{TN}(C_{p_n}, 2\%, 110\%, 90\%)$
	$C_s$	-0.432	$\mathcal{TN}(C_{s_n}, 2\%, 110\%, 90\%)$
	$\theta_p$	-2.227	$\mathcal{TN}(\theta_{p_n}, 2\%, 110\%, 90\%)$
	$\theta_s$	-11.607	$\mathcal{TN}(\theta_{s_n}, 2\%, 110\%, 90\%)$

**Table 5.4** – Operational and Geometrical parameters and uncertainties for the RAE 2822 airfoil problem.

The nominal geometric parameters correspond to the PARSEC [Sob98] (see definition in 2.4.3) coefficients of the RAE 2822 airfoil. Fig. 5.15 illustrates the nominal geometry of the RAE 2822 and the meaning of the parameters in Table5.4.

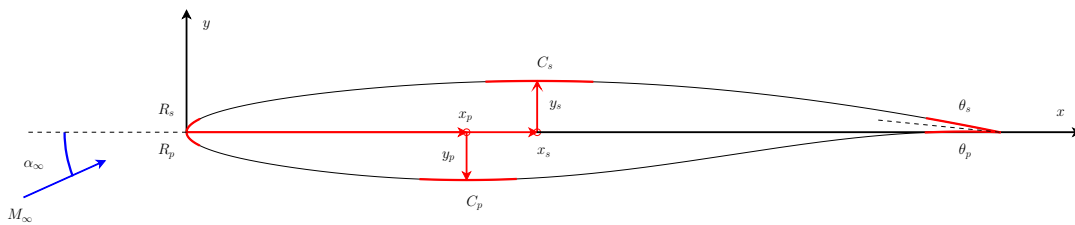


**Figure 5.15** – Geometry of the RAE 2822 transonic airfoil and PARSEC parameters.

**C-MLMC Settings and Grid Hierarchy:** The hierarchy used for this problem is made up of 5 non nested grid levels generated by doubling the number of nodes around the airfoil. Figure 5.16 shows the computational grids, the Mach contour and the pressure coefficient around the airfoil computed on the first four levels in the MLMC hierarchy and Table 5.5 presents the features, computational time and number of CPUs required to compute one realization on each level.

Hereafter the computational cost (CPU time) to compute one sample  $Q_{M_\ell}$  at level  $l$  is obtained by multiplying the physical time required to compute the deterministic simulation ( $\tau_\ell$ ) and the number of CPUs required to compute that simulation ( $n_\ell^{CPU}$ ).

$$C_\ell = \tau_\ell * n_\ell^{CPU}. \tag{5.23}$$

LEVEL	Airfoil nodes	Cells	$\tau_\ell$ [s] ( $n_\ell^{CPU}$ )
<i>L0</i>	67	5197	14.4 (18)
<i>L1</i>	131	9968	21.4 (22)
<i>L2</i>	259	20850	28.8 (28)
<i>L3</i>	515	47476	64.0 (36)
<i>L4</i>	1027	114857	122.1 (44)
<i>L5</i>	2051	283925	314.2 (56)

**Table 5.5** – MLMC 5-levels grid hierarchy for the RAE2822 problem.

In the following subsections we present the results and the performances of the C-MLMC compared to MC method in computing a scalar QoI (lift coefficient  $C_L$ ) and a scalar field QoI (pressure coefficient  $C_p$  around the airfoil).

The parameters that define the computational cost and the tolerance decrease from the initial to the final tolerance and the parameters  $k_1$ ,  $k_2$  that represent the confidence in the bias and variance models (see (5.10)) are presented in Table 5.6. The parameter  $r_1 = 1.25$  for the scalar QoI  $C_L$  and  $r_1 = 1.2$  for the scalar field QoI  $C_p$  have been chosen so that the cost of the MLMC increases of about 25% and 20% respectively going from tolerance  $\varepsilon_i$  to  $\varepsilon_{i+1} < \varepsilon_M$ . The parameter  $r_2 = 1.025$  corresponds to a cost increase of about 2.5%<sup>2</sup> at the final iteration for the simulations for the scalar QoI, while just 1%<sup>2</sup> increase is prescribed for those for the scalar field QoI (in case of optimal complexity).

**Propagation of Uncertainties with C-MLMC - scalar QoI  $C_L$**

We consider here as scalar QoI the lift coefficient  $C_L$  of the RAE 2822 affected by operating and geometric uncertainties.

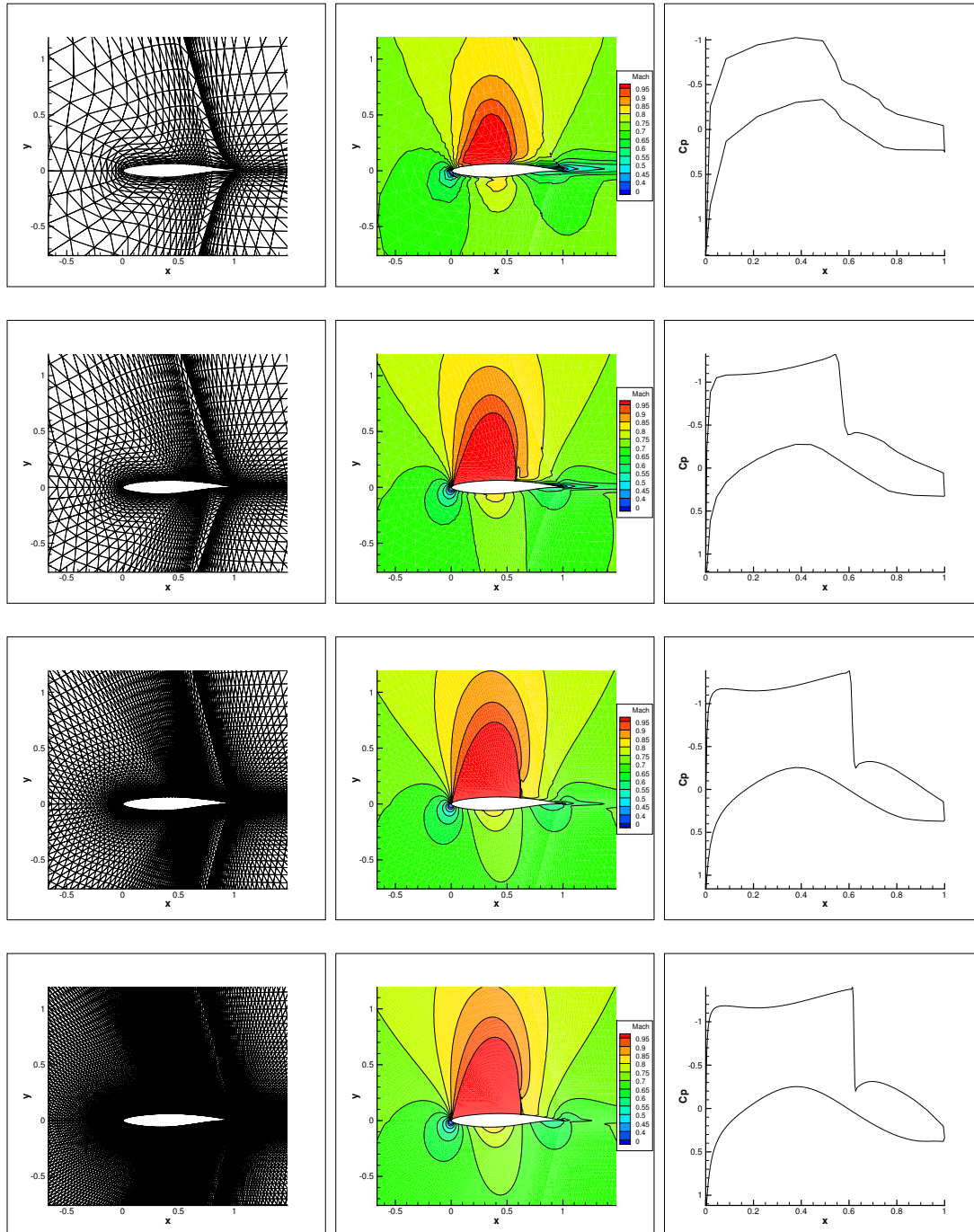


**Figure 5.16** – Grids, Mach contour and  $C_p$  profile around the RAE2822 airfoil for the first four levels in the MLMC hierarchy.

We present in Fig.5.17 few iterations of the C-MLMC algorithm for the approximation of the expectation of the lift coefficient  $C_L$  for the RAE2822 airfoil with two operating uncertainties

## 5.2. C-MLMC for UQ in Inviscid Aerodynamics

Parameters	QoI $C_L$	QoI $C_p$
$r_1$	1.25	1.2
$r_2$	1.025	1.01
$\varepsilon_0$	0.1	0.2
$\varepsilon_M$	0.003	0.05
$i_E$	15	7
$k_0$	0.1	0.1
$k_1$	0.1	0.1

**Table 5.6** – Settings for the C-MLMC algorithm for the computation of the scalar QoI  $C_L$  and the scalar field QoI  $C_p$ .

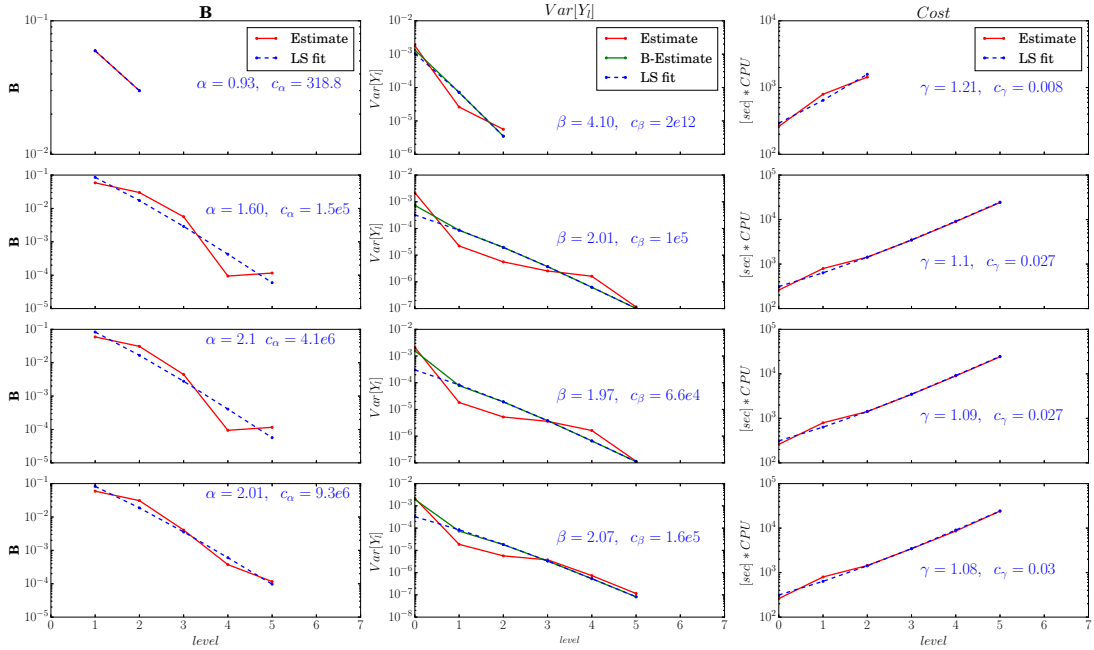


**Figure 5.17** – C-MLMC iterations (0, 11, 14 and the final 15) for the estimation of  $\mathbb{E}[C_L]$  (2 operational uncertainties and 6 geometrical, final relative tolerance  $\varepsilon_r = 0.003$ ). The columns represent, from left to right, the bias, variance of  $Y_\ell$ , cost and number of samples per level.

( $\alpha_\infty$  and  $M_\infty$ ) and six geometric uncertainties ( $R_s, R_p, x_s, x_p, y_s, y_p$ ). The first column shows the estimated bias  $\mathbf{B}$  (Eq. (5.8)) of the estimator and the corresponding LS fit model, the second column the sample variance of  $Y_\ell$  with its Bayesian updated model  $\mathbb{V}^C[Y_\ell]$  and the third column display the cost. Figure 5.18 presents the number of samples per level prescribed at each iteration of the C-MLMC algorithm with decreasing tolerance. As for the nozzle case we observe in Fig.5.17 the robustness of the algorithm in predicting the variance of  $Y_\ell$  also with just five samples at the finest level. It is worth underlying that estimating  $\mathbb{V}ar[Y_\ell]$  through a preliminary screening phase based on samples collected only on the first three levels could

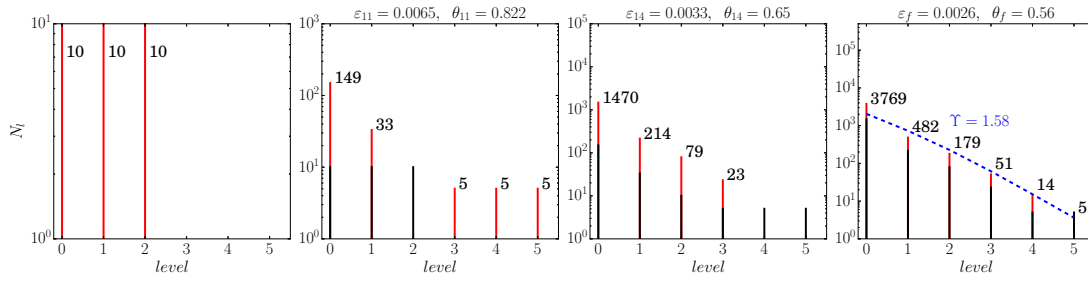


Figure 5.18 – C-MLMC levels and samples per level for iterations 0, 11, 14 and the final 15 for the estimation of  $E[C_L]$ .

lead to a huge over estimation of  $\beta$  and  $c_\beta$  (as it is possible to observe in the first row of Fig.5.17) and hence a smaller number of samples per level than the ones needed to achieve a prescribed tolerance.

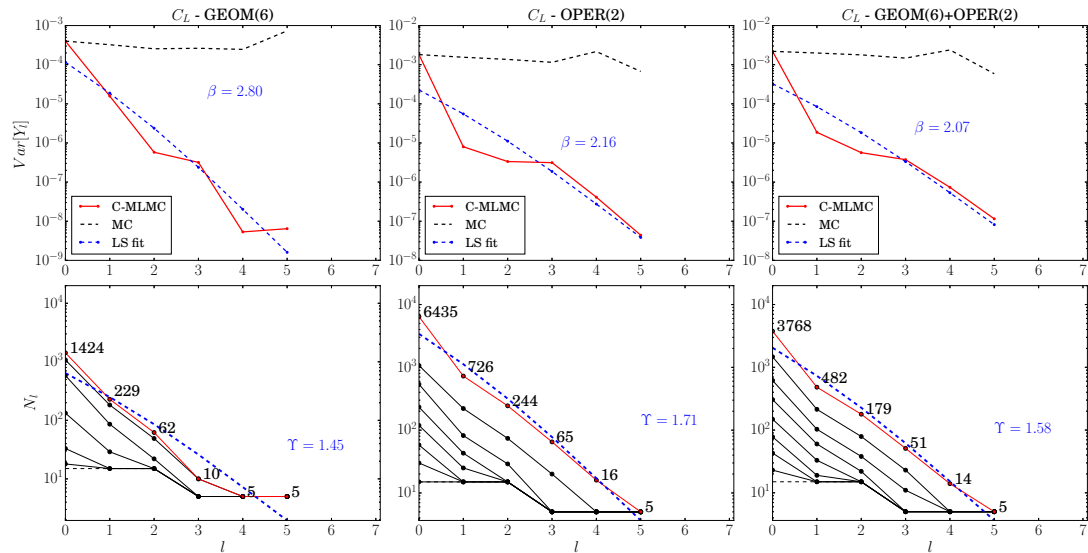


Figure 5.19 – Decay of  $\text{Var}[Y_\ell]$  for the C-MLMC (computed with Eq.(5.12) red solid line) and LS fit blue dashed line) and MC (black dashed line) for three different sets of uncertain parameters (final relative tolerance  $\epsilon_r = 0.003$ ); lower row:  $N_\ell$  for different iterations of the C-MLMC .

In Fig.5.19 we compare the decay rates of  $\text{Var}[Y_\ell]$  (estimated by Eq.(5.12)) for the C-MLMC with the decay rate of  $\text{Var}[Q_\ell]$  (which would influence the performance of a simple MC algorithm) for three different sets of uncertain parameters. In the first column we consider only six geometrical uncertainties, in the second one only two operating ones and in the last column all of them. The second line shows the number of samples  $N_\ell$  prescribed at each iteration of the C-MLMC and the final hierarchy obtained with the final prescribed relative tolerance on the QoI ( $\epsilon_r = 0.003$ ).



**Propagation of Uncertainties with C-MLMC - scalar field QoI  $C_p(x)$**

We now consider as scalar field QoI the pressure coefficient  $C_p(x)$  around the RAE2822 airfoil affected by operating and geometric uncertainties.

In the following Figure 5.20 we present the results obtained in different test cases with increasing number of uncertain parameters. As for the case of the nozzle, we recognize a wide region of uncertainty in correspondence of the shock location on the suction side of the airfoil. We can observe a higher sensitivity of the pressure coefficient on the suction side due to operating uncertainties, while the pressure side of the airfoil looks slightly more affected by geometric uncertainties. Compared to the computation of the scalar QoI  $C_L$ , we witness a slower asymptotic decay rate of  $\beta$ , as well as a slower decay on  $N_\ell$  with  $l$  (Figure 5.21).

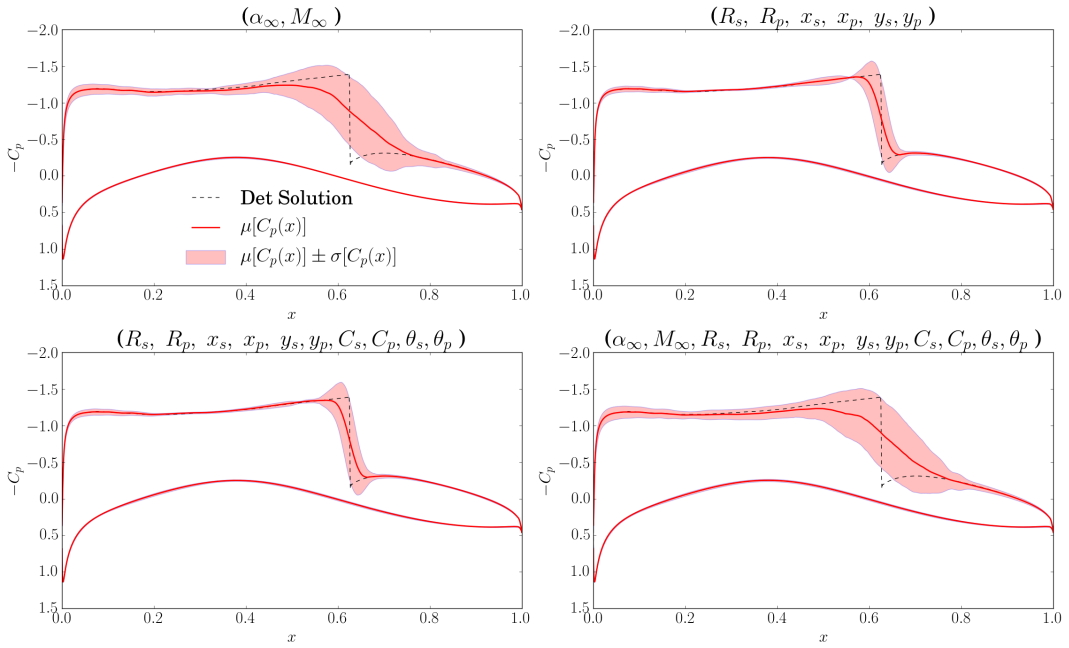


**Figure 5.20** – Mean  $C_p$  profile around the RAE2822 airfoil (red solid line) affected by increasing number of uncertainties, *cloud* of uncertainty corresponding to one standard deviation and deterministic solution.

Finally in Figure 5.22 we compare the performances of the C-MLMC and MC method. The total cost required by MLMC method to achieve a RMSE of  $\epsilon$  is proportional to  $\epsilon^2$  for the scalar QoI (lift coefficient  $C_L$ ) and a scalar field QoI (pressure coefficient  $C_p$  around the airfoil) as  $\beta > \gamma$  while for MC the total cost is proportional to  $\epsilon^{-2-\gamma/\alpha}$ .

Lastly in Figure 5.23 we compare the cost required by our implementation of C-MLMC and MC method to achieve a RMSE of  $\epsilon$  for an increasing number of uncertain parameters. We do not observe, as theory suggests, an increase in the cost with the number of uncertain parameters. It is interesting to underline that the simulations performed with operating (resp. operating + geometric) uncertainties require less computational time that the simulations with only

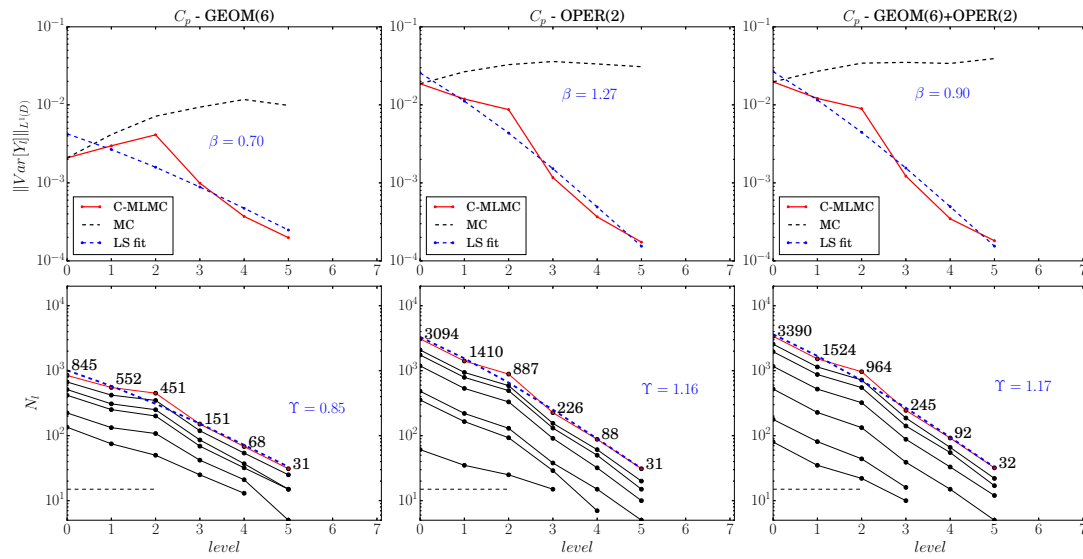


**Figure 5.21** – Decay of  $\|\text{Var}[\mathcal{Y}_\ell]\|_{L^1(D)}$  for the C-MLMC (computed with Eq.(5.12) red solid line and LS fit blue dashed line) and MC (black dashed line) for three different sets of uncertain parameters (final relative tolerance  $\varepsilon_r = 0.05$ ); lower row:  $N_\ell$  for different iterations of the C-MLMC .

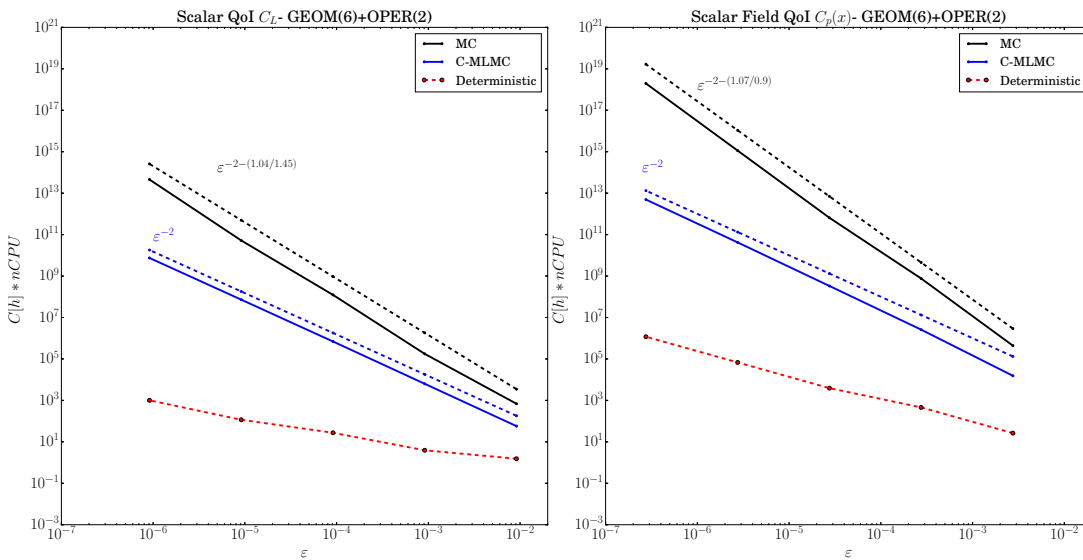


**Figure 5.22** – Cost required to achieve prescribed tolerance requirements for C-MLMC (blue line) and MC (black line). The red dashed line represents the cost for a deterministic simulation at the finest level.

geometrical uncertainties. The features and the physics of the problem suggest that the QoI depends smoothly with respect to the set of operating parameters while the geometrical ones have a sharper effect leading to an additional cost.

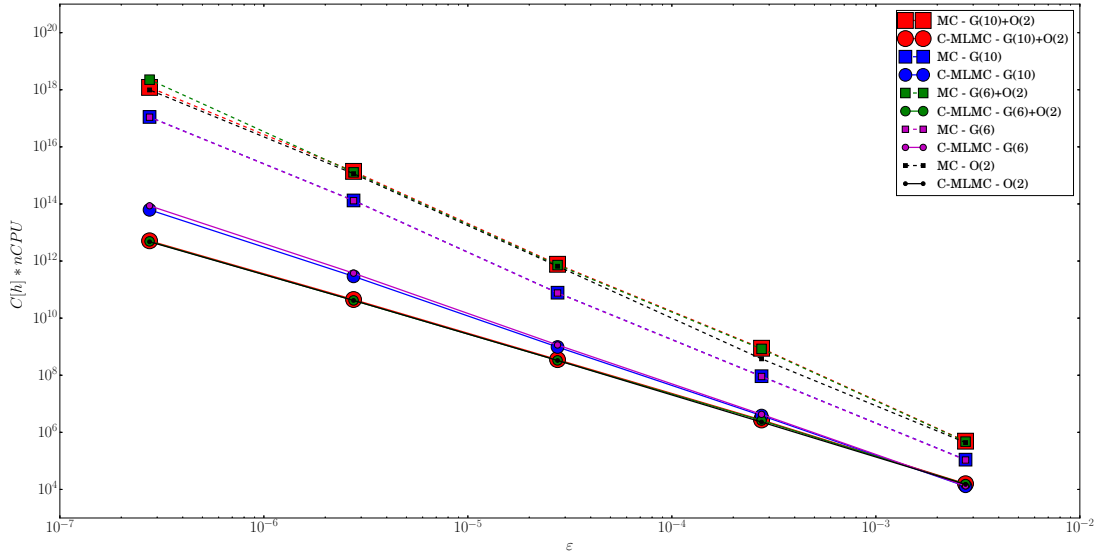


**Figure 5.23** – Cost required to achieve prescribed tolerance requirements for C-MLMC and MC for different sets of uncertainties.

### 5.3 Extension to Turbulent Problems

In this section, we revisit the C-MLMC algorithm presented in the previous sections and particularize it to the specific setting of viscous compressible aerodynamics simulations, affected by operational and geometrical uncertainties, modeled by Favre Reynolds Average Navier Stokes (F-RANS) models.

We focus here on the application of the algorithm to a specific external aerodynamics benchmark test cases defined during the European Union's FP7 project UMRIDA (Uncertainty Management for Robust Industrial Design in Aeronautics (UMRIDA)), namely the transonic RAE 2822 airfoil.

In particular, we detail how we have constructed the grid hierarchy in order to achieve appropriate grid convergence rates for the C-MLMC to be effective and we provide a comparison with a standard Monte Carlo method which shows a huge speedup in terms of computational complexity.

We consider turbulent compressible flows modeled by the Navier Stokes equations presented in Chapter 2.1.1. In particular we employ a F-RANS approximation and as turbulence closure we use the the Spalart-Allmaras turbulence model (with quadratic constitutive relation [MBWS13] in the CFD++ software environment [GPC<sup>+</sup>97, CPGP98]). The equations are discretized on structured grids (finite volume method) and advanced in time using a fully implicit time stepping scheme. Local time-stepping and algebraic multigrid (AMG) are used for convergence acceleration to the steady-state solution.

### 5.3.1 Transonic Airfoil Model Problem: RAE2822

The RAE2822 (UMRIDA BC-02) is a supercritical airfoil which has become a standard test-case for transonic flows. A detailed description of the airfoil geometry, the original experimental set-up and a series of simulations can be found in [HBE<sup>+</sup>13, VA79]. For this specific problem we consider as scalar field QoI the pressure coefficient  $C_p$  of the RAE 2822 affected by operating and geometric uncertainties due to fluctuations in the surrounding flow and manufacturing tolerances. The nominal geometry of the RAE2822 airfoil is defined with a set of PARSEC parameters [Sob98] (see Chapter 2.4.3). The following table summarizes these parameters and the operating conditions considered hereafter (corrected flow conditions for case 6 in [VA79]).

	Symbol	Reference Value
Operating	$\alpha_\infty$	2.31
	$M_\infty$	0.729
	$Re_c$	$6.5 \cdot 10^6$
	$p_\infty [Pa]$	101325
	$T_\infty [K]$	288.5
	Symbol	Design Value
Geometric	$R_s$	0.00839
	$R_p$	0.00853
	$x_s$	0.431
	$x_p$	0.346
	$y_s$	0.063
	$y_p$	-0.058
	$C_s$	-0.432
	$C_p$	0.699
	$\theta_s$	-11.607
	$\theta_p$	-2.227

Table 5.7 – Geometric and Operating reference parameters for the RAE2822 problem.

Fig. 5.24 illustrates the nominal geometry of the RAE 2822 and the meaning of the parameters in Table 5.7.

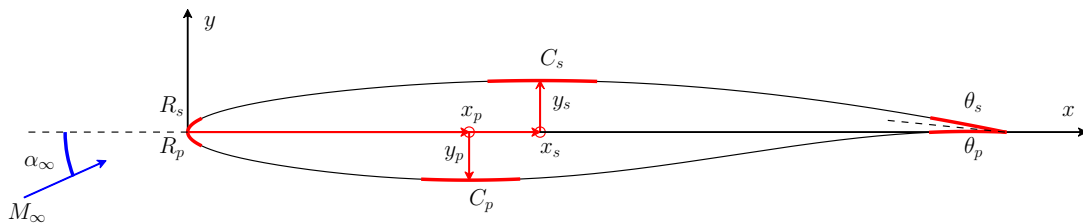


Figure 5.24 – Geometry of the RAE 2822 transonic airfoil and PARSEC parameters that define the geometry of the airfoil.

### Deterministic results

The properties of the 4-levels structured C-grid hierarchy used in the C-MLMC simulations are presented in the following Table 5.8 and Figure 5.25 along with the average computational time required to compute one deterministic simulation using CFD++ software environment. A closeup view of the structured grid in the proximity of the leading edge for level 0 and level 1 is presented in Fig. 5.26.

We ensure that near the boundaries the  $y^+$  is between 1 and 2 for all the grid levels to fulfill the requirements of the Spalart-Allmaras turbulence model. In particular, we increase the number of nodes in vertical direction with respect to the airfoil (V nodes) but we require the first grid node to be always placed at the same distance ( $y^+$ ) and distribute the remaining points following a geometric grow rate. We keep the same resolution in the boundary layer but increase the density of the grid points just outside of it (Figure 5.26).

In Fig. 5.27 we compare the computational results obtained with the finest grid level (L4) and experimental measurements [V.A79] and we observe a good agreement.

LEVEL	Airfoil nodes	V nodes	H nodes	Cells	$y^+$	$CTime[s]$ ( $n.cpu$ )
L0	160	40	20	7722	1 – 2	13.9 (16)
L1	320	80	40	31442	1 – 2	49.7 (24)
L2	640	160	80	126882	1 – 2	336.9 (32)
L3	1280	320	160	509762	1 – 2	2145.5 (40)
L4	2560	640	320	2043522	1 – 2	6854.3 (48)

**Table 5.8** – MLMC 4-levels grid hierarchy for the RAE2822 problem.  $CTime[s]$  is the real time in seconds required to compute one deterministic simulation on the prescribed number of cpus.

### Stochastic Results using C-MLMC

We now propagate geometric and operating uncertainties in the model to study their effects on the  $C_p$  profile of the airfoil using the C-MLMC approach. We consider operating uncertainties in the far-field Mach number and angle of attach and geometric uncertainties in the PARSEC coefficients that define the shapes of the airfoil. In case of geometric uncertainties that affect the shape of the airfoil, for each random geometry (set of PARSEC coefficients) we deform the existing grid levels by solving a linear elasticity problem on the volume grid to accommodate the new boundary definition (Fig. 5.28).

The following Table 5.9 and Fig. 5.29 summarize the operating and geometric parameters and their uncertainties modeled as truncated Gaussian random variables (see definition in 4.22)).

In Fig. 5.30 we present the stochastic results for the pressure coefficient profile  $C_p$  around the airfoil under operating uncertainties (2 uncertain parameters hereafter denoted as **OPER(2)**), geometric uncertainties (8 uncertainties denoted as **GEOM(8)**) and operating and geometric

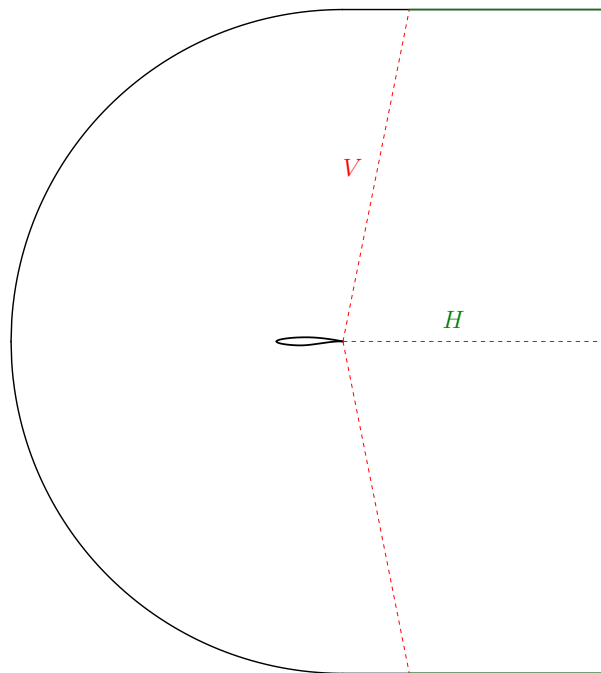


Figure 5.25 – Details for the structured RAE-2822 grid setting.

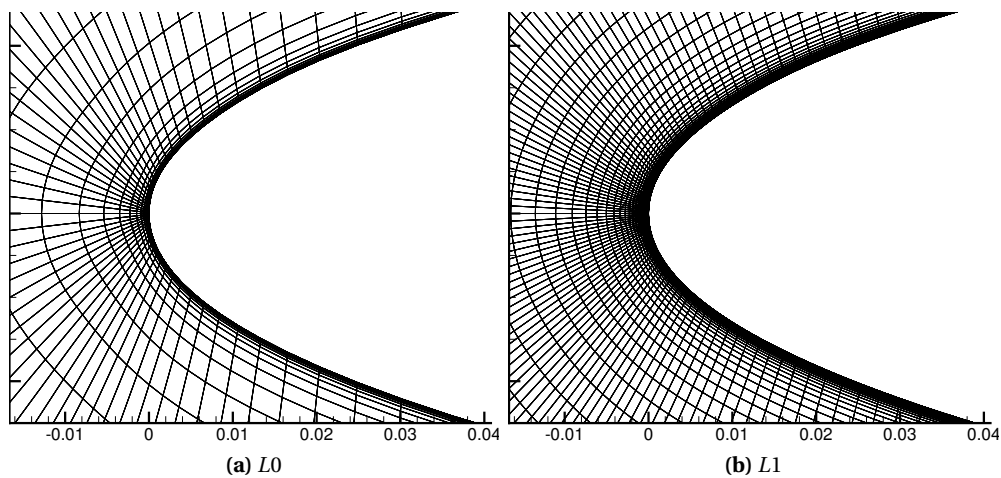


Figure 5.26 – Leading edge closeup view of level 0 and 1 grids for the RAE2822 problem.

uncertainties at the same time (10 uncertainties denoted as **OPER(2)+GEOM(8)**) presented in Table 5.9.

The decay rates of deterministic and statistical error computed during the C-MLMC analysis are  $\alpha = 0.7$ ,  $\beta = 1.06$  for the case with only operating uncertainties (**OPER(2)**) and  $\alpha = 0.6$ ,  $\beta = 1.05$  for that with operating and geometric uncertainties (**OPER(2)+GEOM(8)**).

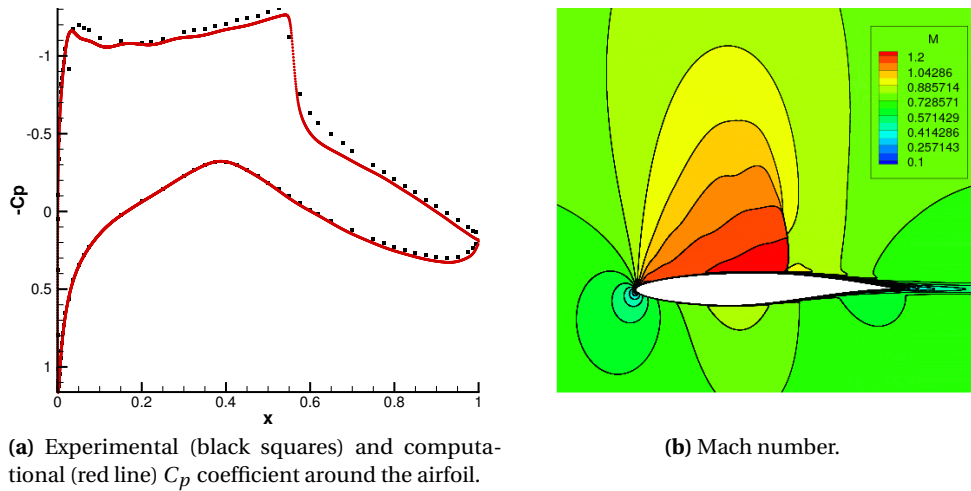


Figure 5.27 – Deterministic results for the RAE2822 airfoil.

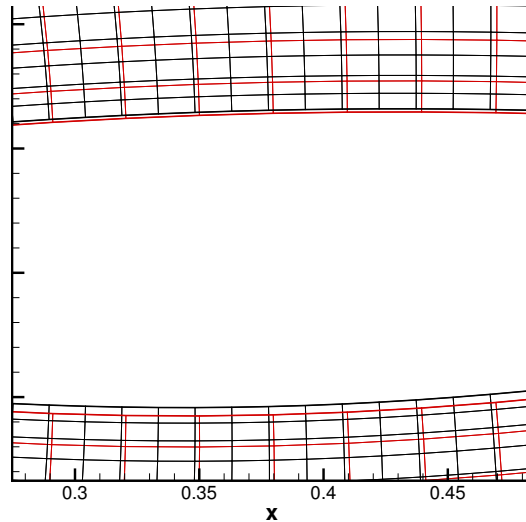


Figure 5.28 – Grid deformation to accommodate the geometric uncertainty.

Lastly we present in Fig. 5.31 the level sample sizes at each iteration of the C-MLMC algorithm to achieve a relative error  $\varepsilon_r = 0.6\%$  on the L2 norm of the pressure coefficient for the **OPER(2)** and **OPER(2)+GEOM(8)** cases. Additionally we compare the aggregate cost (total CPU time) required by our implementation of C-MLMC with the MC method to achieve a RMSE of  $\varepsilon$ . Notice how the performance of the C-MLMC is only mildly affected by the number of uncertain parameters. Moreover for the target relative tolerance  $\varepsilon_r = 0.6\%$  the gain in computational cost of C-MLMC over MC is about 2 orders of magnitude and is expected to increase even further if smaller tolerances are prescribed. The results match nicely the theoretical estimates.

	Quantity	Reference ( $r$ )	Uncertainty $\mathcal{T}\mathcal{N}(\mu, \sigma, X_{LO}, X_{UP})$
Operating	$\alpha_\infty$	2.31	$\mathcal{T}\mathcal{N}(r, 2\%, -2\%, +2\%)$
	$M_\infty$	0.729	$\mathcal{T}\mathcal{N}(r, 5\%, -5\%, +5\%)$
	$Re_c$	$6.5 \cdot 10^6$	–
	$p_\infty$ [Pa]	101325	–
	$T_\infty$ [K]	288.5	–
Geometric	$R_s$	0.00839	$\mathcal{T}\mathcal{N}(r, 0.25\%, -1\%, +1\%)$
	$R_p$	0.00853	$\mathcal{T}\mathcal{N}(r, 0.25\%, -1\%, +1\%)$
	$x_s$	0.431	$\mathcal{T}\mathcal{N}(r, 0.5\%, -1\%, +1\%)$
	$x_p$	0.346	$\mathcal{T}\mathcal{N}(r, 0.5\%, -1\%, +1\%)$
	$y_s$	0.063	$\mathcal{T}\mathcal{N}(r, 0.5\%, -3\%, +3\%)$
	$y_p$	-0.058	$\mathcal{T}\mathcal{N}(r, 0.5\%, -3\%, +3\%)$
	$C_s$	-0.432	$\mathcal{T}\mathcal{N}(r, 0.5\%, -1\%, +1\%)$
	$C_p$	0.699	$\mathcal{T}\mathcal{N}(r, 0.5\%, -1\%, +1\%)$
	$\theta_s$	-11.607	–
	$\theta_p$	-2.227	–

Table 5.9 – Operating and geometric uncertainties for the RAE2822 stochastic analysis.

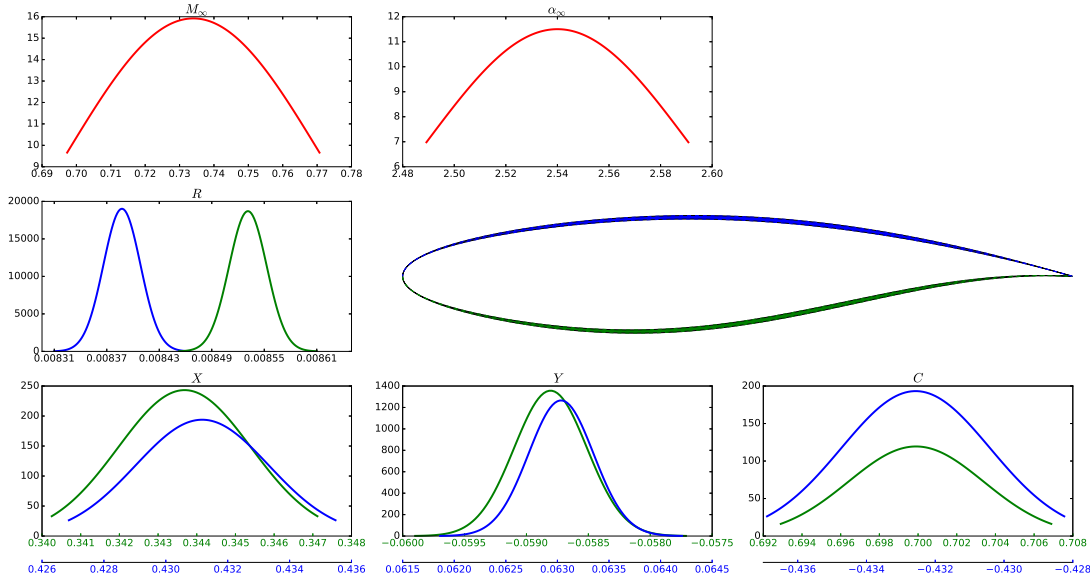
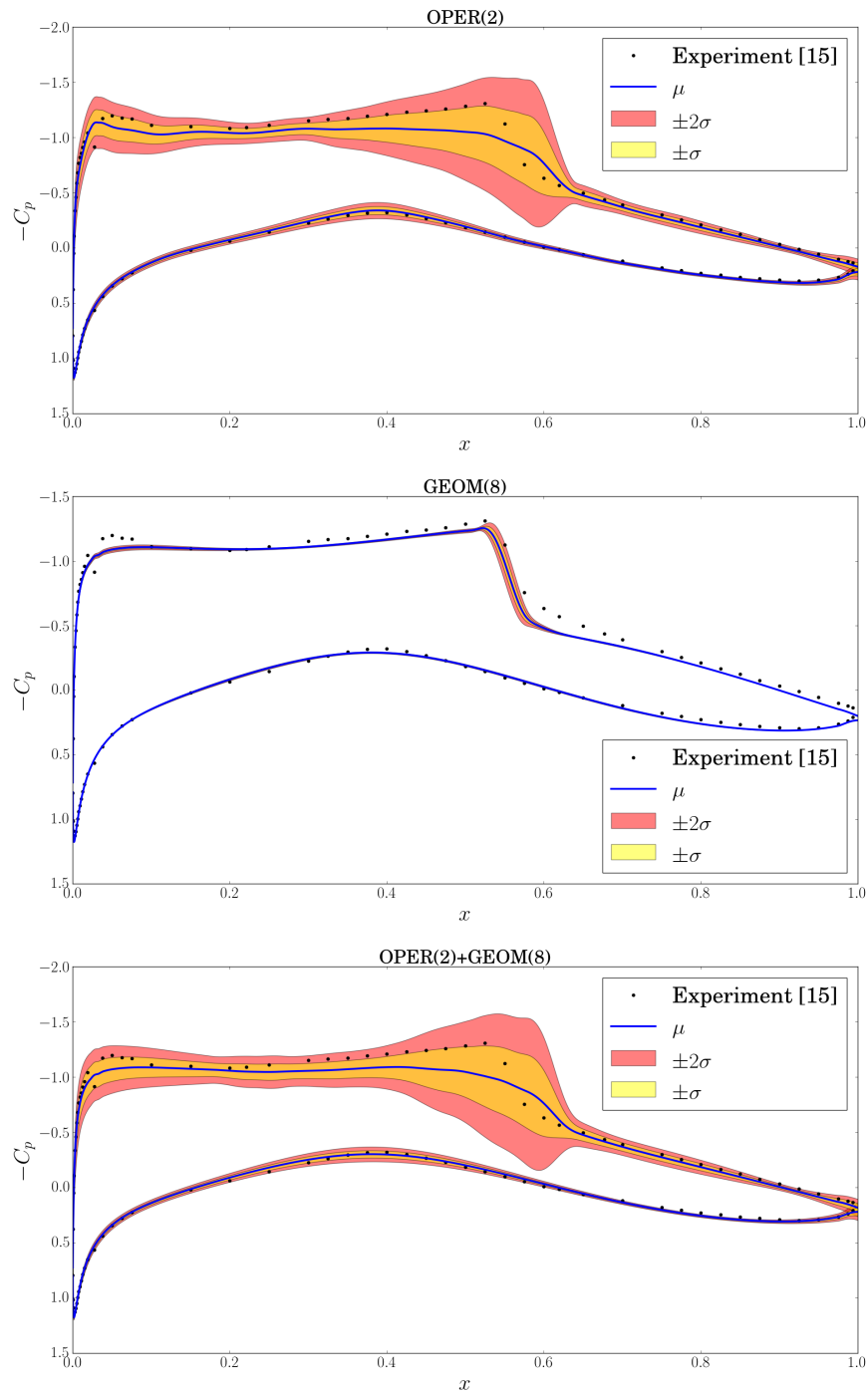


Figure 5.29 – Probability density functions of the operating (red) and geometric (blue suction side and green pressure side) parameters for the RAE2822 stochastic analysis.

## 5.4 Summary

In this chapter we have presented the Continuation Multi Level Monte Carlo (C-MLMC) algorithm and its application to inviscid and viscous compressible aerodynamics problems. The key features of the continuation procedure is that the problem and hierarchy dependent parameters that control the number of levels and samples per level are computed on the fly





**Figure 5.30** – UQ analysis results for the RAE2822 presenting the mean pressure coefficient profile around the airfoil and its standard deviation. Experimental data from [VA79].

using a Bayesian update procedure. By doing so it is possible to reduce the overall computational cost required to set up and perform an uncertainty analysis (no need for a screening procedure to compute the bias and variance decay rates). It has been shown in the numerical

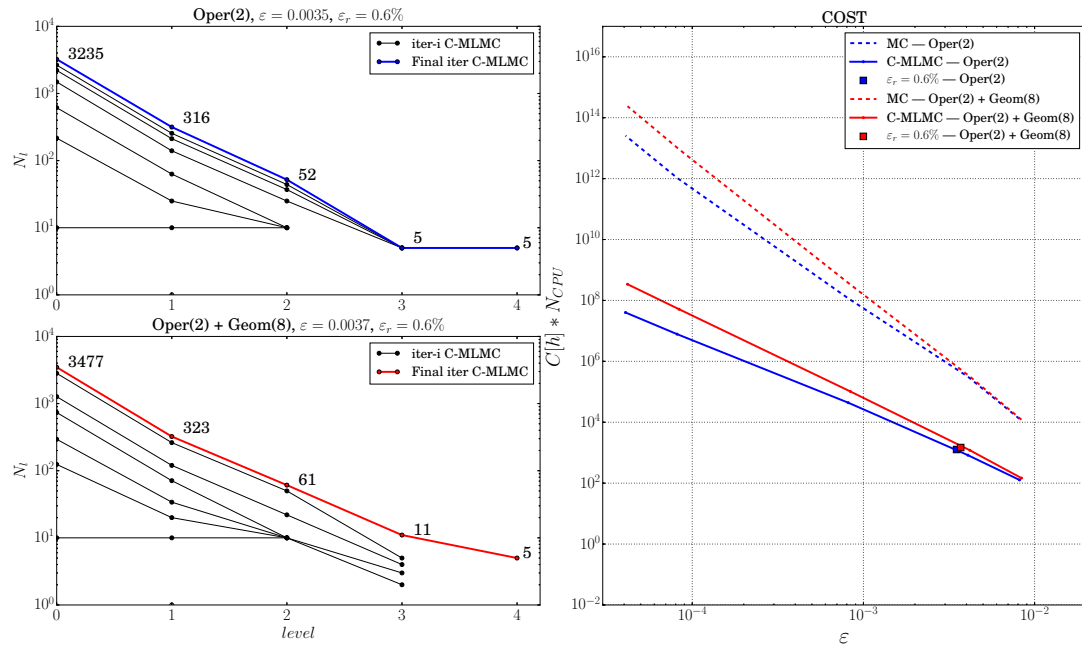


**Figure 5.31** – C-MLMC hierarchies for two different sets of uncertain parameters (left) and aggregate computational cost compared with MC (right). The solid lines in the cost plot are an extrapolated model based on the rates and constants  $(\alpha, c_\alpha, \beta, c_\beta, \gamma, c_\gamma)$  fitted in C-MLMC. The red and blue squares are the actual computed cost and error in the C-MLMC simulations.

examples presented above that the iterative learning of the decay rates leads to a robust and accurate algorithm also for problems that present sharp discontinuities as those that naturally arise in compressible inviscid/viscous flow problems.

In this chapter we only focused on the accurate computation of expected values of scalar and scalar field QoI. In particular, the C-MLMC has been tuned to the computation of such expectations and the variance have been obtained as a post-processing. Another interesting question is how to set up the MLMC and C-MLMC for the accurate computation of higher order moments, quantiles, or the full CFD. Results in this direction will be developed in Chapter 6 and Chapter 7.

# 6 MLMC for Central Statistical Moments

In the previous Chapters we investigated and applied the Multi Level Monte Carlo and the Continuation Multi Level Monte Carlo to accurately compute the mean of scalar and scalar field quantities of interest. In addition to the mean, many important features of random variable's distribution, such as dispersion, asymmetry and tailedness can be assessed through the analysis of statistical moments.

## 6.1 Introduction: Central Moments

The statistical moments that are computed about the mean are called central moments. Specifically, the  $p$ -th central moment  $\mu_p$  of a random variable  $Q$  is defined as

$$\mu_p = \mathbb{E}[(Q - \mu)^p], \quad \text{with } \mu = \mathbb{E}[Q],$$

provided the right-hand side exists. Following the definition of  $\mu_p$ , the first central moment (i.e.  $p = 1$ ) is equal to zero. The second central moment  $\mu_2$  is the variance (often also denoted as  $\sigma^2$ ) and, together with the mean  $\mu = \mathbb{E}[Q]$ , is one of the most commonly used quantities to characterize a random variable.

The third central moment  $\mu_3$  offers insight into the asymmetry of a random variable's distribution about its mean. Specifically, the skewness  $\gamma = \mu_3 / \sqrt{\mu_2^3}$ , which is the standardized counterpart of the third central moment, is commonly used as a measure of probability distribution's asymmetry. Indeed, the skewness (or equivalently the third central moment  $\mu_3$ ) of a symmetric distribution about the mean is zero. Negative values of the skewness indicate that the probability distribution has a left tail that is longer compared to the right one. Analogously, positive values indicate a longer right tail. A measure of a probability distribution's asymmetry is very important in many engineering risk/reliability assessments and financial applications related to stock prices and assets. In fact, Mandelbrot et al. [Man63] observed that the majority of financial assets returns are non-normal. This is due to the appearance of extreme events more likely than predicted by a normal distribution [BG74] and due to the fact that crashes

occur more often than booms [SW86]. For this reason, investment decisions based only on the mean and variance cannot discriminate whether a given future event will be more or less likely to appear on the left or right side of the mean [KL76, PB00]. Applied to investment returns, negatively skewed distributions indicate greater chance of extremely negative outcomes, while in positive skewed distributions extremely bad scenarios are not as likely. Assuming a normal distribution, when in fact data sets are skewed, can lead to the so called skewness risk [CCJ13]. Similar problems arise in many applications across science and technology where decisions based on a reliability or risk measure need to be taken.

The fourth central moment  $\mu_4$  and its standardized counterpart, which is known as kurtosis  $Kurt = \mu_4 / \mu_2^2$ , provide some further important insights into a random variable's distribution. In fact, the kurtosis can be used to measure whether the output random variable are heavy-tailed (high level of kurtosis) or light-tailed (low level of kurtosis) compared to a normal distribution, for which  $Kurt = 3$ . Heavy-tailed distributions are common in problems where extreme events are likely to appear. Random variables with low levels of kurtosis tend to have light tails and lack of extreme events. In other words high levels of kurtosis indicate that most of the variability in the distribution is due to extreme deviations from the mean.

In this Chapter we consider efficient sampling-based estimators for central moments of a QoI  $Q$  output of a complex probabilistic model. We address in particular probabilistic models that involve differential equations for which typically the random system output  $Q$  cannot be sampled exactly and only approximate sampling can be accessed with a given accuracy (e.g. by solving the differential equation via some numerical scheme). As a consequence of this inexact sampling, a bias is introduced that has to be accounted for.

In Chapter 4 we introduced a MLMC estimator for  $\mathbb{E}[Q]$  of  $Q$ , here we extend the MLMC concepts to the estimation of arbitrary order central moments  $\mu_p$ . Specifically, we introduce and analyze a novel multilevel Monte Carlo method that allows an efficient sampling-based estimation from inexact/approximate samples. One of the method's key ingredients is the use of  $h$ -statistics [Dwy37] as unbiased central moment estimators with minimal variance for the level-wise contributions. That is, instead of the monte carlo (MC) level-wise contributions that are used in the estimation of the mean (see (4.1) and (4.2)):

$$\mathbb{E}^{\text{MLMC}} := \mathbb{E}^{\text{MC}}(Q_{N_0, M_0}^0) + \sum_{\ell=1}^L \left( \mathbb{E}^{\text{MC}}(Q_{N_\ell, M_\ell}^\ell) - \mathbb{E}^{\text{MC}}(Q_{N_{\ell-1}, M_{\ell-1}}^\ell) \right), \quad (6.1)$$

here we use terms of the form  $h_p(Q_{N_\ell, M_\ell}^\ell) - h_p(Q_{N_{\ell-1}, M_{\ell-1}}^\ell)$ , where  $h_p$  denotes an appropriate  $h$ -statistic or order  $p$ .

Consequently, the MLMC estimator  $\mathfrak{m}_p^{\text{MLMC}}$  for arbitrary order  $p$  central moments considered here is of the form

$$\mathfrak{m}_p^{\text{MLMC}} = h_p(Q_{N_0, M_0}^0) + \sum_{\ell=1}^L \left( h_p(Q_{N_\ell, M_\ell}^\ell) - h_p(Q_{N_{\ell-1}, M_{\ell-1}}^\ell) \right).$$

We note that a multilevel Monte Carlo estimator for the variance  $\mu_2$  of a random variable  $Q$  has already been introduced in [BC15]. There the authors define the multilevel Monte Carlo estimator by telescoping on the unbiased sample variance estimator for the level-wise contributions. Our approach based on  $h$ -statistics thus offers an alternative derivation of said estimator, which allows for a straightforward complexity analysis in fact. Moreover, the approach introduced here is easily generalized to arbitrary order central moments, as we will illustrate in the following. In fact, the results presented here for estimating  $\mu_p$  for  $p \geq 3$  appear to be novel. Finally, we mention that somewhat related work on multilevel Monte Carlo techniques for arbitrary order central moment estimators can be found in [BC16]. However, there the authors construct the estimators for  $p \geq 3$  based on biased estimators for the level-wise contributions. Consequently, the method introduced in the aforementioned work requires to carefully control this additional bias. Moreover, the mean squared error analysis is also affected by this bias, in the sense that the error is quantified using worst-case bounds based on triangle inequalities. Instead our work, as mentioned earlier already, uses  $h$ -statistics for level-wise contributions, which are unbiased estimators with minimal variance. In fact, these unbiased estimators can be straightforwardly derived in closed-form, allowing for a possibly sharper mean squared error bound. The cost of working with unbiased estimators is that deriving these estimators in closed-form requires somewhat tedious calculations. However, these calculations can be easily carried out automatically by symbolic computer algebra systems, such as `Maple` and `Mathematica`, as we will describe in the following. Lastly, we present a complete algorithm and detail how to tune the MLMC method for central moments to achieve optimal complexity.

In the following sections we present and analyze the sampling-based estimation of central moments. Specifically, in Sect. 6.2 we first consider the classic Monte Carlo method, before introducing the novel multilevel Monte Carlo estimator in Sect. 6.3. Following these theoretical considerations, we discuss various practical aspects and implementation details for the multilevel Monte Carlo methods in Sect. 6.4. In Sect. 6.5 we demonstrate the effectiveness of the developed methodology by applying it to a number of selected examples, for which we estimate the first four statistical central moments. These examples include relevant problems in compressible aerodynamics, namely a transonic airfoil affected by both operating and geometric uncertainties.

## 6.2 Monte Carlo estimation of central moments

The  $p$ -th central moment  $\mu_p \equiv \mu_p(Q)$  of a random variable  $Q$  (also known as the  $p$ -th moment about the mean) is given by

$$\mu_p(Q) := \mathbb{E}\left[(Q - \mathbb{E}[Q])^p\right],$$

for any  $p \in \mathbb{N}$  provided it exists, although the value for  $p = 1$  is trivial ( $\mu_1(Q) = 0$ ). Any central moment can, of course, be expressed in terms of non-centered (so-called raw moments or

moments about the origin) as a consequence of the binomial theorem and the linearity of the expected value:

$$\mu_p(Q) \equiv \mathbb{E}[(Q - \mathbb{E}[Q])^p] = \sum_{j=0}^n \binom{p}{j} (-1)^{p-j} \mathbb{E}[Q^j] \mathbb{E}[Q]^{p-j}.$$

However, approximating the  $p$ -th central moment  $\mu_p(Q)$  by a combination of approximated non-centered moments can be numerically unstable. This may be especially severe if the central moments are small whereas the raw moments are not. To avoid these numerical instabilities, we present here Monte Carlo sampling based estimators for central moments directly. We begin by reviewing classic (single-level) Monte Carlo estimators in the following section before addressing the multilevel estimators.

### 6.2.1 Classic ensemble based Monte Carlo estimator

Starting point for the construction of efficient sampling based estimators for central moments are the so-called  $h$ -statistics [Dwy37]. That is, in the classic single-level setting we consider an i.i.d. sample  $Q_N := (Q_i)_{i=1, \dots, N}$  of size  $N$ , where each  $Q_i$  has the same distribution as  $Q$ . The  $h$ -statistic  $h_p \equiv h_p(Q_N)$  then is an unbiased estimator of  $\mu_p(Q)$ , in the sense that  $\mathbb{E}[h_p(Q_N)] = \mu_p(Q)$ . Moreover, the  $h$ -statistic has the favorable property that its variance  $\text{Var}[h_p(Q_N)] = \mathbb{E}[(h_p(Q_N) - \mu_p(Q))^2]$  is minimal compared to all other unbiased estimators [Hal46]. Based on the sample  $Q_N$  of size  $N$ , the  $h$ -statistic  $h_p(Q)$  is commonly expressed in terms of power sums  $S_a \equiv S_a(Q_N) := \sum_{i=1}^N Q_i^a$ . For example, the first three  $h$ -statistics are

$$\begin{aligned} h_2 &= \frac{NS_2 - S_1^2}{(N-1)N}, \\ h_3 &= \frac{N^2 S_3 - 3NS_2 S_1 + 2S_1^3}{(N-2)(N-1)N}, \\ h_4 &= \frac{(-4N^2 + 8N - 12) S_3 S_1 + (N^3 - 2N^2 + 3N) S_4 + 6NS_2 S_1^2 + (9 - 6N) S_2^2 - 3S_1^4}{(N-3)(N-2)(N-1)N}, \end{aligned}$$

where we have used the shorthand notation  $h_p \equiv h_p(Q_N)$  and  $S_a \equiv S_a(Q_N)$  for brevity (see, e.g., [Dwy37] for the construction of  $h_p$  for arbitrary  $p$ ).

In practice sampling the random variable  $Q$  usually requires the solution of a complex problem (e.g. fluid flow with random initial/boundary conditions, random dynamical system, etc.), which inevitably involves a discretization step. That is, it is often not possible to sample the output quantity of interest (QoI)  $Q_i \equiv Q(\omega_i)$  exactly, where  $\omega_i$  denotes an i.i.d. realization of the random input parameters of the underlying complex problem. Instead, we assume that one can only draw approximate i.i.d. random variables  $Q_{i,M}$ ,  $i = 1, \dots, N$ , from a random variable  $Q_M$ , which is a suitable approximation (in a sense made precise below) of the unknown random variable  $Q$ . In this case the natural Monte Carlo (MC) estimator for the  $p$ -th central moment  $\mu_p(Q)$  by means of an i.i.d. sample of the approximate, computable random variable

$Q_{N,M} := (Q_{i,M})_{i=1,\dots,N}$  is simply the  $h$ -statistic based on  $Q_{N,M}$ :

$$m_p^{\text{MC}} := h_p(Q_{N,M}). \quad (6.2)$$

That is, there are two levels of approximations: the first one due to approximate sampling ( $\mu_p(Q) \approx \mu_p(Q_M)$ ) and the second one due to the Monte Carlo error ( $\mu_p(Q_M) \approx m_p^{\text{MC}}$ ). Consequently, the mean squared error of this Monte Carlo estimator is

$$\text{MSE}(m_p^{\text{MC}}) := \mathbb{E}[(m_p^{\text{MC}} - \mu_p(Q))^2] = (\mu_p(Q_M) - \mu_p(Q))^2 + \text{Var}[h_p(Q_{N,M})], \quad (6.3)$$

from which we identify the bias  $|\mu_p(Q_M) - \mu_p(Q)|$  and the statistical error  $\text{Var}(h_p(Q_{N,M}))$ . Under appropriate assumptions, the statistical error is of order  $\mathcal{O}(N^{-1})$  as usual. In fact, for the first three central moment estimators ( $h_1 \equiv 0$  not included), the MC estimator's variance reads

$$\text{Var}(h_2) = \frac{\mu_4}{N} - \frac{\mu_2^2(N-3)}{(N-1)N}, \quad (6.4a)$$

$$\text{Var}(h_3) = \frac{3\mu_2^3(3N^2 - 12N + 20)}{(N-2)(N-1)N} - \frac{3\mu_4\mu_2(2N-5)}{(N-1)N} + \frac{\mu_6}{N} - \frac{\mu_3^2(N-10)}{(N-1)N}, \quad (6.4b)$$

$$\begin{aligned} \text{Var}(h_4) = & \frac{72\mu_2^4(N^2 - 6N + 12)}{(N-3)(N-2)(N-1)N} + \frac{16\mu_3^2\mu_2(N^2 - 4N + 13)}{(N-2)(N-1)N} \\ & - \frac{24\mu_4\mu_2^2(4N-11)}{(N-2)(N-1)N} + \frac{16\mu_6\mu_2}{(N-1)N} + \frac{\mu_8}{N} - \frac{8\mu_3\mu_5}{N} - \frac{\mu_4^2(N-17)}{(N-1)N}, \end{aligned} \quad (6.4c)$$

where we have suppressed the arguments of  $h_p \equiv h_p(Q_{N,M})$  and  $\mu_p \equiv \mu_p(Q_M)$  for brevity again. It is noteworthy that these quantities can be computed (combinatorial problem) straightforwardly for any  $p$  using the `Mathematica` package `mathstatistica` [RS02], due to the  $h$ -statistic's power sum representation.

If one assumes that the approximate random variable  $Q_M$  is such that the bias term  $|\mu_p(Q_M) - \mu_p(Q)|$  decays at a certain rate when increasing the discretization parameter  $M$ , then it is possible to balance the squared bias and statistical error contributions to the MSE in (6.3). Such a bias assumption is plausible since the bias term is related to the numerical method (assumed to be consistent) used to approximate the underlying complex system. At the same time, generating realizations of  $Q_M$  typically becomes more expensive as  $M$  increases. The following result thus quantifies the computational cost to estimate the  $p$ -th central moment by the MC method, when using optimal discretization parameter  $M$  and optimal sample size  $N$  to achieve a prescribed accuracy. As a matter of fact, the theoretical result below is the central moment analog of the standard result for expectations.

**Proposition 6.2.1.** *Let  $p \in \mathbb{N}$ ,  $p \geq 2$ , and assume that the  $2p$ -th central moment of  $Q_M$  is bounded, so that  $\mu_{2p}(Q_M) < \infty$  for  $M \gg 1$ . Furthermore, suppose that there exist constants  $\alpha$  and  $\gamma$  such that*

## Chapter 6. MLMC for Central Statistical Moments

---

1. the bias decays with order  $\alpha > 0$ , in the sense that  $|\mu_p(Q_M) - \mu_p(Q)| \leq c_\alpha M^{-\alpha}$  for some constant  $c_\alpha > 0$ ,
2. the cost to compute each i.i.d. realization of  $Q_M$  is bounded by  $\text{cost}(Q_M) \leq c_\gamma M^\gamma$  for some constants  $c_\gamma, \gamma > 0$ .

The MC estimator  $\mathbb{m}_p^{\text{MC}} = h_p(Q_{N,M})$  with  $N = \mathcal{O}(\varepsilon^{-2})$  and  $M = \mathcal{O}(\varepsilon^{-1/\alpha})$  satisfies  $\text{MSE}(\mathbb{m}_p^{\text{MC}}) = \mathcal{O}(\varepsilon^2)$  and the cost associated with computing this estimator is bounded by

$$\text{cost}(\mathbb{m}_p^{\text{MC}}) = N \cdot \text{cost}(Q_M) \leq c\varepsilon^{-2-\gamma/\alpha},$$

where  $c$  is independent of  $\varepsilon > 0$ .

Note that the constants appearing in the result above (i.e.  $c$ ,  $c_\alpha$ , and  $c_\gamma$ ) depend on the order  $p$  of the central moment. In fact, also the rates  $\alpha$  and  $\gamma$  may depend on  $p$  in principle. However, numerical evidence suggests that the rates may, in fact, not depend on  $p$  for a large class of problems; cf. the numerical studies presented in following Sect. 6.5.

### Practical aspect: MSE and unbiased variance estimation

A robust implementation of the MC estimator  $\mathbb{m}_p^{\text{MC}}$  should also provide an estimation of the associated MSE. This is also the first step towards building an adaptive MC algorithm in which the sample size  $N$  and/or the discretization parameter  $M$  are progressively increased to achieve a MSE smaller than a prescribed tolerance. The bias term  $|\mu_p(Q_M) - \mu_p(Q)|$  relates only to the numerical discretization of the underlying differential problem. Possible ways of estimating the bias include:

- (i) the calculation on a sequence of refined discretizations with parameters  $M_1 < M_2 < \dots$  and extrapolation of the error;
- (ii) error estimations based on a-posteriori error estimators (see e.g. [Ver94], [AO11]) available for certain type of equations.

We will not detail further this aspect here, as the main goal of this work is on the estimation of the statistical error. For this, a possibly unbiased estimator for the variance  $\text{Var}[h_p(Q_{N,M})]$  based on the same sample  $Q_{N,M}$  of size  $N$  is needed. We discuss hereafter the derivation of one such estimator. As we have seen in (6.4), it holds that  $\text{Var}[h_p(Q_{N,M})] = \mathcal{O}(1/N)$ . It is thus convenient to set  $V_p := N \cdot \text{Var}[h_p(Q_{N,M})]$  and derive unbiased estimators  $\hat{V}_p$  of  $V_p$ . However, the naive approach of simply replacing  $\mu_k$ , for  $k = 2, \dots, 2p$ , in (6.4) by its unbiased estimator  $h_k$  will not result in an unbiased estimator for  $V_p$ , since the statistical error  $\text{Var}[h_p(Q_{N,M})]$  depends non-linearly on the central moments. Instead, we do not only substitute  $h_k$  for  $\mu_k$  but also introduce an additional multiplicative coefficient for each substitution. For example, inspecting equation (6.4a) suggests to make the ansatz  $\hat{V}_2 = a_1 h_4 + a_2 h_2^2$  for  $p = 2$ . Similarly,



### 6.3. Multilevel Monte Carlo estimation of central moments.

$\frac{\hat{V}_2}{N}$	$\frac{N((N-1)^2 NS_4 - (N^2-3)S_2^2) + (6-4N)S_1^4 + 4N(2N-3)S_2S_1^2 - 4(N-1)^2 NS_3S_1}{(N-3)(N-2)(N-1)^2 N^2}$
$\frac{\hat{V}_3}{N}$	$\frac{1}{(N-5)(N-4)(N-3)(N-2)^2(N-1)^2 N^2} \left( -12(3N^2 - 15N + 20)S_1^6 \right. \\ + 36N(3N^2 - 15N + 20)S_2S_1^4 - 24N^2(2N^2 - 9N + 11)S_3S_1^3 \\ + 3NS_1^2((7N^4 - 36N^3 + 79N^2 - 90N + 40)S_4 - 6N(4N^2 - 21N + 29)S_2^2) \\ - 6NS_1((N^3 - 3N^2 + 6N - 8)(N-1)^2S_5 + (-5N^4 + 18N^3 + 13N^2 - 90N + 40)S_2S_3) \\ + N((N-1)^2N(N^3 - 3N^2 + 6N - 8)S_6 + 3(3N^4 - 24N^3 + 71N^2 - 90N + 40)S_2^3 \\ - 3(2N^5 - 11N^4 + 14N^3 + 25N^2 - 70N + 40)S_4S_2 \\ \left. - (N^5 + 4N^4 - 41N^3 + 40N^2 + 100N - 80)S_3^2) \right)$

**Table 6.1** – Closed-form expressions of the unbiased estimators  $\hat{V}_p/N$  for  $\text{Var}[h_p(Q_{N,M})] = V_p/N$ ,  $p = 2, 3$ , as polynomial functions of the power sums  $S_a \equiv S_a(Q_{N,M})$ .

(6.4b) implies the ansatz  $\hat{V}_3 = a_1 h_2^3 + a_2 h_2 h_4 + a_3 h_6 + a_4 h_3^2$  for the case  $p = 3$  and so on. For an ansatz of this form the expected value of  $\hat{V}_p$ ,  $\mathbb{E}[\hat{V}_p]$ , can be computed as a polynomial function of the central moments  $\mu_k$ ,  $k = 2, \dots, 2p$ , using `mathstática`. Consequently, we can derive unbiased estimators by equating the coefficients of such polynomial with the corresponding ones in the expression of  $\mathbb{E}[V_p]$ . For example, for  $p = 2$  we find

$$\mathbb{E}[\hat{V}_2] = \frac{\mu_4(a_2 + a_1 N)}{N} + \frac{a_2 \mu_2^2 (N^2 - 2N + 3)}{(N-1)N},$$

which, after comparing with equation (6.4a), yields  $a_1 = \frac{N-1}{N^2-2N+3}$  and  $a_2 = -\frac{N-3}{N^2-2N+3}$ . The unbiased variance estimators  $\hat{V}_p/N$  of  $\text{Var}[h_p(Q_{N,M})]$  obtained by following this procedure are summarized in Table 6.1, where the final expression has been given directly in terms of the power sums  $S_a \equiv S_a(Q_{N,M})$  instead of the  $h$ -statistics. For the sake of a clear presentation, we present the unbiased estimator for the case  $p = 4$  in A.1. It is noteworthy, that although these formulas are rather lengthy, they are in closed-form, so that they are easily implementable.

### 6.3 Multilevel Monte Carlo estimation of central moments.

Using the results presented in the previous Section and following the general construction of MLMC estimators, we introduce the MLMC estimator for the  $p$ -th central moment as:

$$\mathfrak{m}_p^{\text{MLMC}} := h_p(Q_{N_0, M_0}^0) + \sum_{\ell=1}^L \left( h_p(Q_{N_\ell, M_\ell}^\ell) - h_p(Q_{N_\ell, M_{\ell-1}}^\ell) \right) \equiv \sum_{\ell=0}^L \left( h_p(Q_{N_\ell, M_\ell}^\ell) - h_p(Q_{N_\ell, M_{\ell-1}}^\ell) \right), \quad (6.5)$$

with the convention that  $h_p(Q_{N_0, M_{-1}}^0) \equiv 0$ . Here, the sample  $Q_{N_\ell, M_\ell}^\ell$  of i.i.d. realizations is given by  $Q_{N_\ell, M_\ell}^\ell := (Q_{M_\ell}(\omega_{i, \ell}))_{i=1, \dots, N_\ell}$  for any level  $\ell$ . The superscript  $\ell$  of both samples  $Q_{N_\ell, M_\ell}^\ell$  and  $Q_{N_\ell, M_{\ell-1}}^\ell$  is used to indicate the correlation across two consecutive levels, which is the key ingredient for any multilevel Monte Carlo method. Specifically, the realizations of the sample  $Q_{N_\ell, M_\ell}^\ell$  and those of  $Q_{N_\ell, M_{\ell-1}}^\ell$  are independent, while the  $N_\ell$  realizations of  $Q_{N_\ell, M_\ell}^\ell$  and  $Q_{N_\ell, M_{\ell-1}}^\ell$  are correlated, in the sense that the approximate quantities of interest computed on the finer

discretization (i.e. sample  $Q_{N_\ell, M_\ell}$ ) and those computed on the coarser discretization (i.e. samples of  $Q_{N_\ell, M_{\ell-1}}$ ) correspond to the same uncertain inputs. Consequently, the MLMC estimator's mean squared error is

$$\text{MSE}(\mathfrak{m}_p^{\text{MLMC}}) = (\mu_p(Q_{M_L}) - \mu_p(Q))^2 + \sum_{\ell=0}^L \text{Var}[\Delta_\ell h_p], \quad (6.6)$$

where we have introduced the shorthand notation

$$\Delta_\ell h_p \equiv \Delta_\ell h_p(Q_{N_\ell, M_\ell}^\ell, Q_{N_\ell, M_{\ell-1}}^\ell) := h_p(Q_{N_\ell, M_\ell}^\ell) - h_p(Q_{N_\ell, M_{\ell-1}}^\ell).$$

The bias term  $|\mu_p(Q_{M_L}) - \mu_p(Q)|$  in (6.6) corresponds to the bias of the classic Monte Carlo method described in Sect. 6.2.1 on discretization level  $L$ , cf. equation (6.3). The analysis of the variances  $\text{Var}[\Delta_\ell h_p]$  and their dependence on  $N_\ell$  as well as on the central moments of  $Q_{N_\ell, M_\ell}^\ell$  and  $Q_{N_\ell, M_{\ell-1}}^\ell$  is more cumbersome than for the classic MC estimator. In particular we need to quantify the correlation between  $Q_{N_\ell, M_\ell}^\ell$  and  $Q_{N_\ell, M_{\ell-1}}^\ell$ . To do so, it is convenient to introduce both the sample sum and the sample difference of these samples:

$$\begin{aligned} \mathbf{X}_{N_\ell}^{\ell,+} &:= (X_i^{\ell,+})_{i=1, \dots, N_\ell} \quad \text{with} \quad X_i^{\ell,+} := Q_{M_\ell}(\omega_{i,\ell}) + Q_{M_{\ell-1}}(\omega_{i,\ell}), \\ \mathbf{X}_{N_\ell}^{\ell,-} &:= (X_i^{\ell,-})_{i=1, \dots, N_\ell} \quad \text{with} \quad X_i^{\ell,-} := Q_{M_\ell}(\omega_{i,\ell}) - Q_{M_{\ell-1}}(\omega_{i,\ell}). \end{aligned}$$

In other words, we have that  $\mathbf{X}_{N_\ell}^{\ell,+} = Q_{N_\ell, M_\ell}^\ell + Q_{N_\ell, M_{\ell-1}}^\ell$  and  $\mathbf{X}_{N_\ell}^{\ell,-} = Q_{N_\ell, M_\ell}^\ell - Q_{N_\ell, M_{\ell-1}}^\ell$ . Moreover, we introduce the bivariate power sums  $S_{a,b}$  analogously to the power sums  $S_a$  in the previous Section, that is

$$S_{a,b}((X_i)_{i=1, \dots, N}, (Y_i)_{i=1, \dots, N}) := \sum_{i=1}^N X_i^a Y_i^b,$$

for any two samples  $(X_i)_{i=1, \dots, N}$  and  $(Y_i)_{i=1, \dots, N}$  of the same size  $N$ . Then we can compute the variance  $\text{Var}(\Delta_\ell h_p)$  for each level  $\ell$  as follows:

1. For each  $\ell$ , we express the term  $\Delta_\ell h_p \equiv h_p(Q_{N_\ell, M_\ell}^\ell) - h_p(Q_{N_\ell, M_{\ell-1}}^\ell)$  in terms of bivariate power series  $S_{a,b}$  in  $\mathbf{X}_{N_\ell}^{\ell,+}$  and  $\mathbf{X}_{N_\ell}^{\ell,-}$ , that is in terms of

$$S_{a,b}^\ell \equiv S_{a,b}(\mathbf{X}_{N_\ell}^{\ell,+}, \mathbf{X}_{N_\ell}^{\ell,-}).$$

This can, of course, be achieved by using the identities  $Q_{N_\ell, M_\ell}^\ell = \frac{1}{2}(\mathbf{X}_{N_\ell}^{\ell,+} + \mathbf{X}_{N_\ell}^{\ell,-})$  and  $Q_{N_\ell, M_{\ell-1}}^\ell = \frac{1}{2}(\mathbf{X}_{N_\ell}^{\ell,+} - \mathbf{X}_{N_\ell}^{\ell,-})$  and some algebra.

2. The obtained representation of  $\Delta_\ell h_p$  in terms of these bivariate power sums in  $\mathbf{X}_{N_\ell}^{\ell,+}$  and  $\mathbf{X}_{N_\ell}^{\ell,-}$  is then amenable for further treatment by the `mathstatistica` software. In fact, the software provides an efficient algorithm for treating the combinatorial problem of computing the desired variances, due to the power series representation.

Following this procedure, the first step yields for example

$$\begin{aligned}\Delta_\ell h_2 &= \frac{N_\ell S_{1,1}^\ell - S_{0,1}^\ell S_{1,0}^\ell}{(N_\ell - 1)N_\ell}, \\ \Delta_\ell h_3 &= -\frac{-N_\ell^2 S_{0,3}^\ell - 3N_\ell^2 S_{2,1}^\ell + 3N_\ell S_{0,2}^\ell S_{0,1}^\ell + 3N_\ell S_{2,0}^\ell S_{0,1}^\ell + 6N_\ell S_{1,0}^\ell S_{1,1}^\ell - 2S_{0,1}^{\ell 3} - 6S_{1,0}^{\ell 2} S_{0,1}^\ell}{4(N_\ell - 2)(N_\ell - 1)N_\ell},\end{aligned}$$

where we have again omitted the arguments for brevity. The same procedure can also be used to derive close-form expressions for  $\Delta_\ell h_p$  with  $p \geq 4$ , which become rather lengthy and are thus not presented here for the sake of a clear presentation. Based on these closed-form expressions for  $\Delta_\ell h_p$ , the required expression of the variance  $\mathbb{V}ar[\Delta_\ell h_p]$  on level  $\ell$  then follows accordingly as

$$\mathbb{V}ar[\Delta_\ell h_2] = -\frac{(N_\ell - 2)\mu_{1,1}^2}{(N_\ell - 1)N_\ell} + \frac{\mu_{0,2}\mu_{2,0}}{(N_\ell - 1)N_\ell} + \frac{\mu_{2,2}}{N_\ell}, \quad (6.7a)$$

$$\begin{aligned}\mathbb{V}ar[\Delta_\ell h_3] &= \frac{3(3N_\ell^2 - 12N_\ell + 20)\mu_{0,2}^3}{16(N_\ell - 2)(N_\ell - 1)N_\ell} + \frac{9(N_\ell^2 - 4N_\ell + 8)\mu_{1,1}^2\mu_{0,2}}{4(N_\ell - 2)(N_\ell - 1)N_\ell} \\ &+ \frac{9(N_\ell^2 - 4N_\ell + 12)\mu_{2,0}^2\mu_{0,2}}{16(N_\ell - 2)(N_\ell - 1)N_\ell} + \frac{9(N_\ell^2 - 4N_\ell + 6)\mu_{1,1}^2\mu_{2,0}}{2(N_\ell - 2)(N_\ell - 1)N_\ell} \\ &- + \frac{9(N_\ell - 2)\mu_{2,0}\mu_{0,2}^2}{8(N_\ell - 1)N_\ell} + \frac{9\mu_{4,0}\mu_{0,2}}{16(N_\ell - 1)N_\ell} - \frac{9(N_\ell - 2)\mu_{2,2}\mu_{0,2}}{8(N_\ell - 1)N_\ell} \\ &- \frac{3(2N_\ell - 5)\mu_{0,4}\mu_{0,2}}{16(N_\ell - 1)N_\ell} + \frac{9\mu_{1,2}^2}{4(N_\ell - 1)N_\ell} + \frac{\mu_{0,6}}{16N_\ell} + \frac{3\mu_{2,4}}{8N_\ell} \\ &+ \frac{9\mu_{1,2}\mu_{3,0}}{4(N_\ell - 1)N_\ell} + \frac{9\mu_{4,2}}{16N_\ell} - \frac{3\mu_{0,4}\mu_{2,0}}{8N_\ell} - \frac{3(N_\ell - 4)\mu_{1,1}\mu_{1,3}}{4(N_\ell - 1)N_\ell} \\ &- \frac{9(N_\ell - 2)\mu_{1,1}\mu_{3,1}}{4(N_\ell - 1)N_\ell} - \frac{3(N_\ell - 4)\mu_{0,3}\mu_{2,1}}{8(N_\ell - 1)N_\ell} - \frac{9(N_\ell - 3)\mu_{2,0}\mu_{2,2}}{8(N_\ell - 1)N_\ell} \\ &- \frac{(N_\ell - 10)\mu_{0,3}^2}{16(N_\ell - 1)N_\ell} - \frac{9(N_\ell - 6)\mu_{2,1}^2}{16(N_\ell - 1)N_\ell},\end{aligned} \quad (6.7b)$$

where we present  $\mathbb{V}ar[\Delta_\ell h_4]$  in A.1 for a clearer presentation. Here,  $\mu_{p,q} \equiv \mu_{p,q}(X^{\ell,+}, X^{\ell,-})$  denotes the bivariate central moment of order  $(p, q)$  of  $X^{\ell,+}$  and  $X^{\ell,-}$ , where the bivariate central moment is given by

$$\mu_{p,q}(X, Y) := \mathbb{E}\left[(X - \mathbb{E}(X))^p (Y - \mathbb{E}(Y))^q\right],$$

for any two random variables  $X$  and  $Y$ .

Inspection of the variance expressions for  $\mathbb{V}ar(\Delta_\ell h_p)$  in (6.7) reveals that  $\mathbb{V}ar(\Delta_\ell h_p) = \mathcal{O}(1/N_\ell)$  for any fixed  $\ell$ . Setting  $V_{\ell,p} := N_\ell \mathbb{V}ar(\Delta_\ell h_p)$ , the mean squared error of the MLMC estimator  $\mathfrak{m}_p^{\text{MLMC}}$  can then be written in the somewhat more familiar form

$$\text{MSE}(\mathfrak{m}_p^{\text{MLMC}}) = (\mu_p(Q_{M_L}) - \mu_p(Q))^2 + \sum_{\ell=0}^L \frac{V_{\ell,p}}{N_\ell},$$

which indicates the usual interplay of bias and statistical error. Due to the identities for the variance expressions, the complexity result for the MLMC estimator for central moments follows by the same arguments as the ones used in the standard MLMC result; see, e.g., [Gil15a]. In fact, the only difference to the standard MLMC complexity result is that the notion of bias and variance have to be modified. Then even the formulas for the optimal number of levels and sample size on each level follow immediately; see Sect. 6.4 for further details.

**Proposition 6.3.1.** *Let  $p \in \mathbb{N}$ ,  $p \geq 2$ , and assume that the  $2p$ -th central moment of  $Q_{M_\ell}$  is bounded, so that  $\mu_{2p}(Q_{M_\ell}) < \infty$ , for  $\ell \geq 0$ . Furthermore, suppose that there exist constants  $\alpha$ ,  $\beta$ , and  $\gamma$  such that  $2\alpha \geq \min(\beta, \gamma)$  and*

1. *the bias decays with order  $\alpha > 0$ , in the sense that  $|\mu_p(Q_{M_\ell}) - \mu_p(Q)| \leq c_\alpha M_\ell^{-\alpha}$  for some constant  $c_\alpha > 0$ ,*
2. *the variance  $V_{\ell,p} \equiv \text{Var}[\Delta_\ell h_p] N_\ell$  decays with order  $\beta > 0$ , in the sense that  $V_{\ell,p} \leq c_\beta M_\ell^{-\beta}$  for some constant  $c_\beta > 0$ ,*
3. *the cost to compute each i.i.d. realization of  $Q_{M_\ell}$  is bounded by  $\text{cost}(Q_{M_\ell}) \leq c_\gamma M_\ell^\gamma$  for some constants  $c_\gamma, \gamma > 0$ .*

For any  $0 < \varepsilon < e^{-1}$ , MLMC estimator  $\mathfrak{m}_p^{\text{MLMC}}$  with maximum level  $L \in \mathbb{N}_0$  such that  $|\mu_p(Q_{M_L}) - \mu_p(Q)| \leq \frac{\varepsilon}{\sqrt{2}}$  and with sample size  $N_\ell \in \mathbb{N}$  on level  $\ell$  given by

$$N_\ell = \left\lceil \frac{2}{\varepsilon^2} \sqrt{\frac{V_{\ell,p}}{\text{cost}(Q_{M_\ell})} \sum_{j=0}^L \sqrt{\text{cost}(Q_{M_j}) V_{j,p}}} \right\rceil, \quad 0 \leq \ell \leq L,$$

satisfies  $\text{MSE}(\mathfrak{m}_p^{\text{MLMC}}) \leq \varepsilon^2$  at a computational cost that is bounded by

$$\text{cost}(\mathfrak{m}_p^{\text{MLMC}}) \leq c \begin{cases} \varepsilon^{-2} \ln(\varepsilon^{-1})^2, & \text{if } \beta = \gamma, \\ \varepsilon^{-\left(2 + \frac{\gamma - \beta}{\alpha}\right)}, & \text{if } \beta < \gamma, \\ \varepsilon^{-2}, & \text{if } \beta > \gamma, \end{cases}$$

where  $c$  is independent of  $\varepsilon > 0$ .

As remarked after Prop. 6.2.1 already, it is also the case for the MLMC estimator that the appearing constants depend on the order  $p$ . It may also be the case that the rates depend on  $p$ , although numerical experiments suggest that this is not the case for a large class of problems; see Sect. 6.5. Finally, we mention that the proposition above can be stated in terms of the  $\text{cost}(Q_{M_\ell})$  instead of the  $\text{cost}(\Delta_\ell h_p)$  due to the availability of the closed-form expressions for  $\Delta_\ell h_p$ , whose evaluation cost is negligible compared to  $\text{cost}(Q_{M_\ell})$ .

### 6.3.1 Practical aspect: MSE and unbiased level-wise variance estimation

As for the classic Monte Carlo method described in Sect. 6.2.1, also robust implementation of the MLMC estimator should provide an estimation of the associated MSE. Moreover, estimations of  $\mathbb{V}ar[\Delta_\ell h_p]$  are further needed to determine the optimal sample size  $N_\ell$  on each level to achieve a prescribed tolerance  $\varepsilon$ , and we detail hereafter a practical construction of unbiased estimators for  $V_{\ell,p}$ . Concerning the bias term, the same considerations made for the classic MC estimator hold here as well. However, since the MLMC estimator already uses a sequence of discretizations, the situation is somewhat simplified as a natural way to estimate the bias is  $|\mu_p(Q_{M_\ell}) - \mu_p(Q)| \approx |\Delta_L h_p(Q_{N_\ell, M_\ell}^L, Q_{N_\ell, M_{\ell-1}}^L)|$ . Conversely, we discuss here how to construct an unbiased estimator of the variance  $\mathbb{V}ar[\Delta_\ell h_p]$  on each level  $\ell$ , or equivalently of  $V_{\ell,p} \equiv \mathbb{V}ar[\Delta_\ell h_p] N_\ell$ , based on the samples  $Q_{N_\ell, M_\ell}^\ell$  and  $Q_{N_\ell, M_{\ell-1}}^\ell$ . Similarly to the derivation of an unbiased variance estimator for the MC method (cf. Sect. 6.2.1), an unbiased estimator of the level-wise variance  $V_{\ell,p}$  is not straightforward to construct. In fact, here the situation is even slightly more complicated due to the highly nonlinear combination of the bivariate central moments  $\mu_{k,l}$ , cf. the expressions in (6.7). However, also for the bivariate central moments  $\mu_{k,l}$  there exist unbiased estimators, namely the  $h_{k,l}$ -statistic [RS02]. As a consequence, the procedure to construct unbiased variance estimators described in Sect. 6.2.1 can be followed for the most parts with only minor modifications. Specifically, to construct unbiased estimators of  $\mathbb{V}ar[\Delta_\ell h_p] \equiv V_{\ell,p}/N_\ell$ , we proceed as follows:

1. We make an initial generic ansatz for the estimator  $\hat{V}_{\ell,p}$  of  $V_{\ell,p}$  based upon replacing the central moments  $\mu_{k,l}$  in (6.7) by their multivariate  $h_{k,l}$ -statistics, so that  $\hat{V}_{\ell,p} = \sum_i a_i h_{p_i, q_i}^{m_i} h_{r_i, s_i}^{n_i}$  with the same powers  $m_i$  and  $n_i$  appearing in (6.7).
2. We compute the expectation  $\mathbb{E}[\hat{V}_{\ell,p}]$  of the considered ansatz explicitly as a polynomial function of the central moments  $\mu_{k,l}$ . Again, this combinatorial manipulation can be carried out efficiently using the `mathstatica` software.
3. We assemble a linear system of equations for the unknown coefficients  $(a_i)_i$  in the considered ansatz by equating the coefficients in (6.7) with those of  $\mathbb{E}[\hat{V}_{\ell,p}]/N_\ell$ , obtained by ordering with respect to the central moments  $\mu_{k,l}$ .
4. If the linear system is not uniquely solvable, then we augment the ansatz for the estimator to account for the newly introduced central moment terms by computing  $\mathbb{E}[\hat{V}_{\ell,p}]$  and repeat steps 2–4.

Obviously, it is also possible to directly consider an ansatz that contains all unique combinations of  $\mu_{p_1, q_1}^{k_1} \mu_{p_2, q_2}^{k_2}$ , such that  $k_1(p_1 + q_1) + k_2(p_2 + q_2) = 2p$ . However, the procedure described above offers the advantage that it may result in a lower dimensional linear system, which needs to be solved.

We detail here the procedure for  $p = 2$ . In view of (6.7a) we first make the initial ansatz  $\hat{V}_{\ell,2} = a_1 h_{1,1}^2 + a_2 h_{0,2} h_{2,0} + a_3 h_{2,2}$ . Next, we compute the expectation of this ansatz, which can

be written as

$$\mathbb{E}[\hat{V}_{\ell,2}] = \frac{2a_2 + ((N_\ell - 1)^2 + 1)a_3}{(N_\ell - 1)N_\ell} \mu_{1,1}^2 + \frac{a_2(N_\ell - 1)^2 + a_3}{(N_\ell - 1)N_\ell} \mu_{0,2}\mu_{2,0} + \frac{a_1N_\ell + a_2 + a_3}{N_\ell} \mu_{2,2}.$$

By equating the coefficients of the right-hand side above and those in (6.7a) we then obtain a linear system of equations for the coefficients  $a_1$ ,  $a_2$ , and  $a_3$ . Finally, solving this linear system yields  $a_1 = \frac{N_\ell - 1}{N_\ell^2 - 2N_\ell + 3}$ ,  $a_2 = \frac{N_\ell - 1}{N_\ell^3 - 4N_\ell^2 + 7N_\ell - 6}$ , and  $a_3 = \frac{-N_\ell^2 + 4N_\ell - 5}{N_\ell^3 - 4N_\ell^2 + 7N_\ell - 6}$ . Using these coefficients, we can eventually express the unbiased sample-based estimator of  $\mathbb{V}ar[\Delta_\ell h_2] = V_{\ell,2}/N_\ell$  as a polynomial function of the bivariate power sums as

$$\begin{aligned} \frac{\hat{V}_{\ell,2}}{N_\ell} = & \frac{1}{(N_\ell - 3)(N_\ell - 2)(N_\ell - 1)^2 N_\ell^2} \left( N_\ell \left( (-N_\ell^2 + N_\ell + 2) S_{1,1}^{\ell 2} \right. \right. \\ & + (N_\ell - 1)^2 (N_\ell S_{2,2}^\ell - 2S_{1,0}^\ell S_{1,2}^\ell) + (N_\ell - 1) S_{0,2}^\ell (S_{1,0}^{\ell 2} - S_{2,0}^\ell) \left. \left. + S_{0,1}^{\ell 2} \left( (6 - 4N_\ell) S_{1,0}^{\ell 2} \right. \right. \right. \\ & \left. \left. + (N_\ell - 1) N_\ell S_{2,0}^\ell \right) - 2N_\ell S_{0,1}^\ell \left( (N_\ell - 1)^2 S_{2,1}^\ell + (5 - 3N_\ell) S_{1,0}^\ell S_{1,1}^\ell \right) \right), \end{aligned} \quad (6.8)$$

where  $S_{a,b} \equiv S_{a,b}(\mathbf{X}_{N_\ell}^{\ell,+}, \mathbf{X}_{N_\ell}^{\ell,-})$  for brevity. The same procedure can also be applied to obtain unbiased estimators for higher order (i.e. for any  $p \geq 2$ ) central moments, which become rather lengthy though. However, we emphasize that the obtained unbiased variance estimators are in closed-form, so that an efficient implementation is possible. For example, in A.2 we present the unbiased estimator for the case  $p = 3$ , while we refer to our implementation details for the formula for  $p = 4$ .

We reiterate that the procedure introduced here yields unbiased sample-based variance estimators, which are needed for the practical error control and tuning of the MLMC approach introduced in this work; see the following Section for details. The fact that these variance estimators are unbiased and not just asymptotically unbiased is particularly important on finer levels  $\ell$ , on which the sample size  $N_\ell$  will be small. For example, for  $p = 2$  the bias of the naive variance estimator, which is obtained by simply replacing the bivariate central moments  $\mu_{k,l}$  by the corresponding  $h_{k,l}$ -statistics, is  $\frac{(N_\ell^2 - 4N_\ell + 6)\mu_{1,1}^2 + (3 - 2N_\ell)\mu_{0,2}\mu_{2,0} - (N_\ell^2 - 4N_\ell + 3)\mu_{2,2}}{(N_\ell - 1)^2 N_\ell^2}$ . Although this additional bias as a function of the sample size  $N_\ell$  is of order  $\mathcal{O}(N_\ell^{-2})$ , it may still contribute to a non-negligible error of the MLMC estimator, in particular due to fine levels for which  $N_\ell$  will be small. Finally, we also emphasize that, as a consequence of being based on unbiased estimators, the MLMC method for central moments introduced in this work does not come at the expense of introducing an additional systematic error (i.e. a bias) that needs to be accounted for, unlike other works on central moment estimators, such as [BC16].

### 6.3.2 From mean squared errors to confidence intervals

The discussion of both the MC method and the MLMC method above was solely based on the mean squared error as an accuracy measure. However, for some applications it is often also desirable to associate confidence intervals (or, equivalently, failure probabilities) to an

estimator. Specifically, let  $\hat{\theta}$  be a generic estimator of the deterministic value  $\theta$  with mean squared error given by  $\text{MSE}(\hat{\theta}) = \mathbb{E}[(\hat{\theta} - \theta)^2]$ . For a confidence  $p_c \in (0, 1)$ , the associated confidence interval can then be characterized by the value  $\delta > 0$ , such that

$$\mathbb{P}(|\hat{\theta} - \theta| < \delta) \geq p_c.$$

In the absence of any further knowledge of the probability distribution of  $|\hat{\theta} - \theta|$ , a sufficient condition for the length  $\delta$  of the confidence interval can be derived using Chebyshev's inequality:

$$\mathbb{P}(|\hat{\theta} - \theta| \leq \delta) \leq \frac{\text{MSE}(\hat{\theta})}{\delta^2} = 1 - p_c \quad \Rightarrow \quad \delta = \sqrt{\frac{\text{MSE}(\hat{\theta})}{1 - p_c}}. \quad (6.9)$$

That is, the confidence interval can be directly linked to the estimator's mean squared error. Consequently, the mean squared error based analysis considered in this work can straightforwardly be used to quantify confidence regions (or failure probabilities) of estimators. It is noteworthy however, that the confidence region identified in (6.9) may be rather conservative due to the use of Chebyshev's inequality.

## 6.4 Implementation details and complete algorithm

In this Section, we address important practical aspects needed for the implementation of the MLMC methodology presented in this Chapter and present a pseudo-code of the complete MLMC algorithm. In fact, here we present a unified framework for the estimation of both the expectation  $\mathbb{E}[Q]$  and any order central moment  $\mu_p(Q)$  of a random variable  $Q$  subject to prescribed mean squared error tolerance.

As the central moment  $\mu_p$  is trivially zero for  $p = 1$ , it will be convenient to denote by  $m_1^{\text{MLMC}}$  the MLMC estimator for  $\mathbb{E}[Q]$ . Specifically, equation (6.5) defines the MLMC central moment estimator for any non-trivial order  $p > 1$ . For  $p = 1$  we still use the definition in equation (6.5) but with a slight abuse of notation by setting  $h_1(Q_{N,M}) := \frac{1}{N} \sum_{i=1}^N Q_{i,M}$  to denote the sample average operator, so that equation (6.5) yields the usual MLMC estimator of the expected value for  $p = 1$ .

In the absence of theoretical estimates for the rates and constants that characterize the bias and statistical error decays as well as the cost model for the problem under investigation (cf. Prop. 6.3.1), these rates and constants need to be estimated as they are required to optimally tune the MLMC method. That is, to be able to compute the optimal number of levels and sample sizes, a common practice is to perform an initial *screening* procedure. Such a screening procedure consists, for example, of the evaluation of a predefined number of  $\bar{N}$  realizations on few (coarse) levels  $\{0, \dots, \bar{L}\}$ . Based on these simulations, it is possible to fit these rates and constants (e.g. via a least squares procedure), which then determines the models for the bias, statistical error, and cost per sample.

## Chapter 6. MLMC for Central Statistical Moments

---

Once the rates and constants are determined, the pivotal step for achieving the theoretical complexity of the MLMC method subject to a prescribed mean squared error tolerance, is the choice of both the number of levels  $L$  and the sample size  $N_\ell$  required on each level  $0 \leq \ell \leq L$ . To determine these parameters a precise estimation of the mean squared error (MSE),

$$\text{MSE} = \mathbf{B}^2 + \mathbf{SE},$$

specifically of its two error contributions bias ( $\mathbf{B}$ ) and statistical error ( $\mathbf{SE}$ ), is required as described in Sect. 6.3. In order to present a general procedure for the unified MLMC approach to both the expectation and central moments, we recall that

$$\Delta_\ell h_p = h_p(Q_{N_\ell, M_\ell}^\ell) - h_p(Q_{N_\ell, M_{\ell-1}}^\ell), \quad h_p(Q_{N, M}) = \begin{cases} \frac{1}{N} \sum_{i=1}^N Q_{i, M}, & \text{if } p = 1, \\ p\text{-th } h\text{-statistic}, & \text{if } p > 1. \end{cases} \quad (6.10)$$

In practice the bias contribution  $\mathbf{B}$  is thus estimated by

$$\mathbf{B} \approx |\Delta_L h_p|. \quad (6.11)$$

On the other hand, the statistical error  $\mathbf{SE}$  is approximated by

$$\mathbf{SE} \approx \sum_{\ell=0}^L \frac{\mathcal{V}_{\ell, p}}{N_\ell}, \quad (6.12)$$

where  $\mathcal{V}_{\ell, p}$  denotes the estimated variance  $\text{Var}[\Delta_\ell h_p]$  on level  $\ell$ . Specifically, we use  $\mathcal{V}_{\ell, p} = \hat{V}_{\ell, p}$  on those levels  $\ell$  for which simulations have been run during the screening procedure (i.e.  $\ell \leq \bar{L}$ ). Here,  $\hat{V}_{\ell, p}$  is the unbiased sample-based variance estimator introduced in Sect. 6.3.1. On levels  $\ell$  for which no sample exists yet (i.e. for  $\ell > \bar{L}$ ), we extrapolate the fitted model and use  $\mathcal{V}_{\ell, p} = c_\beta M_\ell^{-\beta}$  as an estimator.

To achieve a prescribed mean squared error of  $\varepsilon^2$ , we thus require

$$\mathbf{B} \leq \sqrt{1 - \theta} \varepsilon, \quad (6.13a)$$

$$\mathbf{SE} \leq \theta \varepsilon^2, \quad (6.13b)$$

where we have additionally introduced a splitting parameter  $\theta \in (0, 1)$  to offer the possibility of weighting the two MSE contributions differently. Specifically, the bias constraint (6.13a) is satisfied for  $L \in \mathbb{N}$  such that

$$M_L \geq \left( \frac{\sqrt{1 - \theta} \varepsilon}{c_\alpha} \right)^{-\frac{1}{\alpha}}, \quad (6.14)$$

in view of Prop. 6.3.1(i). Moreover, the theoretical complexity result in Prop. 6.3.1 also suggests that the statistical error constraint (6.13b) is satisfied with optimal complexity by selecting the



## 6.4. Implementation details and complete algorithm

---

sample size  $N_\ell \in \mathbb{N}$  on level  $\ell$  as

$$N_\ell = \left\lceil \frac{1}{\theta \varepsilon^2} \sqrt{\frac{\mathcal{V}_{\ell,p}}{C_\ell}} \sum_{k=0}^L \sqrt{C_k \mathcal{V}_{k,p}} \right\rceil, \quad \ell = 0, 1, \dots, L, \quad (6.15)$$

where  $C_\ell = \text{cost}(Q_{M_\ell})$ .

In Algorithm 3 we provide a detailed pseudo-code of the full MLMC algorithm, which is based on the discussion above. There  $\text{SOLVE}_\ell$  denotes a ‘‘black-box’’ solver that, for a given realization  $\omega_i$  of the random parameters, returns the approximation  $Q_{M_\ell}(\omega_i)$  on the discretization level  $\ell$ . For the sake of completeness, the pseudo-code also contains a possible screening

---

**Algorithm 3:** MLMC Algorithm for the expectation and central moments of order  $p$ .

---

**SCREENING**( $\bar{N}, \bar{L}, p, \varepsilon_r, \theta$ )

```

for  $\ell = 0 : \bar{L}$  do
  for  $i = 0 : \bar{N}$  do
    Generate random sample:  $\omega_{i,\ell}$ 
     $Q_{M_\ell}(\omega_{i,\ell}) \leftarrow \text{SOLVE}_\ell(\omega_{i,\ell})$ 
     $Q_{M_{\ell-1}}(\omega_{i,\ell}) \leftarrow \text{SOLVE}_{\ell-1}(\omega_{i,\ell})$ 
     $\Delta_\ell h_p = h_p(Q_{N,M_\ell}^\ell) - h_p(Q_{N,M_{\ell-1}}^\ell)$ , where  $h_p(Q_{N,M})$  as in (6.10)
  estimate  $\varepsilon = \varepsilon_r \cdot m_p^{\text{MLMC}}[Q]$ 
  estimate  $\{C_\ell\}_{\ell=0}^{\bar{L}}, \mathcal{V}_{\ell,p}$ 
  compute  $\mathcal{P} = \{c_\alpha, c_\beta, c_\gamma, \alpha, \beta, \gamma\}$  using LS fit
  compute  $L$  using (6.14) and  $N_\ell$  using (6.15)
  return  $L, \{N_\ell\}_{\ell=0}^{\bar{L}}$ 

```

**MLMC**( $L, \{N_\ell\}_{\ell=0}^L, p$ )

```

for  $\ell = 0 : L$  do
  for  $i = 0 : N_\ell$  do
    Generate random sample:  $\omega_{i,\ell}$ 
     $Q_{M_\ell}(\omega_{i,\ell}) \leftarrow \text{SOLVE}_\ell(\omega_{i,\ell})$ 
     $Q_{M_{\ell-1}}(\omega_{i,\ell}) \leftarrow \text{SOLVE}_{\ell-1}(\omega_{i,\ell})$ 
  return  $m_p^{\text{MLMC}}[Q]$ 

```

---

procedure. Eventually, Algorithm 1 returns the MLMC estimator  $m_p^{\text{MLMC}}[Q]$  of the QoI for a prescribed mean squared error tolerance. We emphasize that the implementation presented here takes as an input a *relative* MSE tolerance  $\varepsilon_r$ , which is related to the commonly used absolute MSE tolerance  $\varepsilon$  via

$$\varepsilon = \varepsilon_r \begin{cases} \mathbb{E}[Q], & \text{if } p = 1, \\ \mu_p(Q), & \text{if } p > 1. \end{cases}$$

$\mathbb{E}(Q)$	central moment $\mu_p(Q)$		
	$p = 2$	$p = 3$	$p = 4$
1.045058356	2.16660855	5.6966642	31.191899

**Table 6.2** – Reference values for the expected value  $\mathbb{E}[Q]$  and various central moments  $\mu_p(Q)$  for the QoI  $Q$  derived from the geometric Brownian motion SDE.

## 6.5 Numerical Experiments

In this section we apply the introduced Multi Level Monte Carlo technique to various examples. We begin by scrutinizing the methodology for rather simple toy problems for which exact (or highly accurate) solutions are easily available; see Sects. 6.5.1 and 6.5.2. Then we move on to study a more challenging problem in Sect. 6.5.3, namely the one of a transonic airfoil under operational and/or geometric uncertainties.

### 6.5.1 Stochastic differential equation model: a financial option

Let us begin with a simple example involving a stochastic differential equation (SDE). Specifically, we consider the case that the SDE models (example borrowed from [Gil15b]\*Sect. 5) a financial call option with the asset being a geometric Brownian motion, viz.

$$dS = rS dt + \sigma S dW, \quad S(0) = S_0. \tag{6.16}$$

Here,  $r$ ,  $\sigma$ , and  $S_0$  are given positive numbers. For this asset we are interested in quantifying the uncertainties in the “discounted payoff”, so that we set the quantity of interest  $Q$  as

$$Q := e^{-rT} \max(S(T) - K, 0), \tag{6.17}$$

where  $K > 0$  denotes the agreed strike price and  $T > 0$  the pre-defined expiration date. Due to the fact that the solution to (6.16) at time  $T$ , i.e.  $S(T)$ , is a log-normally distributed random variable with mean  $S_0 e^{rT}$  and variance  $S_0^2 e^{2rT} (e^{\sigma^2 T} - 1)$ , it is straightforward to compute highly accurate approximations to statistics of  $Q$ . In fact, Table 6.2 lists approximated reference values for the expected value and for the first three central moments of  $Q$  corresponding to the parameter values  $r = \frac{1}{20}$ ,  $\sigma = \frac{1}{5}$ ,  $T = 1$ ,  $K = 10$ , and  $S_0 = 10$ . These reference values were obtained using a high precision numerical quadrature.

For the numerical experiments based on the Multi Level Monte Carlo method that will follow, we discretize the SDE (6.16) via the Milstein method.

$$S_\ell^{n+1} = S_\ell^n + \delta_\ell r S_\ell^n + \sigma S_\ell^n \sqrt{\delta_\ell} \xi_n + \frac{\sigma^2}{2} \delta_\ell S_\ell^n (|\xi_n|^2 - 1), \quad S_\ell^0 = S_0,$$

so that  $S_\ell^{n+1} \approx S(n\delta_\ell)$ , where  $\delta_\ell = 2^{-\ell} T$  and  $(\xi_n)_{n \geq 0}$  denotes a sequence of i.i.d. standard

normally distributed random variables. That is, we employ a discretization with a nested grid hierarchy with  $M_\ell = T/\delta_\ell = 2^\ell$  DOFs, which corresponds to the number of time steps needed to integrate the SDE from time  $t = 0$  to the final time  $T$ .

In order to validate the MLMC methodology discussed in this Chapter, we provide in Table 6.3 a sample based estimation of the MSE of the MLMC estimators, using 100 independent repetitions of the algorithm. Specifically, the table offers a comparison between the required relative root MSE tolerance and the achieved sample based root mean squared error for both the expected value and the first three central moments for various tolerances. The results

<b>Tol</b>	$m_1^{\text{MLMC}}$	$m_2^{\text{MLMC}}$	$m_3^{\text{MLMC}}$	$m_4^{\text{MLMC}}$
$\varepsilon_r = 0.1$	0.0647	0.0857	0.0785	0.0991
$\varepsilon_r = 0.05$	0.0435	0.0429	0.0415	0.0495
$\varepsilon_r = 0.025$	0.0237	0.0217	0.0231	0.0223
$\varepsilon_r = 0.01$	0.0087	0.0099	0.0091	0.0083

**Table 6.3** – Sample estimate of relative root MSE based on 100 repetitions of the MLMC algorithm for computing  $m_p^{\text{MLMC}}$  for different relative tolerance requirements.

in Table 6.3 demonstrate that the MLMC implementation described in the previous Section does indeed provide estimators that satisfy the tolerance requirement. Additionally, in the top row of Figure 6.1 we show the actual computed values of these 100 repetitions of the MLMC algorithm (red circles) compared with the reference solution (green stars). To quantify the range of the MLMC estimators, we also indicate the 90% confidence intervals based on a Chebyshev bound (blue bars; see Eq. (6.9)) in these plots.

The bottom row in Figure 6.1 presents the corresponding MLMC hierarchies (both number of levels and sample size per level) required to achieve prescribed relative tolerance requirements when estimating the expectation and various central moments of the QoI  $Q$ . It is interesting to observe that the computational cost required to compute central moments is proportional to that for the expectation up to a multiplicative constant. The latter can be further observed in Figure 6.2, where we plot the computed bias and variance of the estimators, respectively, for various tolerance demands. It can be inferred that the decay rate for the estimator’s bias and variances is the same, while the constants are increasing with increasing  $p$ .

### 6.5.2 Elliptic PDE in two spatial dimensions

We consider a random Poisson equation in two spatial dimensions,

$$-\Delta u = f, \quad \text{in } D = (0, 1)^2, \tag{6.18}$$

with homogeneous Dirichlet boundary conditions. Here, the forcing term  $f$  is given by

$$f(x) = -K\xi(x_1^2 + x_2^2 - x_1 - x_2),$$

## Chapter 6. MLMC for Central Statistical Moments

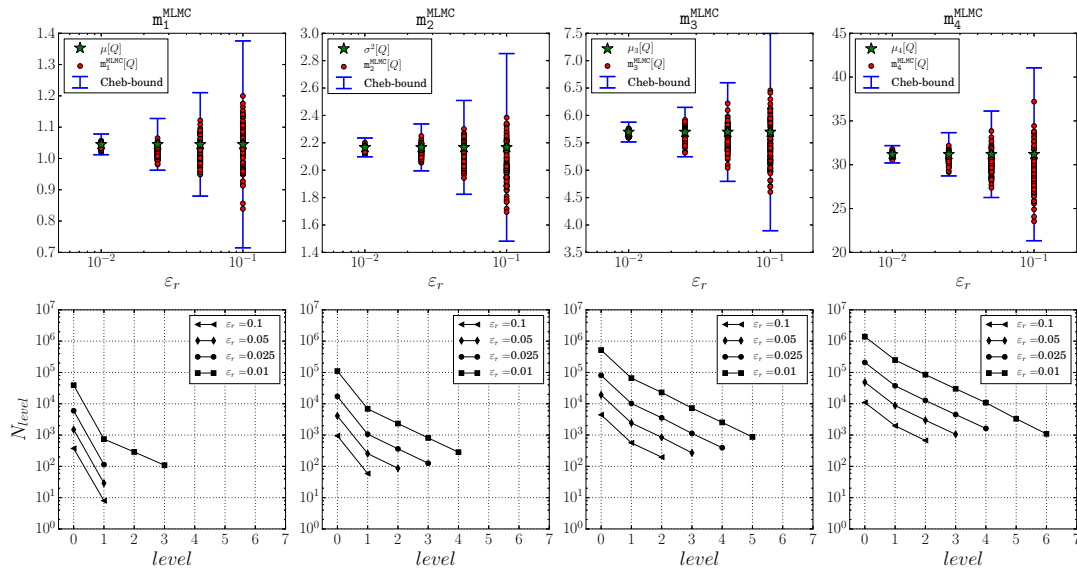


**Figure 6.1** – Computed values of 100 repetitions of the MLMC algorithm compared with the reference solution (first row) and MLMC hierarchies (number of levels and sample size per level) required to achieve prescribed relative tolerance requirements when estimating the expectation and various central moments of the QoI  $Q$  (second row) for the SDE problem.

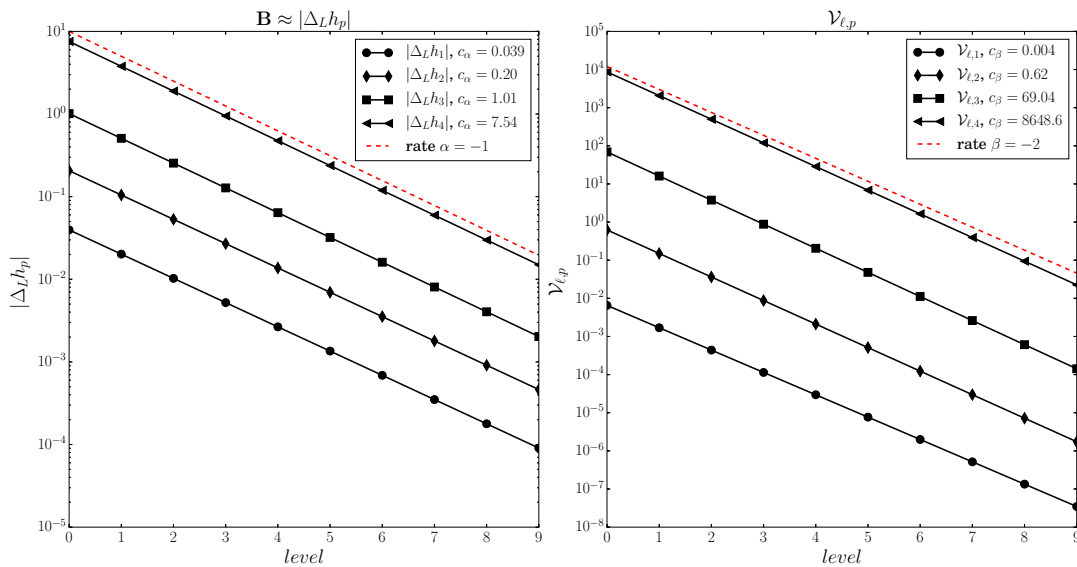


**Figure 6.2** – Decay rates for the bias and variances of MLMC estimator with increasing  $p$  for the SDE problem.

with  $\xi$  being a non-negative random variable and  $K > 0$  a positive constant. For this forcing term the solution to the PDE can be computed explicitly and reads  $u(x_1, x_2) = K\xi x_1 x_2 (1 -$

central moment $\mu_p(Q)$			
$\mathbb{E}(Q)$	$p = 2$	$p = 3$	$p = 4$
1.5	0.75	0.45	1.748863636

**Table 6.4** – Reference values for the expected value  $\mathbb{E}[Q]$  and the first three central moments  $\mu_p(Q)$  for the QoI  $Q$  derived from the random Poisson problem.

$x_1)(1 - x_2)/2$ . As quantity of interest we consider the spatial average of the solution, that is

$$Q := \int_D u dx = \frac{K}{72} \xi.$$

This explicit representation of  $Q$  in terms of the random input  $\xi$  to the PDE model (6.18) allows us to easily compute the exact mean as well as central moments of  $Q$ , which we will use to verify the numerical experiments that follow. Specifically, here we use  $\xi \sim \text{Beta}(2, 6)$  and  $K = 432$ . Table 6.4 then lists approximations to the corresponding mean and the first three central moments of  $Q$ . For the numerical experiments based on Multi Level Monte Carlo method we discretize the PDE (6.18) using a second order finite difference scheme on a regular grid. That is, we employ a nested grid hierarchy with  $M_\ell = (5 \cdot 2^\ell - 2)^2$  DOFs, which correspond to the values of the solution  $u$  at grid points that are not on the boundary  $\partial D$ .

As for the previous example, in Table 6.5 we present the (sample based) root mean squared errors obtained by repeating the MLMC algorithm for the expectation and central moments 100 times and for various tolerances. Also for this example we find that the MLMC implementation

<b>Tol</b>	$m_1^{\text{MLMC}}$	$m_2^{\text{MLMC}}$	$m_3^{\text{MLMC}}$	$m_4^{\text{MLMC}}$
$\varepsilon_r = 0.1$	0.0674	0.0616	0.0587	0.0777
$\varepsilon_r = 0.05$	0.0350	0.0401	0.0351	0.0259
$\varepsilon_r = 0.025$	0.0182	0.0183	0.0156	0.0206
$\varepsilon_r = 0.01$	0.0069	0.0078	0.0062	0.0084

**Table 6.5** – Sample estimate of relative root MSE of 100 repetitions of the MLMC estimators  $m_p^{\text{MLMC}}$  for different relative tolerance requirements.

does indeed satisfy the required tolerance goals.

In the top row of Figure 6.3 the actual computed values for 100 repetitions of the MLMC algorithm (red circles) are compared with the reference values (green stars). Also for this example we observe an accurate estimation within the imposed tolerance goal and within the confidence region (blue bars, 90% confidence; see Eq. (6.9)). In the second row of Figure 6.3 we report the hierarchies required to achieve the prescribed tolerances. As it is possible to observe the number of levels and samples per level (and hence the cost) increase consistently with the central moment we are computing. Such can be also inferred by looking at the decays of the bias and variance of the MLMC estimators for moments presented in Figure 6.4. These plots moreover confirm the observation from the previous example, namely that the decay

## Chapter 6. MLMC for Central Statistical Moments

rates for the estimator's bias and variance are the same for different values of  $p$ , and only the constants vary.

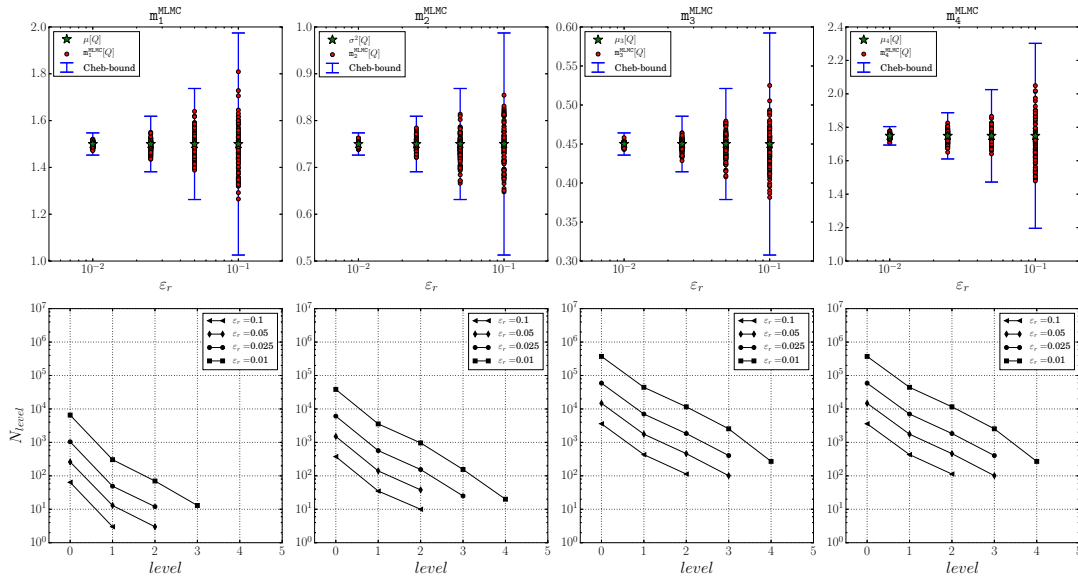


**Figure 6.3** – Computed values of 100 repetitions of the MLMC algorithm compared with the reference solution (first row) and MLMC hierarchies (number of levels and sample size per level) required to achieve prescribed relative tolerance requirements when estimating the expectation and various central moments of the QoI  $Q$  (second row) for the Elliptic PDE problem.

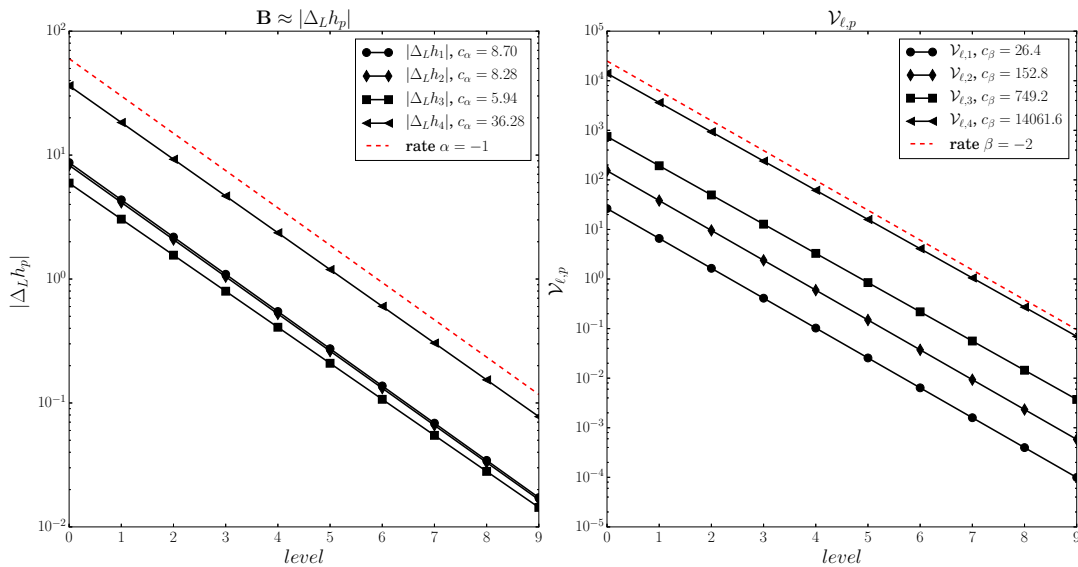


**Figure 6.4** – Decay rates for the bias and variances of MLMC estimator with increasing  $p$  for the Elliptic PDE problem.

### 6.5.3 Transonic Airfoil: 2d

We consider hereafter a transonic supercritical RAE-2822 airfoil [HBE<sup>+</sup>13, V.A79], which has become a standard test-case for transonic flows, subject to both operating and geometric uncertainties.

The fluid flowing around an airfoil generates a local force on each point of the body. The normal and tangential components of such force are the pressure and the shear stress. By integrating the force and stress distribution around the surface of the airfoil we obtain a total force  $F$  and a moment  $M$  about a reference point (so called center of pressure). The parallel and perpendicular component of  $F$  with respect to the free-stream direction  $M_\infty$  are the lift  $L$  and drag  $D$  forces respectively. Figure 2.1 shows a sketch of this concept. For an airfoil shape with surface  $S$  we define the following lift, drag, and moment dimensionless coefficients:

$$C_L = \frac{L}{q_\infty S}, \quad C_D = \frac{D}{q_\infty S}, \quad \text{and} \quad C_M = \frac{M}{q_\infty S L_{ref}}, \quad (6.19)$$

respectively. Here,  $q_\infty = \frac{1}{2} M_\infty^2 \gamma_g p_\infty$  denotes the dynamic pressure and  $\gamma_g = 1.4$  is the ratio of specific heats of the gas. As we are considering 2D normalized airfoils we set the reference length  $L_{ref} = 1$  and the reference surface  $S = 1$ .

The nominal geometry of the RAE-2822 airfoil is defined by a set of PARSEC parameters (see [Sob98] for details). The advantage of the PARSEC approach over other parametrizations (i.e. Bezier, NURBS, FFD) is that we can easily perturb the geometrical parameters on the suction and pressure side of the airfoil which are most relevant for the study that follows. Among other things, Table 6.6 summarizes the geometric definition of the airfoil as well as the set of operating parameters for three different flow conditions considered here. Specifically, CASE-6 denotes the mild transonic case (corresponding to experimental cases 6 from AGARD [V.A79]), CASE-S is a subsonic case with  $M_\infty = 0.6$ , and CASE-R is a higher Reynolds number case.

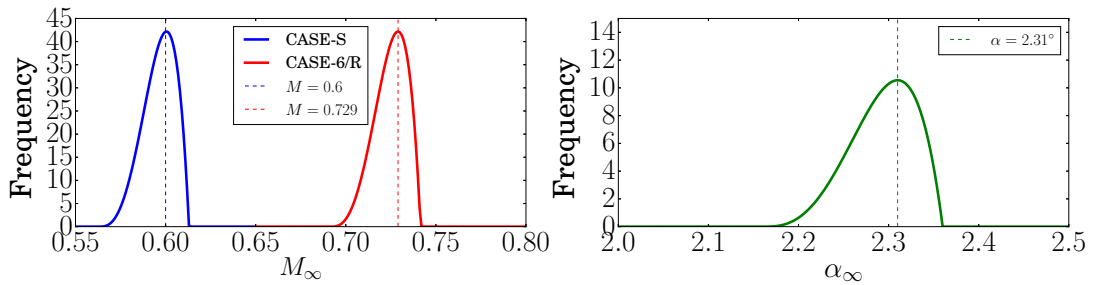


**Figure 6.5** – Exemplary probability density functions of two uncertain operating input parameters for the random RAE-2822.

In what follows, we consider the RAE-2822 airfoil in three different operating regimes with increasing number of uncertain parameters. Specifically, we use the letter  $G$  to denote stochastic simulations where we consider only *geometric* uncertainties (i.e. 10 random input parameters),

	Name	Nominal value			Uncertainty
		CASE-6	CASE-S	CASE-R	
Operating	$Re_c$	$6.5e6$ [-]	$6.5e6$ [-]	$10e6$ [-]	–
	$M_\infty$	$0.729$ [-]	$0.6$ [-]	$0.729$ [-]	$\mathcal{B}(4, 2, 0.05, M_\infty - 0.037)$
	$\alpha_\infty$	$2.31^\circ$	$2.31^\circ$	$2.31^\circ$	$\mathcal{B}(4, 2, 0.2, 2.16)$
Geometric	$R_p$	$8.60311920e - 03$			$\mathcal{U}$ (98%, 102%)
	$R_s$	$8.36101985e - 03$			$\mathcal{U}$ (98%, 102%)
	$x_p$	$3.44224863e - 01$			$\mathcal{U}$ (98%, 102%)
	$x_s$	$4.31244633e - 01$			$\mathcal{U}$ (98%, 102%)
	$y_p$	$-5.88259641e - 02$			$\mathcal{U}$ (98%, 102%)
	$y_s$	$6.30175650e - 02$			$\mathcal{U}$ (98%, 102%)
	$C_p$	$7.03608884e - 01$			$\mathcal{U}$ (98%, 102%)
	$C_s$	$-4.30110180e - 01$			$\mathcal{U}$ (98%, 102%)
	$\theta_p$	$-2.06545825e + 00$			$\mathcal{U}$ (98%, 102%)
	$\theta_s$	$-1.15335351e + 01$			$\mathcal{U}$ (98%, 102%)

**Table 6.6** – Operational and geometrical parameters as well as uncertainties for the RAE-2822 airfoil.

$O$  to denote the regime with only *operating* uncertainties (i.e. two random input parameters, namely the angle of attack  $\alpha_\infty$  and the Mach number  $M_\infty$ , see Figure 6.5) and  $OG$  to denote the setting with *geometric plus operating* uncertainties (i.e. 12 uncertain input parameters). All uncertainties and reference nominal operating and geometric parameters are presented in Table 6.6. The operating uncertainties are modeled as beta distributions denoted by  $\mathcal{B}(a, b, s, loc)$ , where  $a$  and  $b$  are the distribution parameters. As the beta distribution is defined on the  $[0, 1]$  interval, the parameters  $s$  and  $loc$  are used to scale and shift the distribution's support, respectively. On the other hand the geometric uncertainties are modeled as uniform distributions, denoted by  $\mathcal{U}(x_{low}, x_{up})$  with  $x_{low} < x_{up}$  denoting range of the support. The types and ranges of uncertainties for this model problem are representative of a flight condition with natural atmospheric gusts that affect both the angle of attack and the Mach number. Additionally, the geometrical uncertainties are reasonably accounting for manufacturing tolerances and shape deformation of a airfoil due to different loadings on an aircraft wing (aeroelastic twist).

For the numerical study that follows we use the MSES collection of programs for the analysis of airfoils (see [Dre07] for detail) as deterministic 'black-box' solver. The MSES collection solves the steady Euler equations with a finite volume discretization over a streamline grid and is coupled, via the displacement thickness, with a two-equation integral solver for the viscous regions of the boundary layer and trailing wakes. The performance of this 'black-box' solver, when using a 5-levels structured MLMC grid hierarchy, is summarized in Table 6.7. There the features of the grid levels, along with the average computational time  $CTime$  required to compute one deterministic simulation (on one CPU) are shown.

Based on the problem description of the uncertain airfoil problem considered here, in the following study we apply the developed MLMC estimator for central moments to various aerodynamic performance parameters. In order to present the estimated expectations and



Level	Airfoil nodes	Cells	CTime[s]
L0	47	1739	1.9
L1	71	2627	3.2
L2	107	3959	5.7
L3	161	5957	7.5
L4	243	8991	14.7
L5	365	13505	17.9

**Table 6.7** – MLMC 5-levels grid hierarchy for the RAE2822 problem.

central moments estimators for the three different cases (CASE-6, CASE-S, and CASE-R) with increasing number of uncertain parameters ( $G$ ,  $O$ , and  $OG$ ) in a compact and informative way, we introduce in Figure 6.6 a set of bars that are designed to provide the relevant information. Specifically, there the mean, the standard deviation, the skewness, and the kurtosis of different QoIs related to the airfoil, such as lift coefficient  $C_L$ , drag coefficient  $C_D$ , moment coefficient  $C_M$ , and lift-drag ratio  $L/D$ , are presented. Moreover, we compare the deterministic value (obtained with nominal geometric and operating parameters) of a QoI (dashed black lines) with a classical mean plus/minus two standard deviation interval (black bars). The red bars identifies the skewness corrected mean plus/minus two standard deviation, where the skewness correct mean is given by  $\mu + \gamma_1$ . Moreover, the triangles define the kurtosis: yellow inward triangles identify the *platykurtic* distributions while red outward triangles denote *leptokurtic* ones. A distribution is called platykurtic, if the kurtosis  $Kurt < 3$ , which means that the distribution has thinner tails than a Gaussian distribution. Similarly, a distribution is called leptokurtic if  $Kurt > 3$ , which implies fatter tails.

It is interesting to observe in Figure 6.6 the effects of uncertainties on the performance parameters in the three different flow conditions. The two transonic cases CASE-6 and CASE-R are the most sensitive to uncertainties due to the appearance of shock waves in different regions on the airfoil upper side (see also Figure 6.7). In such cases we additionally notice that the drag coefficient  $C_D$  becomes leptokurtic in the presence of both operating and geometric uncertainties, indicating that the distribution is heavy-tailed. We believe that this is due to the appearance of separation bubbles in the front part of the airfoil and stronger shock waves, but further investigations are necessary to confirm this hypothesis. The variability in the forward part of the airfoil can be observed also in the green  $C_p$  plot in Figure 6.7. Further investigation are needed to confirm this hypothesis.

Additionally, in Figure 6.7 we compare the pressure coefficients  $C_p$  of the RAE 2822 airfoil in the different conditions and uncertainty scenarios introduced above as well as the reconstructed lift-drag ratio  $L/D$  distributions computed from the statistical moments using the Gram-Charlier series of type A PDF approximation [Wal58]. The latter is a formal series expansions in terms of a known distribution, most commonly with respect to a Normal distribution. Using

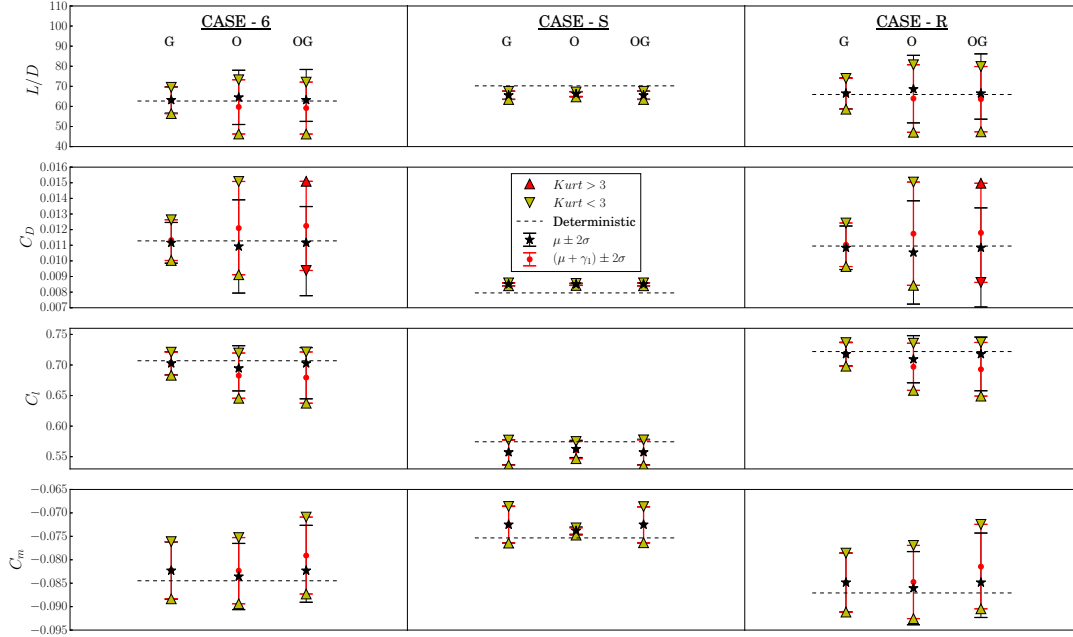


Figure 6.6 – Airfoil LD PDFs.

this approach, an unknown density  $f$  can be approximated by

$$\hat{f}(x) := \frac{1}{\sqrt{2\pi\mu_2}} \exp\left(-\frac{(x-\mu)^2}{2\mu_2}\right) \left(1 + \frac{\mu_3}{3!\mu_2^{3/2}} H_3\left(\frac{x-\mu}{\sqrt{\mu_2}}\right) + \frac{\mu_4 - 3\mu_2^2}{4!\mu_2^2} H_4\left(\frac{x-\mu}{\sqrt{\mu_2}}\right)\right), \quad (6.20)$$

where  $H_3(x) = x^3 - 3x$  and  $H_4(x) = x^4 - 6x^2 + 3$  are Hermite polynomials. Although  $\hat{f}$  may formally not be a proper density as it is not guaranteed to be positive, it nonetheless offers an easy to compute density approximation, based on the MLMC estimators for  $\mu$ ,  $\mu_2$ ,  $\mu_3$ , and  $\mu_4$ . By looking at the  $C_p$  profiles and the reconstructed PDF approximations we can further observe the sensitivity of the airfoil on operating and geometric parameters in the three different flow cases as previously noticed in Figure 6.6. It is worth underlining that the PDF presented here are simply reconstructed from the first four central moments computed with the MLMC method. The background histograms are obtained from a MC simulation with 1000 samples on the finest level. A more efficient and accurate procedure to compute directly the PDF and CDF of QoIs will be presented in the forthcoming Chapter 7.

Finally, in Figure 6.8 we present the computational complexity in CPU hours required to achieve a certain tolerance requirement. Specifically, the complexities of the MLMC method and the classic MC approach are compared for approximating the expectation and central moments for the  $L/D$  QoI in CASE-6 with both operating and geometric uncertainties. The dashed lines indicate the computational complexity predicted by the theory. We immediately observe a significant speedup of the MLMC method compared to the MC method. Practically speaking, by employing a cluster node with 28 CPUs we are able to compute the first four

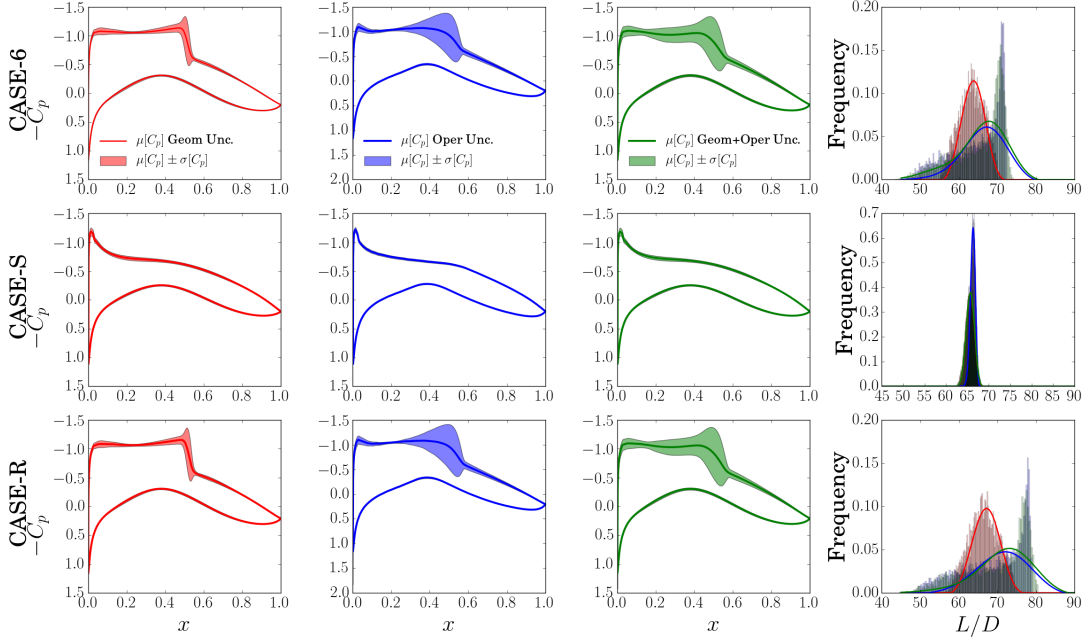


**Figure 6.7** – Pressure coefficients  $C_p$  of the RAE 2822 airfoil in the different conditions and uncertainty scenarios and the reconstructed lift-drag ratio  $L/D$  distributions.

central moments of the airfoil problem and guarantee a relative tolerance of 1% (i.e.  $\varepsilon_r = 0.01$ ) in 3.6 [h] with our MLMC implementation, while we would need to invest 14.8 [days] with the classic MC method.

## 6.6 Summary

In this chapter we introduced a methodology and algorithmic extension of the Multi Level Monte Carlo concepts for the efficient computation of central statistical moments. The key feature of our procedure is the use of  $h$ -statistics as unbiased central moment estimators with minimal variance for the level-wise contributions. It has been shown in the numerical examples that the proposed MLMC estimator based on  $h$ -statistics satisfy the tolerance requirement and require a computational cost proportional to that for the estimation of expectations (up to a multiplicative constant). Additionally we observed that the decay rate for the estimator's bias and variances is the same for arbitrary order central moment  $\mu_p$ , while the constants are increasing with increasing  $p$ .

In the airfoil problem we observed that central moments can provide relevant information regarding random variable distribution in view of decision making processes and optimization under uncertainty approaches. We tested a distribution reconstruction approach based on series expansion from the statistical moment (Gram-Charlier approximation) and observed that the approximation of the distribution is not always satisfactory. The reconstruction is not

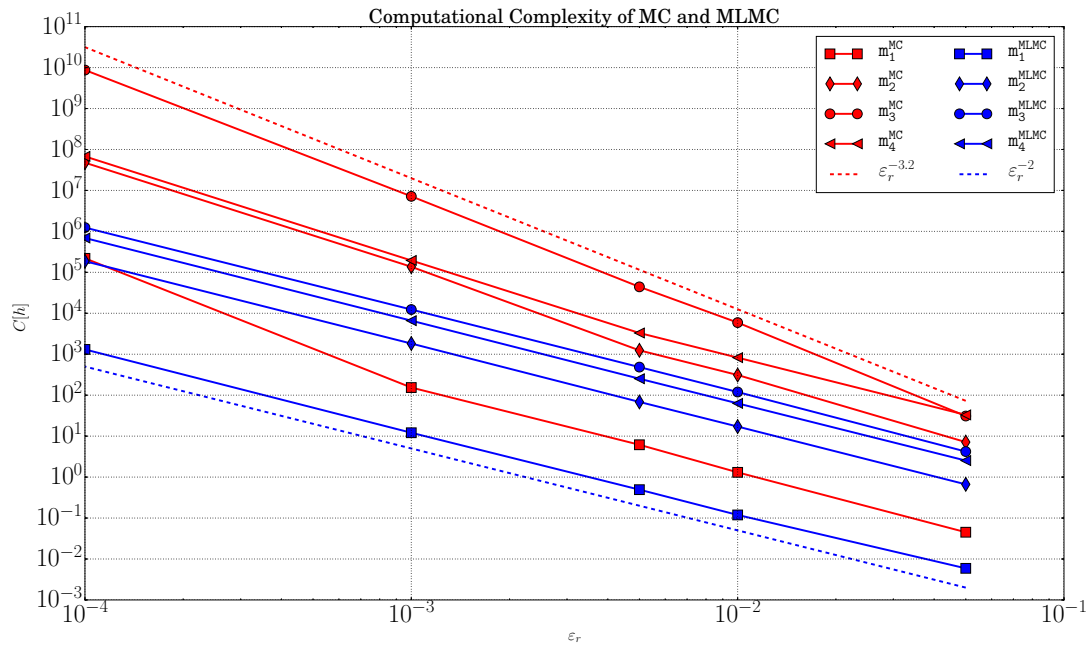


**Figure 6.8** – Computational complexity of MC and MLMC (in CPU hours) required to achieve a certain tolerance requirement for the first central moments.

guaranteed to be a proper probability distribution and seems to lead to large inaccuracies in capturing asymmetric behaviors and heavy tails. In order to overcome these issues, we present in the following Chapters another extension of the MLMC approach to accurately approximate distributions and compute risk measures.

## 7 MLMC for Distributions and Risk Measures

In Chapter 4 we introduced a MLMC estimator for computing the expectation  $\mathbb{E}[Q]$  of a QoI  $Q$  and in Chapter 6 we extend the MLMC concepts to the estimation of arbitrary order central moments  $\mu_p[Q]$  of  $Q$ . As presented in Chapter 6, central moments can provide valuable information regarding characteristic features of a random variable distribution, such as location, dispersion, asymmetry, tailedness, etc. However, the analysis of a random system may require, in some applications, the accurate approximation of its entire distribution (probability density function or the cumulative function). The reconstruction of the distribution using formal series expansions from the random variable statistical moments (see Gram-Charlier approximation [Wal58] used in Chapter 6 for example) is a viable option only for certain classes of distributions. Indeed, the reconstruction is not guaranteed to be a proper probability distribution (the reconstructed density may not be positive everywhere) and can lead to large inaccuracies in capturing heavy tails. Additionally, various decision making processes and optimization under uncertainty require the knowledge of risk indicators, such as quantiles (also known as value at risk, VaR) or coherent risk measures [Del00] such as the conditional value at risk (CVaR, [Roc07]). These indicators cannot be expressed as moments and are hence usually not easily accessible.

In this Chapter we present a novel MLMC method for the efficient approximation of parametric expectations. Specifically, here we particularize the MLMC method introduced in [KN17] to the accurate and robust computation of an uncertain system output's cumulative distribution function (CDF), quantiles (Value at Risk, VaR) and conditional value at risk (CVaR) using cubic splines interpolation operators.

The approach relies on accurately approximating parametric expectations, i.e. expectations that depend on a parameter uniformly on a given range for the parameter. For a general function  $\phi$  and a random variable  $Q$ , **parametric expectations** are defined as follow:

$$\Phi(\vartheta) = \mathbb{E}(\phi(\vartheta, Q)) \quad (7.1)$$

In the following sections we will first present how to set up a MLMC analysis for the accurate

estimation of a general function  $\Phi(\vartheta)$  and its derivatives and subsequently how to define estimators for the computation of CDFs, VaR and CVaR while each estimated quantity satisfies a prescribed tolerance goal. Indeed all of these quantities, for a random variable QoI  $Q$ , can be defined as parametric expectations for a specific function  $\phi$  or derived from a parametric expectation.

For instance, the CDF corresponds to  $\Phi(\vartheta) = \mathbb{P}(Q \leq \vartheta) = \mathbb{E}[\mathbb{1}_{Q \leq \vartheta}]$ , although, as we will see later this representation is not the best for MLMC approximations of CDFs and we will actually resort to an alternative one.

As in the previous chapters, we assume here, that it is not possible to sample from the distribution of the QoI  $Q$  exactly. Instead, we assume that one can only draw approximate i.i.d. random variables  $Q_{i,M_\ell}$ ,  $i = 1, \dots, N$ , from a random variable  $Q_{M_\ell}$ , which is a suitable approximation (in a sense made precise in Chapter 4) of the unknown random variable  $Q$ . Hence, we consider also in this framework a hierarchy of approximations on different levels  $\ell$ , in the sense that the level  $\ell$  approximation  $Q_{M_\ell}$  corresponds to an approximation of  $Q$  with a discretization parameter  $M_\ell$  (number of DOFs) with  $M_0 < M_1 < \dots < M_L = M$ . Recall that in this work  $Q_{M_\ell}$  is derived from an approximate solution to a stochastic/random partial differential equation obtained via an appropriate numerical scheme.

Based on this multilevel hierarchy we aim at approximating parametric expectations  $\Phi(\vartheta) = \mathbb{E}(\phi(\vartheta, Q))$  and its derivatives  $\Phi^{(m)}(\vartheta)$  on some compact interval  $\Theta \subset \mathbb{R}$  for a given function  $\phi: \Theta \times \mathbb{R} \rightarrow \mathbb{R}$ .

We first detail in the next section the MLMC approximation of parametric expectations and extend afterwards the approach to the accurate approximation of its derivatives.

## 7.1 Multi Level Monte Carlo approximation of parametric expectations

The intuitive idea of this approach is to build a MLMC approximation for parametric expectations  $\Phi$  (on the interval  $\Theta$ ) by first evaluating  $\Phi$  in a set of suitably chosen nodes in  $\Theta$  by a standard MLMC estimator and then appropriately interpolating the collected values to obtain an actual function on  $\Theta$ . Let us denote by

$$\theta := (\theta_1, \theta_2, \dots, \theta_n)^T \in \Theta^n, \quad \theta_j \in \Theta, \quad 1 \leq j \leq n, \quad (7.2)$$

a uniform deterministic grid (other choices may be possible and the interested reader is referred to the abstract result in [KN17]) of  $n \in \mathbb{N}$  nodes on  $\Theta$ . Moreover, we denote by  $f(\theta)$  the vector with components  $f(\theta_j)$ ,  $j = 1, \dots, n$ , for any function  $f: \mathbb{R} \rightarrow \mathbb{R}$ .

Following the general construction of MLMC estimators presented in Chapter 6, a collection

## 7.1. Multi Level Monte Carlo approximation of parametric expectations

---

of pointwise MLMC estimators of a function  $\phi$  is defined as:

$$\bar{\Phi}^{\text{MLMC}}(\theta) := \left[ \sum_{\ell=0}^L \frac{1}{N_\ell} \sum_{i=1}^{N_\ell} \phi(\theta_j, Q_{M_\ell}^i) - \phi(\theta_j, Q_{M_{\ell-1}}^i) \right]_{1 \leq j \leq n}, \quad (7.3)$$

with  $\phi(\cdot, Q_{M_{-1}}) \equiv 0$ .

The extension of this collection of pointwise estimators by means of interpolation leads to the MLMC estimator for the function  $\Phi$  on  $\Theta$ . Here we use

$$P_\Phi^{\text{MLMC}} := \mathcal{S}_n(\bar{\Phi}^{\text{MLMC}}(\theta)) \quad (7.4)$$

where  $\mathcal{S}_n$  denotes a spline interpolation operator of degree  $k$ . Different options are possible, as discussed in [KN17].

Observe that in (7.3) the evaluations  $\{Q_{M_\ell}^i\}$ , which involve heavy computational models, in general are the same for all the evaluation points  $\theta_j$ ,  $j = 1, \dots, n$ .

The accuracy of the spline interpolation operator  $\mathcal{S}_n$  depends on the regularity of the function  $\Phi$ . In this work we employ cubic splines ( $k = 3$ ). Hence we can rely on the following lemma [DBDBM<sup>+</sup>78] [QSS10]:

**Lemma 1** (Cubic spline interpolation operator). *The sequence of cubic spline interpolation operators  $\mathcal{S}_n: \mathbb{R}^n \rightarrow L^\infty(\Theta)$  based on the set of nodes  $\theta \in \Theta^n$  and function evaluations  $f(\theta) \in \mathbb{R}^n$ , satisfies*

$$(a) \quad \|f - \mathcal{S}_n(f(\theta))\|_{L^\infty(\Theta)} \leq c_1 \|f^{(4)}\|_{L^\infty(\Theta)} n^{-4} \text{ for any } f \in C^4(\Theta),$$

$$(b) \quad \|\mathcal{S}_n(\theta)\|_{L^\infty(\Theta)} \leq c_2 \|\theta\|_{\ell^\infty} \text{ for any } \theta \in \mathbb{R}^n,$$

for all  $n \in \mathbb{N}$ . The constants  $c_1, c_2 > 0$  are independent of  $n$ .

As in the previous chapters, we quantify the error of the MLMC estimator through the mean square error (MSE). However, in this case, we are approximating a whole function  $\phi(\theta)$ , hence an appropriate function norm is necessary. A natural choice is the  $L^\infty(\Theta)$  norm, so that the MSE reads:

$$\text{MSE}(P_\Phi^{\text{MLMC}}) := \mathbb{E} \left( \|P_\Phi^{\text{MLMC}} - \Phi\|_{L^\infty(\Theta)}^2 \right). \quad (7.5)$$

The MSE can be decomposed in two main contributions:

$$\begin{aligned} \text{MSE}(P_\Phi^{\text{MLMC}}) &\equiv \mathbb{E} \left( \|\Phi - \mathcal{S}_n(\Phi(\theta)) + \mathcal{S}_n(\Phi(\theta) - \bar{\Phi}^{\text{MLMC}}(\theta))\|_{L^\infty(\Theta)}^2 \right) \\ &\leq 2 \left( \|\Phi - \mathcal{S}_n(\Phi(\theta))\|_{L^\infty(\Theta)}^2 + \mathbb{E} \left( \|\mathcal{S}_n(\Phi(\theta) - \bar{\Phi}^{\text{MLMC}}(\theta))\|_{L^\infty(\Theta)}^2 \right) \right). \end{aligned} \quad (7.6)$$

## Chapter 7. MLMC for Distributions and Risk Measures

The first term on the right hand side,  $\|\Phi - \mathcal{S}_n(\Phi(\theta))\|_{L^\infty(\Theta)}^2$  is the interpolation error introduced by the spline operator, while  $\mathbb{E}\left(\|\mathcal{S}_n(\Phi(\theta)) - \bar{\Phi}^{\text{MLMC}}(\theta)\|_{L^\infty(\Theta)}^2\right)$  is the MLMC error contribution, in this specific case, defined for the pointwise estimator  $\bar{\Phi}^{\text{MLMC}}(\theta)$ .

We can further decompose the MSE into bias and statistical error (variance of the estimator) contributions:

$$\begin{aligned} \text{MSE}(\mathbb{P}_\Phi^{\text{MLMC}}) &\leq 2\left(\|\Phi - \mathcal{S}_n(\Phi(\theta))\|_{L^\infty(\Theta)}^2 + c_2^2 \mathbb{E}\left(\|\Phi(\theta) - \bar{\Phi}^{\text{MLMC}}(\theta)\|_{\ell^\infty}^2\right)\right) \\ &\leq 2\left(\|\Phi - \mathcal{S}_n(\Phi(\theta))\|_{L^\infty(\Theta)}^2 + 2c_2^2 \|\Phi(\theta) - \mathbb{E}(\bar{\Phi}^{\text{MLMC}}(\theta))\|_{\ell^\infty}^2 + 2c_2^2 \text{Var}(\bar{\Phi}^{\text{MLMC}}(\theta))\right), \end{aligned} \quad (7.7)$$

where we denote by  $\text{Var}(X)$  with  $X \in \mathbb{R}^n$  a random vector, the quantity:

$$\text{Var}(X) := \mathbb{E}\left[\|X - \mathbb{E}[X]\|_{L^\infty(\Theta)}^2\right] = \mathbb{E}\left[\max_{k=1,\dots,n} (X_k - \mathbb{E}[X_k])^2\right] \quad (7.8)$$

The complexity result for the MLMC estimator  $\mathbb{P}_\Phi^{\text{MLMC}}$  for parametric expectations follows by similar arguments as the ones used in the standard MLMC result (see Chapter 4). The main differences to the standard MLMC complexity result are the notion of bias and statistical error and the interpolation error contribution introduced by the spline operator:

$$\mathbf{I} = \|\Phi - \mathcal{S}_n(\Phi(\theta))\|_{L^\infty(\Theta)}. \quad (7.9)$$

The bias term can be finally bounded by:

$$\mathbf{B} = \|\Phi(\theta) - \mathbb{E}(\bar{\Phi}^{\text{MLMC}}(\theta))\|_{\ell^\infty} = \max_{1 \leq j \leq n} |\mathbb{E}(\phi(\theta_j, Q) - \phi(\theta_j, Q_{M_L}))| \leq \sup_{\vartheta \in \Theta} |\mathbb{E}(\phi(\vartheta, Q) - \phi(\vartheta, Q_{M_L}))|. \quad (7.10)$$

On the other hand, the statistical error (variance of the estimator) term, can be bounded as follows (see [KN17]):

$$\begin{aligned} \mathbf{SE} = \text{Var}(\bar{\Phi}^{\text{MLMC}}(\theta)) &\leq c \ln(n) \sum_{\ell=0}^L \frac{\text{Var}(\phi(\theta, Q_{M_\ell}) - \phi(\theta, Q_{M_{\ell-1}}))}{N_\ell} \\ &\leq c \ln(n) \sum_{\ell=0}^L \frac{\mathbb{E}\left(\sup_{\vartheta \in \Theta} |\phi(\vartheta, Q_{M_\ell}) - \phi(\vartheta, Q_{M_{\ell-1}})|^2\right)}{N_\ell} \end{aligned} \quad (7.11)$$

We consider now the following proposition.

**Proposition 7.1.1.** *Suppose there exist constants  $\alpha, \beta, \gamma > 0$  such that  $2\alpha \geq \min(\beta, \gamma)$  and:*

(a) *the bias decays with order  $\alpha > 0$ , meaning that*



## 7.1. Multi Level Monte Carlo approximation of parametric expectations

---

$$\sup_{\vartheta \in \Theta} |\mathbb{E}(\phi(\vartheta, Q) - \phi(\vartheta, Q_{M_\ell}))| \leq c_\alpha M_\ell^{-\alpha},$$

(b) the variance of the differences decays with order  $\beta > 0$ , meaning that

$$\mathbb{E}\left(\sup_{\vartheta \in \Theta} |\phi(\vartheta, Q_{M_\ell}) - \phi(\vartheta, Q_{M_{\ell-1}})|^2\right) \leq c_\beta M_\ell^{-\beta},$$

(c) the cost to compute each i.i.d. realization of  $Q_{M_\ell}$  is bounded by

$$\text{cost}(Q_{M_\ell}) \leq c_\gamma M_\ell^\gamma \text{ for some constants } c_\gamma, \gamma > 0.$$

(d) given  $Q_{M_\ell}$ , the cost to evaluate  $\phi(\vartheta, Q_{M_\ell})$  is negligible w.r.t. the cost of evaluating  $Q_{M_\ell}$

for all  $\ell \in \mathbb{N}_0$  with positive constants  $c_\alpha, c_\beta, c_\gamma$  independent of  $\ell$ .

Following Lemma 1, then for any  $\varepsilon > 0$  there exists an optimal number of levels  $L$ , and sample sizes  $\{N_\ell\}_{\ell=0}^L$  such that the MLMC estimator  $\mathbb{P}_\Phi^{\text{MLMC}}$  satisfies

$$\mathbb{E}\left(\|\mathbb{P}_\Phi^{\text{MLMC}} - \Phi\|_{L^\infty(\Theta)}^2\right) = \mathcal{O}(\varepsilon^2) \tag{7.12}$$

at a computational cost that is bounded by

$$\mathbf{C}(\mathbb{P}_\Phi^{\text{MLMC}}) \lesssim \ln(\varepsilon^{-1}) \begin{cases} \varepsilon^{-2} \ln(\varepsilon^{-1})^2, & \text{if } \beta = \gamma, \\ \varepsilon^{-\left(2 + \frac{\gamma - \beta}{\alpha}\right)}, & \text{if } \beta < \gamma, \\ \varepsilon^{-2}, & \text{if } \beta > \gamma. \end{cases} \tag{7.13}$$

Notice that this complexity results is only slightly worse ( $\ln(\varepsilon^{-1})$  factor) than the complexity result for  $\mathbb{E}[Q]$  stated in Chapter 4.

A practical methodology to compute the optimal number of levels  $L$ , and sample sizes  $\{N_\ell\}_{\ell=0}^L$  is presented in the following section. For the sake of completeness, it is important to mention that in this work we assume that the cost to generate a sample on the coarsest level is not dominated by the cost for evaluating  $\phi$  (valid assumption in problems that require the solution of a computational intensive model as those treated in this thesis), otherwise a slightly modified version of the methodology should be used; see [KN17].

### 7.1.1 Practical aspects: computation of the MSE and optimal hierarchy

A robust and practical implementation of a MLMC estimator for the computation of a parametric expectation, should also provide an estimation of the associated bias and variance terms of the MSE needed to assess that the prescribed tolerance has been met and to optimize the hierarchy to achieve optimal complexity. We detail here a practical procedure for the MSE estimation.

In absence of theoretical estimates for the rates and constants that characterize the bias and variance decays as well as the cost model for the problem under investigation, we can apply also in this framework the *screening* procedure presented in the previous Chapters that uses a

fixed sample size  $\bar{N}$  over  $\bar{L}$  levels. Once the rates and constants are estimated by the *screening* procedure, the pivotal step for achieving the theoretical complexity of the MLMC method subject to a prescribed mean squared error tolerance, is the choice of both the number of levels  $L$  and the sample sizes  $N_\ell$   $0 \leq \ell \leq L$ .

To determine these parameters a precise estimation of the mean squared error (MSE) contributions is crucial. As presented above, the MSE for the MLMC estimator  $P_\Phi^{\text{MLMC}}$  include three contributions:

$$\text{MSE}(P_\Phi^{\text{MLMC}}) \lesssim 2\mathbf{I}^2 + 4c_2^2\mathbf{B}^2 + 4c_2^2\mathbf{SE}. \quad (7.14)$$

Thanks to the properties of the cubic spline interpolation operator  $\mathcal{S}_n$ , it follows from Lemma 1(a) that the interpolation error can be bounded by (see [QSS10]):

$$\mathbf{I} \leq c_1 n^{-4} \|\Phi^{(4)}\|_{L^\infty(\Theta)}, \quad c_1 = \frac{5}{384} \quad \text{if } \Phi \in C^4(\Theta). \quad (7.15)$$

As stated above, in this work we assume that the cost to generate a sample on the coarsest level is not dominated by the cost for evaluating  $\phi$ . Based on this assumption, we are free to choose a number of nodes  $n$  in the uniform grid for the construction of the pointwise MLMC estimator  $\bar{\Phi}^{\text{MLMC}}(\theta)$  to overkill the interpolation error without effectively affecting the computational cost. We will also have the benefit of a nicer visualization of the estimated function. For this reason we don't consider anymore the contribution of  $\mathbf{I}$  in the subsequent analysis.

To achieve a prescribed mean squared error of  $\varepsilon^2$ , we thus require

$$\mathbf{B} \leq 0.5\sqrt{1-\theta}\varepsilon, \quad (7.16a)$$

$$\mathbf{SE} \leq 0.25\theta\varepsilon^2, \quad (7.16b)$$

where we have additionally introduced a splitting parameter  $\theta \in (0, 1)$  to offer the possibility of weighting the two MSE contributions differently.

Concerning the bias term, the same considerations made in the previous chapters hold here as well. Since the MLMC estimator already uses a sequence of discretizations, a natural way to estimate the bias is:

$$\mathbf{B} \approx \max_{1 \leq j \leq n} \left| \mathbb{E} \left( \phi(\theta_j, Q_{M_{L-1}}) - \phi(\theta_j, Q_{M_L}) \right) \right|. \quad (7.17)$$

We can then define the bias estimate on all levels as:

$$\hat{B}_\ell = \begin{cases} \max_{1 \leq j \leq n} \left| \mathbb{E} \left( \phi(\theta_j, Q_{M_{\ell-1}}) - \phi(\theta_j, Q_{M_\ell}) \right) \right|, & \text{if } \ell \leq \bar{L}, \\ c_\alpha M_\ell^{-\alpha}, & \text{if } \ell > \bar{L}. \end{cases} \quad (7.18)$$

## 7.1. Multi Level Monte Carlo approximation of parametric expectations

---

where we use estimate 7.17 on those levels for which simulations have been run during the screening procedure or a C-MLMC iterative loop ( $\ell \leq \bar{L}$ ). On levels  $\ell$  for which no sample exists yet (for  $\ell > \bar{L}$ ), we extrapolate using the model in Proposition 7.1.1(a), with fitted parameters  $c_\alpha, \alpha$ .

With the same spirit we denote the cost of computing one MLMC sample on level  $\ell$  as:

$$\hat{C}_\ell = \begin{cases} \text{cost}(Q_{M_\ell}), & \text{if } \ell \leq \bar{L}, \\ c_\gamma M_\ell^\gamma, & \text{if } \ell > \bar{L}. \end{cases} \quad (7.19)$$

Finally, the bias constraint (7.16a) is satisfied for  $L \in \mathbb{N}$  such that:

$$M_L = \underset{\substack{M_\ell \in \{M_0, \dots, M_{LMAX}\} \\ \text{s.t. } \hat{B}_\ell \leq 0.5\sqrt{1-\theta}\varepsilon}}{\text{argmin}} \hat{C}_\ell \quad (7.20)$$

On the other hand, the statistical error **SE** is approximated by

$$\mathbf{SE} \approx \ln(n) \sum_{\ell=0}^L \frac{\mathbb{E} \left( \max_{1 \leq j \leq n} \left| \phi(\theta_j, Q_{M_{\ell-1}}) - \phi(\theta_j, Q_{M_\ell}) \right|^2 \right)}{N_\ell} \approx \ln(n) \sum_{\ell=0}^L \frac{\hat{V}_{\ell, \theta}}{N_\ell}. \quad (7.21)$$

Here,  $\hat{V}_{\ell, \theta}$  corresponds to the Monte Carlo level sampled second moment  $S_{\ell, \theta}^{2, \text{MC}}$  for  $\max_{1 \leq j \leq n} \left| \phi(\theta_j, Q_{M_{\ell-1}}) - \phi(\theta_j, Q_{M_\ell}) \right|$  on those levels  $\ell$  for which simulations have been run during the screening procedure ( $\ell \leq \bar{L}$ ). On the other hand, on levels  $\ell$  for which no sample exists yet (i.e. for  $\ell > \bar{L}$ ), we extrapolate a fitted model by assuming that  $\hat{V}_{\ell, \theta} \approx c_\beta M_\ell^{-\beta}$  (following Proposition 7.1.1(b)). That is, we use the approximation

$$\hat{V}_{\ell, \theta} = \begin{cases} S_{\ell, \theta}^{2, \text{MC}}, & \text{if } \ell \leq \bar{L}, \\ c_\beta M_\ell^{-\beta}, & \text{if } \ell > \bar{L}. \end{cases} \quad (7.22)$$

Thanks to Proposition 1(a) and (7.16b) we obtain that the statistical error constraint is satisfied with optimal complexity by selecting the sample size  $N_\ell \in \mathbb{N}$  on level  $\ell$  as

$$N_\ell = \left\lceil \frac{1}{\theta \varepsilon^2} \ln \left( \varepsilon^{-\frac{1}{4}} \right) \sqrt{\frac{\hat{V}_{\ell, \theta}}{\hat{C}_\ell} \sum_{k=0}^L \sqrt{\hat{C}_k \hat{V}_{k, \theta}}} \right\rceil, \quad \ell = 0, 1, \dots, L. \quad (7.23)$$

## 7.2 Multi Level Monte Carlo approximation of derivatives

As we will see hereafter, it is often advantageous to construct a MLMC estimator  $\mathbb{P}_\Phi^{\text{MLMC}}$  that does not only have a uniform MSE of order  $\mathcal{O}(\varepsilon^2)$ , but whose first  $m$  derivatives are also accurate with the same uniform MSE order.

In order to characterize the accuracy in approximating derivatives, we recall additional properties of the spline interpolation operator [QSS10].

**Lemma 2** (Derivatives of the spline interpolation operator). *For  $m \in \mathbb{N}_0$ ,  $m < 4$ , the sequence of cubic spline interpolation operators  $\mathcal{S}_n: \mathbb{R}^n \rightarrow C^m(\Theta)$  based on the set of nodes  $\theta \in \Theta^n$  and function evaluations  $f(\theta) \in \mathbb{R}^n$ , satisfies*

$$(a) \quad \left\| f^{(m)} - \frac{d^m}{d\vartheta^m} \mathcal{S}_n(f(\theta)) \right\|_{L^\infty(\Theta)} \leq c_4 \|f^{(4)}\|_{L^\infty(\Theta)} n^{-(4-m)} \quad \text{for any } f \in C^4(\Theta),$$

$$(b) \quad \left\| \frac{d^m}{d\vartheta^m} \mathcal{S}_n(\theta) \right\|_{L^\infty(\Theta)} \leq c_5 n^m \|\mathcal{S}_n(\theta)\|_{L^\infty(\Theta)} \quad \text{for any } \theta \in \mathbb{R}^n.$$

Here, the constants  $c_4, c_5 > 0$  are independent of  $n$  but may depend on  $m$ .

As in the previous section, we quantify the error of the MLMC estimator through the mean squared error (MSE), which can be decomposed as follows:

$$\begin{aligned} \text{MSE} \left( \frac{d^m}{d\vartheta^m} \mathbb{P}_\Phi^{\text{MLMC}} \right) &:= \mathbb{E} \left( \left\| \Phi^{(m)} - \frac{d^m}{d\vartheta^m} \mathbb{P}_\Phi^{\text{MLMC}} \right\|_{L^\infty(\Theta)}^2 \right) \\ &\leq 2 \left( \left\| \Phi^{(m)} - \frac{d^m}{d\vartheta^m} \mathcal{S}_n(\Phi(\theta)) \right\|_{L^\infty(\Theta)}^2 + 2 \mathbb{E} \left( \left\| \frac{d^m}{d\vartheta^m} \mathcal{S}_n(\Phi(\theta)) - \bar{\Phi}^{\text{MLMC}}(\theta) \right\|_{L^\infty(\Theta)}^2 \right) \right) \end{aligned} \quad (7.24)$$

Also in this case we identify the interpolation error introduced by the spline operator, and the MLMC error contribution, defined for the pointwise estimator  $\bar{\Phi}^{\text{MLMC}}(\theta)$  on the right hand side of (7.24). Thanks to Lemma 2(b) we can further manipulate the second term to obtain:

$$\text{MSE}(\mathbb{P}_\Phi^{\text{MLMC}}) \leq 2 \left( \left\| \Phi^{(m)} - \frac{d^m}{d\vartheta^m} \mathcal{S}_n(\Phi(\theta)) \right\|_{L^\infty(\Theta)}^2 + 2c_5^2 c_2^2 n^{2m} \mathbb{E} \left( \|\Phi(\theta) - \bar{\Phi}^{\text{MLMC}}(\theta)\|_{\ell^\infty}^2 \right) \right). \quad (7.25)$$

By further decomposing the MLMC error into bias and statistical error (variance of the estimator) contributions, using the arguments presented in the previous section we finally get:

$$\begin{aligned} \text{MSE}(\mathbb{P}_\Phi^{\text{MLMC}}) &\leq 2 \left( \left\| \Phi^{(m)} - \frac{d^m}{d\vartheta^m} \mathcal{S}_n(\Phi(\theta)) \right\|_{L^\infty(\Theta)}^2 \right. \\ &\quad \left. + 2c_5^2 c_2^2 n^{2m} \|\Phi(\theta) - \mathbb{E}(\bar{\Phi}^{\text{MLMC}}(\theta))\|_{\ell^\infty}^2 + 2c_5^2 c_2^2 n^{2m} \text{Var}(\bar{\Phi}^{\text{MLMC}}(\theta)) \right). \end{aligned} \quad (7.26)$$

## 7.2. Multi Level Monte Carlo approximation of derivatives

The interpolation error contribution introduced by the spline interpolation operator is now defined as:

$$\mathbf{I}_m = \left\| \Phi^{(m)} - \frac{d^m}{d\vartheta^m} \mathcal{S}_n(\Phi(\vartheta)) \right\|_{L^\infty(\Theta)}^2. \quad (7.27)$$

The bias  $\mathbf{B}$  and statistical errors  $\mathbf{SE}$  have exactly the same definition as in (7.10) and (7.11) but now they are multiplied by  $n^{2m} c_5^2$ .

Concerning the complexity of the algorithm we state the result from [KN17]:

**Proposition 7.2.1.** *Let  $m \in \mathbb{N}$ ,  $m < 4$  and  $\phi(\vartheta, Q)$  and  $\Phi(\vartheta) = \mathbb{E}[\phi(\vartheta, Q)]$  satisfy the assumptions of Proposition 7.1.1, with  $\phi \in C^4(\Theta)$ , then for any  $\varepsilon > 0$  there exist an optimal number of levels  $L$  and optimal sample sizes  $\{N_\ell\}_{\ell=0}^L$  such that the MLMC estimator  $\mathbb{P}_\Phi^{\text{MLMC}}$  satisfies*

$$\mathbb{E} \left( \left\| \Phi^{(m)} - \frac{d^m}{d\vartheta^m} \mathbb{P}_\Phi^{\text{MLMC}} \right\|_{L^\infty(\Theta)}^2 \right) = \mathcal{O}(\varepsilon^2) \quad (7.28)$$

and the corresponding computational cost results in

$$\mathbf{C} \left( \frac{d^m}{d\vartheta^m} \mathbb{P}_\Phi^{\text{MLMC}} \right) \lesssim \ln(\varepsilon^{-1}) \begin{cases} \varepsilon^{-2\frac{4}{4-m}} \ln(\varepsilon^{-1})^2, & \text{if } \beta = \gamma, \\ \varepsilon^{-(2+\frac{\gamma-\beta}{\alpha})\frac{4}{4-m}}, & \text{if } \beta < \gamma, \\ \varepsilon^{-2\frac{4}{4-m}}, & \text{if } \beta > \gamma. \end{cases} \quad (7.29)$$

It can be easily verified that for  $m = 0$  we recover the results obtained in the previous section.

### 7.2.1 Practical aspects: computation of the MSE and optimal hierarchy

Under these slightly strengthened assumptions, and following exactly the same procedure presented in Section 7.1.1 we can build a MLMC estimator  $\mathbb{P}_\Phi^{\text{MLMC}}$  that does not only have a uniform MSE of order  $\mathcal{O}(\varepsilon^2)$ , but whose first  $m$  derivatives are also accurate with the same uniform MSE.

As presented above, the MSE for the MLMC estimator  $\mathbb{P}_\Phi^{\text{MLMC}}$  include three contributions:

$$\text{MSE}(\mathbb{P}_\Phi^{\text{MLMC}}) \lesssim 2\mathbf{I}_m^2 + 4c_5^2 c_2^2 n^{2m} \mathbf{B}^2 + 4c_5^2 c_2^2 n^{2m} \mathbf{SE}, \quad (7.30)$$

Thanks to the properties of the derivatives of the spline operator  $\mathcal{S}_n$ , it follows from Lemma 2(a) that the interpolation error can be bounded by:

$$\mathbf{I}_m = c_4 n^{-(4-m)} \|\Phi^{(4)}\|_{L^\infty(\Theta)}, \quad \text{if } \Phi \in C^4(\Theta), \quad \text{with} \quad \begin{cases} c_4 = \frac{1}{24} & \text{if } m = 1 \\ c_4 = \frac{3}{8} & \text{if } m = 2 \end{cases} \quad (7.31)$$

We choose also here a large number of nodes  $n$  in the uniform grid, for the construction of the pointwise MLMC estimator  $\bar{\Phi}^{\text{MLMC}}(\theta)$ , to overkill the interpolation error without effectively affecting the computational cost. Also in this setup we do not consider anymore the contribution of  $I_m$  in the subsequent analysis.

The MSE reduces to:

$$\text{MSE}(\mathbb{P}_{\Phi}^{\text{MLMC}}) \lesssim 4c_5^2 c_2^2 n_o^{2m} \mathbf{B}^2 + 4c_5^2 c_2^2 n_o^{2m} \mathbf{SE}, \quad (7.32)$$

where we denote with  $n_o = c_4 \|\phi^{(4)}\|_{L^\infty(\Theta)} \lceil \varepsilon^{-\frac{1}{4-m}} \rceil$  the minimum number of nodes in the uniform grid required to achieve the prescribed tolerance requirement (see Lemma 2(a)).

Hence, to achieve a prescribed mean squared error of  $\varepsilon^2$ , we require now

$$\mathbf{B} \leq 0.5 \sqrt{1-\theta} \frac{\varepsilon}{n_o^m}, \quad (7.33a)$$

$$\mathbf{SE} \leq 0.25 \theta \frac{\varepsilon^2}{n_o^{2m}}, \quad (7.33b)$$

Concerning the bias term, the same considerations made in the previous section holds here as well, hence we get:

$$M_L = \underset{\substack{M_\ell \in [M_0, \dots, M_{LMAX}] \\ \text{s.t. } \hat{B}_\ell \leq 0.5 \sqrt{1-\theta} \frac{\varepsilon}{n_o^m}}}{\text{argmin}} \hat{C}_\ell, \quad (7.34)$$

where  $\hat{C}_\ell$  denotes the cost of computing one MLMC sample on level  $\ell$  (see 7.19).

On the other hand, the statistical error  $\mathbf{SE}$  constrain is satisfied with optimal complexity by selecting the sample size  $N_\ell \in \mathbb{N}$  on level  $\ell$  as

$$N_\ell = \left\lceil \frac{n_o^{2m}}{\theta \varepsilon^2} \ln(\varepsilon^{-\frac{1}{4-m}}) \sqrt{\frac{\hat{V}_{\ell, \theta}}{\hat{C}_\ell}} \sum_{k=0}^L \sqrt{\hat{C}_k \hat{V}_{k, \theta}} \right\rceil, \quad \ell = 0, 1, \dots, L. \quad (7.35)$$

### 7.3 MLMC estimators for Distributions and Risk Functions

In this section we present different MLMC estimators based on parametric expectations that can be employed to compute QoI distributions and risk measures using the procedures introduced in the previous sections. The only practical difference in the following MLMC estimator is the function  $\phi$  considered during the computation.

### 7.3.1 MLMC estimator for the Cumulative Distribution Function

One of the most commonly used ways to characterize the distribution of a random variable  $Q$  is via its cumulative distribution function (CDF).

**Definition 13.** *The **cumulative distribution function** (CDF)  $F_Q : \mathbb{R} \rightarrow [0, 1]$  of a random variable  $Q$ , is the function that gives the probability that  $Q$  will take a value less than or equal to  $\vartheta$ :*

$$F_Q(\vartheta) = \mathbb{P}(Q \leq \vartheta) = \int_{-\infty}^{\vartheta} f_Q(x) dx \quad (7.36)$$

where  $f_Q$  denotes the probability density function (PDF) of  $Q$ .

The CDF of  $Q$  can be written as a parametric expectation in the form:

$$F_Q(\vartheta) = \mathbb{E}(\mathbb{1}_{Q \leq \vartheta}) \quad (7.37)$$

where  $I$  denotes the indicator function that it is equal to 1 when  $Q \leq \vartheta$ , and zero otherwise.

Even if the CDF of a random variable  $Q$  can be explicitly expressed as a parametric expectation, it has been underlined in [KN17] and [GNR15], that the direct MLMC approximation of  $F_Q$  is inefficient (rates  $\alpha$  and  $\beta$  in Proposition 7.1.1 may deteriorate) due to the discontinuity introduced by the indicator function. An effective approach to overcome this difficulty introduced in [KN17] seeks at finding an appropriate function  $G_Q : \Theta \rightarrow \mathbb{R}$  such that  $G'_Q = F_Q$ . One candidate that satisfy this requirement is:

$$G_Q(\vartheta) = \mathbb{E}(\phi(Q - \vartheta)), \quad \text{with } \phi(z) = |z|I(z \leq 0). \quad (7.38)$$

By doing so we obtain a function  $\phi$  that is Lipschitz continuous and  $G_Q$  is even more regular than the actual CDF  $F_Q$ . In order to accurately compute the CDF up to a prescribed tolerance we are now required to follow the procedure presented in section 7.2. Practically, we first construct a MLMC approximation  $P_G^{\text{MLMC}}$  for the function  $G_Q(\vartheta)$  using the procedure presented in Section 7.2.1 such that also  $F_Q = G'_Q$  is accurately approximated up to a prescribed tolerance requirement.

Following this procedure, one could also obtain a MLMC estimator of the PDF  $f_Q$  by also requiring an accurate estimation of the second derivative  $m = 2$  in section 7.2.

### 7.3.2 MLMC estimator for the Characteristic function

The characteristic function is another convenient and elegant tool to characterize the distribution of the random variables.

**Definition 14.** *The **characteristic function**  $\varphi_Q(\vartheta) : \mathbb{R} \rightarrow \mathbb{C}$  of a random variable  $Q$  is defined*

as:

$$\varphi_Q(\vartheta) = \int_{\mathbb{R}} e^{i\vartheta x} dF_Q(x) = \int_{\mathbb{R}} e^{i\vartheta x} f_Q(x) dx \quad (7.39)$$

where  $i$  is the imaginary unit,  $F_Q$  is the cumulative distribution function of  $Q$ ,  $f_Q$  is the probability density function (PDF) of  $Q$  and the first integral in (7.39) is a generalization of the Riemann integral known as Riemann–Stieltjes integral.

The characteristic function of a distribution always exists, even when the probability density function or moment-generating function do not. If the random variable  $Q$  admits a probability density function  $f_Q$ , then the characteristic function is the Fourier transform of the probability density function.

It follows from the definition above that the characteristic function can be written as a parametric expectation:

$$\varphi_Q(\vartheta) = \mathbb{E}(e^{i\vartheta Q}). \quad (7.40)$$

In order to avoid the treatment of complex-valued functions in our MLMC formulation, we employ Euler's formula and get:

$$\varphi_Q(\vartheta) = \mathbb{E}(\cos(\vartheta Q)) + i\mathbb{E}(\sin(\vartheta Q)) = \Phi_1(\vartheta) + i\Phi_2(\vartheta). \quad (7.41)$$

Following the definition of parametric expectation (7.1),  $\Phi_r(\vartheta) := \mathbb{E}(\phi_r(\vartheta, Q))$ ,  $r = 1, 2$  with  $\phi_1(\vartheta, Q) = \cos(\vartheta Q)$ ,  $\phi_2(\vartheta, Q) = \sin(\vartheta, Q)$ .

We can now write a MLMC estimator  $P_\varphi^{\text{MLMC}}$  for the characteristic function  $\varphi_Q(\vartheta)$  on a set  $\Theta \subset \mathbb{R}$  using the methodology presented in the section 7.1 by simultaneously constructing two multilevel Monte Carlo approximations  $P_{\Phi_1}^{\text{MLMC}}$  and  $P_{\Phi_2}^{\text{MLMC}}$  for the real part  $\Phi_1$  and imaginary part  $\Phi_2$ :

$$P_\varphi^{\text{MLMC}} = P_{\Phi_1}^{\text{MLMC}} + iP_{\Phi_2}^{\text{MLMC}}. \quad (7.42)$$

It is worth underlining that the two MLMC estimators for  $\Phi_1$  and  $\Phi_2$  are built using the same samples so that the computational overload of approximating two functions simultaneously is negligible.

### 7.3.3 MLMC estimator for the simultaneous computation of VaR, CVar and CDF

In addition to characterize a random variable's distribution from its CDF or its characteristic function, many decision making process under uncertainty require the knowledge and the accurate computation of quantiles (or VaR).

**Definition 15.** *Quantiles* (also known as value at risk, VaR) are cutpoints dividing the range of



### 7.3. MLMC estimators for Distributions and Risk Functions

a probability distribution. The  $\alpha$ -quantile  $q_\alpha$  is given by:

$$q_\alpha = VaR_\alpha = F_Q^{-1}(\alpha) \equiv \inf\{\vartheta \in \mathbb{R} : F_Q(\vartheta) \geq \alpha\} \quad \alpha \in (0, 1). \quad (7.43)$$

The conditional value at risk (CVaR, also known as excess loss, mean shortfall, tail VaR, average value at risk or expected shortfall) is another well known risk indicator employed in many financial and scientific applications, introduced by Rockafellar [RU02] as an extension of VaR.

**Definition 16.** *CVaR is a risk measure defined as the mean of the so called generalized  $\alpha$ -tail distribution:*

$$CVaR_\alpha = \int_{-\infty}^{\infty} z dF_Q^\alpha(z), \quad F_Q^\alpha = \begin{cases} 0, & \text{if } z < VaR_\alpha(Q) \\ \frac{F_Q(z) - \alpha}{1 - \alpha}, & \text{if } z \geq VaR_\alpha(Q) \end{cases} \quad \alpha \in (0, 1). \quad (7.44)$$

The following procedure, which is taken from [KN17], enables a simultaneous approximation of the CDF, VaR and CVaR with an accuracy of order  $\varepsilon$ .

Following a similar argument used for the definition of the MLMC estimator for the CDF, we can consider now a function  $H_Q : \Theta \rightarrow \mathbb{R}$  with  $\tau \in (0, 1)$ :

$$H_Q(\vartheta) = \mathbb{E}(\phi(\vartheta, Q)), \quad \text{with} \quad \phi(\vartheta, Q) = \vartheta + \frac{1}{1 - \tau}(Q - \vartheta)^+. \quad (7.45)$$

where  $(Q - \vartheta)^+$  denotes the positive part, i.e.  $(Q - \vartheta)^+ = Q - \vartheta$  if  $Q \geq \vartheta$  and  $(Q - \vartheta)^+ = 0$  if  $Q < \vartheta$ . Following the procedure presented in section 7.2.1 with  $m = 1$ , we obtain a MLMC estimator  $P_H^{\text{MLMC}}(\vartheta)$  for the function  $H_Q(\vartheta)$  and its derivatives with a uniform MSE of order  $\varepsilon^2$ .

In fact considering (7.45) offers the various beneficial proprieties that can be used to estimate the VaR, CVaR and CDF of  $Q$  through the following post-processing procedure.

1. The CDF of  $Q$  can be expressed as,  $F_Q(\vartheta) = (1 - \tau)H_Q'(\vartheta) + \tau$  and accurately approximated by computing the derivative of  $P_H^{\text{MLMC}}$ :

$$F_Q(\vartheta) \approx (1 - \tau) \frac{d}{d\vartheta} P_H^{\text{MLMC}}(\vartheta) + \tau. \quad (7.46)$$

2. If there exists a unique  $\tau$ -quantile  $q_\tau$ , then  $H_Q(\theta)$  is strictly convex;
3. The  $\tau$ -quantile  $q_\tau$  ( $VaR_\tau$ ) is available via minimization of  $P_H^{\text{MLMC}}(\vartheta)$ :

$$q_\tau := \underset{\vartheta \in \mathbb{R}}{\operatorname{argmin}} H_Q(\vartheta) \approx \underset{\vartheta \in \Theta}{\operatorname{argmin}} P_H^{\text{MLMC}}(\vartheta) \quad (7.47)$$

4. The approximation of  $CVaR_\tau$  on the other hand can be computed as [RU02]:

$$CVaR_\tau := \min_{\vartheta \in \mathbb{R}} H_Q(\vartheta) \approx \min_{\vartheta \in \Theta} P_H^{\text{MLMC}}(\vartheta) \quad (7.48)$$

Consequently, a simultaneous estimation of these quantities is possible, once an MLMC estimator  $P_H^{\text{MLMC}}(\vartheta)$  of  $H_Q(\vartheta)$  is accessible.

Following the analysis in [KN17] it can be proved that once we tune the MLMC algorithm in order to achieve an uniform approximation of  $H'_Q(\vartheta)$  with tolerance  $\varepsilon$ , we also obtain an approximation of the CDF  $q_\tau$  and  $CVaR_\tau$  that fulfill an accuracy of order  $\varepsilon$ .

## 7.4 Numerical Experiments

### 7.4.1 Stochastic differential equation model: a financial option

Let us consider, as in the previous Chapter 6.5.1, the stochastic differential equation (SDE) of a financial call option with the asset price modeled as a Geometric Brownian motion:

$$dS = rS dt + \sigma S dW, \quad S(0) = S_0. \quad (7.49)$$

Here,  $r$ ,  $\sigma$ , and  $S_0$  are given positive numbers. For this asset we are interested in quantifying the uncertainties in the "discounted payoff", so that we set the quantity of interest  $Q$  as

$$Q := e^{-rT} \max(S(T) - K, 0), \quad (7.50)$$

where  $K > 0$  denotes the agreed strike price and  $T > 0$  the pre-defined expiration date. Due to the fact that the solution to (6.16) at time  $T$ , i.e.  $S(T)$ , is a log-normally distributed random variable with mean  $S_0 e^{rT}$  and variance  $S_0^2 e^{2rT} (e^{\sigma^2 T} - 1)$ , it is straightforward to write explicitly the cumulative distribution function (CDF) of  $Q$  as:

$$F_Q(q) = \begin{cases} \frac{1}{2} + \frac{1}{2} \operatorname{erf}\left(\frac{\sqrt{2}(\sigma^2 T - 2rT + 2\ln(K + e^{rT}q)) - 2\ln(S_0)}{4\sigma\sqrt{T}}\right), & q \geq 0, \\ 0, & q < 0, \end{cases} \quad (7.51)$$

with  $\operatorname{erf}(z) = \frac{2}{\sqrt{\pi}} \int_0^z e^{-s^2} ds$ . Using this CDF formula, it is straightforward to compute highly accurate reference values to scrutinize the numerical tests that follow. For example, Table 7.1 lists various quantiles and conditional values at risk of  $Q$  corresponding to the parameter values  $r = \frac{1}{20}$ ,  $\sigma = \frac{1}{5}$ ,  $T = 1$ ,  $K = 10$ , and  $S_0 = 10$ .

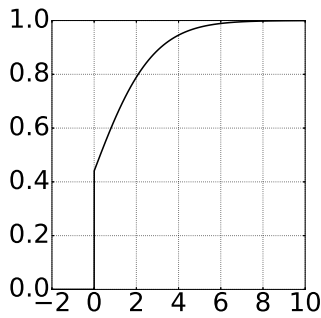


Figure 7.1 – CDF of  $Q$  for the SDE problem showing an atom in  $\{0\}$ .

$\tau$	$q_\tau = F_Q^{-1}(\tau)$	CVaR
0.5	0.28969248806044	2.07289994377492
0.6	0.79915147910402	2.45589763914500
0.7	1.37357115613536	2.91495294881199
0.8	2.08659501069246	3.51568432394181
0.9	3.15337857121734	4.46029755618034
0.95	4.10793072742060	5.33760617797560
0.99	6.09681496883100	7.22485804514000

Table 7.1 – Quantiles and conditional values at risk for the quantity of interest associated with the geometric Brownian motion SDE.

For the numerical experiments based on multilevel Monte Carlo method, the SDE (7.49) is discretized via the Milstein method (see details in the previous chapter 6.5.1)

In order to validate the MLMC methodology discussed in this chapter we provide in Figure 7.2 the sample based estimated MSE (using 100 independent repetitions of the algorithm) for VaR (red line), CVaR (blue line) and CDF (green line) of  $Q$  compared with the required absolute MSE tolerance. We specifically considered in this experiment the MLMC estimator  $P_H^{\text{MLMC}}(\vartheta)$  of  $H_Q(\vartheta)$  discussed in 7.3.3. The different plots in Figure 7.2 report the estimated MSE for different values of  $\tau$ . We can observe that the MLMC implementation does indeed satisfy the required tolerance goals for VaR, CVaR and CDF. Additionally we witness that the implementation is actually quite conservative in particular for the CDF for high value of  $\tau$ , in the sense that it produces estimates that are more accurate than required.

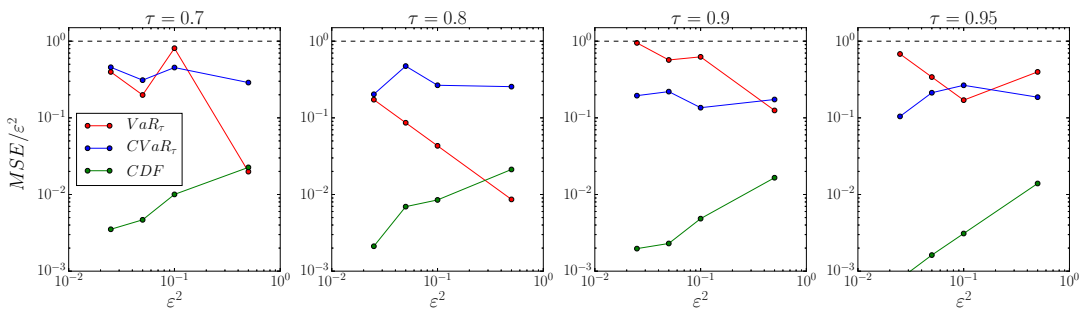
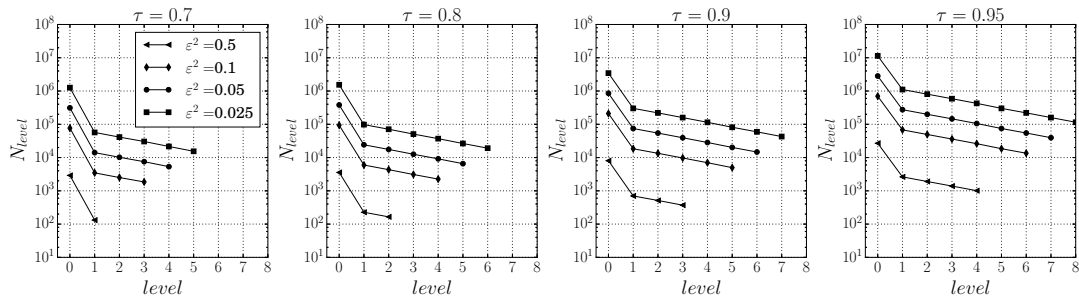


Figure 7.2 – Error vs. tolerance demand for different value of  $\tau$  for the SDE problem.

In Figure 7.3 we report the hierarchies required to achieve the prescribed tolerances discussed above. As it is possible to observe the number of levels and samples per level (and hence the computational cost) increase consistently with  $\tau$ . Such can be also inferred by looking at Figure 7.4 where we can observe that the decay rate for the estimator’s bias and variances is the same, while the constants are increasing with increasing  $\tau$ .

Notice that  $Q$  has a mixed distribution, in the sense that it has a continuous distribution on



**Figure 7.3** – MLMC hierarchies (number of levels and sample size per level) required to achieve prescribed relative tolerance requirements when estimating simultaneously VaR, CVaR and CDF of  $Q$  for different value of  $\tau$  for the SDE problem.

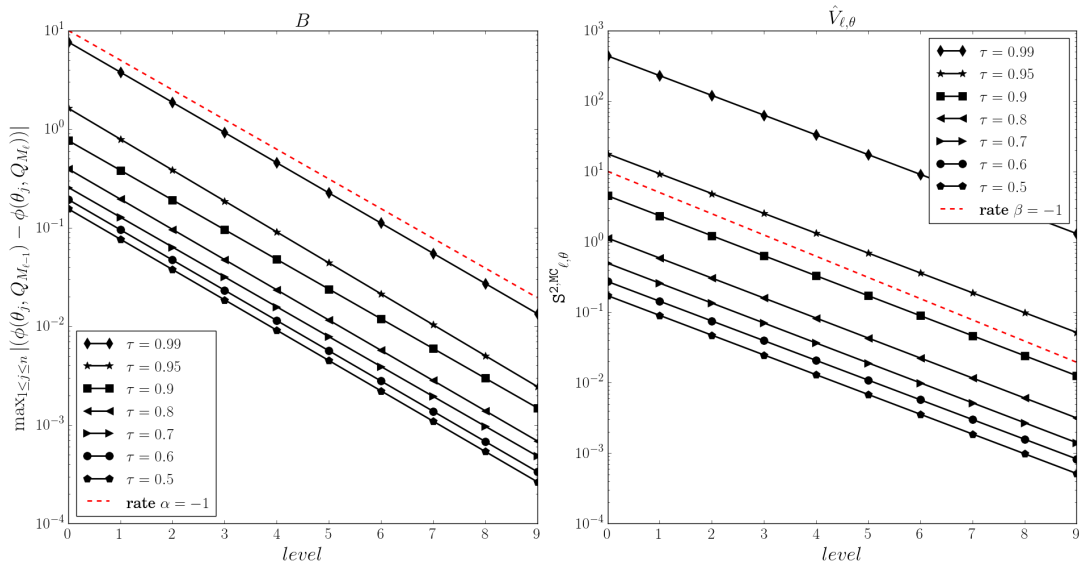


**Figure 7.4** – Decay rates for the bias and variances of MLMC estimator  $P_H^{MLMC}(\vartheta)$  of  $H_Q(\vartheta)$  for different value of  $\tau$  for the SDE problem.

$(0, \infty)$  and an atom in  $\{0\}$  (see Figure 7.1). This discontinuity does not prevent the use of our approach but reduces the decay rate of the variance of the estimator  $\beta$  from two, as in the case of central statistical moment (see Figure 6.2 in the previous Chapter), to one.

### 7.4.2 Elliptic PDE in two spatial dimensions

We now consider a random Poisson equation in two spatial dimensions,

$$-\Delta u = f, \quad \text{in } D = (0, 1)^2, \tag{7.52}$$

with homogeneous Dirichlet boundary conditions. Here, the forcing term  $f$  is given by

$$f(x) = -K\xi(x_1^2 + x_2^2 - x_1 - x_2),$$

with  $\xi$  being a non-negative random variable and  $K > 0$  a positive constant. For this forcing term the solution to the PDE can be computed explicitly and reads  $u(x_1, x_2) = K\xi x_1 x_2(1 - x_1)(1 - x_2)/2$ . As quantity of interest we consider the spatial average of the solution, that is

$$Q := \int_D u dx = \frac{K}{72}\xi.$$

This explicit representation of  $Q$  in terms of the random input  $\xi$  to the PDE model (7.52) allows us to easily compute the exact mean as well as central moments of  $Q$ , which we will use to verify the numerical experiments that follow. Specifically, here we use  $\xi \sim \text{Beta}(2, 6)$  and  $K = 432$ , so that the CDF of  $Q$  reads

$$F_Q(q) = \begin{cases} 0, & q < 0, \\ \frac{q^2(27216 - 15120q + 3780q^2 - 504q^3 + 35q^4 - q^5)}{46656}, & 0 \leq q < 6, \\ 1, & 6 \leq q. \end{cases}$$

In fact, using the CDF of  $Q$  it is straightforward to compute reference values for the quantiles and conditional values at risk, as is shown in Table 7.2.

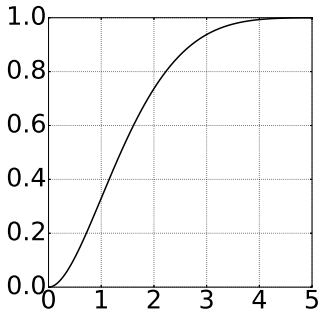


Figure 7.5 – CDF of  $Q$  for the Elliptic PDE problem.

$\tau$	$q_\tau = F_Q^{-1}(\tau)$	CVaR
0.5	1.37093978103957	2.19362427969856
0.6	1.61107689488803	2.36980305732596
0.7	1.88569618239293	2.57820388360315
0.8	2.22516910158006	2.84332656764439
0.9	2.71538966014680	3.23647287923313
0.95	3.12421784154784	3.57085205229115
0.99	3.86018736077886	4.18269815233762

Table 7.2 – Quantiles and conditional values at risk for the quantity of interest associated with random Poisson equation.

For the numerical treatment with the multilevel Monte Carlo method, the PDE (7.52) is discretized via a second order finite difference scheme (see details in the previous Chapter 6.5.2).

As for the previous example, we report in Figure 7.6 the hierarchies required to achieve prescribed tolerances requirements. Also for this problem the number of levels and samples per level increase consistently with  $\tau$ .

Figure 7.7 reports the decay rate for the estimator’s bias and variances. The distribution of  $Q$  is continuous in this case (see Figure 7.5) and we observe the same decay rates as obtained for

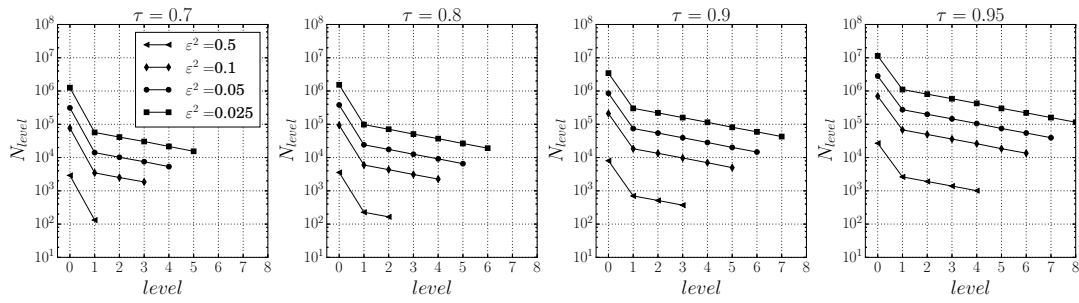


Figure 7.6 – MLMC hierarchies (number of levels and sample size per level) required to achieve prescribed relative tolerance requirements when estimating simultaneously VaR, CVaR and CDF of  $Q$  for different value of  $\tau$  for the Elliptic PDE problem.

the estimation of central statistical moment (see Figure 6.4 in the previous Chapter).

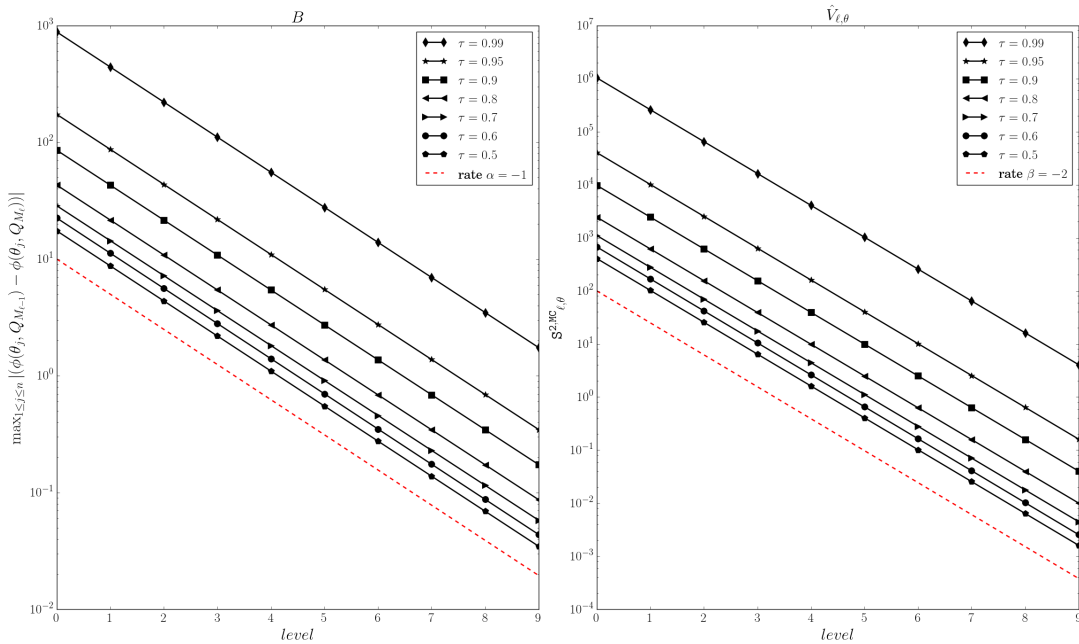


Figure 7.7 – Decay rates for the bias and variances of MLMC estimator  $P_H^{MLMC}(\vartheta)$  of  $H_Q(\vartheta)$  for different value of  $\tau$  for the Elliptic PDE problem.

### 7.5 Summary

In this chapter we presented a practical extension of the Multi Level Monte Carlo paradigm for the accurate computation of parametric expectation and its derivatives based on a cubic spline interpolation operator and we defined different MLMC estimators for the computation of CDFs, VaR and CVaR and characteristic functions. Finally we validated the accuracy and effectiveness of the proposed approach on benchmark problems for which we can compute highly accurate reference values.

The application of this approach on aerodynamic problems will be provided in the following two Chapters. In Chapter 8 we will compute the entire CDF of aerodynamic performance parameters for the NASA Common Research Model wide-body transport aircraft configuration under operating uncertainties while in Chapter 9 we will leverage the computation of risk measure in the context of robust and reliability based design optimization of transonic airfoils.





# 8 C-MLMC Application to Industrial Problems

In this section we apply the MLMC and C-MLMC methodologies presented in the previous chapter to large scale internal and external aerodynamic systems affected by operating uncertainties. Namely we consider the NASA ROTOR-37 and the NASA Common Research Model (CRM).

## 8.1 Turbomachinery Model Problem: NASA ROTOR-37

The first problem we consider in this chapter is the well established turbomachinery test case NASA ROTOR-37 (defined in the UMRIDA project as BC-01), a transonic axial flow compressor. The rotor has 36 blades and an aspect ratio of 1.19, rotates at  $17188.7 [rpm]$  ( $1800 [rad/s]$ ), leading to a tip-speed of  $454 [m/s]$ . A detailed description of the geometry, the original experimental set-up and a series of simulations can be found in [Dun98, RM78].

The design parameters of the rotor are summarized in the following Table 8.1:

Quantity	Symbol	Design Value
Rotor Total Pressure Ratio	$P_2/P_1$	2.106
Rotor Total Temperature Ratio	$T_2/T_1$	1.270
Rotor Adiabatic Efficiency	$\eta_{ad}$	0.877
Mass Flow [ $kg/s$ ]	$\dot{m}$	20.188

**Table 8.1** – Design values for the NASA ROTOR-37 problem.

### 8.1.1 Deterministic results

The computational model (Fig.8.1(b)) consists of one blade with periodic boundary conditions. The rotation is imposed to the hub and the blade, while the shroud is kept fixed. Total pressure and total temperature profiles derived from experiments [Dun98] are imposed at the inlet

boundary and the static pressure is varied at the outlet to change the mass flow.

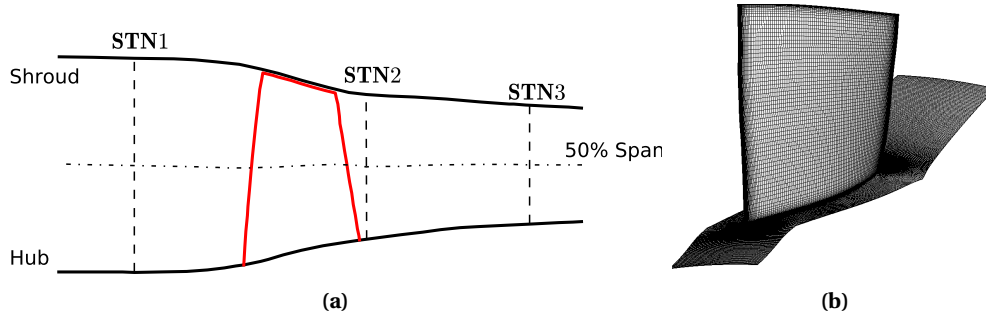


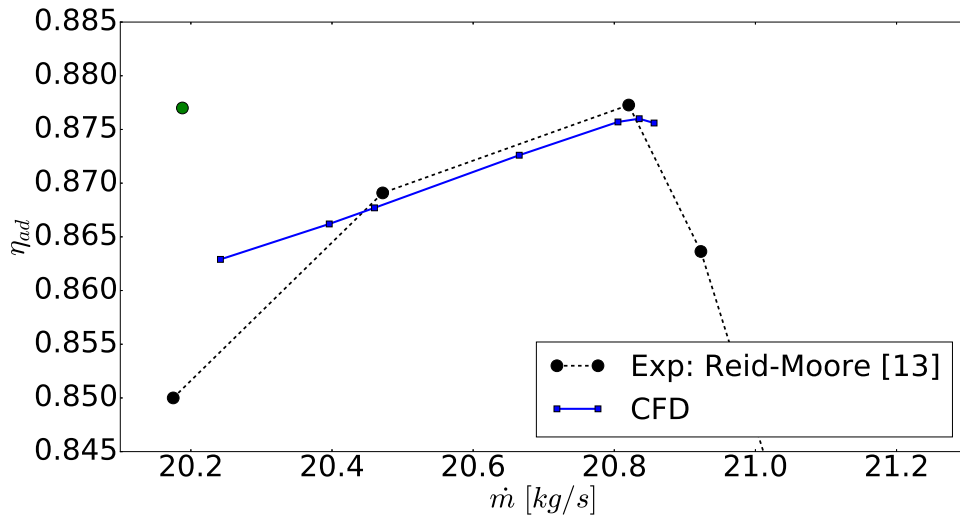
Figure 8.1 – (a) NASA Rotor 37 and (b) computational model.

The proprieties of the multi-block structured 4-levels grid hierarchy used in the C-MLMC, generated using NUMERCA Autogrid, are presented in the following Table 8.2 along with the average computational time required to compute one deterministic simulation using CFD++ software environment.

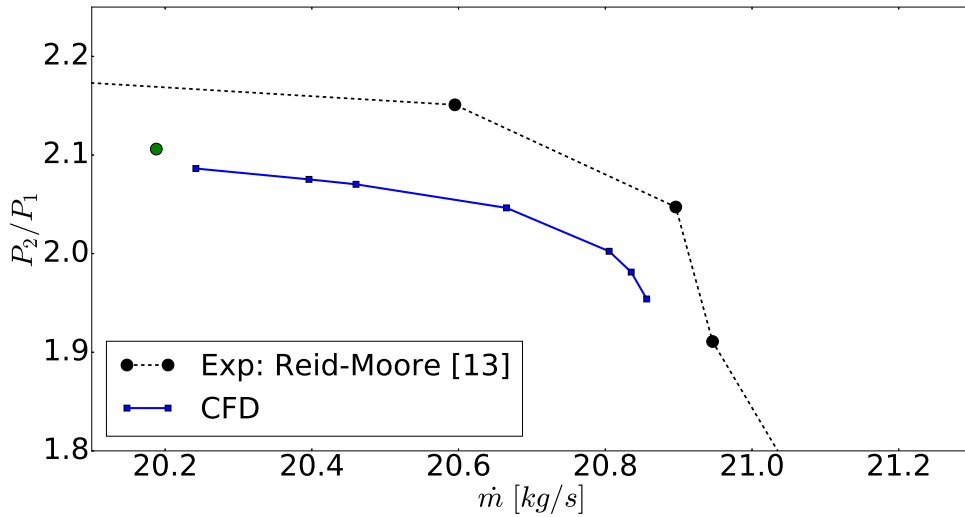
LEVEL	Blade nodes	Spanwise nodes	Cells	y+	CTime[s] (n.cpu)
L0	113	33	156769	1 – 2	110 (80)
L1	169	53	536669	1 – 2	225 (128)
L2	209	73	1244133	1 – 2	435 (192)
L3	249	93	2241801	1 – 2	837 (224)
L4	305	113	4253889	1 – 2	1588 (256)

Table 8.2 – MLMC 4-levels grid hierarchy for the ROTOR-37 problem. CTime[s] is the real time in seconds required to compute one deterministic simulation on the prescribed number of cpus.

We ensure an appropriate refinement near the small tip clearance (0.356 [mm]) and that the  $y^+$  is between 1 and 2 near the boundaries, for all the grid levels, to accommodate the requirements of Spalart-Allmaras turbulence model employed in the CFD simulations. In Table 8.2 we report the number of nodes set on the blade section and spanwise on each level. The number of nodes in the perpendicular direction to the blade surface is set proportional to the number of spanwise nodes, and their distribution has a fixed growth rate. In the Fig. 8.2 we observe a good agreement between the computational results obtained with the finest grid level (L4) and experimental measurements of Reid and Moore [RM78]. The significant differences between numerical results and measurements are in the rotor stall region. For this reason we will only consider operating points before stall conditions ( $\dot{m} > 20.5$  [kg/s]).



(a) Rotor adiabatic efficiency



(b) Rotor total pressure ratio

**Figure 8.2** – Experimental and computational compressor maps of the ROTOR-37. The green circles indicate the design parameters presented in the previous table.

Fig. 8.3 presents the flow features on the suction and pressure side of the blade and at 50% of the span for the maximum adiabatic efficiency conditions ( $\eta_{ad} = 0.876$ ). We distinguish the bow shock at the leading edge of the blade and a classical  $\lambda$ -shock region (Fig. 8.3(g)) on the suction side where the shock impacts the boundary layer. Downstream of the shock-boundary layer interaction we identify a flow separation region. Such separation can be inferred also by looking at the skin friction (Fig. 8.3(c)), at the boundary layer transition and at the turbulence index (Fig. 8.3(e)) at the wall. Additionally the boundary layer transition induces a sudden increase of eddy viscosity (Fig. 8.3(h)).

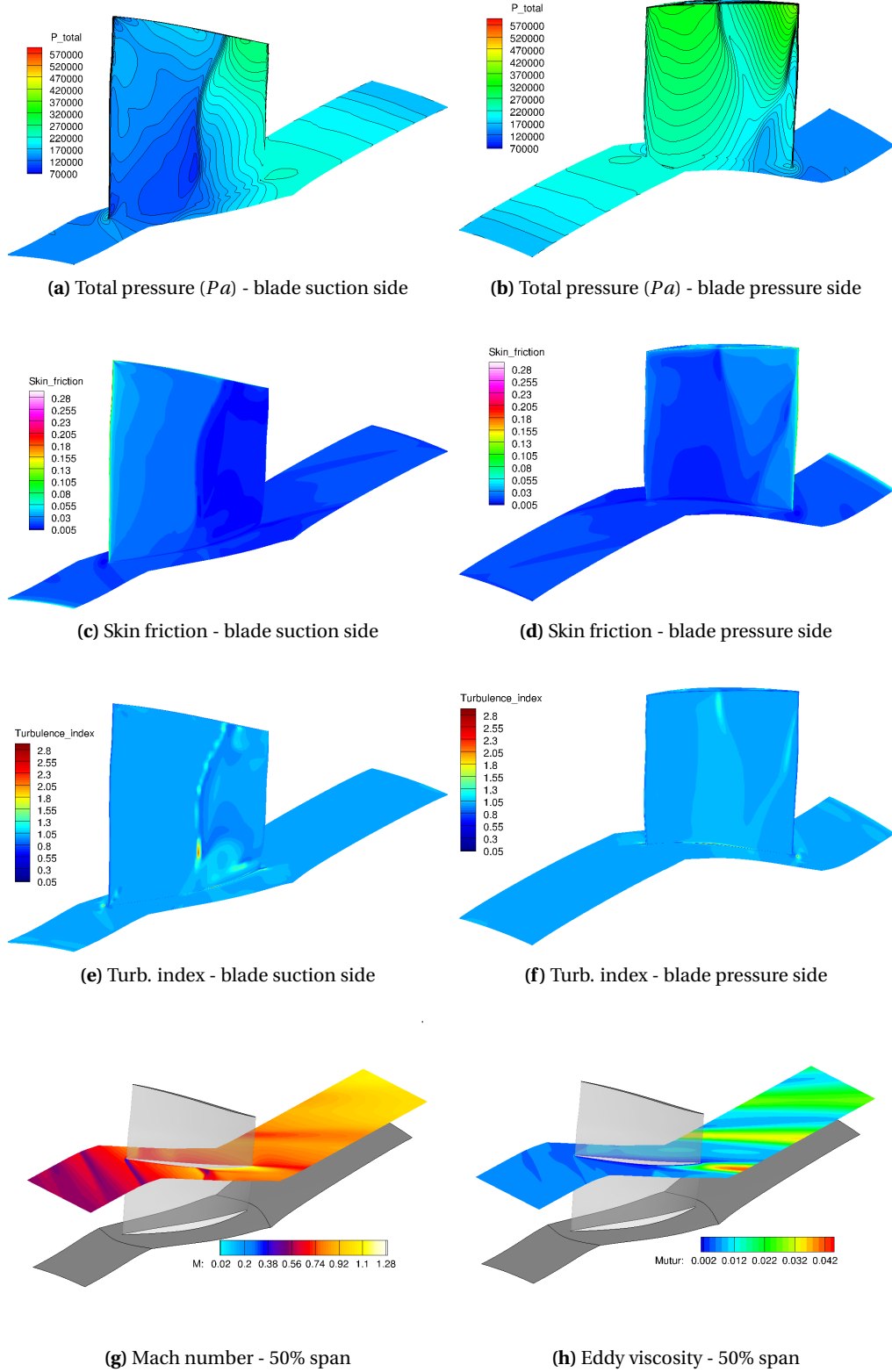


Figure 8.3 – Deterministic results for the ROTOR-37. Left: suction side; right: pressure side.

8.1.2 Stochastic Results using C-MLMC

After assessing the validity of the CFD model, we now propagate uncertainties to study their effects on the performances of the rotor using the C-MLMC approach presented in the previous chapters. We consider operating uncertainties in the inlet total pressure and total temperature profile and the outlet static pressure. The uncertainties on the parameters are modeled as truncated Gaussian random variables (see definition in Eq. (4.22)).

The following Table 8.3 summarizes the reference operating parameters and the uncertainties considered for the following simulations.

	Quantity	Reference ( $r$ )	Uncertainty $\mathcal{T}\mathcal{N}(\mu, \sigma, X_{LO}, X_{UP})$
INLET	$P_{tot}$	18 pt. profile (see Fig. 8.4)	$\mathcal{T}\mathcal{N}(r, 1\%, -2\%, +2\%)$
	$T_{tot}$	18 pt. profile (see Fig. 8.4)	$\mathcal{T}\mathcal{N}(r, 1\%, -2\%, +2\%)$
OUTLET	$p_o$	C1 = 92500.0 [Pa]	$\mathcal{T}\mathcal{N}(r, 1\%, -2\%, +2\%)$
		C2 = 99215.0 [Pa]	$\mathcal{T}\mathcal{N}(r, 1\%, -2\%, +2\%)$
		C3 = 110000.0 [Pa]	$\mathcal{T}\mathcal{N}(r, 1\%, -2\%, +2\%)$

Table 8.3 – Operating uncertainties for the ROTOR-37 stochastic analysis.

Fig. 8.4 depicts the inlet uncertain total pressure and total temperature profiles. The same random perturbation from the reference profile of the total pressure and temperature is applied to every point on the inlet (fully correlated perturbation).

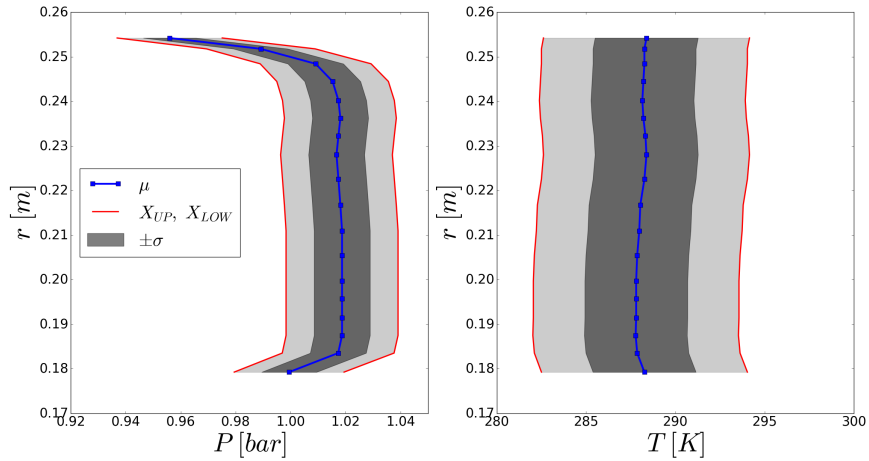


Figure 8.4 – Uncertain total pressure and total temperature inlet profiles. The blue line represents the mean profile ( $\mu$ ), the shaded gray area is one standard deviation ( $\pm\sigma$ ) and the red lines are the upper and lower boundaries of the uncertain range ( $X_{LOW}, X_{UP}$ ).

In Fig. 8.5 we present the stochastic results for the adiabatic efficiency, rotor total pressure ratio, stage total pressure ratio and mass flow for the ROTOR-37 affected by operating uncertainties (3 uncertain parameters). For the three analyzed cases (C1, C2, C3 in the mean outlet pressure

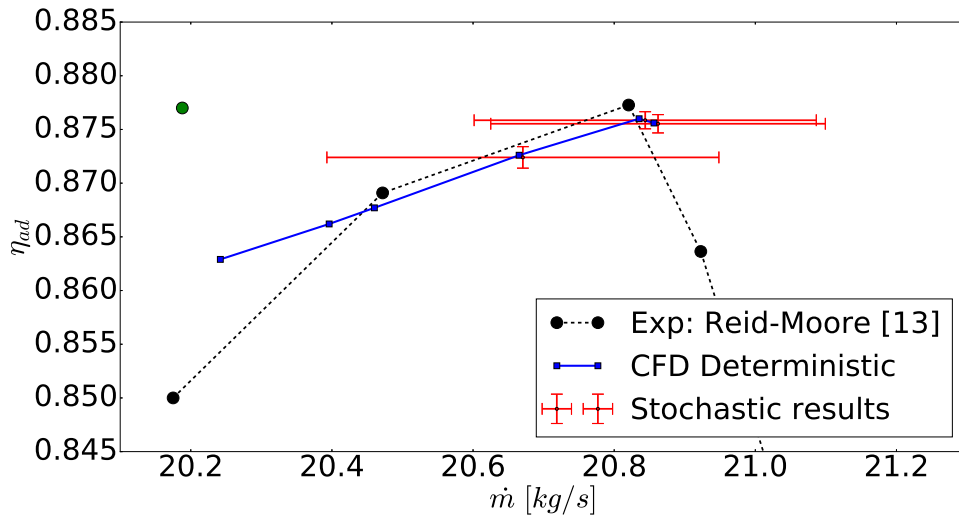
$p_0$ ) we plot the compressor map with mean  $\pm$  standard deviation for the four quantities of interest. We notice that the mean values of  $\dot{m}$ ,  $\eta_{ad}$ ,  $P_2/P_1$  and  $P_3/P_1$  in the stochastic case are comparable with the deterministic ones, as observed by [LB10, GBMA09]. Additionally we also observe that the mass flow  $\dot{m}$  is the most sensitive quantity to variations in the operating parameters as quantified in Table 8.4. The variability of  $\dot{m}$ ,  $\eta_{ad}$ ,  $P_2/P_1$  and  $P_3/P_1$  seems to increase as we approach the stall conditions.

CASE - $p_o$	Deterministic	Stochastic (% $\sigma$ )	C-MLMC rates
C1 = 92500.0 [Pa]	$\dot{m} = 20.8564$ [kg/s] $\eta_{ad} = 0.8756$ $P_2/P_1 = 1.9540$ $P_3/P_1 = 1.9255$	$\dot{m} = 20.8621 \pm 0.2371$ [kg/s] (1.13%) $\eta_{ad} = 0.8755 \pm 0.0009$ (0.10%) $P_2/P_1 = 1.9534 \pm 0.0093$ (0.47%) $P_3/P_1 = 1.9252 \pm 0.0105$ (0.54%)	$\alpha = 1.7$ $\beta = 2.6$
C2 = 99215.0 [Pa]	$\dot{m} = 20.8564$ [kg/s] $\eta_{ad} = 0.8760$ $P_2/P_1 = 1.9813$ $P_3/P_1 = 1.9559$	$\dot{m} = 20.8440 \pm 0.2424$ [kg/s] (1.16%) $\eta_{ad} = 0.8758 \pm 0.0008$ (0.09%) $P_2/P_1 = 1.9812 \pm 0.0113$ (0.57%) $P_3/P_1 = 1.9558 \pm 0.0106$ (0.54%)	$\alpha = 1.6$ $\beta = 2.2$
C3 = 110000.0 [Pa] [Pa]	$\dot{m} = 20.6653$ [kg/s] $\eta_{ad} = 0.8726$ $P_2/P_1 = 2.0464$ $P_3/P_1 = 2.0204$	$\dot{m} = 20.6706 \pm 0.2777$ [kg/s] (1.34%) $\eta_{ad} = 0.8724 \pm 0.0010$ (0.11%) $P_2/P_1 = 2.0451 \pm 0.0137$ (0.67%) $P_3/P_1 = 2.0190 \pm 0.0135$ (0.67%)	$\alpha = 1.8$ $\beta = 2.1$

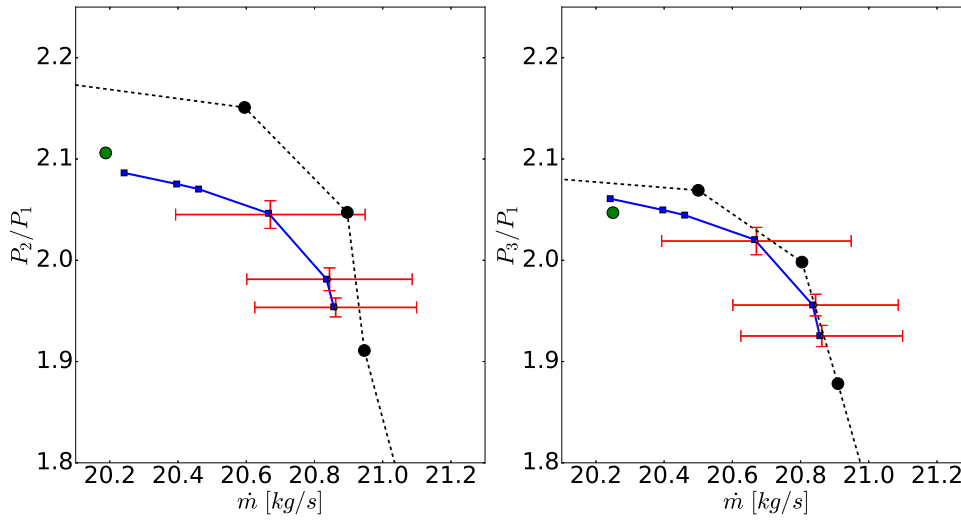
**Table 8.4** – Deterministic and stochastic results for the ROTOR-37.

In all simulation we have imposed a relative tolerance of 0.5% on the mean value of the mass flow rate. In Table 8.4 we report in the last column also the estimated rates computed during the C-MLMC simulation. As it is possible to observe the statistical error decay ( $\beta$ ) degrades as we move closer to the stall region while the lowest deterministic error decay ( $\alpha$ ) is measured for the simulation with highest adiabatic efficiency (C2).

### 8.1. Turbomachinery Model Problem: NASA ROTOR-37



(a) Rotor adiabatic efficiency



(b) Rotor total pressure ratio ( $P_2/P_1$ ) and Stage total pressure ratio ( $P_3/P_1$ )

**Figure 8.5** – Experimental, deterministic and stochastic results for the compressor map of the ROTOR-37. Each red interval correspond to mean  $\pm$  standard deviation.

## 8.2 NASA Common Research Model

In this section we consider the NASA Common Research Model (CRM), an aircraft configuration equipped with a contemporary supercritical transonic wing and a fuselage that is representative of a wide-body commercial transport aircraft. The model has been developed by NASA in order to answer the scientific and industrial community quest for a modern well-defined experimental database for the purpose of validation and verification (V&V) of CFD applications [VDRW08]. Indeed, AIAA Drag Prediction Workshop (DPW) series concentrated in the last years on the NASA CRM in order to understand and improve the criticalities of CFD solvers in accurately predicting the drag and moments of complex aircraft configurations.

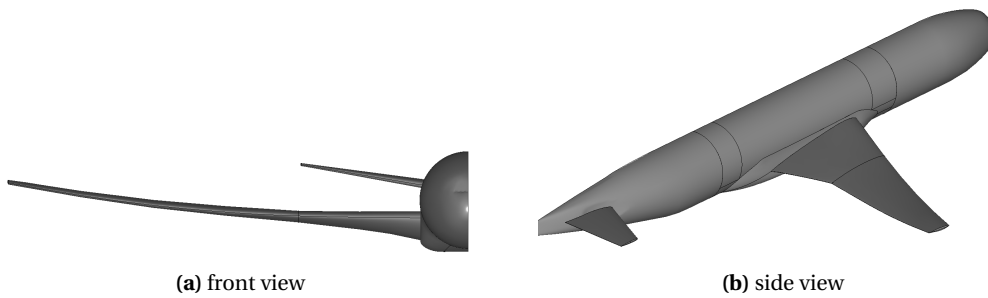


Figure 8.6 – NASA CRM (WBT: wing body tail) geometry.

The CRM is designed for a cruise at Mach  $M_\infty = 0.85$  and a corresponding design lift coefficient of  $C_L = 0.5$ . We specifically consider in this study the wing-body-tail configuration defined in the AIAA 5th DPW (see Figure 8.6). The aircraft geometrical parameters of the NASA CRM are summarized in the following Table 8.5.

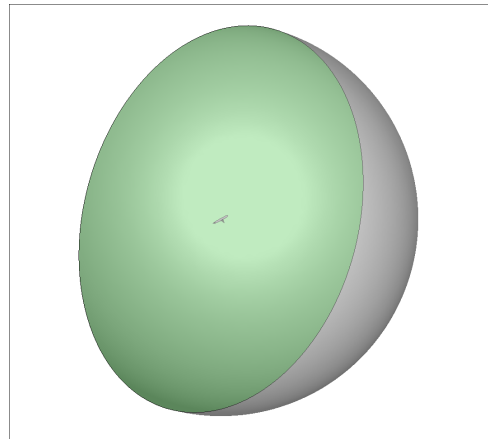
Quantity	Symbol	Design Value
Wing Aspect Ratio	$AR$	9.0
Wing Taper Ratio	$\lambda_w$	0.275
Wing Span	$span$	58.7629 [m] (2313.50 [in])
Reference area	$S_{ref}$	383.68955 [m <sup>2</sup> ] (594720.0 [in <sup>2</sup> ])
Reference chord	$c_{REF}$	7.00532 [m] (275.8 [in])
X Moment reference center	$X_{REF}$	33.67786 [m] (1325.90 [in])
Z Moment reference center	$Z_{REF}$	4.51993 [m] (177.95 [in])

Table 8.5 – NASA CRM geometrical parameters.

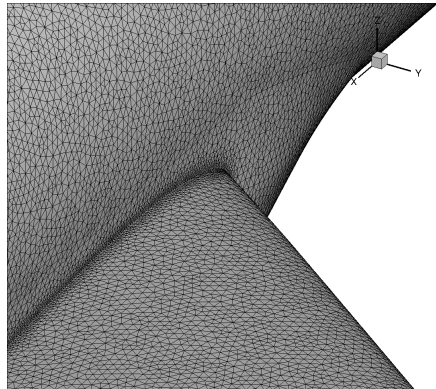
### 8.2.1 Deterministic results

The computational model for the NASA CRM consists of half aircraft with symmetry boundary conditions at the symmetry plane and far-field condition imposed on the half sphere (see Figure 8.6 and 8.7(a)).

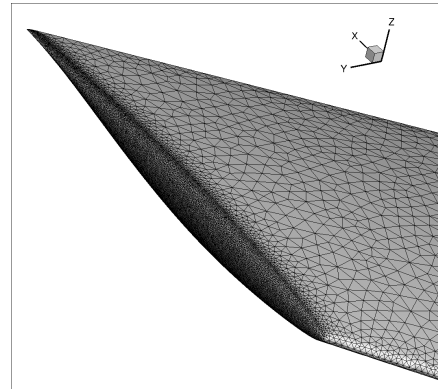




(a) Computational domain for the NASA CRM



(b) grid refinement at the wing fairing intersection



(c) grid refinement at the wing tip

**Figure 8.7** – NASA CRM computational domain and details of the hybrid unstructured grid.

For this problem we employ a hierarchy of hybrid unstructured grids and ensure an appropriate refinement at the wing-fairing and tail-fuselage intersection and at the wing tip (see Figure 8.6(b)-(c)). Additionally we assure that near the boundaries the  $y^+$  is between 1 and 2, for all the grid levels, to accommodate the requirements of Spalart-Allmaras turbulence model employed in the CFD simulations. In Table 8.7 we report the number of nodes and the average CPU time required to perform a deterministic simulation on all levels of the grid hierarchy.

Before performing the actual stochastic analysis we validate the deterministic computational model with the data available from the AIAA 5th DPW [LLT<sup>+</sup>13] using the flow conditions presented in Table 8.6.

In Figure 8.3 we observe a good agreement between the computational results obtained with the finest grid level (L3) with the other CFD results obtained during the AIAA 5th DPW (pink region in the figure representative of mean  $\pm$  standard deviation of the CFD results obtained during the workshop). Additionally we report also the experimental measurements performed

Quantity	Symbol	Design Value
Freestream Mach number	$M_\infty$	0.85
Chord Reynolds number	$Re_c$	$5 \cdot 10^6$
Reference Temperature	$T_{ref}$	310.928 [K] (100 [F])
Lift Coefficient	$C_L$	0.5

**Table 8.6** – Flow conditions and lift coefficient for the validation of the NASA CRM deterministic simulations.

at the NASA Langley National Transonic Facility (NTF Test 197, green region in the Figure 8.3) and the NASA Ames 11-ft transonic wind tunnel (Ames Test 216, blue region in the Figure 8.3) [RD11] for the prediction of the aircraft total drag coefficient  $C_D^T$ .

LEVEL	Cells	y+	CTime on 280 CPUs
L0	$2.3 \cdot 10^6$	1 – 2	400 [s] (0.11 [h])
L1	$5.0 \cdot 10^6$	1 – 2	825 [s] (0.23 [h])
L2	$9.8 \cdot 10^6$	1 – 2	1250 [s] (0.35 [h])
L3	$21.3 \cdot 10^6$	1 – 2	3200 [s] (0.89 [h])

**Table 8.7** – MLMC 3-levels grid hierarchy for the NASA CRM. CTime[s] is the real time required to compute one deterministic simulation on 280 CPUs.

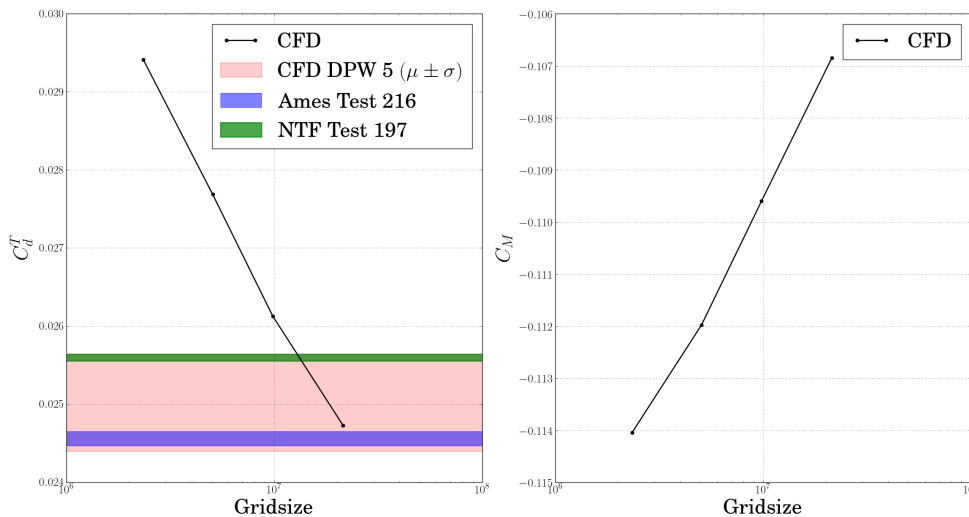
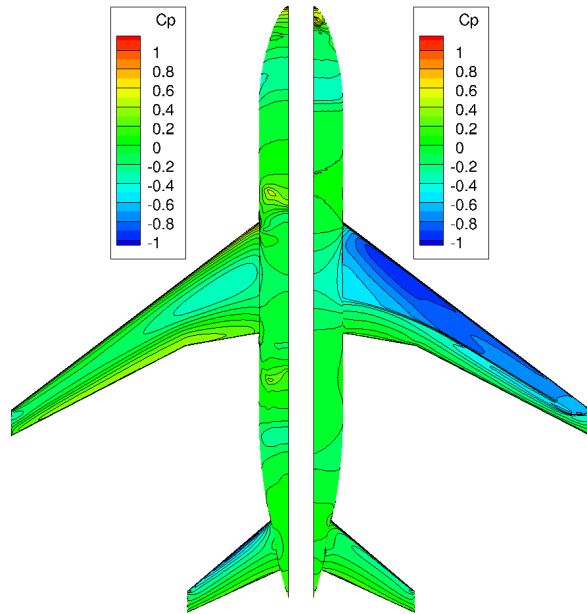
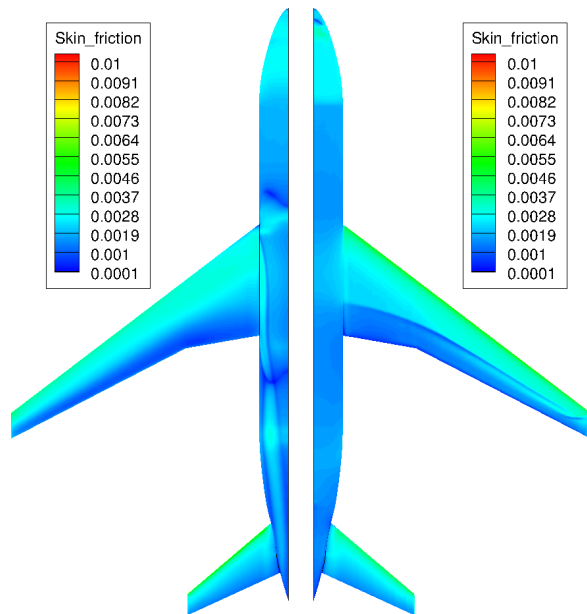


**Figure 8.8** – Comparison of CFD results obtained with the hybrid unstructured grids used in this study (black line), other CFD results obtained during the 5th AIAA DPW (pink region representative of mean±standard deviation) and experimental measurements performed at the NASA Langley National Transonic Facility (NTF Test 197, green region) and the NASA Ames 11-ft transonic wind tunnel (Ames Test 216, blue region). On the right we report the moment coefficient obtained with our grid hierarchy.

Figure 8.9 and 8.10 present the flow features (pressure coefficient and skin friction) on flow around the aircraft at cruise design conditions presented in Table 8.6.



(a) Pressure coefficient - lower view      (b) Pressure coefficient - upper view



(c) Skin friction - lower view      (d) Skin friction - upper view

**Figure 8.9** – Surface pressure and skin friction coefficient of the NASA CRM at  $M = 0.85$ ,  $C_L = 0.5$  (upper and lower views).

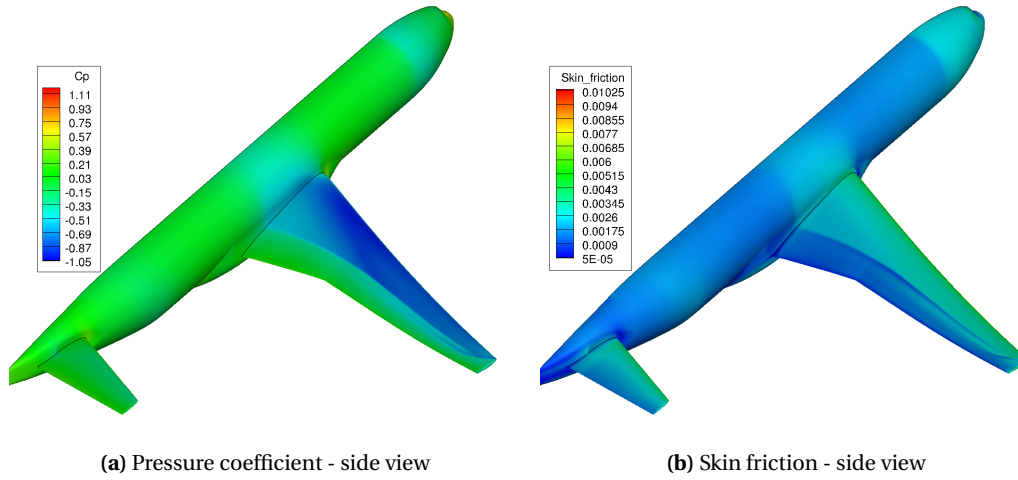


**Figure 8.10** – Surface pressure and skin friction coefficient of the NASA CRM at  $M = 0.85$ ,  $C_L = 0.5$  (upper and lower views).

### 8.2.2 Stochastic Results using C-MLMC

After assessing the validity of the CFD model we now propagate operating uncertainties to study their effects on the performances of NASA CRM at different lift conditions using the C-MLMC methodologies presented in the previous chapters. We consider operating uncertainties in the farfield Mach number and flow temperature. The uncertainties on these parameters are modeled as symmetric Beta distributions. The following Table 8.8 summarizes the reference operating parameters and the uncertainties considered for the following simulations.

Quantity	Reference	Uncertainty
$M_\infty$	0.85	$\mathcal{B}(2, 2, 0.05, M_\infty - 0.025)$
$Re_c$	$5 \cdot 10^6$	–
$T_{ref}$	310.928 [K]	$\mathcal{B}(2, 2, 30, T_{ref} - 15)$
$C_L$	0.3, 0.4, 0.5, 0.55	–

**Table 8.8** – Operating uncertainties and lift conditions for the NASA CRM stochastic analysis.

In Figure 8.11 we present the cumulative density function of total drag  $C_D^T$ , inviscid drag  $C_D^I$  (pressure drag components), viscous drag (skin friction drag component)  $C_D^V$  and moment coefficient  $C_M$  for four different lift conditions  $C_L = 0.3, 0.4, 0.5, 0.55$  for the NASA CRM under operating uncertainties. Additionally in Figure 8.12 we present the mean  $\pm$  two standard deviation plot for the same coefficient. The total drag coefficient is compared with the experimental results performed at the NASA Langley National Transonic Facility (NTF Run 44, black circles). All the results are computed with the MLMC methodology presented in Chapter 6 and 7 by imposing a relative tolerance of 0.1% on the variance of the total drag coefficient (and

terminate the simulations when we achieve at least an absolute error on the approximation of the CDF lower than 10%). In order to achieve those tolerances we performed a C-MLMC simulation on the 3-level hierarchy presented in Table 8.7 with an average number of samples per levels of 200, 110, 50, 10. Hence, each C-MLMC simulation took approximately 72 hours on 280 CPUs.

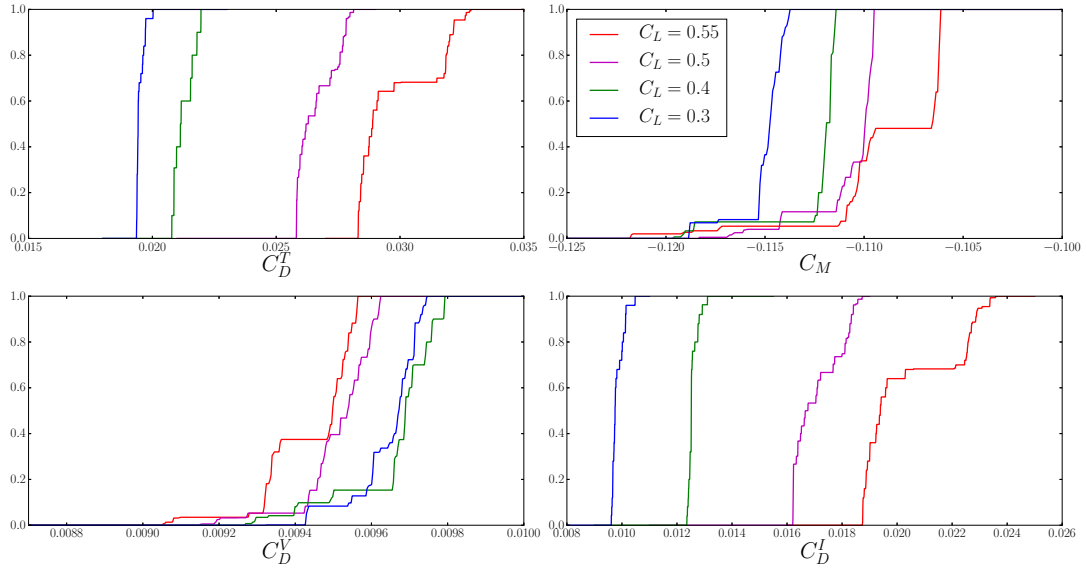


**Figure 8.11** – Cumulative density function (CDF) of total drag  $C_D^T$ , inviscid drag  $C_D^I$  (pressure drag components), viscous drag (skin friction drag component)  $C_D^V$  and moment coefficient  $C_M$  for four different lift conditions  $C_L = 0.3, 0.4, 0.5, 0.55$  for the NASA CRM under operating uncertainties.

In Figure 8.12 we can observe a good agreement of the mean value of the stochastic simulations with the experimental results. We notice an increase in the variability and absolute value of the drag as the lift increases mainly due to the pressure drag component. Also the moment coefficient follows the same trend. On the other hand, the skin friction drag component  $C_D^V$  does not seem to significantly vary with the lift coefficient.

### 8.3 Conclusion and Recommendations

In the previous Chapters we presented the different MLMC approaches and procedure to perform UQ in inviscid and viscous aerodynamic problems affected by operating and geometric uncertainties. The numerical examples provide clear indications on the computational reduction that can be achieved with MLMC with respect to MC. Additionally we proposed in Chapter 5 a grid hierarchy refinement strategy methodology to design CFD grids in order to achieve appropriate convergence for the bias and statistical error in MLMC simulations of viscous flows. In this Chapter we followed such approach and presented two test cases relevant in turbo-machinery and external aircraft aerodynamics, affected by operating uncertainties.

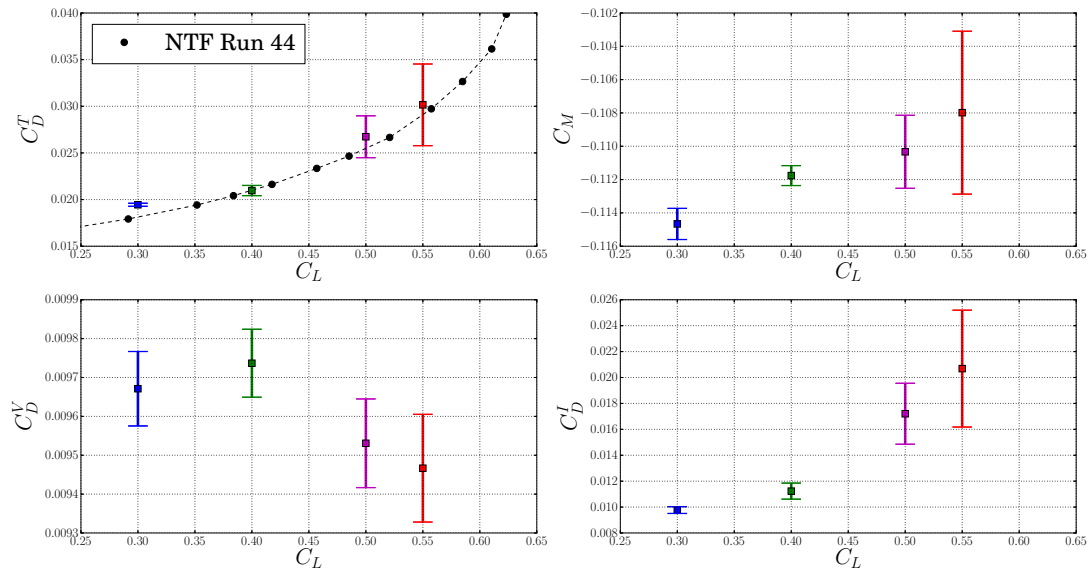


**Figure 8.12** – Total drag  $C_D^T$ , inviscid drag  $C_D^I$  (pressure drag components), viscous drag (skin friction drag component)  $C_D^V$  and moment coefficient  $C_M$  mean  $\pm 2$  standard deviation for four different lift conditions  $C_L = 0.3, 0.4, 0.5, 0.55$  for the NASA CRM under operating uncertainties. The total drag coefficient is compared with the experimental results performed at the NASA Langley National Transonic Facility (NTF Run 44, black circles).

We believe that, at this stage, MLMC can be efficiently applied to provide valuable informations and quantifications of the variability of large scale aerodynamic systems affected by uncertainties.

The essential features that one should foresee to efficiently apply the MLMC method to large scale industrial problems are:

- deterministic grid convergence for the problem under investigation corroborated by a verification and validation of the CFD results with experimental measurements
- robust numerical solver that provides consistent solutions of the deterministic problem also on coarse grids,
- appropriate grid hierarchy refinement strategy necessary to achieve optimal complexity for the C-MLMC.

In our approach we applied a parallel execution of the simulations on a given hierarchy level. The optimal parallelization of the C-MLMC (level-wise, sample-wise and mesh-wise) and the optimal allocation of resources at each iteration of the algorithm for large scale problems on massively parallel HPC is still an open topic. Some ideas of parallelization and load balancing techniques for "standard" MLMC algorithms have been proposed in [ŠMS12, GDR<sup>+</sup>16].

*The reasonable man adapts himself to the world; the unreasonable one persists in trying to adapt the world to himself. Therefore all progress depends on the unreasonable man.*

*George Bernard Shaw*





# 9 Airfoil Design Optimization Under Uncertainty

As presented in the previous chapters, the majority of problems in aircraft production and operation require decisions made in the presence of uncertainty. For this reason aerodynamic designs obtained with traditional deterministic optimization techniques seeking only optimality in a specific set of conditions may have very poor off-design performances or may even be unreliable. As we will concentrate in this chapter on transonic airfoils affected by uncertainties, we introduce hereafter the main concepts and features of transonic airfoil design.

## 9.1 Transonic Airfoil Design

In the early days of aviation, the limitations due to propeller propulsion avoided airplanes from flying fast enough to encounter transonic/supersonic phenomena. During the Second World War fighters started reaching transonic speeds and encountered major difficulties in recovering from dives during maneuvering, controllability issues related to sharp pitching moment changes with the Mach number and Mach induced changes in control effectiveness. Since the introduction of jet engines in civil aviation, practically all commercial transports aircrafts now fly at transonic speeds.

Transonic conditions occur during a flight when there are subsonic and supersonic local flows in the same flow field surrounding an aircraft. Generally that happens in a range of speeds between the so called *critical Mach number* (around Mach 0.72), when some parts of the airflow start becoming supersonic, and the speed when all of the airflow is supersonic (around Mach 1.05 in conventional airfoils, see Figure 9.1(a)). At transonic speed, the supersonic regions of the flow are generally followed by a shock wave, that slows down the flow to subsonic conditions.

The fuel consumption due to rapid increase of wave and viscous drag with the Mach number (shocks get stronger and pressure rise through a shock wave thickens the boundary layer) typically limits the cruise speed of commercial aircrafts. Additionally, as the airflow moving around an airfoil locally reaches the speed of sound, the region in front of the shock wave

## Chapter 9. Airfoil Design Optimization Under Uncertainty

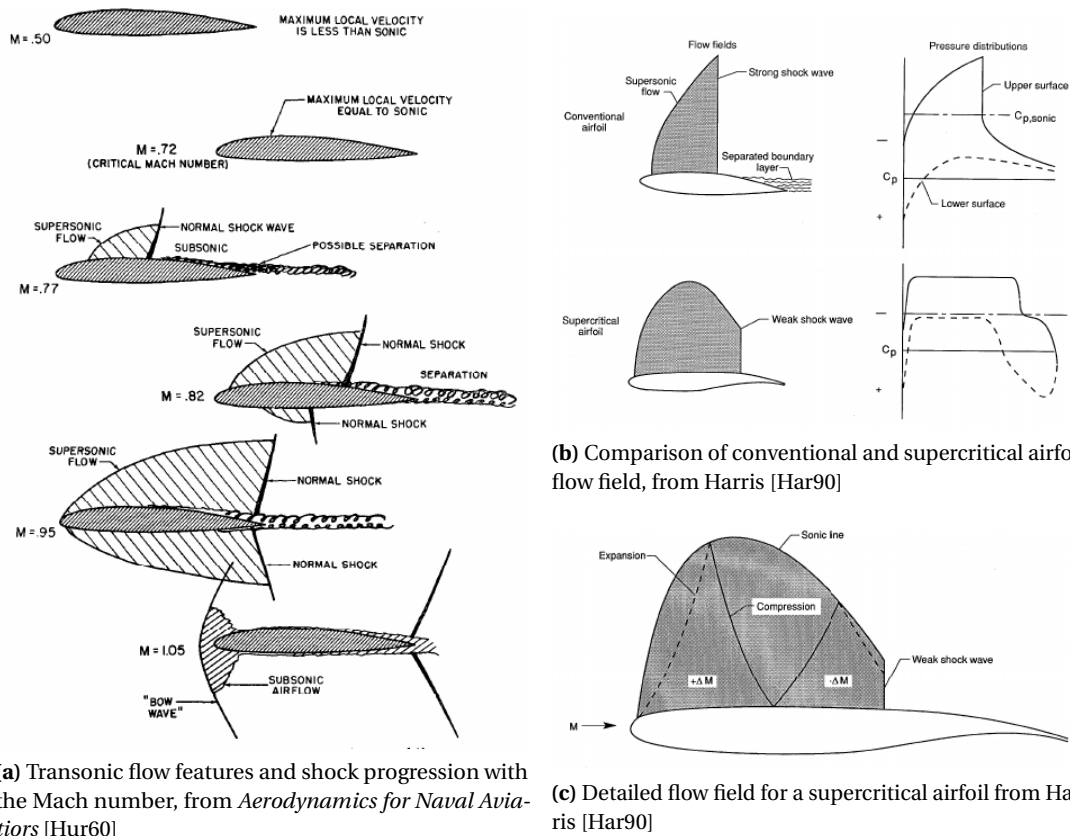


**Figure 9.1** – Transonic flow features and comparison of conventional and supercritical airfoils.

generates high lift. As the speed increases, shocks get stronger and move rearward, creating higher lift further back on the lifting bodies (see Figure 9.2). This rearward movement of lift with the Mach number causes the airfoil to tuck or pitch nose-down and is called *Mach tuck*.

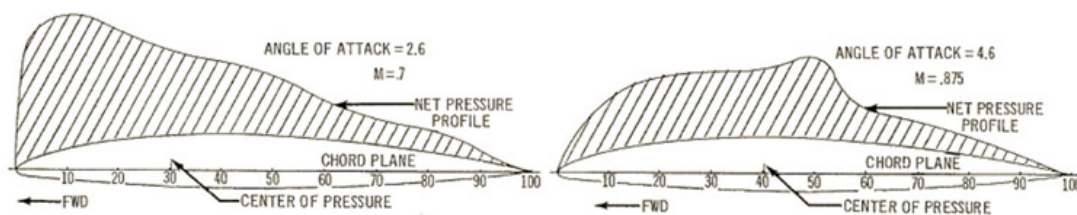


**Figure 9.2** – Pressure profile at Mach 0.7 (left image) with center of pressure about 30% of the chord and pressure profile at Mach 0.875 (right image) with a center of pressure about 40% of the chord (from Boeing Airliner July 1959).

Without enough *elevator authority* to maintain the trim and the cruise altitude, the aircraft may enter a steep unrecoverable dive [Off04]. To prevent such undesirable and potentially catastrophic stall aircrafts have been equipped with Mach trimmer devices that varies the pitch trim automatically with the Mach number and maintain the cruise flight level, larger

stabilizers powerful enough to correct large trim changes or as in the case of the Concorde, tanks that move the fuel location in order to change the position of the center of mass to match the changing location of the center of pressure, hence minimizing the aerodynamic trim required.

Notwithstanding it is possible to design a shock free airfoil, this situation usually takes place only for a single combination of Mach number and lift coefficient. For this reasons, many attempts and research have been concentrated from the 1960s, following the pioneering work of Whitcomb on supercritical airfoil [Whi74], with the objective of reducing the shock drag and increase the controllability in a range of Mach number without fully suppressing the shocks. Supercritical airfoils were designed to achieve higher drag rise Mach number by controlling the expansion of the flow to supersonic speed and its subsequent recompression without affecting the lifting performances (see Figure 9.1 (c)). Supercritical airfoils generally present a relatively large leading edge radius to expand the flow in the upper surface and obtaining more lift than conventional airfoils in the bow part (region near the leading edge). In addition to that, a flatter upper surface, compared to conventional airfoils, maintains the supersonic flow along a constant pressure plateau or even slow it down slightly approaching the shock. Thanks to that, a relatively weak shock is produced (see Figure 9.1 (b)). In some cases also an augmented aft camber (region near the trailing edge) can be employed to produce more lift than conventional airfoils. In Figure 9.3 we can observe the shape of the NASA-Langley Whitcomb integral supercritical airfoil compared with the RAE 2822 transonic airfoil and their relative drag coefficients for different Mach numbers.

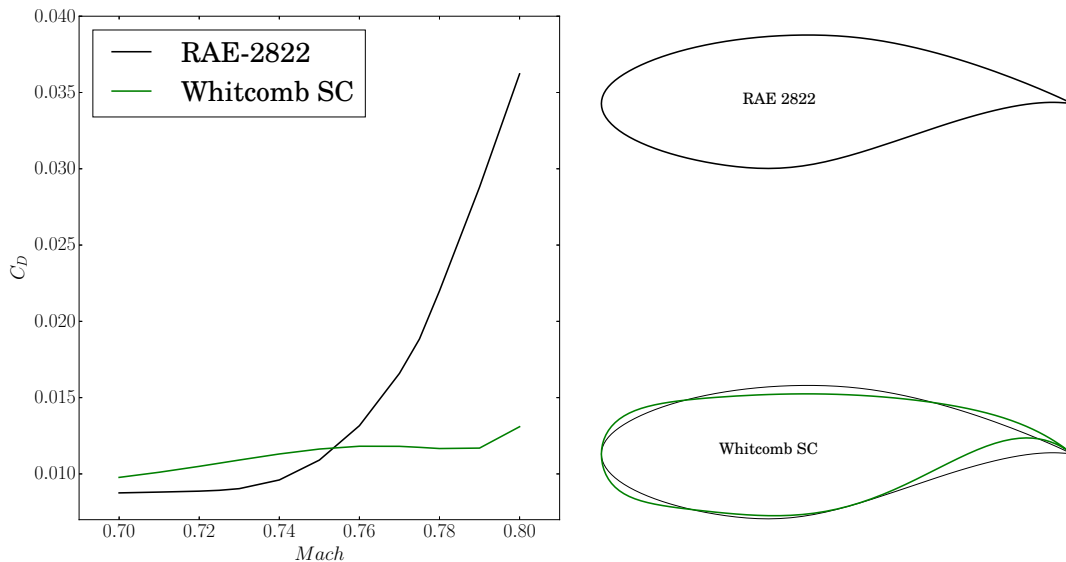


**Figure 9.3** – NASA-Langley Whitcomb integral supercritical airfoil and RAE 2882 transonic airfoil shapes and drag coefficients for different Mach number at fixed lift ( $C_L = 0.5$ ).

Although theoretically superior with respect to conventional airfoils, promising supercritical sections led to serious problems when actually incorporated into an aircraft wing. Practical

experiences revealed that some supercritical sections, as shock-free designs, are often very sensitive to Mach, lift and geometrical uncertainties and hence may perform dramatically poorly at off-design conditions.

Optimizing a transonic airfoil shape using classical deterministic optimization methodologies seeking optimality only in a single operating condition generally leads to the appearance of the so called *drag creep*, a situation in which the drag increases at Mach numbers below the designed value. On the other hand, multi-point optimization approaches, seeking optimality in multiple discrete operating points can alleviate the drag creep phenomenon but are unable to adequately remedy the problem of localized optimization [LH01].

In the following sections we introduce the notations and the formulations of deterministic and stochastic design optimization problem treated in this chapter.

## 9.2 Deterministic Shape Optimization

In a deterministic framework, the airfoil shape optimization problem consists of determining the set of geometric design parameters  $x$  that minimize (or maximize) a prescribed deterministic loss (or fitness in case of maximization) function  $\mathcal{D} : \mathbb{R}^q \rightarrow \mathbb{R}$

$$\text{SO-DO} : \begin{cases} \min_{x \in \mathbb{R}^n} \mathcal{D}[\mathbf{Q}_d^q(x, p)] \\ \text{s.t. } \mathcal{C}_i[\mathbf{Q}_c^m(x, p)] \leq k_i \quad i = 1, \dots, s \\ x_L \leq x \leq x_U \end{cases} \quad (9.1)$$

where

$$\mathbf{Q}_d^q(x, p) = [Q_d^1(x, p), \dots, Q_d^q(x, p)] \quad (9.2)$$

is the vector QoI that enter in the expression of the objective function and

$$\mathbf{Q}_c^m(x, p) = [Q_c^1(x, p), \dots, Q_c^m(x, p)] \quad (9.3)$$

is the vector (of dimension  $m$ ) of QoI subject to  $s$  constraints (defined by the functions  $\mathcal{C}_i : \mathbb{R}^m \rightarrow \mathbb{R}$ ,  $i = 1, \dots, s$ ).  $p$  is the vector of system parameters.

The set of design parameters  $x$ , defining the shape of the airfoil, is a vector of dimension  $n$ , with  $n$  being the number of design variables.  $x_L$  and  $x_U$  are lower and upper bounds of the design variables and the relation  $x_L \leq x \leq x_U$  should be interpreted component wise.

In this work we use as design parameters the set of PARSEC parameters or the position of control box nodes for an FFD box (see 2.4.3 for definitions).

**Definition 17.** *The feasible design space  $X$  is defined as the set  $X = \{x \in \mathbb{R}^n \mid \mathcal{C}_i [\mathbf{Q}_c^m(x, p)] \leq k_i, i = 1, \dots, s \text{ and } x_L \leq x \leq x_U\}$*

The loss function  $\mathcal{D}$  may involve one QoI or a wighted sum of more QoI  $Q_d$  as in the case of multi-point optimization.

We now define with  $\mathbf{D}^\Phi [\mathbf{Q}_d^q(x, p)]$ ,  $\mathbf{D}^\Phi : \mathbb{R}^q \rightarrow \mathbb{R}^\Phi$  a vector of loss functions:

$$\mathbf{D}^\Phi [\mathbf{Q}_d^q(x, p)] = [\mathcal{D}_1 [\mathbf{Q}_d^q(x, p)], \dots, \mathcal{D}_\Phi [\mathbf{Q}_d^q(x, p)]] \quad (9.4)$$

Using the same notation we can generalize (9.1) and define the multi-objective design optimization problem (MO-DO) as :

$$\text{MO-DO: } \begin{cases} \text{P-min}_{x \in \mathbb{R}^n} \mathbf{D}^\Phi [\mathbf{Q}_d^q(x, p)] \\ \text{s.t } \mathcal{C}_i [\mathbf{Q}_c^m(x, p)] \leq k_i \quad i = 1, \dots, s \\ x_L \leq x \leq x_U \end{cases} \quad (9.5)$$

where  $\Phi$  is the number of objective functions and P-min denotes all Pareto optimal values of  $\mathbf{D}^\Phi$  on the feasible set  $X \subset \mathbb{R}^n$ .

**Definition 18.** *A feasible point  $x^* \in X$  is Pareto optimal if and only if there does not exist another feasible point  $x \in X$  such that  $\mathbf{D}^\Phi [\mathbf{Q}_d^q(x, p)] \leq \mathbf{D}^\Phi [\mathbf{Q}_d^q(x^*, p)]$ , and  $\mathcal{D}_i [\mathbf{Q}_d^q(x, p)] < \mathcal{D}_i [\mathbf{Q}_d^q(x^*, p)]$  for at least one objective ( $i = 1, \dots, \Phi$ ).*

The main difference between SO-DO and MO-DO is that in the latter usually there is no single solution, but a set of points that fit a predetermined definition for optimum.

In airfoil shape design, one is generally interested in minimizing the drag coefficient of the airfoil or maximizing its lift-drag ratio. Constraints are generally imposed on the geometry of the airfoil, in order to achieve a final optimized shape that fulfill specific structural and mission requirements, and/or on the lift and moment coefficient. Examples of loss functions and constraints considered in this thesis are provided in the following Table 9.1. We indicate with  $L/D^{(M_\infty, \alpha_\infty)}$  the lift coefficient of the airfoil at prescribed Mach number  $M_\infty$  and angle of attack  $\alpha_\infty$ , while  $C_D^{(M_\infty, C_L^*)}$  and  $C_M^{(M_\infty, C_L^*)}$  respectively denote the drag and momentum coefficient at prescribed Mach number  $M_\infty$  and cruise lift coefficient  $C_L^*$ .

	Loss Functions	Constraints
SO (SP)	$\mathcal{D}[L/D] = L/D^{(M_\infty, \alpha_\infty)}$	geom.
SO (SP)	$\mathcal{D}[C_D] = C_D^{(M_\infty, C_L^*)}$	geom.
SO (MP)	$\mathcal{D}[C_D^w] = \sum_{i=1}^m w_i \cdot C_d^{(M_\infty^i, C_L^*)}$	geom.
MO	$\mathcal{D}[C_D, C_L] = \{C_D^{(M_\infty, C_L^*)}, C_L^{(M_\infty, C_L^*)}\}$	geom.

**Table 9.1** – Deterministic loss functions and constraints for airfoil shape optimization problems. (SP) indicate deterministic single point optimization problems solved for a single flight Mach number condition, while (MP) indicates multi point deterministic optimization problems.

### 9.3 Shape Optimization Under Uncertainties

The ever-increasing demand for aircrafts with better performance, higher reliability and robustness at lower cost requires optimization techniques seeking optimality under uncertain conditions that may arise during design, manufacture and operation of the vehicle. Indeed, the geometrical and operational parameters, that characterize aerodynamic systems, are naturally affected by aleatory uncertainties due to the intrinsic variability of the manufacturing processes and the surrounding environment.

Reducing the geometrical uncertainties due to manufacturing tolerances can be prohibitively expensive while reducing the operational uncertainties due to atmospheric turbulence in external aerodynamics is simply impossible.

**Optimization under uncertainty** (OUU) refers to a broad class of methodologies that address the following two problems:

- **Robust Design Optimization (RDO)**: focuses on the performances of a system under perturbations of the design conditions. Prescribed probabilistic measures of robustness (involving mean, variance or higher moments) as objective functions are used to "robustify" the design. The optimal design should, in this framework, be as much insensitive as possible to uncertain conditions meaning that its performance should not drop below a prescribed quality level. The final objective of RDO is to achieve an improvement of the performance of the system over the entire range of uncertain conditions [LHP02] by reducing the performance variability (a graphical interpretation of RDO is provided in Figure 9.4(a)).
- **Reliability-based Design Optimization (RBDO)**: focuses on safety-under-uncertainty aspects of the system. The most conservative and classical approach for RBDO is the worst-case analysis (also known as min-max strategy) that seeks a design with the best worst-case performance [Win94], [HPLL02]. More modern and advanced methodologies seek the optimization of an objective functions subject to probabilistic constraints that involve failure probability (quantiles, CVaR) or reliability indexes. The optimal de-

sign has, in this framework, a higher degree of confidence and guarantees a prescribed minimum level of reliability under uncertain conditions (a graphical interpretation of RBDO is provided in Figure 9.4(b)).

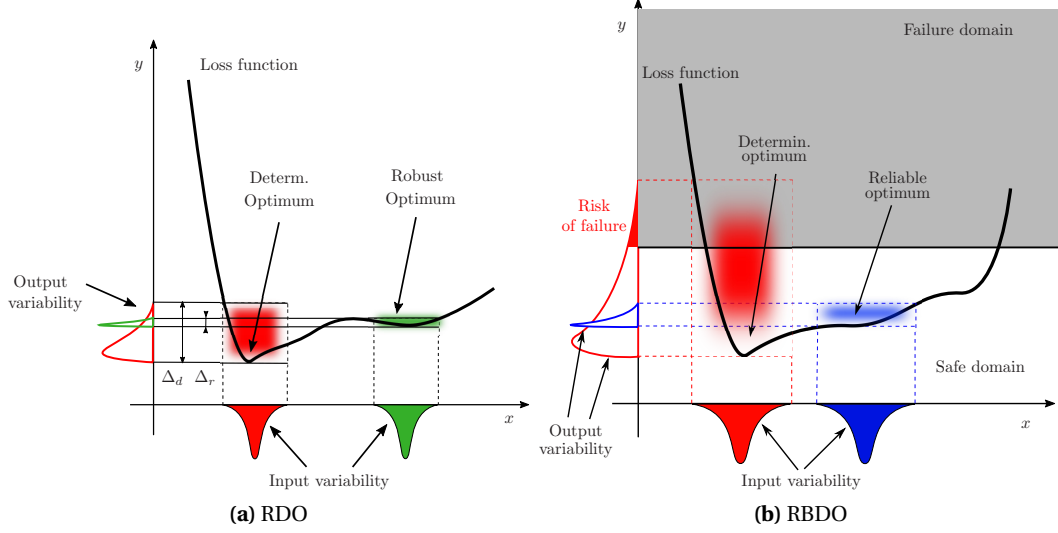


**Figure 9.4** – Graphical interpretation of robust design optimization (RDO) and reliability-based design optimization (RBDO).

In this work we present a general framework that can be employed to solve RDO and RBDO problems depending on the choice of objective functions and constraints.

A general formulation of a single objective optimization problem under uncertainties (SO-OUU) reads as follows:

$$\text{SO-OUU} : \begin{cases} \min_{x \in \mathbb{R}^n} \mathcal{R} [\mathbf{Q}_r^q(\tilde{x}(x, \omega), p(\psi))] \\ \text{s.t. } \mathcal{C}_i [\mathbf{Q}_c^m(\tilde{x}(x, \omega), p(\psi))] \leq k_i \quad i = 1, \dots, s \\ x_L \leq x \leq x_U \end{cases} \quad (9.6)$$

where

$$\mathbf{Q}_r^q(\tilde{x}(x, \omega), p(\psi)) = [Q_r^1(\tilde{x}(x, \omega), p(\psi)), \dots, Q_r^q(\tilde{x}(x, \omega), p(\psi))] \quad (9.7)$$

is the vector of dimension  $q$  of QoI affected by uncertainty that enter in the robust loss function and

$$\mathbf{Q}_c^m(\tilde{x}(x, \omega), p(\psi)) = [Q_c^1(\tilde{x}(x, \omega), p(\psi)), \dots, Q_c^m(\tilde{x}(x, \omega), p(\psi))] \quad (9.8)$$

the vector (of dimension  $m$ ) of QoI affected by uncertainty that are subject to  $s$  constraints.

$x$  is the vector of design variables. Its actual realization  $\tilde{x}(x, \omega)$  as well as the vector of system

parameters  $p(\psi)$  may be affected by uncertainties. The design vector belongs to  $\mathbb{R}^n$  with  $n$  being the number of design variables. We denote the uncertainties by  $\omega \in \Omega$  and  $\psi \in \Psi$ , where  $\Omega$  and  $\Psi$  are respectively the sample spaces of the design and system variables.  $\mathcal{R}$  is a robust loss function (or fitness in case of maximization) involving one or more QoI  $Q_r$  (e.g. weighted sum) that has to be optimized.  $\mathcal{C}_i$  denotes a set of deterministic and probabilistic constraints ( $s$  is the number of constraints) applied on the set of QoI  $\mathbf{Q}_c^m$ .  $x_L$  and  $x_U$  are lower and upper bounds of the design variables.

The loss function  $\mathcal{R}$  is a measure of robustness/reliability against the uncertainties in the design and system parameters.

Classical robust optimization approaches generally consider optimizing performance under 'worst-case' outcomes (min-max formulations). This approach is known to generally produce overly conservative designs with suboptimal performance in the uncertainty range.

In this work we consider different probabilistic loss functions and constraints that involve the weighted sums of central statistical moments, Value at Risk (VaR, also known as quantile) and Conditional Value at Risk (CVaR) of the quantities of interest that have to be optimized.

We now define with  $\mathbf{R}^\Phi [\mathbf{Q}_r^q(\tilde{x}(x, \omega), p(\psi))]$  a vector of  $\Phi$  robust loss functions:

$$\mathbf{R}^\Phi [\mathbf{Q}_r^q(\tilde{x}(x, \omega), p(\psi))] = [\mathcal{R}_1 [\mathbf{Q}_r^q(\tilde{x}(x, \omega), p(\psi))], \dots, \mathcal{R}_\Phi [\mathbf{Q}_r^q(\tilde{x}(x, \omega), p(\psi))]] \quad (9.9)$$

We can now further generalize (9.6) and define the multi-objective robust optimization problem under uncertainties (MO-OUU) as :

$$\text{MO-RDO} : \begin{cases} \text{P-min}_{x \in \mathbb{R}^n} \mathbf{R}^\Phi [\mathbf{Q}_r^q(\tilde{x}(x, \omega), p(\psi))] \\ \text{s.t } \mathcal{C}_i [\mathbf{Q}_c^m(\tilde{x}(x, \omega), p(\psi))] \leq k_i \quad i = 1, \dots, s \\ x_L \leq x \leq x_U \end{cases} \quad (9.10)$$

where  $\Phi$  is the number of objective functions and P-min denote all Pareto optimal values of  $\mathbf{R}^\Phi$  over  $X$ .

## 9.4 Continuation Multilevel Monte Carlo Evolutionary Algorithm

In this work we employ Single and Multi Objective Covariance Matrix Adaptation Evolutionary Strategies (CMA-ES) to solve the SO-OUU and MO-OUU problems presented above. We hereafter introduce the general idea of CMA-ES and we then introduce the modifications required to treat optimization problems under uncertainty. Finally we present a the full C-MLMC CMA-ES algorithm.



### 9.4.1 Covariance Matrix Adaptation Evolutionary Strategies (CMA-ES)

CMA-ES are a class of stochastic derivative-free evolutionary algorithms for numerical optimization of non-linear and non-convex black-box optimization problems introduced by Hansen [HO01].

Based on the principle of biological evolution, evolutionary algorithms, are characterized by the repeated interplay of variation and selection operators. At each generation (iteration of the algorithm) new individuals (candidate solutions) are generated by variation of the current parental individuals via recombination and possibly mutation. The individuals with the best fitness (objective function value) are then selected and become the parents in the next generation. Thanks to this repeated process, individuals with increasingly better fitness are generated.

In classical ES a new population of  $\lambda \geq 2$  candidate solutions is sampled at each generation according to a multivariate normal distribution in  $\mathbb{R}^n$ ,  $n$  being the number of design variables:

$$x_k^{(i+1)} \sim m^{(i)} + \sigma^{(i)} \mathcal{N}(0, C^{(i)}) \sim \mathcal{N}(m^{(i)}, (\sigma^{(i)})^2 C^{(i)}) \quad \text{for } k = 1, \dots, \lambda \quad (9.11)$$

where  $x_k^{(i+1)} \in \mathbb{R}^n$  denotes the  $k$ -th individual in generation  $i + 1$ ,  $m^{(i)} \in \mathbb{R}^n$  the mean of the distribution at generation  $i$ ,  $C^{(i)} \in \mathbb{R}^{n \times n}$  is a scaled covariance matrix of the distribution and  $\sigma^{(i)} \in \mathbb{R}$  is a scaling parameter (step-size).

The **recombination** operator is responsible of updating at each generation the mean value of the distribution (moving the mean of the distribution in the design space). Dependencies between the  $n$  variables in the distribution are represented by a covariance matrix. The covariance matrix adaptation (CMA) is a method to update the covariance matrix, the mean and the standard deviation of this distribution at each iteration.

The **adaptation** of the covariance matrix resembles the approximation of the inverse Hessian matrix in Quasi-Newton methods. The key difference to those methods is that fewer assumptions on the nature of the underlying objective function are made. Neither derivatives nor even the function values are required in the CMA-ES approach. Only a ranking between candidate solutions is exploited to adapt the covariance.

### 9.4.2 Practical aspects: Evolution meets C-MLMC

We developed and presented in Chapter 5, 6 and 7 a Continuation Multi Level Monte Carlo (C-MLMC) algorithm capable of efficiently computing statistics of all the required QoI. In a classical CMA-ES methodology, the deterministic objective function  $\mathcal{D}: \mathbb{R}^n \rightarrow \mathbb{R}$  is computed by solving the underlying deterministic problem with parameters prescribed by  $x_k$ . By combining the CMA-ES and our implementation of C-MLMC we are now able to optimally control

the cost required to compute each individual robust loss function, up to a prescribed tolerance, in the population of candidate solutions and guarantee a prescribed tolerance on the statistics of the QoIs that are required to compute the robust/reliable loss functions  $\mathcal{R} : \mathbb{R}^n \rightarrow \mathbb{R}$  and constraints.

### Sorting

At each generation  $i$ , once we have performed a C-MLMC simulation for each design  $x_k^{(i)}$ , we sort the candidate solutions according to their robust/reliable loss function:

$$\mathcal{R}\left(x_{\pi(l)}^{(i)}\right) \leq \mathcal{R}\left(x_{\pi(k)}^{(i)}\right) \quad l \leq k \quad (9.12)$$

where  $\pi(\cdot)$  is the permutation of  $\{1, \dots, \lambda\}$  providing the ordering.

### Selection and Recombination

In order to update the mean of the distribution for the next generation, we now follow the procedure of Hansen [Han16]. The new mean is simply the weighted average of the best  $\xi < \lambda$  candidates:

$$m^{(i+1)} = \sum_{k=1}^{\xi} w_k x_{\pi(k)}^{(i)} = m_i + \sum_{k=1}^{\xi} w_k (x_{\pi(k)}^{(i)} - m_i), \quad \sum_{k=1}^{\xi} w_k = 1 \quad (9.13)$$

where  $w_k$ ,  $k = 1, \dots, \xi \in \mathbb{R}_{>0}$  are positive weight. In our implementation we choose  $w_k = \frac{1}{\xi}$  and  $\xi = \frac{1}{4}\lambda$  to avoid extremely fast convergence of the algorithm towards a local minimum. Different alternatives for the weights and the number best candidate solutions considered to update the mean are available depending on the complexity and dimensionality of the problem.

### Adaptation of the covariance

In order to introduce the concept of covariance adaptation, let us consider the population of  $\lambda$  candidates at generation  $i + 1$  and the following unbiased estimator for the covariance matrix  $\sigma^{(i)2} C^{(i+1)}$ :

$$\hat{C}_{\lambda}^{(i+1)} = \frac{1}{\lambda} \sum_{k=1}^{\lambda} \left(x_k^{(i+1)} - m^{(i)}\right) \left(x_k^{(i+1)} - m^{(i)}\right)^T \quad (9.14)$$

where  $T$  denotes the transpose.

Following the same *weighted selection* argument used for the mean in (9.13), we can define a

covariance estimator based only on the best  $\xi$  individuals as:

$$\hat{C}_\xi^{(i+1)} = \sum_{k=1}^{\xi} w_k \left( x_{\pi(k)}^{(i+1)} - m^{(i)} \right) \left( x_{\pi(k)}^{(i+1)} - m^{(i)} \right)^T. \quad (9.15)$$

The key difference between (9.14) and (9.15) is that the former estimates the covariance between the so called *sampled steps*  $x_k^{(i+1)} - m^{(i)}$  in the population, while the latter just consider the best (successful)  $\xi$  selected steps. Hence, sampling from  $C_\xi^{(i+1)}$  will promote the reproduction of successful steps.

In order to achieve an effective adaptation of the covariance, information from previous generations should be included. Indeed, after a sufficient number of generations, the scaled covariance matrix could be estimated as an average over all generations of the estimates  $\hat{C}^{(i+1)}/\sigma^{(i)2}$ :

$$C^{(i+1)} = \frac{1}{i+1} \sum_{j=0}^i \frac{1}{\sigma^{(j)2}} \hat{C}_\xi^{(j+1)} \quad (9.16)$$

where the variance  $\sigma^{(j)}$  has been included in order to make the covariances of different generations comparable. In (9.16), all generation steps have the same weight. To assign to the most recent generations a higher weight, exponential smoothing and an appropriate *learning rate*  $0 < c_\xi \leq 1$  are introduced:

$$\begin{aligned} C^{(i+1)} &= (1 - c_\xi) C^{(i)} + c_\xi \frac{1}{\sigma^{(i)2}} C_\xi^{(i+1)} \\ &= (1 - c_\xi) C^{(i)} + c_\xi \sum_{k=1}^{\xi} w_k y_{\pi(k)}^{(i+1)} y_{\pi(k)}^{(i+1)T} \end{aligned} \quad (9.17)$$

and  $y_{\pi(k)}^{(i+1)}$  reads as follow:

$$y_{\pi(k)}^{(i+1)} = \frac{x_{\pi(k)}^{(i+1)} - m^{(i)}}{\sigma^{(i)}} \quad (9.18)$$

In our simulation we choose the learning rate for updating the covariance matrix as  $c_\xi = \frac{\xi}{4}$ . The covariance matrix update in (9.17) is called rank- $\xi$ -update as the sum of outer products is of rank  $\min(\xi, n)$  with probability one [HMK03].

### Step size control

The last step required in order to make the C-MLMC CMA-ES algorithm effective is the control of the step-size  $\sigma^{(i)}$  (that appears in (9.18)), in other words the *scale* of the distribution. In addition to the previously presented adaptation rule, Hansen proposed an approach to control the step size based on the concept of cumulative step-size control, or cumulative step length

adaptation (CSA). The interested reader can consult [Han16] for further details. Practically, the step-size is updated as:

$$\sigma^{(i+1)} = \sigma^{(i)} \exp\left(\frac{c_\sigma}{d_\sigma} \left(\frac{\|p_\sigma^{(i+1)}\|}{\alpha(n)} - 1\right)\right) \quad (9.19)$$

where  $\alpha(n) = \mathbb{E} \|z\|$  with  $z \sim \mathcal{N}(0, I)$ ,  $d_\sigma \approx 1$  is a damping parameter used to scales the change magnitude of  $\sigma^{(i)}$  and  $p_\sigma \in \mathbb{R}^n$  is called evolution path and denotes a sequence of of successive steps over a number of generations:

$$p_\sigma^{(i+1)} = (1 - c_\sigma)p_\sigma^{(i)} + \sqrt{c_\sigma(2 - c_\sigma)} \frac{\lambda}{4} \left(C^{(i)}\right)^{-1/2} \frac{m^{(i+1)} - m^{(i)}}{\sigma^{(i)}}. \quad (9.20)$$

Finally,  $c_\sigma$  is a backward time horizon of the evolution path that we choose to be equal to  $\sqrt{n}$

### 9.4.3 C-MLMC CMA-ES Algorithm

In the following Algorithm 4 we denote with  $i_{max}$  the maximum number of iterations (generation) of the algorithm,  $\epsilon$  a vector of size  $i_{max}$  that defines how the tolerance of the C-MLMC algorithm should be reduced during the optimization loop.

The same strategy and updates presented above can be effectively applied and extended to tackle multi objective optimization problems. However, a multi-objective selection approach should be introduced at the sorting and selection step of the algorithm. We follow the approach of Igel [IHR07] and apply a non-dominated sorting methodology based on the crowding-distance.

## 9.5 Application to Single-Objective Optimization Under Uncertainties

The above presented methodology is now applied to single objective optimization of the RAE-2822 airfoil under operating and geometric uncertainties. We first introduce the MLMC grid hierarchy and deterministic solver employed to compute the performances of the airfoil. Afterwards, we present the single objective optimization problems under uncertainties (solved with different robust/reliable objective functions) and we compare the results with the solution of the corresponding deterministic optimization problems.

**MLMC Grid Hierarchy and Deterministic Solver** In this section we employ a 4-levels structured grid hierarchy for the C-MLMC simulations. The features of the grid levels are presented in Table 9.2 along with the average computational time required to compute one deterministic simulation (on one CPU) using the MSES collection of programs for the analysis of airfoils

---

**Algorithm 4:** C-MLMC CMA-ES for Robust Optimization.
 

---

**CMA-ES**( $\lambda, \sigma_0, m_0, i_{MAX}, \boldsymbol{\epsilon}$ )  
**Initialize**( $i = 0, C_i = I, m_i = m_0, \sigma_i = \sigma_0$ )  
**while** (*Stop-criteria*) **OR**  $i < i_{MAX}$  **do**  
     **for**  $k = 1, \dots, \lambda$  **do**  
          $x_k \sim \mathcal{N}(m_i, \sigma_i^2 C_i)$   
          $\epsilon_i = \boldsymbol{\epsilon}[i]$   
         **C-MLMC**( $\mathbf{Q}_r^q, \mathbf{Q}_c^m, \epsilon_i, x_k$ )  
             **return**  $\mathcal{R}_k[\mathbf{Q}_r^q(\tilde{x}_k(x_k, \omega), p(\psi))], \mathcal{C}_k[\mathbf{Q}_c^m(\tilde{x}_k(x_k, \omega), p(\psi))]$   
     **Sort:** best  $\xi$  candidates out of  $\lambda$  (9.12)  
     **Mean  $m$  update** based on  $\xi$  candidates using (9.13)  
     **Step-size  $\sigma$  update:** using (9.19)  
     **Covariance  $C$  update** using (9.17)  
     **Generation:**  $i = i + 1$   
**return**  $\xi$  candidates  
  
**C-MLMC**( $Q_r, Q_c, \epsilon_i, x_k$ )  
**Apply uncertainties on design**  $x_k \rightarrow \tilde{x}_k(x_k, \omega)$   
**compute** C-MLMC iterations  $i_E$  using (5.2)  
**while** ( $j < i_E$ ) **AND** ( $\epsilon_j > \epsilon_i$ ) **do**  
     **compute** ( $L^{(j)}, \theta^{(j)}$ )  
     **compute**  $\{N_l^{(j)}\}_{l=0}^{L^{(j)}}$  to satisfy  $\epsilon^{(j)}$   
     **MLMC**( $L^{(j)}, \{N_l^{(j)}\}_{l=0}^{L^{(j)}}$ )  
     **update** C-MLMC parameters using (5.12)  
      $j = j + 1$   
**return**  $\mathcal{R}_k[Q_r(\tilde{x}_k(x_k, \omega), p(\psi))], \mathcal{C}_k[Q_c(\tilde{x}_k(x_k, \omega), p(\psi))]$

---

[Dre07]. MSES solves the steady Euler equations with a finite volume discretization over a streamline grid and is coupled, via the displacement thickness, with a two-equation integral solver for the viscous regions of the boundary layer and trailing wakes.

LEVEL	Airfoil nodes	Cells	CTime[s]
L0	47	1739	1.9
L1	71	2627	3.2
L2	107	3959	5.7
L3	161	5957	7.5
L4	243	8991	14.7

**Table 9.2** – MLMC 5-levels grid hierarchy for the RAE2822 problem.

### 9.5.1 Maximization of Lift-Drag Ratio

**Deterministic Single Point Maximization of Lift-Drag ratio at fixed Angle: SP-DO1** An interesting problem that arises during the preliminary stage of the design process is the maximization of the lift-drag ratio  $L/D$  of the airfoil for a specific combination of angle of attack and Mach number. We can particularize the SO-DO in (9.1) for a specific cruise Mach number condition  $M_\infty$  and angle of attack  $\alpha_\infty$  (see Table 9.3 column "reference") and define the following single point deterministic shape optimization problem:

$$\text{SO-DO1} : \begin{cases} \max_{x \in X} L/D^{(M_\infty, \alpha_\infty)}(x, p) \\ \text{s.t. } x_L \leq x \leq x_U \end{cases} \quad (9.21)$$

In the feasible design space  $X$ , we constrain the shape of the airfoil by requiring enough space for the fuel/torque box (see Figure 9.5) and the final shape to be at least 75% of the original section of the RAE-2822.

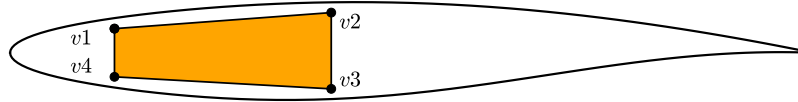


Figure 9.5 – Geometrical trapezoid box constraint.

The coordinates of the box vertex are:  $v1 = (0.13, 0.03)$ ,  $v2 = (0.4, 0.05)$ ,  $v3 = (0.4, -0.045)$ ,  $v4 = (0.13, -0.03)$ . This is a reasonable requirement to build an aircraft wing with an appropriate inner volume to accommodate the fuel tank and a torque box. Additionally such requirement naturally rejects, from the population of candidate individuals, all degenerate airfoil shapes.

The design parameters  $x$  are the PARSEC coefficients (see 2.4.3 for definition).

**Robust Single Objective Maximization of Lift-Drag ratio: SO-RDO1** Instead of solving the optimization problem for a single combination of Mach number and angle of attack, as in SP-DO1 (see 9.21), we now consider the problem of robustly optimize the shape of the RAE-2822 airfoil affected by operating (system parameters  $p(\psi)$ , Mach number and angle of attack in Table 9.3) and geometric uncertainties (Table 9.4) at the same time. The operating uncertainties considered in this problem are representative of mild atmospheric gust that an aircraft may encounter during cruise. The geometric uncertainties, on the other hand, are representative of manufacturing tolerances.

The geometric uncertain set and the design set are the PARSEC coefficients of the airfoil (see Table 9.4). All uncertain parameters are modeled as truncated Gaussian random variables (see definition in Eq. (4.22)).

The design parameters  $x$  are the PARSEC parameters in Table 9.4 (column "PARSEC (r)"). In

## 9.5. Application to Single-Objective Optimization Under Uncertainties

	Quantity	Reference ( $r$ )	Uncertainty
Operating parameters	$\alpha_\infty$	2.31	$\mathcal{T}\mathcal{N}(r, 2\%r, -2\%r, +2\%r)$
	$M_\infty$	0.730	$\mathcal{T}\mathcal{N}(r, 2\%r, -2\%r, +2\%r)$
	$Re_c$	$6.5 \cdot 10^6$	–
	$p_\infty$ [Pa]	101325	–
	$T_\infty$ [K]	288.5	–

**Table 9.3** – Operating parameters and uncertainties for the RAE2822 problem.

	Quantity	PARSEC( $r$ )	Uncertainty	Design range
Geometric parameters	$R_s$	0.00839	$\mathcal{T}\mathcal{N}(r, 1\%r, -1\%r, +1\%r)$	[70% $r$ , 130% $r$ ]
	$R_p$	0.00853	$\mathcal{T}\mathcal{N}(r, 1\%r, -1\%r, +1\%r)$	[70% $r$ , 130% $r$ ]
	$x_s$	0.431	$\mathcal{T}\mathcal{N}(r, 1\%r, -2\%r, +2\%r)$	[50% $r$ , 150% $r$ ]
	$x_p$	0.346	$\mathcal{T}\mathcal{N}(r, 1\%r, -2\%r, +2\%r)$	[50% $r$ , 150% $r$ ]
	$y_s$	0.063	$\mathcal{T}\mathcal{N}(r, 1\%r, -2\%r, +2\%r)$	[70% $r$ , 130% $r$ ]
	$y_p$	-0.058	$\mathcal{T}\mathcal{N}(r, 1\%r, -2\%r, +2\%r)$	[70% $r$ , 130% $r$ ]
	$C_s$	-0.432	$\mathcal{T}\mathcal{N}(r, 1\%r, -1\%r, +1\%r)$	[50% $r$ , 150% $r$ ]
	$C_p$	0.699	$\mathcal{T}\mathcal{N}(r, 1\%r, -1\%r, +1\%r)$	[50% $r$ , 150% $r$ ]
	$\theta_s$	-11.607	–	–
	$\theta_p$	-2.227	–	–

**Table 9.4** – PARSEC parameters of the RAE2822 airfoil, and geometric uncertainties applied on the shape and design range for the geometric parameters.

the actual stage of the airfoil, uncertainty is added to those parameters (see Table 9.4 column "uncertainty")

Instead of using a deterministic loss function, as in SO-DO1, we consider here a robust loss function defined as the difference of the mean and the standard deviation of the lift-drag ratio  $L/D$  of the airfoil.

$$\text{SO-RDO1} : \begin{cases} \max_{x \in X} \mathcal{R} [L/D(\tilde{x}(x, \omega), p(\psi))] = \mu_{L/D}(\tilde{x}(x, \omega), p(\psi)) - \sigma_{L/D}(\tilde{x}(x, \omega), p(\psi)) \\ s.t. \ x_L \leq x \leq x_U \end{cases} \quad (9.22)$$

In the feasible design space we constraint, as in the deterministic problem SO-DO1, the shape of the airfoil by requiring enough space for the fuel/torque box (see Figure 9.5) and the final shape to be at least 75% of the original section of the RAE-2822. It is worth underline that the geometrical constraint is enforced only on the deterministic shape  $x$ , not on the perturbed one  $\tilde{x}$ .

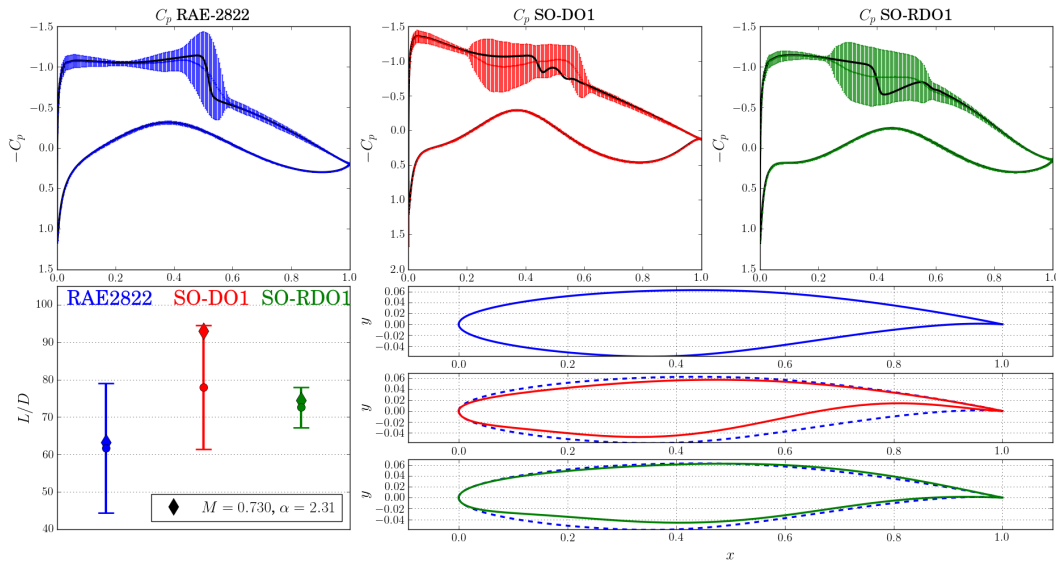


**Figure 9.6** – Performances of the SO-RDO1 and SO-DO1 airfoil compared with the original RAE-2822. The upper plots present the uncertain  $C_p$  profile of the airfoils under operating and geometric uncertainties. The lower plots present the  $L/D$  variation (mean  $\pm$  two standard deviations). The diamond symbol represents the performance of the airfoil at design condition (airfoil operating at  $M_\infty = 0.730$ ,  $\alpha_\infty = 2.31$ ).

**Comparison of Optimized Shapes** In Figure 9.6 and Table 9.5 we present the result of the robust (SO-RDO1) and deterministic (SO-DO1) optimization of the  $L/D$  ratio. We can observe that the deterministically optimized airfoil is able to achieve the best performance at design condition however the  $L/D$  ratio is highly sensitive to small variations of the geometry and operating conditions.

The robust airfoil is equipped with a relatively large leading edge and much wider pressure side trailing edge angle. The quasi constant pressure plateau and the large aft chamber, compared to the SO-DO2, are capable to reduce the  $L/D$  dispersion.

	RAE2822	SO-DO1	SO-RDO1
$M = 0.729$ $\alpha = 2.31$ Fixed Geom.	$L/D = 63.2$	<b><math>L/D = 92.8</math></b>	$L/D = 74.5$
$M = \mathcal{FN}(r, 2\%, -2\%, +2\%)$ $\alpha = \mathcal{FN}(r, 2\%, -2\%, +2\%)$ Uncertain Geom.	$L/D = 61.7$ $\pm 8.6$ (14%)	<b><math>L/D = 77.9</math></b> $\pm 8.2$ (10.5%)	$L/D = 72.9$ $\pm 2.6$ (3.5%)

**Table 9.5** – Performances and variabilities (mean  $\pm$  two standard deviations) of the SO-DO2 and SO-RDO2 airfoil compared with the original RAE-2822 at design conditions and when they operate in an uncertain environment.



### 9.5.2 Minimization of Drag Coefficient

In a later stage of the design process, when structural considerations are introduced and the aircraft mission is appropriately defined, we might have tighter geometrical constraints and we are required to match a specific cruise lift condition.

**Deterministic Single Point Minimization of Drag at fixed Lift: SO-DO2 (SP)** We can particularize SO-DO (9.1) problem for a specific cruise Mach number condition  $M_\infty$  and lift coefficient  $C_L^*$  and define the following single point deterministic shape optimization problem:

$$\text{SO-DO2 (SP)} : \begin{cases} \min_{x \in X} C_D^{(M_\infty, C_L^*)}(x, p) \\ \text{s.t. } x_L \leq x \leq x_U \end{cases} \quad (9.23)$$

It is worth underline that in order to enforce the  $C_L^*$  constraint on each design candidate, we compute for each of them a converged solution with an initial angle of attach  $\alpha$  that we then gradually increase/decrease in order to match the prescribed lift coefficient.

The constraints in  $X$  are now imposed on the thickness of the airfoil in order to attain a shape capable of matching the required structural requirements. In our simulations we set the thickness of the airfoil to match exactly that of the original RAE-2822 airfoil (see Figure 9.7 for comparison of optimal and initial reference RAE2822 airfoil).

Also for this problem, the design parameters  $x$  are the PARSEC coefficients (see 2.4.3 for definition).

As presented in [Dre98], such optimization problems generally lead to airfoil shapes that are optimal only in a narrow range of Mach numbers (leading to so called *localized optimization*). The optimal shape will generally be shock-less and/or will present a bump in a specific location in order to fill the transitional separation bubble to reduce the drag in the specific cruise condition. The performance of such shapes degrades quite fast away form the design conditions as the bump location and the curvature of the airfoil are not able to avoid the shock and/or fill the separation bubble for other combinations of Mach number and lift coefficient. Additionally if the geometry of the airfoil is affected by uncertainties due to manufacturing tolerances and/or temporary factors such as icing or aeroelastic deformation of the wing, the shape can be ineffective even in the prescribed design conditions.

Figure 9.7 presents the results of single point optimization of the RAE 2822 airfoil for different cruise Mach number ( $M = 0.7, 0.725, 0.75, 0.775, 0.8$ ) and fixed  $C_L^* = 0.5$ .

**Multi Point Minimization of Drag at fixed Lift: SO-DO2 (MP)** An intuitive approach to improve off-design performances of transonic airfoils, generally denoted as multi-point opti-

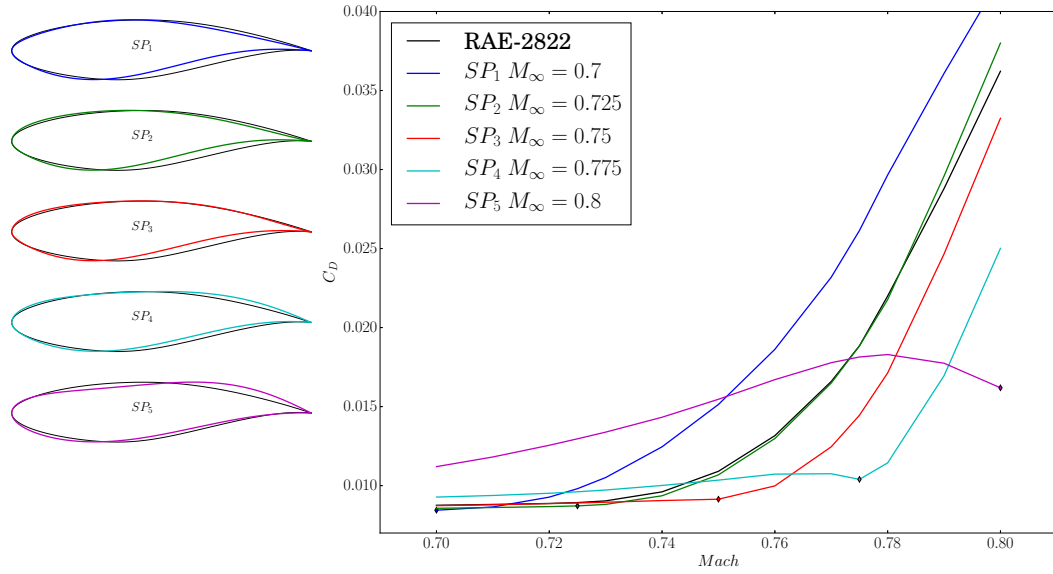


**Figure 9.7** – Single Point optimization of the RAE 2822 airfoil for different cruise Mach number and fixed  $C_L^* = 0.5$ . The thickness of the airfoils is constrained to be the same as the original RAE 2822 airfoil, while the other PARSEC geometrical parameters are free.

mization, is based on trade off between different design conditions [Cam98] [EP98].

Instead of optimizing an objective function for a single discrete flight condition as in SP-DO1 (9.23), we can consider a weighted linear combination of  $m$  flight conditions:

$$\text{SO-DO2 (MP)} : \begin{cases} \min_{x \in X} \sum_{i=1}^m w_i \cdot C_D^{(M_\infty^i, C_L^*)}(x, p) \\ \text{s.t. } x_L \leq x \leq x_U \end{cases} \quad (9.24)$$

The number of  $m$  flight conditions, the choice of  $M_\infty^i$  and the wights  $w_i$  are determined by the designer in order to fulfill specific performance or mission requirements (no sound theoretical principles are available for these choices). Empirical sophisticated ways of choosing multi point flight conditions and their weights can be found in [LKM14].

In this analysis we choose two, three and five equally weighted flight conditions between  $M_\infty = 0.7$  and  $0.8$  for the design respectively denoted as  $MP_2^U$ ,  $MP_3^U$ ,  $MP_5^U$  in Figure 9.8. Additionally we also consider three and five flight conditions weighted using the area underlying a symmetric beta distribution centered in  $M_\infty = 0.75$  ( $\mathcal{B}(2, 2, 0.1, M_\infty - 0.05)$ ) for the designs  $MP_3^\beta$ ,  $MP_5^\beta$  (see Table 9.6).

Figure 9.8 presents the results of the multi point shape optimization of the RAE 2822 airfoil for different cruise Mach number ( $M = 0.7, 0.725, 0.75, 0.775, 0.8$ ) and fixed  $C_L^* = 0.5$ .

A critical discussion is postponed to the next section where these results are also compared to

## 9.5. Application to Single-Objective Optimization Under Uncertainties

MP Design	Flight conditions ( $M_\infty^l$ )	Weights ( $w_i$ )
$MP_2^U$	0.7, 0.8	0.5, 0.5
$MP_3^U$	0.7, 0.75, 0.8	1/3, 1/3, 1/3
$MP_3^\beta$	0.7, 0.75, 0.8	0.15625, 0.6875, 0.15625
$MP_5^U$	0.7, 0.725, 0.75, 0.775, 0.8	1/5, 1/5, 1/5, 1/5, 1/5
$MP_5^\beta$	0.7, 0.725, 0.75, 0.775, 0.8	0.04296875, 0.2734375, 0.3671875, 0.2734375, 0.04296875

**Table 9.6** – Flight conditions and weight for deterministic multi point optimization.

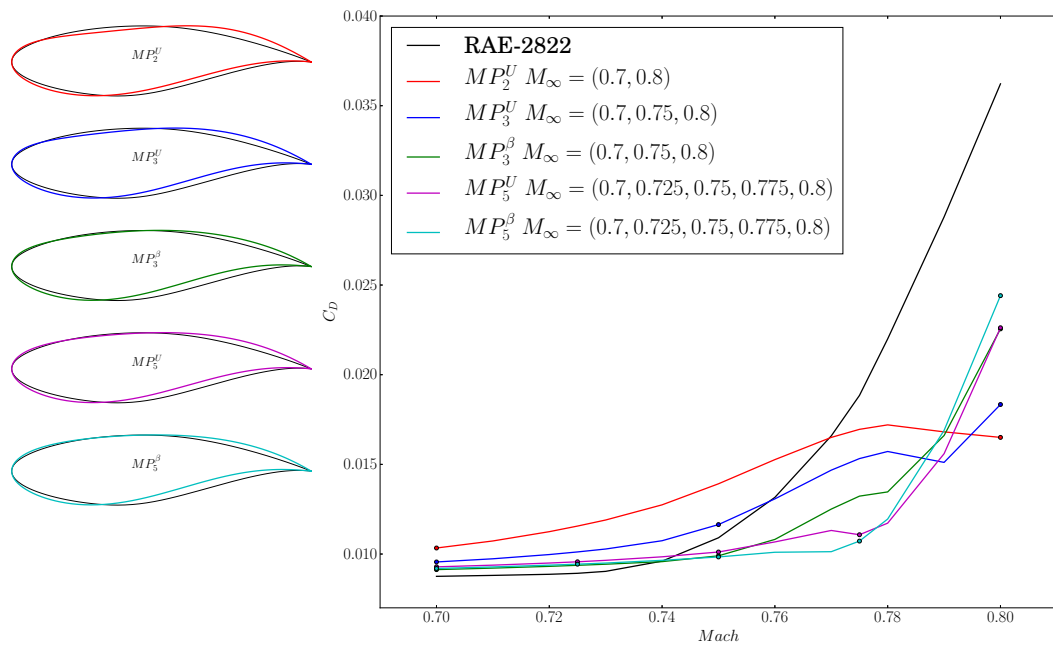


**Figure 9.8** – Multi Point optimization of the RAE 2822 airfoil for different choices of cruise Mach number and weights (fixed  $C_L^* = 0.5$ ). The thickness of the airfoils is constrained to be the same as the original RAE 2822 airfoil, while the other PARSEC geometrical parameters are free.

those obtained in the OUU case.

**Robust and Reliable Single Objective Minimization of Drag: SO-RDO2** Instead of solving the optimization problem for a single combination of Mach number and lift coefficient, as in SP-DO2 (see 9.23), or a weighted sum of flight conditions, as in MP-DO2 (see 9.24), we now consider the problem of optimizing the shape of the RAE-2822 airfoil affected by uncertainties using different robust and reliable loss functions.

The operating uncertainty, namely the Mach number, is modeled as a beta distribution denoted by  $\mathcal{B}(a, b, s, loc)$ , where  $a$  and  $b$  are the distribution parameters. As the beta distribution is defined on the  $[0, 1]$  interval, the parameters  $s$  and  $loc$  are used to scale and shift the distri-

bution's support, respectively (see Table 9.7).

	Quantity	Reference ( $r$ )	Uncertainty
Operating parameters	$C_L$	0.5	–
	$M_\infty$	0.75	$\mathcal{B}(2, 2, 0.1, M_\infty - 0.05)$
	$Re_c$	$6.5 \cdot 10^6$	–
	$p_\infty [Pa]$	101325	–
	$T_\infty [K]$	288.5	–

Table 9.7 – Operating parameters and uncertainties for the RAE2822 problem.

The operating uncertainties considered in this problem are representative of atmospheric fluctuations during a flight mission (see discussion in 2.4.1). The reference nominal PARSEC parameters are presented in Table 9.8 together with the design space range for the geometric parameters. No geometrical uncertainties are considered in this case.

	Quantity	PARSEC - RAE-2822( $r$ )	Design range
Geometric parameters	$R_s$	0.00839	$[70\%r, 130\%r]$
	$R_p$	0.00853	$[70\%r, 130\%r]$
	$x_s$	0.431	$[50\%r, 150\%r]$
	$x_p$	0.346	$[50\%r, 150\%r]$
	$y_s$	0.063	–
	$y_p$	–0.058	–
	$C_s$	–0.432	$[50\%r, 150\%r]$
	$C_p$	0.699	$[50\%r, 150\%r]$
	$\theta_s$	–11.607	$[50\%r, 150\%r]$
	$\theta_p$	–2.227	$[50\%r, 150\%r]$

Table 9.8 – PARSEC parameters of the RAE2822 airfoil and feasible design space range for the geometric parameters.

In order to compare the advantages and effectiveness of different probabilistic loss functions we consider here the following optimization problem:

$$\text{SO-RDO2: } \begin{cases} \min_{x \in X} \mathcal{R} [C_D(x, p(\psi))] \\ \text{s.t. } C_L(x, p(\psi)) = C_L^* \quad x_L \leq x \leq x_U \end{cases} \quad (9.25)$$

and define the following loss functions:

**Comparison of Optimized Shapes** In Figure 9.9 we present the pressure coefficient and shape of the deterministic optimized shapes (SP and MP) and the robust/reliable obtained

## 9.5. Application to Single-Objective Optimization Under Uncertainties

---

$\mathcal{R}_\mu [C_D]$	$\mu_{C_D}(\tilde{x}(x, \omega), p(\psi))$
$\mathcal{R}_{\mu, \sigma} [C_D]$	$\mu_{C_D}(x, p(\psi)) + \sigma_{C_D}(\tilde{x}(x, \omega), p(\psi))$
$\mathcal{R}_{\mu, \sigma, \gamma} [C_D]$	$\mu_{C_D}(x, p(\psi)) + \sigma_{C_D}(x, p(\psi)) + (\mu_{C_D}(x, p(\psi)) \cdot \gamma_{C_D}(x, p(\psi)))$
$\mathcal{R}_{VaR^{90}} [C_D]$	$VaR_{C_D}^{90}(x, p(\psi))$
$\mathcal{R}_{CVaR^{90}} [C_D]$	$CVaR_{C_D}^{90}(x, p(\psi))$

**Table 9.9** – Probabilistic loss functions for problem SO-RDO2.

shapes with different probabilistic loss function (Table 9.9) under operating uncertainties presented in Table 9.7.

The first observation we can draw from Figure 9.9 is that MP designs are able to effectively reduce the variability in the pressure coefficient compared to SP designs. Indeed, we can observe, in particular for  $M_5^U$  and  $M_5^\beta$ , quasi constant pressure plateau on the suction side of the airfoils, capable of reducing the intensity of the shock wave. The geometries of  $M_5^U$  and  $M_5^\beta$  are characterized by relatively large leading edge radius, low curvature suction side and an increased aft chamber. The pressure profile and the geometry of the airfoil obtained by minimizing just the expectation of drag coefficient  $\mathcal{R}_\mu [C_D]$  appear very similar to  $M_5^\beta$ . This is indeed justified by the choice of weights in  $M_5^\beta$  that mimic an empirical mean on five flight conditions. On the other hand the airfoils obtained by minimizing the CVaR of  $C_D$   $\mathcal{R}_{CVaR^{90}} [C_D]$  as well as those obtained by minimizing the first three statistical moments  $\mathcal{R}_{\mu, \sigma, \gamma} [C_D]$  seem to promote the development of the shock in the front part of the airfoil in order to reduce the variability in the aft part of it.

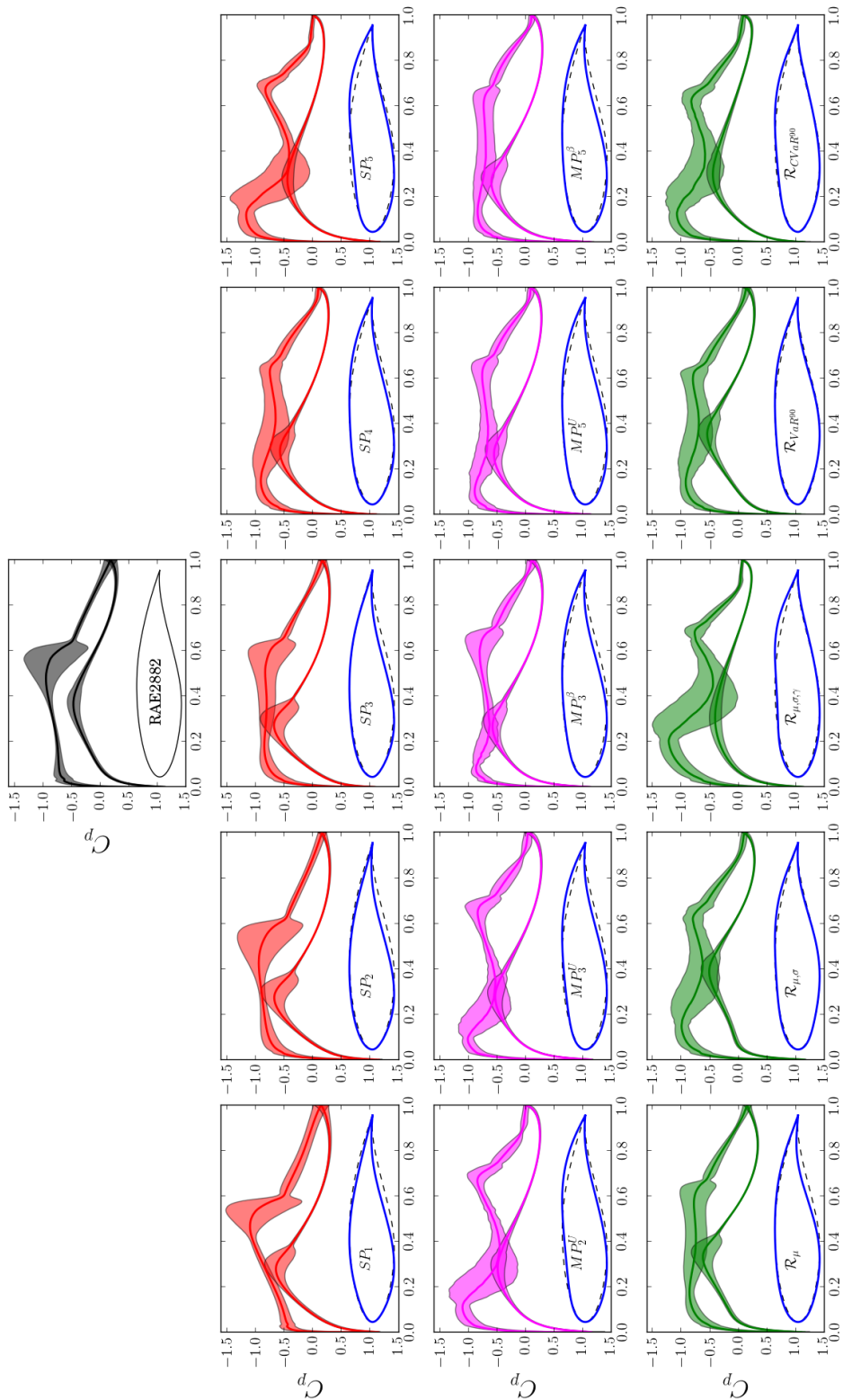


**Figure 9.9** – Pressure coefficient  $C_p$  (mean  $\pm$  two standard deviations) and shape of the RAE 2822 (in black), the deterministic optimized shapes (SP in red and MP in magenta) and robust/reliable shapes obtained with different probabilistic loss functions (in green) under operating uncertainties.

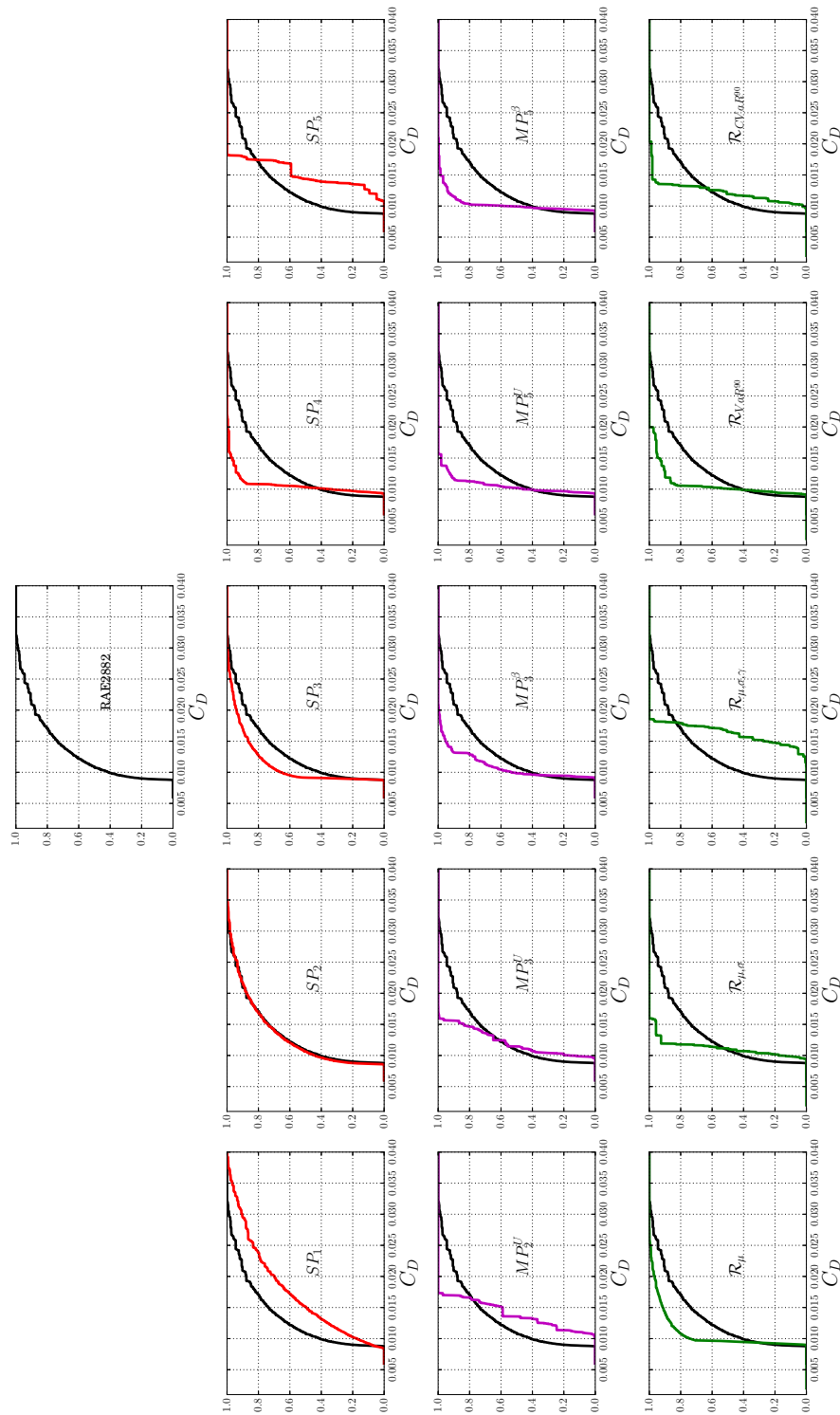


**Figure 9.10** – CDF of the drag coefficient  $C_D$  of the RAE 2822 (in black), the deterministic optimized shapes (SP in red and MP in magenta) and robust/reliable shape obtained with different probabilistic loss functions (in green) under operating uncertainties.

In order to effectively analyze the performances of the deterministic and robust/reliable optimized shapes in the uncertain environment, we present in Figure 9.10 the CDFs of the drag coefficient  $C_D$  computed using the MLMC methodology presented in Chapter 7. We can observe, as underlined above for the  $C_p$ , that MP designs are able to reduce the variability in the drag coefficient compared to SP designs. The airfoil obtained by minimizing the first three statistical moments  $\mathcal{R}_{\mu,\sigma,\gamma}[C_D]$  presents an heavy tail on the side of low drag and seems the most reliable candidate. The airfoil obtained with VaR minimization  $\mathcal{R}_{VaR^{90}}[C_D]$  is indeed the candidate that have the lowest 90%-quantile  $C_D$  but presents an heavy tail on the side of high drag. On the other hand, the airfoil obtained with CVaR minimization  $\mathcal{R}_{CVaR^{90}}[C_D]$  is able to effectively control the tail of the distribution at the price of an higher mean value of  $C_D$ .

## 9.6 Application to Multi-Objective Optimization Under Uncertainties

In this section, the above presented methodology is applied to multi objective optimization under uncertainties of the RAE-2822 airfoil.

### 9.6.1 Optimization of Lift and Drag

**Deterministic Multi Objective Optimization of Lift and Drag: MO-DO1** We now consider two competing objectives to be optimized simultaneously, namely minimize the drag coefficient  $C_D$  maximize the lift coefficient  $C_L$  for a specific combination of Mach number and angle of attack:

$$\text{MO-DO1 : } \begin{cases} \text{P-min}_x \{C_D^{(M_\infty, C_L^*)}(x, p), -C_L^{(M_\infty, C_L^*)}(x, p)\} \\ \text{s.t. } x_L \leq x \leq x_U \end{cases} \quad (9.26)$$

We use as design variables  $x$  the position of 15 nodes Free Form Deformation (FFD) box (Figure 9.11 and definition in 2.4.3).

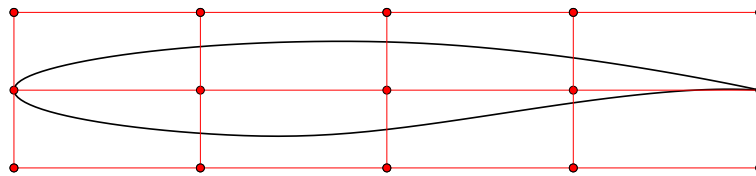


Figure 9.11 – 15 nodes FFD box for the RAE2822.



**Multi Objective Robust Design Optimization of Lift and Drag: MO-RDO1** We now consider two competing robust objectives to be optimized simultaneously, namely minimize the drag coefficient  $C_D$  and its dispersion and maximise the lift coefficient and reduce its dispersion. We consider, first, only operating uncertainties (see Table 9.3) affecting the flow surrounding the airfoil and we use as design variables  $x$  the Free Form Deformation (FFD) box coefficients (Figure 9.11).

$$\text{MO-RDO1 : } \begin{cases} \text{P-min}_{x \in X} \{ \mathcal{R}_D [C_D(x, p(\psi))], \mathcal{R}_L [C_L(x, p(\psi))] \} \\ \text{s.t. } x_L \leq x \leq x_U \end{cases} \quad (9.27)$$

with:

$$\begin{aligned} \mathcal{R}_D [C_D(x, p(\psi))] &= \mu_{C_D}(x, p(\psi)) + \sigma_{C_D}(x, p(\psi)) \\ \mathcal{R}_L [C_L(x, p(\psi))] &= -\mu_{C_L}(x, p(\psi)) + \sigma_{C_L}(x, p(\psi)) \end{aligned} \quad (9.28)$$

We consider as uncertain operating parameters those defined for the single objective problem SO-RDO2 (see Table 9.3)

In Figure 9.12 we present the results of MO-DO1 and MO-RDO1. For the candidate designs in the deterministic Pareto set (blue points, with lift coefficient higher and drag coefficient lower than the original RAE2822) and the RAE-2822 airfoil (black point) we perform an uncertainty analysis and compute the mean value (red square) and dispersion of the airfoils  $C_D$  and  $C_L$  (red ellipses correspond to two standard deviations) when they are operated in the uncertain environment. The blue stars represent candidates in the deterministic Pareto set that are very unstable when operating in the uncertain environment. Small variations in the angle of attack and Mach number lead to separated flow on the suction side of such airfoils (no ellipse is drawn for those candidates). We perform the same uncertainty analysis also for the candidate design obtained by solving the MO-RDO1 (yellow points in the robust pareto front indicate the value of the robust loss function for  $C_L$  and  $C_D$ ) and compute the mean value (green square) and dispersion (green ellipses).

It is interesting to notice in Figure 9.12 a gathering of robust optimal candidates and their means around  $C_L \approx 0.75$  and  $C_D \approx 0.011$ . Such robust candidates have quite similar performances and dispersion around the mean.

**Multi Objective Robust Design Optimization of Lift and Drag: MO-RDO2** Lastly we consider the multi objective problem of minimizing the drag coefficient  $C_D$  and its dispersion and maximizing the lift coefficient and reduce its dispersion with operating (system parameters  $p(\psi)$ , Mach number and angle of attack in Table 5.9) and geometric uncertainties at the same time (Table 5.9 and Table 9.4). In this set of simulations the design parameters  $x$ , are PARSEC parameters (Table 9.4 second column) and in the actual shape of the airfoil, uncertainty is

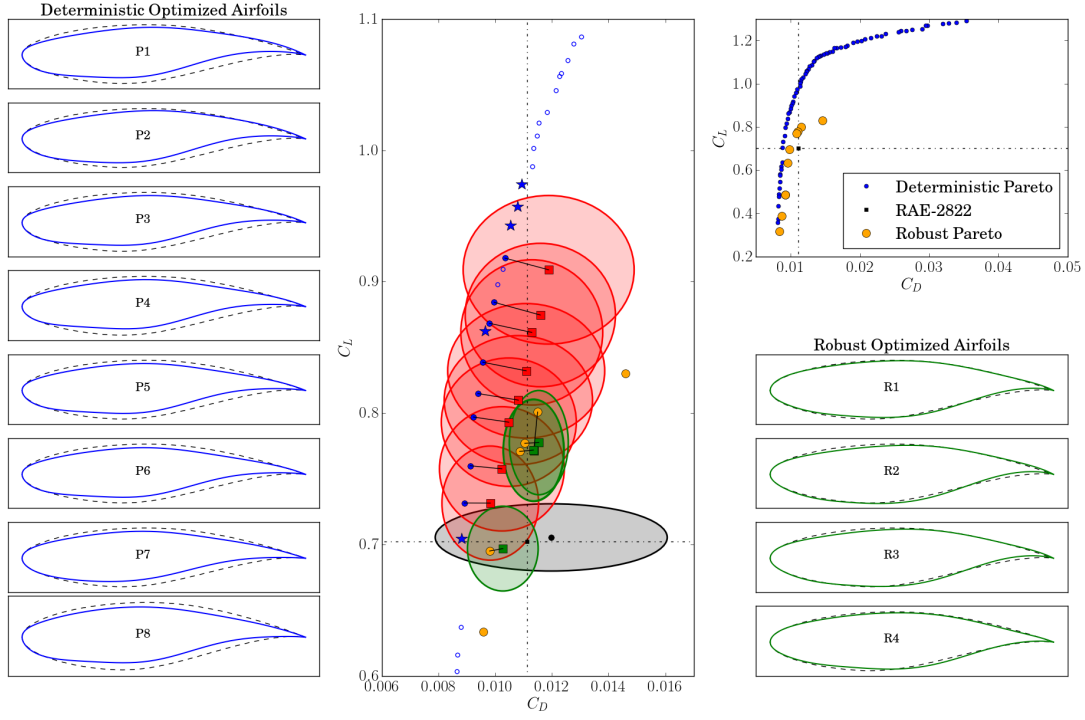


**Figure 9.12** – Deterministic and Robust Pareto fronts obtained by solving respectively the MO-DO1 and the MO-RDO1. The central plot is a blow-up view of the full Pareto. The red squares are the mean of  $C_L$  and  $C_D$  when the airfoils are operated in the uncertain environment, while the red ellipses are the dispersion around such mean values (two standard deviations). The green squares are the mean values of the robust optimal points and the green ellipses are their dispersion around such mean values (two standard deviations). Finally the black point and grey ellipse correspond to the RAE-2822 airfoil.

added to those parameters.

$$\text{MO-RDO2: } \begin{cases} \text{P-min}_x \{ \mathcal{R}_D [C_D(\tilde{x}(x, \omega), p(\psi))], \mathcal{R}_L [C_L(\tilde{x}(x, \omega), p(\psi))] \} \\ \text{s.t. } x_L \leq x \leq x_U \end{cases} \quad (9.29)$$

with:

$$\begin{aligned} \mathcal{R}_D [C_D(\tilde{x}(x, \omega), p(\psi))] &= \mu_{C_D}(\tilde{x}(x, \omega), p(\psi)) + \sigma_{C_D}(x, p(\psi)) \\ \mathcal{R}_L [C_L(\tilde{x}(x, \omega), p(\psi))] &= -\mu_{C_L}(\tilde{x}(x, \omega), p(\psi)) + \sigma_{C_L}(\tilde{x}(x, \omega), p(\psi)) \end{aligned} \quad (9.30)$$

We compare the results with MO-DO1 but in this set of simulations we use the PARSEC coefficients as design parameters.

In Figure 9.13 we present the results of MO-RDO2 and MO-DO1. We perform, as for the previ-

## 9.6. Application to Multi-Objective Optimization Under Uncertainties

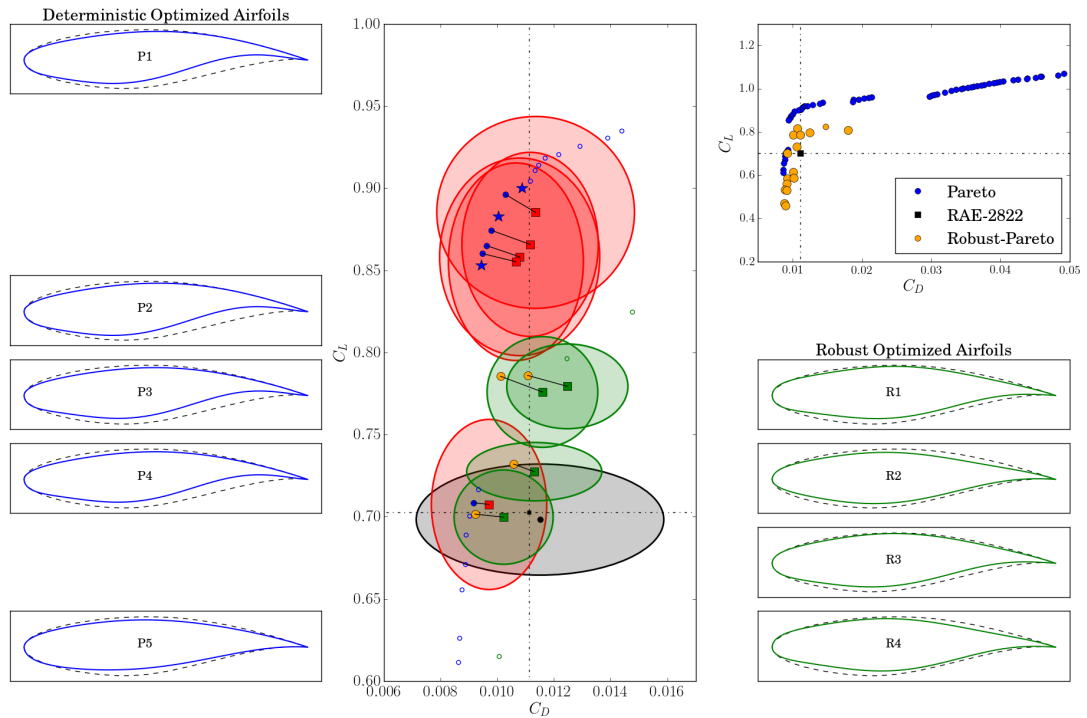


**Figure 9.13** – Deterministic and Robust Pareto fronts obtained by solving respectively the MO-DO1 (using PARSEC as design parameters) and the MO-RDO2. The central plot is a blow-up view of the full Pareto. The red squares are the mean of  $C_L$  and  $C_D$  when the airfoils are operated in the uncertain environment, while the red ellipses are the dispersion around such mean values (two standard deviations). The green squares are the mean values of the robust optimal points and the green ellipses are their dispersion around such mean values (two standard deviations).

ous case, an uncertainty analysis for the deterministic and robust candidates that dominate the original RAE-2822 (with lift coefficient higher and drag coefficient lower) and compute the mean value (red squares for the deterministic optimal and yellow squares for the robust optimal candidates) and dispersion of the airfoils  $C_D$  and  $C_L$  (red ellipses for the deterministic and green for robust candidates that correspond to two standard deviations) when they are operated in the uncertain environment. The blue stars represent candidates in the deterministic Pareto set that are very unstable when operating in the uncertain environment. Small variations in the geometry, angle of attack or Mach number lead to separated flow on the suction side of such airfoils. We can clearly identify, even better than in the previous case with only operating uncertainties, a much higher stability of the performances of the robust optimized airfoils when operated in an uncertain environment and when affected by geometrical uncertainties.

## **9.7 Conclusions**

In this Chapter we have presented how the MLMC approach can be efficiently integrated in with an optimization evolutionary strategy algorithm to perform single and multi objective robust and reliability based design optimization of transonic airfoils affected by a considerable number of operating and geometric uncertainties.

Thanks to the extensions of MLMC presented in the previous Chapters we can now efficiently compute loss functions and probabilistic constraints that include central statistical moments and risk measures. Additionally, by employing the robustness of the C-MLMC approach, the number of levels and simulations per levels required to achieve a prescribed tolerance requirement can be computed on the fly for each candidate design in the optimization loop.

We demonstrated with single and multi objective optimization problems that such methodology can be efficiently employed to design transonic airfoils that are less sensitive to uncertainties. We believe that the technique has the potential to be extended to more complex problems as those presented in Chapter 8 where the stability and the reliability of the aerodynamic system is of crucial importance.

# 10 Conclusions and Perspectives

## 10.1 Conclusions

In this thesis we analyzed and developed uncertainty quantification methodologies to efficiently study the effect of uncertainties on aerodynamic systems.

We started by extending the Multi Level Monte Carlo approach, proposed by Heinrich [Hei98] in the context of parametric integration and extended by Giles [Gil08] to approximate stochastic differential equations (SDEs) in financial mathematics, in order to treat aerodynamic systems, modeled by Computational Fluid Dynamic simulation, affected by operating and geometric uncertainties.

After assessing the effectiveness of the Multi Level Monte Carlo (MLMC) approach compared to classical Monte Carlo (MC) method in computing accurate statistics of scalar quantities of interest, we proposed an extension to estimate scalar field quantities such as the uncertain pressure profile around airfoils and wings. Following the successful completion of the latter objective, we investigated the Continuation Multi Level Monte Carlo (C-MLMC) methodology in order to further reduce the computational time required to set up and perform an uncertainty analysis. The continuation algorithm proved to be a robust and self-tuning approach that estimates on the fly the optimal number of levels and realizations per level necessary to meet a prescribed tolerance requirement.

In order to be relevant for realistic industrial applications we revisited the continuation algorithm and particularized to the specific setting of viscous compressible aerodynamic simulations. We focused on the application of the algorithm to specific external and internal aerodynamics benchmark test cases and we detailed how to construct an appropriate grid hierarchy to achieve grid convergence rates for the C-MLMC to be effective.

With the end goal of improving the understanding of the effect of uncertainties on the performances of aerodynamic system we extended the MLMC approach to compute central statistical moments. In fact, in addition to the mean, many important features of a random

variable distribution, such as location, dispersion, or asymmetry, can be assessed through the analysis of statistical moments. Specifically, we introduced a novel multilevel Monte Carlo method that allows for an efficient sampling-based estimation from inexact/approximate samples. One of the method's key ingredients of our approach is the use of  $h$ -statistics as unbiased central moment estimators with minimal variance for the level-wise contributions.

With the same spirit we investigated the MLMC extension to compute parametric expectations. Specifically, we particularize the MLMC method introduced in [KN17] and detailed how to effectively set up a MLMC simulation to accurately compute an uncertain system output's cumulative distribution function, quantiles and conditional value at risk using cubic splines interpolation operators.

Finally we combined the above mentioned MLMC/C-MLMC approaches with single and multi-objective evolutionary algorithm in order to perform shape optimization under uncertainties. In the context of transonic airfoil shape design, we described how to perform robust and reliability based design optimization and demonstrated that our methodology can be efficiently employed to effectively design airfoils that are less sensitive to geometric and operating uncertainties.

### 10.2 Perspectives

We hope that the methodologies introduced and investigated in this thesis can boost the application and further development of accurate and time-effective uncertainty quantification and robust/reliability-based design optimization techniques in the industrial aeronautic sector. In order to achieve this objective, we outline some further computational challenges besides the ones investigated in this thesis and provide some promising perspectives research paths.

In our numerical experiments we applied a parallel execution of the simulations on a given hierarchy level. The **optimal level-wise, sample-wise and mesh-wise parallelization of the C-MLMC simulations** together with an optimal allocation of resources at each iteration of the algorithm for large scale problems solved on massively parallel HPC is still an open topic. Some ideas of parallelization and load balancing techniques for "standard" MLMC algorithms have been proposed in [ŠMS12, GDR<sup>+</sup>16]. We believe that the combination of these parallelization techniques and the C-MLMC approach should be the starting point for an effective application of uncertainty quantification of large scale aeronautic problems in an industrial environment.

In Chapter 6 and Chapter 7 we presented two MLMC extensions for the accurate computation of central statistical moments, distributions and risk measures. The numerical experiments provided a clear indication of the effectiveness of our MLMC implementation compared to a classical Monte Carlo approach. However, the computational cost required to accurately compute such statistics for large scale industrial problems still remains huge. We believe that the appropriate **combination of MLMC with adaptive importance sampling techniques** can dramatically reduce the computational cost and increase the accuracy of the approximations

in particular for high statistical moments and tail probabilities. Such is indeed required in order to apply the C-MLMC/MLMC approach in reliability based design frameworks where probabilistic loss functions and constraints are computed for each design candidate.

In Chapter 9 we investigated the combination of C-MLMC and the Covariance Matrix Adaptation Evolutionary Strategy in the context of shape optimization under uncertainties. Each candidate design in the evolving population in our algorithm requires a C-MLMC simulation for the accurate estimation of probabilistic loss functions and constraints. We are convinced that the tolerance on those simulations can be effectively reduced (and hence the computational time) by employing **bootstrap techniques** that provide indication on the tolerance required to appropriately discriminate the best and the worst candidate design in the population.





# A Appendix

## A.1 Unbiased variance estimator for $p = 4$ for MC method

Below we report the closed-form expressions of the unbiased estimators  $\hat{V}_4/N$  for  $\mathbb{V}\text{ar}[h_4(\mathbf{Q}_{N,M})] = V_4/N$ ,  $S_a \equiv S_a(\mathbf{Q}_{N,M})$ :

$$\begin{aligned} \frac{\hat{V}_4}{N} = & \frac{1}{(N-7)(N-6)(N-5)(N-4)(N-3)^2(N-2)^2(N-1)^2N^2} \{-72(2N^3 - 21N^2 + 79N - 105)S_1^8 + 288N(2N^3 - 21N^2 + 79N - 105)S_2S_2^6 \\ & - 48(7N^5 - 85N^4 + 443N^3 - 1199N^2 + 1734N - 1260)S_3S_1^5 - 12(3(17N^5 - 167N^4 + 505N^3 - 61N^2 - 1734N + 1260)S_2^2 \\ & + N(-13N^5 + 157N^4 - 851N^3 + 2387N^2 - 3336N + 2016)S_4)S_1^4 - 24N(2(-11N^5 + 134N^4 - 682N^3 + 1804N^2 - 2667N + 2142)S_2S_3 \\ & + (3N^6 - 40N^5 + 250N^4 - 812N^3 + 1319N^2 - 972N + 252)S_5)S_1^3 + 4(18N(2N^5 - 11N^4 - 59N^3 + 581N^2 - 1467N + 1134)S_2^3 \\ & - 3N(11N^6 - 114N^5 + 452N^4 - 714N^3 + 77N^2 + 828N - 1260)S_4S_2 - 4(7N^7 - 114N^6 + 847N^5 - 3603N^4 + 9532N^3 - 15867N^2 + 15318N - 7560)S_3^2 \\ & + N(7N^7 - 106N^6 + 778N^5 - 3136N^4 + 7387N^3 - 10798N^2 + 9396N - 3528)S_6)S_1^2 \\ & - 8(N(N^6 - 15N^5 + 109N^4 - 417N^3 + 934N^2 - 1332N + 936)S_7(N-1)^2 + 6(2N^7 - 15N^6 - 25N^5 + 627N^4 - 2785N^3 + 6120N^2 - 7344N + 3780)S_2^2S_3 \\ & + N(-6N^7 + 101N^6 - 792N^5 + 3626N^4 - 10470N^3 + 18917N^2 - 19260N + 9324)S_3S_4 \\ & - 3N(N^7 - 7N^6 - 14N^5 + 350N^4 - 1715N^3 + 3941N^2 - 4320N + 1764)S_2S_5)S_1 - 36(2N^6 - 17N^5 - 23N^4 + 659N^3 - 2493N^2 + 3672N - 1890)S_2^4 \\ & + 12N(11N^6 - 135N^5 + 581N^4 - 909N^3 + 20N^2 + 540N + 252)S_2^2S_4 + 4N(N^3 - 6N^2 + 11N - 6)S_2(4(N^4 - 7N^3 + 2N^2 + 118N - 294)S_3^2 \\ & + (-13N^4 + 124N^3 - 527N^2 + 1148N - 1092)S_6) + N((-N^8 + N^7 + 148N^6 - 1694N^5 + 9715N^4 - 33983N^3 + 70850N^2 - 76356N + 32760)S_4^2 \\ & + (N^3 - 6N^2 + 11N - 6)(N(N^5 - 11N^4 + 63N^3 - 145N^2 + 248N - 156)S_8 - 8(N^5 - 14N^4 + 93N^3 - 346N^2 + 854N - 1092)S_3S_5)) \end{aligned}$$

## A.2 Unbiased variance estimator on level $\ell$ for $p = 3$

$$\begin{aligned} \frac{\hat{V}_{\ell,3}}{N_\ell} = & \frac{1}{16(N_\ell - 5)(N_\ell - 4)(N_\ell - 3)(N_\ell - 2)^2(N_\ell - 1)^2 N_\ell^2} \{-12(3(N_\ell - 5)N_\ell + 20)S_{0,1}^6 \\ & + 36(2N_\ell S_{2,0}(N_\ell - 3)^2 + (3(N_\ell - 5)N_\ell + 20)(N_\ell S_{0,2} - 2S_{1,0}^2))S_{0,1}^4 \\ & + 24N_\ell(-N_\ell(2N_\ell - 9) + 11)(N_\ell S_{0,3} - 6S_{1,0}S_{1,1}) - 3((N_\ell - 3)(N_\ell - 2)N_\ell + 2)S_{2,1}S_{0,1}^3 \\ & + 3(-6N_\ell^2(N_\ell(4N_\ell - 21) + 29)S_{0,2}^2 + 12N_\ell(8N_\ell^2 - 42N_\ell + 58)S_{1,0}^2 \\ & + (2 - (N_\ell - 3)N_\ell(3N_\ell - 10))S_{2,0}S_{0,2} + (N_\ell - 2)(N_\ell - 1)N_\ell(N_\ell(7N_\ell - 15) + 20)S_{0,4} \\ & + 3(-12(3(N_\ell - 5)N_\ell + 20)S_{1,0}^4 + 8N_\ell(N_\ell(5N_\ell - 24) + 31)S_{2,0}S_{1,0}^2 \\ & - 8(N_\ell - 2)(N_\ell - 1)^2 N_\ell(2S_{1,2} + S_{3,0})S_{1,0} + N_\ell(-8(N_\ell - 2)(N_\ell - 1)^2 S_{1,1}^2 \\ & - 2((N_\ell - 1)N_\ell(2N_\ell - 7) + 12)S_{2,0}^2 + (N_\ell - 2)(N_\ell - 1)(2(N_\ell(3N_\ell - 7) + 8)S_{2,2} \\ & + ((N_\ell - 1)N_\ell + 4)S_{4,0})))S_{0,1}^2 - 6N_\ell(4S_{2,3}N_\ell^5 - 6S_{1,1}S_{1,2}N_\ell^4 - 10S_{1,0}S_{1,3}N_\ell^4 \\ & - 5S_{0,3}S_{2,0}N_\ell^4 - 9S_{2,0}S_{2,1}N_\ell^4 - 20S_{2,3}N_\ell^4 - 6S_{1,1}S_{3,0}N_\ell^4 - 18S_{1,0}S_{3,1}N_\ell^4 + 12S_{0,3}S_{1,0}^2 N_\ell^3 \\ & + 48S_{1,0}S_{1,3}N_\ell^3 + 30S_{0,3}S_{2,0}N_\ell^3 + 60S_{1,0}S_{1,1}S_{2,0}N_\ell^3 + 48S_{1,0}^2 S_{2,1}N_\ell^3 + 30S_{2,0}S_{2,1}N_\ell^3 \\ & + 52S_{2,3}N_\ell^3 + 24S_{1,1}S_{3,0}N_\ell^3 + 96S_{1,0}S_{3,1}N_\ell^3 - 60S_{0,3}S_{1,0}^2 N_\ell^2 - 96S_{1,0}^3 S_{1,1}N_\ell^2 \\ & + 90S_{1,1}S_{1,2}N_\ell^2 - 106S_{1,0}S_{1,3}N_\ell^2 - 35S_{0,3}S_{2,0}N_\ell^2 - 324S_{1,0}S_{1,1}S_{2,0}N_\ell^2 - 228S_{1,0}^2 S_{2,1}N_\ell^2 \\ & + 45S_{2,0}S_{2,1}N_\ell^2 - 92S_{2,3}N_\ell^2 - 6S_{1,1}S_{3,0}N_\ell^2 - 210S_{1,0}S_{3,1}N_\ell^2 + 72S_{0,3}S_{1,0}^2 N_\ell + 504S_{1,0}^3 S_{1,1}N_\ell \\ & - 180S_{1,1}S_{1,2}N_\ell + 132S_{1,0}S_{1,3}N_\ell - 30S_{0,3}S_{2,0}N_\ell + 480S_{1,0}S_{1,1}S_{2,0}N_\ell + 276S_{1,0}^2 S_{2,1}N_\ell \\ & - 210S_{2,0}S_{2,1}N_\ell + 88S_{2,3}N_\ell - 60S_{1,1}S_{3,0}N_\ell + 228S_{1,0}S_{3,1}N_\ell + 24S_{0,3}S_{1,0}^2 \\ & + (N_\ell - 2)(N_\ell - 1)^2((N_\ell - 1)N_\ell + 4)S_{0,5} - 696S_{1,0}^3 S_{1,1} + 96S_{1,1}S_{1,2} - 64S_{1,0}S_{1,3} \\ & + 16S_{0,3}S_{2,0} - 72S_{1,0}S_{1,1}S_{2,0} + 48S_{1,0}^2 S_{2,1} + 72S_{2,0}S_{2,1} \\ & + S_{0,2}(N_\ell(N_\ell(N_\ell(18 - 5N_\ell) + 13) - 90) + 40)S_{0,3} + 36((N_\ell - 3)(N_\ell - 2)N_\ell + 2)S_{1,0}S_{1,1} \\ & - 3(N_\ell(3N_\ell^3 - 14N_\ell^2 + N_\ell + 50) - 16)S_{2,1} - 32S_{2,3} + 48S_{1,1}S_{3,0} - 96S_{1,0}S_{3,1} \\ & + 3(N_\ell - 2)(N_\ell - 1)^2((N_\ell - 1)N_\ell + 4)S_{4,1}S_{0,1} + N_\ell(S_{0,6}N_\ell^6 + 6S_{2,4}N_\ell^6 - 9S_{2,1}^2 N_\ell^5 \\ & - 5S_{0,6}N_\ell^5 - 12S_{1,1}S_{1,3}N_\ell^5 - 12S_{1,0}S_{1,4}N_\ell^5 - 6S_{0,4}S_{2,0}N_\ell^5 - 18S_{2,0}S_{2,2}N_\ell^5 - 30S_{2,4}N_\ell^5 \\ & - 36S_{1,1}S_{3,1}N_\ell^5 - 36S_{1,0}S_{3,2}N_\ell^5 + 12S_{0,4}S_{1,0}^2 N_\ell^4 - 36S_{1,2}^2 N_\ell^4 + 13S_{0,6}N_\ell^4 + 48S_{1,1}S_{1,3}N_\ell^4 \\ & + 60S_{1,0}S_{1,4}N_\ell^4 + 72S_{1,1}^2 S_{2,0}N_\ell^4 + 42S_{0,4}S_{2,0}N_\ell^4 + 36S_{1,0}S_{1,2}S_{2,0}N_\ell^4 + 144S_{1,0}S_{1,1}S_{2,1}N_\ell^4 \\ & + 72S_{1,0}^2 S_{2,2}N_\ell^4 + 90S_{2,0}S_{2,2}N_\ell^4 + 78S_{2,4}N_\ell^4 - 36S_{1,2}S_{3,0}N_\ell^4 + 216S_{1,1}S_{3,1}N_\ell^4 \\ & + 180S_{1,0}S_{3,2}N_\ell^4 - 72S_{0,4}S_{1,0}^2 N_\ell^3 - 216S_{1,0}^2 S_{1,1}^2 N_\ell^3 + 144S_{1,2}^2 N_\ell^3 + 225S_{2,1}^2 N_\ell^3 - 23S_{0,6}N_\ell^3 \\ & - 72S_{1,0}^3 S_{1,2}N_\ell^3 - 12S_{1,1}S_{1,3}N_\ell^3 - 156S_{1,0}S_{1,4}N_\ell^3 - 576S_{1,1}^2 S_{2,0}N_\ell^3 - 78S_{0,4}S_{2,0}N_\ell^3 \\ & - 72S_{1,0}S_{1,2}S_{2,0}N_\ell^3 - 648S_{1,0}S_{1,1}S_{2,1}N_\ell^3 - 360S_{1,0}^2 S_{2,2}N_\ell^3 - 90S_{2,0}S_{2,2}N_\ell^3 - 138S_{2,4}N_\ell^3 \\ & + 144S_{1,2}S_{3,0}N_\ell^3 - 324S_{1,1}S_{3,1}N_\ell^3 - 468S_{1,0}S_{3,2}N_\ell^3 + 156S_{0,4}S_{1,0}^2 N_\ell^2 + 1224S_{1,0}^2 S_{1,1}^2 N_\ell^2 \\ & - 36S_{1,2}^2 N_\ell^2 - 324S_{2,1}^2 N_\ell^2 + 22S_{0,6}N_\ell^2 + 288S_{1,0}S_{1,2}N_\ell^2 - 312S_{1,1}S_{1,3}N_\ell^2 + 276S_{1,0}S_{1,4}N_\ell^2 \\ & + 1656S_{1,1}^2 S_{2,0}N_\ell^2 + 6S_{0,4}S_{2,0}N_\ell^2 - 252S_{1,0}S_{1,2}S_{2,0}N_\ell^2 + 72S_{1,0}S_{1,1}S_{2,1}N_\ell^2 + 792S_{1,0}^2 S_{2,2}N_\ell^2 \\ & - 306S_{2,0}S_{2,2}N_\ell^2 + 132S_{2,4}N_\ell^2 - 36S_{1,2}S_{3,0}N_\ell^2 - 288S_{1,1}S_{3,1}N_\ell^2 + 828S_{1,0}S_{3,2}N_\ell^2 \\ & - 144S_{0,4}S_{1,0}^2 N_\ell - 1728S_{1,0}^2 S_{1,1}^2 N_\ell - 360S_{1,2}^2 N_\ell - 540S_{2,1}^2 N_\ell - 8S_{0,6}N_\ell - 360S_{1,0}^3 S_{1,2}N_\ell \\ & + 672S_{1,1}S_{1,3}N_\ell - 264S_{1,0}S_{1,4}N_\ell - 2016S_{1,1}^2 S_{2,0}N_\ell + 84S_{0,4}S_{2,0}N_\ell + 720S_{1,0}S_{1,2}S_{2,0}N_\ell \\ & + 2160S_{1,0}S_{1,1}S_{2,1}N_\ell - 936S_{1,0}^2 S_{2,2}N_\ell + 756S_{2,0}S_{2,2}N_\ell - 48S_{2,4}N_\ell - 360S_{1,2}S_{3,0}N_\ell \\ & + 1008S_{1,1}S_{3,1}N_\ell - 792S_{1,0}S_{3,2}N_\ell + 9(N_\ell - 2)(N_\ell - 1)^2((N_\ell - 1)N_\ell + 4)S_{4,2}N_\ell \\ & + 3(N_\ell - 2)(N_\ell - 1)(3(N_\ell - 5)N_\ell + 20)S_{0,2}^3 \\ & - (N_\ell(N_\ell(N_\ell(N_\ell(N_\ell + 4) - 41) + 40) + 100) - 80)S_{0,3}^2 + 48S_{0,4}S_{1,0}^2 - 144S_{1,0}^2 S_{1,1}^2 \\ & + 288S_{1,2}^2 + 432S_{2,1}^2 + 144S_{1,0}^3 S_{1,2} - 384S_{1,1}S_{1,3} + 96S_{1,0}S_{1,4} + 864S_{1,1}^2 S_{2,0} - 48S_{0,4}S_{2,0} \\ & - 432S_{1,0}S_{1,2}S_{2,0} + 18(N_\ell - 2)(N_\ell - 1)S_{0,2}^2((N_\ell - 4)(N_\ell - 1)S_{2,0} - 2(N_\ell - 3)S_{1,0}^2) \\ & - 864S_{1,0}S_{1,1}S_{2,1} + 6S_{0,3}(4(N_\ell(N_\ell + 3)((N_\ell - 6)N_\ell + 10) - 8)S_{1,0}S_{1,1} \\ & - (N_\ell((N_\ell - 2)N_\ell(N_\ell^2 - 17) + 40) - 32)S_{2,1}) + 432S_{1,0}^2 S_{2,2} - 432S_{2,0}S_{2,2} + 288S_{1,2}S_{3,0} \\ & - 576S_{1,1}S_{3,1} + 288S_{1,0}S_{3,2} - 3(N_\ell - 2)(N_\ell - 1)S_{0,2}((N_\ell(N_\ell(2N_\ell - 5) - 5) + 20)S_{0,4} \\ & + 3(-4S_{1,0}^4 + 4(N_\ell + 1)S_{2,0}S_{1,0}^2 + 4(-N_\ell^2 + N_\ell + 4)S_{1,2} - 2(N_\ell - 1)S_{3,0})S_{1,0} \\ & - ((N_\ell - 5)N_\ell + 12)S_{2,0}^2 + 2N_\ell((N_\ell - 3)N_\ell - 2)S_{2,2} + (N_\ell - 1)N_\ell S_{4,0} + 4(-((N_\ell - 5)N_\ell + 8)S_{1,1}^2 \\ & + 4S_{2,2} + S_{4,0}))) \end{aligned}$$





# Bibliography

- [AO11] Mark Ainsworth and J Tinsley Oden. *A posteriori error estimation in finite element analysis*, volume 37. John Wiley & Sons, 2011.
- [ASM06] ASME. Guide for verification and validation in computational solid mechanics. Technical report, American Society of Mechanical Engineers, ASME V&V 10-2006, 2006.
- [ASM09] ASME. Standard for verification and validation in computational modeling of fluid dynamics and heat transfer. Technical report, American Society of Mechanical Engineers, ASME V&V 20-2009, 2009.
- [Atm75] Standard Atmosphere. International organization for standardization. *ISO*, 2533:1975, 1975.
- [Bat90] John T Batina. Unsteady euler airfoil solutions using unstructured dynamic meshes. *AIAA journal*, 28(8):1381–1388, 1990.
- [BC15] C. Bierig and A. Chernov. Convergence analysis of multilevel Monte Carlo variance estimators and application for random obstacle problems. *Numer. Math.*, 130(4):579–613, 2015.
- [BC16] C. Bierig and A. Chernov. Estimation of arbitrary order central statistical moments by the multilevel Monte Carlo method. *Stoch. Partial Differ. Equ. Anal. Comput.*, 4(1):3–40, 2016.
- [BF84] Vincent Braibant and Claude Fleury. Shape optimal design using b-splines. *Computer Methods in Applied Mechanics and Engineering*, 44(3):247–267, 1984.
- [BG74] Robert C Blattberg and Nicholas J Gonedes. A comparison of the stable and student distributions as statistical models for stock prices. *The journal of business*, 47(2):244–280, 1974.
- [Bla15] Jiri Blazek. *Computational fluid dynamics: principles and applications*. Butterworth-Heinemann, 2015.

## Bibliography

---

- [BLS13] Andrea Barth, Annika Lang, and Christoph Schwab. Multilevel Monte Carlo method for parabolic stochastic Partial Differential Equations. *BIT Numerical Mathematics*, 53(1):3–27, 2013.
- [BNT07] Ivo Babuška, Fabio Nobile, and Raul Tempone. A stochastic collocation method for elliptic partial differential equations with random input data. *SIAM Journal on Numerical Analysis*, 45(3):1005–1034, 2007.
- [BSZ11] Andrea Barth, Christoph Schwab, and Nathaniel Zollinger. Multi-level Monte Carlo finite element method for elliptic PDEs with stochastic coefficients. *Numerische Mathematik*, 119(1):123–161, 2011.
- [Cam98] Richard L Campbell. Efficient viscous design of realistic aircraft configurations. *AIAA paper*, 2539:1998, 1998.
- [CCJ13] Bo Young Chang, Peter Christoffersen, and Kris Jacobs. Market skewness risk and the cross section of stock returns. *Journal of Financial Economics*, 107(1):46–68, 2013.
- [CDI09] Tonkid Chantrasmi, Alireza Doostan, and Gianluca Iaccarino. Padé–Legendre approximants for uncertainty analysis with discontinuous response surfaces. *Journal of Computational Physics*, 228(19):7159–7180, 2009.
- [CGST11] KA Cliffe, MB Giles, Robert Scheichl, and Aretha L Teckentrup. Multilevel Monte Carlo methods and applications to elliptic PDEs with random coefficients. *Computing and Visualization in Science*, 14(1):3–15, 2011.
- [CHAN<sup>+</sup>14] Nathan Collier, Abdul-Lateef Haji-Ali, Fabio Nobile, Erik von Schwerin, and Raúl Tempone. A continuation Multilevel Monte Carlo algorithm. *BIT Numerical Mathematics*, pages 1–34, 2014.
- [CKR<sup>+</sup>03] Richard Curran, A Kundu, Srinivasan Raghunathan, D Eakin, and R McFadden. Influence of manufacturing tolerance on aircraft direct operating cost (doc). *Journal of Materials Processing Technology*, 138(1):208–213, 2003.
- [CKRM02] Richard Curran, A Kundu, Srinivasan Raghunathan, and R McFadden. Impact of aerodynamic surface tolerance on aircraft cost driver. *Proceedings of the Institution of Mechanical Engineers, Part G: Journal of Aerospace Engineering*, 216(1):29–39, 2002.
- [CPGP98] Sukumar Chakravarthy, Oshin Perroomian, Uriel Goldberg, and Sampath Palaniswamy. The cfd++ computational fluid dynamics software suite. *SAE Technical Paper*, 985564, 1998.
- [CST13] Julia Charrier, Robert Scheichl, and Aretha L Teckentrup. Finite element error analysis of elliptic PDEs with random coefficients and its application to Multi level Monte Carlo methods. *SIAM Journal on Numerical Analysis*, 51(1):322–352, 2013.

- [CW00] Michael Casey and Torsten Wintergerste. Ercoftac special interest group on “quality and trust in industrial cfd”: Best practice guidelines. *European Research Community on Flow, Turbulence and Combustion*, page 123, 2000.
- [DBDBM<sup>+</sup>78] Carl De Boor, Carl De Boor, Etats-Unis Mathématicien, Carl De Boor, and Carl De Boor. *A practical guide to splines*, volume 27. Springer-Verlag New York, 1978.
- [Del00] Freddy Delbaen. Coherent risk measures. *Blätter der DGVMF*, 24(4):733–739, 2000.
- [DKL86] Armen Der Kiureghian and Pei-Ling Liu. Structural reliability under incomplete probability information. *Journal of Engineering Mechanics*, 112(1):85–104, 1986.
- [DNP<sup>+</sup>04] Bert J Debuschere, Habib N Najm, Philippe P Pébay, Omar M Knio, Roger G Ghanem, and Olivier Le Maitre. Numerical challenges in the use of polynomial chaos representations for stochastic processes. *SIAM journal on scientific computing*, 26(2):698–719, 2004.
- [DoD08] DoD. Documentation of verification, validation, and accreditation (vv&a) for models and simulations. Technical report, Department of Defense, MIL-STD-3022., 2008.
- [Dre98] Mark Drela. Pros and cons of airfoil optimization. *Frontiers of computational fluid dynamics*, 1998, 1998.
- [Dre07] Mark Drela. A user’s guide to mses 3.05. *Massachusetts Institute of Technology (MIT), Cambridge*, 2007.
- [Dun98] John Dunham. CFD validation for propulsion system components (la validation cfd des organes des propulseurs). Technical report, DTIC Document, 1998.
- [Dwy37] P. S. Dwyer. Moments of any rational integral isobaric sample moment function. *Ann. Math. Stat.*, 8(1):21–65, 1937.
- [EB09] MS Eldred and John Burkardt. Comparison of non-intrusive polynomial chaos and stochastic collocation methods for uncertainty quantification. *AIAA paper*, 976(2009):1–20, 2009.
- [EDC16] WN Edeling, Richard P Dwight, and Pasquale Cinnella. Simplex-stochastic collocation method with improved scalability. *Journal of Computational Physics*, 310:301–328, 2016.
- [EP98] Jonathan Elliott and Jaume Peraire. Constrained, multipoint shape optimisation for complex 3d configurations. *The Aeronautical Journal*, 102(1017):365–376, 1998.

## Bibliography

---

- [ETD07] TP Evans, P Tattersall, and JJ Doherty. Identification and quantification of uncertainty sources in aircraft related cfd computations—an industrial perspective. In *Proceedings of NATO RTO-AVT-147 symposium on computational uncertainty in military vehicle design, paper*, 2007.
- [Fav65] A Favre. Equations des gaz turbulents compressibles. 2. methode des vitesses moyennes methode des vitesses macroscopiques ponderees par la masse volumique. *Journal de mecanique*, 4(4):391, 1965.
- [FDKL98] Ch Farhat, C Degand, B Koobus, and M Lesoinne. Torsional springs for two-dimensional dynamic unstructured fluid meshes. *Computer methods in applied mechanics and engineering*, 163(1-4):231–245, 1998.
- [FK10] Jasmine Foo and George Em Karniadakis. Multi-element probabilistic collocation method in high dimensions. *Journal of Computational Physics*, 229(5):1536–1557, 2010.
- [GBMA09] Naveen Prasad Gopinathrao, David Bagshaw, Christophe Mabilat, and Sohail Alizadeh. Non-deterministic cfd simulation of a transonic compressor rotor. In *ASME Turbo Expo 2009: Power for Land, Sea, and Air*, pages 1125–1134. American Society of Mechanical Engineers, 2009.
- [GDR<sup>+</sup>16] Björn Gmeiner, Daniel Drzisga, Ulrich Ruede, Robert Scheichl, and Barbara Wohlmuth. Scheduling massively parallel multigrid for multilevel monte carlo methods. *arXiv preprint arXiv:1607.03252*, 2016.
- [Gib97] JK Gibson. *ECMWF re-analysis project report series: ERA description*, volume 1. European Centre for Medium-Range Weather Forecasts, 1997.
- [Gil08] Michael B Giles. Multilevel Monte Carlo path simulation. *Operations Research*, 56(3):607–617, 2008.
- [Gil15a] M. B. Giles. Multilevel Monte Carlo methods. *Acta Numer.*, 24:259–328, 2015.
- [Gil15b] Michael B Giles. Multilevel monte carlo methods. *Acta Numerica*, 24:259–328, 2015.
- [GNR15] Michael B Giles, Tigran Nagapetyan, and Klaus Ritter. Multilevel monte carlo approximation of distribution functions and densities. *SIAM/ASA Journal on Uncertainty Quantification*, 3(1):267–295, 2015.
- [God59] SK Godunov. A finite difference method for the computation of discontinuous solutions of the equations of fluid dynamics. *Sbornik: Mathematics*, 47(8-9):357–393, 1959.
- [GPC<sup>+</sup>97] Uriel Goldberg, Oshin Perroomian, Sukumar Chakravarthy, Balu Sekar, Uriel Goldberg, Oshin Perroomian, Sukumar Chakravarthy, and Balu Sekar. Validation



- of cfd++ code capability for supersonic combustor flowfields. In *33rd Joint Propulsion Conference and Exhibit*, page 3271, 1997.
- [GS03] Roger G Ghanem and Pol D Spanos. *Stochastic finite elements: a spectral approach*. Courier Corporation, 2003.
- [Hal46] P. R. Halmos. The theory of unbiased estimation. *Ann. Math. Statist.*, 17(1):34–43, 1946.
- [Han16] Nikolaus Hansen. The cma evolution strategy: A tutorial. *arXiv preprint arXiv:1604.00772*, 2016.
- [Har90] Charles D Harris. Nasa supercritical airfoils: a matrix of family-related airfoils. 1990.
- [HBE<sup>+</sup>13] Werner Haase, Frans Brandsma, Eberhard Elsholz, Michael Leschziner, and Dieter Schwamborn. *EUROVAL An European Initiative on Validation of CFD Codes: Results of the EC/BRITE-EURAM Project EUROVAL, 1990–1992*, volume 42. Springer-Verlag, 2013.
- [Hei98] Stefan Heinrich. Monte Carlo complexity of global solution of integral equations. *Journal of Complexity*, 14(2):151–175, 1998.
- [HH78] Raymond M Hicks and Preston A Henne. Wing design by numerical optimization. *Journal of Aircraft*, 15(7):407–412, 1978.
- [HMK03] Nikolaus Hansen, Sibylle D Müller, and Petros Koumoutsakos. Reducing the time complexity of the derandomized evolution strategy with covariance matrix adaptation (cma-es). *Evolutionary computation*, 11(1):1–18, 2003.
- [HO01] Nikolaus Hansen and Andreas Ostermeier. Completely derandomized self-adaptation in evolution strategies. *Evolutionary computation*, 9(2):159–195, 2001.
- [HPLL02] Luc Huyse, Sharon L Padula, R Michael Lewis, and Wu Li. Probabilistic approach to free-form airfoil shape optimization under uncertainty. *AIAA journal*, 40(9):1764–1772, 2002.
- [HS99] Stefan Heinrich and Eugène Sindambiwe. Monte Carlo complexity of parametric integration. *Journal of Complexity*, 15(3):317–341, 1999.
- [Hur60] HH Hurt. Aerodynamics for naval aviators; navweps 00-80t-80. *Naval Air Systems Command*, 1960.
- [HW10] Serhat Hosder and Robert W Walters. Non-intrusive polynomial chaos methods for uncertainty quantification in fluid dynamics. In *48th AIAA Aerospace Sciences Meeting*, pages 4–7, 2010.

## Bibliography

---

- [HWB07] Serhat Hosder, Robert W Walters, and Michael Balch. Efficient sampling for non-intrusive polynomial chaos applications with multiple uncertain input variables. *AIAA paper*, 1939:2007, 2007.
- [Iac11] Gianluca Iaccarino. Introduction to uncertainty representation and propagation, avt-193 short course on uncertainty quantification. Technical report, Technical Report. NATO Research and Technology Organization, Neuilly-sur-Seine, France, 2011.
- [IHR07] Christian Igel, Nikolaus Hansen, and Stefan Roth. Covariance matrix adaptation for multi-objective optimization. *Evolutionary computation*, 15(1):1–28, 2007.
- [IRG98] SS Isukapalli, A Roy, and PG Georgopoulos. Stochastic response surface methods (srsms) for uncertainty propagation: application to environmental and biological systems. *Risk analysis*, 18(3):351–363, 1998.
- [Jam88] Antony Jameson. Aerodynamic design via control theory. *Journal of scientific computing*, 3(3):233–260, 1988.
- [JST81] Antony Jameson, Wolfgang Schmidt, and Eli Turkel. Numerical solutions of the Euler equations by finite volume methods using Runge-Kutta time-stepping schemes. In *AIAA 14th Fluid and Plasma Dynamic Conference*, volume 81. AIAA Paper, 1981.
- [JTY05] Forrester T Johnson, Edward N Tinoco, and N Jong Yu. Thirty years of development and application of cfd at boeing commercial airplanes, seattle. *Computers & Fluids*, 34(10):1115–1151, 2005.
- [KB<sup>+</sup>06] Brenda M Kulfan, John E Bussioletti, et al. Fundamental parametric geometry representations for aircraft component shapes. In *11th AIAA/ISSMO multidisciplinary analysis and optimization conference*, volume 1, pages 547–591. sn, 2006.
- [Kea96] R Baker Kearfott. Interval computations: Introduction, uses, and resources. *Euromath Bulletin*, 2(1):95–112, 1996.
- [KL76] Alan Kraus and Robert H Litzenberger. Skewness preference and the valuation of risk assets. *The Journal of Finance*, 31(4):1085–1100, 1976.
- [KN17] Sebastian Krumscheid and Fabio Nobile. Multilevel monte carlo approximation of functions. Technical report, 2017.
- [LB08] GJA Loeven and Hester Bijl. *Airfoil analysis with uncertain geometry using the probabilistic collocation method*. American Institute of Aeronautics and Astronautics, 2008.

- [LB10] GJA Loeven and Hester Bijl. *The application of the probabilistic collocation method to a transonic axial flow compressor*. American Institute of Aeronautics and Astronautics (AIAA), 2010.
- [LH01] R Michael Lewis and Luc Huyse. Aerodynamic shape optimization of two-dimensional airfoils under uncertain conditions. Technical report, INSTITUTE FOR COMPUTER APPLICATIONS IN SCIENCE AND ENGINEERING HAMP-TON VA, 2001.
- [LHP02] Wu Li, Luc Huyse, and Sharon Padula. Robust airfoil optimization to achieve drag reduction over a range of mach numbers. *Structural and Multidisciplinary Optimization*, 24(1):38–50, 2002.
- [LKM14] Zhoujie Lyu, Gaetan KW Kenway, and Joaquim RRA Martins. Aerodynamic shape optimization investigations of the common research model wing benchmark. *AIAA Journal*, 2014.
- [LLT<sup>+</sup>13] David W Levy, Kelly R Laflin, Edward N Tinoco, John C Vassberg, Mori Mani, Ben Rider, Chris Rumsey, Richard A Wahls, Joseph H Morrison, Olaf P Brodersen, et al. Summary of data from the fifth aiaa cfd drag prediction workshop. 2013.
- [LMNP<sup>+</sup>07] Olivier P Le Maître, Habib Najm, Philippe Pébay, Roger Ghanem, and Omar M Knio. Multi-resolution-analysis scheme for uncertainty quantification in chemical systems. *SIAM Journal on Scientific Computing*, 29(2):864–889, 2007.
- [LWB07] GJA Loeven, JAS Witteveen, and H Bijl. Probabilistic collocation: an efficient non-intrusive approach for arbitrarily distributed parametric uncertainties. In *Proceedings of the 45th AIAA Aerospace Sciences Meeting and Exhibit, AIAA paper*, volume 317, 2007.
- [Man63] Benoit Mandelbrot. The variation of certain speculative prices. *The journal of business*, 36(4):394–419, 1963.
- [MBC79] Michael D McKay, Richard J Beckman, and William J Conover. Comparison of three methods for selecting values of input variables in the analysis of output from a computer code. *Technometrics*, 21(2):239–245, 1979.
- [MBWS13] Mortaza Mani, DA Babcock, CM Winkler, and PR Spalart. Predictions of a supersonic turbulent flow in a square duct. *AIAA Paper*, 860, 2013.
- [MC95] William J Morokoff and Russel E Caflisch. Quasi-monte carlo integration. *Journal of computational physics*, 122(2):218–230, 1995.
- [MCM03] Michael R Mendenhall, Robert E Childs, and Joseph H Morrison. Best practices for reduction of uncertainty in cfd results. 2003.

## Bibliography

---

- [MTR<sup>+</sup>15] Dominic A Masters, Nigel J Taylor, TCS Rendall, Christian B Allen, and Daniel J Poole. Review of aerofoil parameterisation methods for aerodynamic shape optimisation. In *53rd AIAA Aerospace Sciences Meeting*, pages 2015–0761, 2015.
- [MV02] David Moens and Dirk Vandepitte. Fuzzy finite element method for frequency response function analysis of uncertain structures. *AIAA journal*, 40(1):126–136, 2002.
- [Off04] U.S. Government Printing Office. *Airplane Flying Handbook*, volume FAA-8083-3A. Federal Aviation Administration, Washington D.C., U.S, 2004.
- [OT02] William L. Oberkampf and Timothy G. Trucano. Verification and validation in computational fluid dynamics. *Progress in Aerospace Sciences*, 38(3):209–272, 2002.
- [OT07] William L. Oberkampf and Timothy G. Trucano. Predictive capability maturity model for computational modeling and simulation. Technical report, Sandia National Laboratories, 2007.
- [OTH04] William L Oberkampf, Timothy G Trucano, and Charles Hirsch. Verification, validation, and predictive capability in computational engineering and physics. *Applied Mechanics Reviews*, 57(5):345–384, 2004.
- [PB00] Gamini Premaratne and Anil K Bera. Modeling asymmetry and excess kurtosis in stock return data. 2000.
- [PBL98] Ernest Perry, Richard Balling, and Mark Landon. A new morphing method for shape optimization. In *Proceedings of 7th AIAA/USAF/NASA/ISSMO Symposium on Multidisciplinary Analysis & Optimization, Saint-Louis, Etats-Unis*, number 2896, 1998.
- [PCA<sup>+</sup>13] Francisco Palacios, Michael R Colonno, Aniket C Aranake, Alejandro Campos, Sean R Copeland, Thomas D Economon, Amrita K Lonkar, Trent W Lukaczyk, Thomas WR Taylor, and Juan J Alonso. Stanford University Unstructured (SU2): An open-source integrated computational environment for multi-physics simulation and design. *AIAA Paper*, 287:2013, 2013.
- [PDL09] Gaël Poëtte, Bruno Després, and Didier Lucor. Uncertainty quantification for systems of conservation laws. *Journal of Computational Physics*, 228(7):2443–2467, 2009.
- [PEA<sup>+</sup>14] Francisco Palacios, Thomas D Economon, Aniket C Aranake, Sean R Copeland, Amrita K Lonkar, Trent W Lukaczyk, David E Manosalvas, Kedar R Naik, A Santiago Padrón, Brendan Tracey, et al. Stanford University Unstructured (SU2): Open-source analysis and design technology for turbulent flows. *AIAA paper*, 243:13–17, 2014.

- [QSS10] Alfio Quarteroni, Riccardo Sacco, and Fausto Saleri. *Numerical mathematics*, volume 37. Springer Science & Business Media, 2010.
- [RD11] Melissa B Rivers and Ashley Dittberner. Experimental investigations of the nasa common research model in the nasa langley national transonic facility and nasa ames 11-ft transonic wind tunnel. *AIAA Paper*, 1126:2011, 2011.
- [Rey94] Osborne Reynolds. On the dynamical theory of incompressible viscous fluids and the determination of the criterion. *Proceedings of the Royal Society of London*, 56(336-339):40–45, 1894.
- [RM78] Lonnie Reid and Royce D Moore. Design and overall performance of four highly loaded, high speed inlet stages for an advanced high-pressure-ratio core compressor. *NASA Technical Report*, 1978.
- [RM94] Robert D Richtmyer and Keith W Morton. Difference methods for initial-value problems. *Malabar, Fla.: Krieger Publishing Co.,| c1994, 2nd ed.*, 1994.
- [Rob04] Christian P Robert. *Monte carlo methods*. Wiley Online Library, 2004.
- [Roc07] R Tyrrell Rockafellar. Coherent approaches to risk in optimization under uncertainty. In *OR Tools and Applications: Glimpses of Future Technologies*, pages 38–61. Informs, 2007.
- [RS02] C. Rose and M. D. Smith. *Mathematical statistics with Mathematica<sup>®</sup>*. Springer, 2002.
- [RU02] R Tyrrell Rockafellar and Stanislav Uryasev. Conditional value-at-risk for general loss distributions. *Journal of banking & finance*, 26(7):1443–1471, 2002.
- [Rub94] PE Rubbert. Aiaa wright brothers lecture: Cfd and the changing world of aircraft development. Technical report, ICAS-94-0.2, September, 1994.
- [SA<sup>+</sup>94] Philipe R Spalart, Steven R Allmaras, et al. A one equation turbulence model for aerodynamic flows. *RECHERCHE AEROSPATIALE-FRENCH EDITION-*, pages 5–5, 1994.
- [Sam04] Jamshid A. Samareh. Aerodynamic shape optimization based on free-form deformation. In *10th AIAA-ISSMO Multidisciplinary Analysis and Optimization Conference*, 2004.
- [SK00] Kambiz Salari and Patrick Knupp. Code verification by the method of manufactured solutions. Technical report, Sandia National Labs., Albuquerque, NM (US); Sandia National Labs., Livermore, CA (US), 2000.
- [Smo63] Sergey Smolyak. Quadrature and interpolation formulas for tensor products of certain classes of functions. In *Soviet Math. Dokl.*, volume 4, pages 240–243, 1963.

## Bibliography

---

- [ŠMS12] Jonas Šukys, Siddhartha Mishra, and Christoph Schwab. Static load balancing for multi-level monte carlo finite volume solvers. *Parallel Processing and Applied Mathematics*, pages 245–254, 2012.
- [Sob98] H. Sobieczky. Parametric Airfoils and Wings. *Notes on Numerical Fluid Mechanics, edited by K. Fujii and G.S. Dulikravich*, 68:71–88, 1998.
- [Sob99] Helmut Sobieczky. Parametric airfoils and wings. In *Recent Development of Aerodynamic Design Methodologies*, pages 71–87. Springer, 1999.
- [SP86] Thomas W Sederberg and Scott R Parry. Free-form deformation of solid geometric models. *ACM SIGGRAPH computer graphics*, 20(4):151–160, 1986.
- [Ste16] Martin J Steele. Standard for models and simulations. *NASA-STD-7009A*, 2016.
- [SW86] J Clay Singleton and John Wingender. Skewness persistence in common stock returns. *Journal of Financial and Quantitative Analysis*, 21(3):335–341, 1986.
- [SWCP99] Fred Stern, Robert V Wilson, Hugh W Coleman, and Eric G Paterson. Verification and validation of cfd simulations. Technical report, IOWA INST OF HYDRAULIC RESEARCH IOWA CITY, 1999.
- [SWCP01] Fred Stern, Robert V Wilson, Hugh W Coleman, and Eric G Paterson. Comprehensive approach to verification and validation of cfd simulations-part 1: methodology and procedures. *Transactions-American Society of Mechanical Engineers Journal of Fluids Engineering*, 123(4):793–802, 2001.
- [TDH<sup>+</sup>04] Ben H. Thacker, Scott W. Doebeling, Francois M. Hemez, Mark C. Anderson, Jason E. Pepin, and Edward A. Rodriguez. Concepts of model verification and validation. Technical report, Los Alamos National Lab., Los Alamos, NM (US), 2004.
- [Tin07] Edward N Tinoco. Cfd uncertainty and validation for commercial aircraft applications. In *NATO Symposium AVT*, volume 147, 2007.
- [TLMNE10] Julie Tryoen, Olivier Le Maitre, Michael Ndjinga, and Alexandre Ern. Intrusive Galerkin methods with upwinding for uncertain nonlinear hyperbolic systems. *Journal of Computational Physics*, 229(18):6485–6511, 2010.
- [TSGU13] AL Teckentrup, R Scheichl, MB Giles, and E Ullmann. Further analysis of Multilevel Monte Carlo methods for elliptic PDEs with random coefficients. *Numerische Mathematik*, 125(3):569–600, 2013.
- [VA79] V.A. EXPERIMENTAL DATA BASE FOR COMPUTER PROGRAM ASSESSMENT - Report of the Fluid Dynamics Panel Working Group. *AGARD-AR-138*, 1979.

- [VDRW08] John C Vassberg, Mark A DeHaan, S Melissa Rivers, and Richard A Wahls. Development of a common research model for applied cfd validation studies. *AIAA paper*, 6919:2008, 2008.
- [VdV00] Aad W Van der Vaart. *Asymptotic statistics*, volume 3. Cambridge university press, 2000.
- [Ver94] Rüdiger Verfürth. A posteriori error estimates for nonlinear problems. finite element discretizations of elliptic equations. *Mathematics of Computation*, 62(206):445–475, 1994.
- [W<sup>+</sup>98] David C Wilcox et al. *Turbulence modeling for CFD*, volume 2. DCW industries La Canada, CA, 1998.
- [WA03] Robb C Wilcox and Bilal M Ayyub. Uncertainty modeling of data and uncertainty propagation for risk studies. In *Proceedings of the 4th International Symposium on Uncertainty Modelling and Analysis*, page 184. IEEE Computer Society, 2003.
- [Wal58] D. L. Wallace. Asymptotic approximations to distributions. *Ann. Math. Statist.*, 29:635–654, 1958.
- [WB06] Jeroen AS Witteveen and Hester Bijl. Modeling arbitrary uncertainties using gram-schmidt polynomial chaos. In *44th AIAA aerospace sciences meeting and exhibit*, page 896, 2006.
- [Whi74] Richard T Whitcomb. Review of nasa supercritical airfoils. *ICAS paper*, (74-10):25–30, 1974.
- [WI13] Jeroen AS Witteveen and Gianluca Iaccarino. Simplex stochastic collocation with eno-type stencil selection for robust uncertainty quantification. *Journal of Computational Physics*, 239:1–21, 2013.
- [Win94] Wayne L Winston. *Operations research. algorithms and applications*, 1994.
- [WK05] Xiaoliang Wan and George Em Karniadakis. An adaptive multi-element generalized polynomial chaos method for stochastic differential equations. *Journal of Computational Physics*, 209(2):617–642, 2005.
- [XH05] Dongbin Xiu and Jan S Hesthaven. High-order collocation methods for differential equations with random inputs. *SIAM Journal on Scientific Computing*, 27(3):1118–1139, 2005.
- [XK02] Dongbin Xiu and George Em Karniadakis. The wiener–askey polynomial chaos for stochastic differential equations. *SIAM journal on scientific computing*, 24(2):619–644, 2002.

## Bibliography

---

- [Yee89] Helen C Yee. A class of high resolution explicit and implicit shock-capturing methods. 1989.
- [YMC08] Wataru Yamazaki, Sylvain Mouton, and Gérald Carrier. Efficient design optimization by physics-based direct manipulation free-form deformation. *AIAA Paper*, 5953:2008, 2008.



**PISARONI MICHELE**

IISS Student and Junior Officer, AIAA Student Member

Date and place of birth : 27-08-1988, Cremona (CR) Italy  
 michele.pisaroni@gmail.com  
 Tel. +39 340 1206172

Chemin de la Rueyre 2  
 Jouxkens-Mezery 1008  
 Vaud, Switzerland

<b>Education</b>	<p><u>Ph.D in Mechanics, EPFL Lausanne, Switzerland</u> <span style="float: right;"><b>Sept. 2013 - Dec. 2017</b></span></p> <ul style="list-style-type: none"> <li>• Thesis: <i>Multi Level Monte Carlo Methods for Uncertainty Quantification and Robust Design Optimization in Aerodynamics</i> (defended 7th November 2017). Thesis jury: Prof Fabio Nobile (EPFL, thesis director), Dr Penelope Leyland (EPFL, thesis director), Prof Christophe Ancey, (EPFL, president of the jury), Prof. Jean-Francois Molinari (EPFL, internal expert), Prof Frederick Stern (U Iowa, external expert), Dr Domenico Quagliarella (CIRA ITA, external expert).</li> <li>• Research carried out at Scientific Computing and Uncertainty Quantification (CSQI) group of Prof. Fabio Nobile on Uncertainty Quantification, Robust/Reliability-based Design Optimization</li> <li>• Development of Python/R/SQL Framework for Data-Driven Optimization under Uncertainties</li> <li>• European FP7 Consortium: Uncertainty Management and Quantification for Robust Industrial Design in Aeronautics (UMRIDA)</li> </ul> <p><u>M.Sc. in Aerospace Engineering TU Delft, The Netherlands</u> <span style="float: right;"><b>Jan. 2011 - Aug 2013</b></span></p> <ul style="list-style-type: none"> <li>• Thesis: <i>Embedded Boundary Method for Aerospace Problems</i></li> <li>• Major: Aerodynamics, Concentration in Aeroelasticity, Optimization.</li> </ul> <p><u>B.S. in Aerospace Engineering, Politecnico di Milano, Italy</u> <span style="float: right;"><b>Sept 2007 - Sep. 2010</b></span></p>
<b>Professional Interests</b>	<p>Operational Research, Uncertainty Quantification, Risk Management, Data Driven Optimization, Decision Making Under Uncertainties</p>
<b>Professional Experience</b>	<p><u>Applied Vehicle Technology (AVT) Technical Team Member, NATO</u> <span style="float: right;"><b>Sept. 2014 - Present</b></span></p> <ul style="list-style-type: none"> <li>• Robust/Reliability Design for Novel and Aging Naval and Aerospace Military Vehicles</li> <li>• R&amp;D on Optimization Techniques to Improve the Performance of Alliance Military Vehicles</li> </ul> <p><u>M.Sc Visiting Student Researcher, Stanford University, CA, USA</u> <span style="float: right;"><b>Oct. 2012 - May 2013</b></span></p> <ul style="list-style-type: none"> <li>• Department of Aeronautics and Astronautics, Prof. Charbel Farhat FRG group</li> <li>• Research on Embedded Boundary Methods for Aerodynamics/Aeroelastic Problems</li> <li>• Validation and Verification of Embedded Boundary CFD solver.</li> </ul> <p><u>M.Sc Student Researcher, TU Delft, Delft, The Netherlands</u> <span style="float: right;"><b>Oct. 2010 - Aug 2013</b></span></p> <ul style="list-style-type: none"> <li>• Development of Novel Optimization Methods for Industrial Rotary Kiln Design.</li> </ul> <p><u>Project Engineer, Almatis B.V., Rotterdam, The Netherlands</u> <span style="float: right;"><b>Oct. 2010 - July 2012</b></span></p> <ul style="list-style-type: none"> <li>• R&amp;D on Design Optimization of Rotary Kiln Furnace Industrial Plant.</li> <li>• Production Optimization, NOx Emission Reduction and Development of New Kiln Design.</li> </ul>
<b>Short Courses and Technical Trainings</b>	<p><b>Mathematical and Algorithmic Aspects of Uncertainty Quantification,</b> <span style="float: right;"><b>July 2014</b></span></p> <ul style="list-style-type: none"> <li>• Summer Course at <b>UT Austin</b>, Austin TX, USA</li> </ul> <p><b>Mathematical Methods and Tools in Uncertainty Management Quantification,</b> <span style="float: right;"><b>Oct 2013</b></span></p> <ul style="list-style-type: none"> <li>• ERCOFTAC course, <b>ONERA</b>, Paris Chatillon, France</li> </ul> <p><b>Programming using MPI and GPU with CUDA,</b> <span style="float: right;"><b>Feb 2012</b></span></p> <ul style="list-style-type: none"> <li>• Faculteit <b>EWI</b>, Numerical Analysis, <b>TU Delft</b>, The Netherlands</li> </ul>
<b>Honors and Awards</b>	<p><b>INTEL ISEF</b>, Atlanta, USA <span style="float: right;"><b>2008</b></span></p> <ul style="list-style-type: none"> <li>• 3rd prize in Computer Science with the project "Simulation of Traffic Problems"</li> </ul> <p><b>FAST (Federation of Scientific and Technological Associations)</b>, Milan, Italy <span style="float: right;"><b>2007</b></span></p> <ul style="list-style-type: none"> <li>• 1st prize in Engineering field with the project "Simulation of Traffic Problems"</li> </ul>
<b>Languages</b>	<p><b>ENGLISH</b> <span style="margin-left: 150px;"><b>ITALIAN</b></span> <span style="float: right;"><b>FRENCH</b></span></p>

<b>Computer Skills</b>	<ul style="list-style-type: none"> <li>• C, C++, Fortran, Python, R, SQLite, SQL, Matlab</li> <li>• Catia, Ansys, Abaqus, NASTRAN</li> </ul>
<b>Publications &amp; Conferences proceeding</b>	<hr/> <ul style="list-style-type: none"> <li>• M. Piaroni, F. Nobile and P. Leyland, <i>A Continuation Multi Level Monte Carlo (C-MLMC) method for uncertainty quantification in compressible inviscid aerodynamics</i>, accepted in Computer Methods in Applied Mechanics and Engineering, 2017.</li> <li>• M. Piaroni, F. Nobile and P. Leyland, <i>A Multilevel Monte Carlo Evolutionary Algorithm for Robust Aerodynamic Shape Design</i>, 18th AIAA/ISSMO Multidisciplinary Analysis and Optimization Conference, Denver, Colorado, USA, 2017.</li> <li>• M. Piaroni, P. Leyland and F. Nobile, <i>A Multi Level Monte Carlo Algorithm for the Treatment of Geometrical and Operational Uncertainties in Internal and External Aerodynamics</i>, AIAA Aviation - 46th AIAA Fluid Dynamics Conference, Washington, D.C, 2016.</li> <li>• M. Piaroni, R. Sadi and D. Lahaye, <i>Counteracting ring formation in rotary kilns</i>, Journal of Mathematics in Industry, vol. 2, n. 3, 2012.</li> </ul>
<b>Technical Reports</b>	<ul style="list-style-type: none"> <li>• M. Piaroni, S. Krumscheid and F. Nobile, <i>Quantifying uncertain system outputs via the multilevel Monte Carlo method - Part I: Central moment estimation</i>, MATHICSE Technical Report 23.2017</li> <li>• M. Piaroni, F. Nobile and P. Leyland, <i>Continuation Multi-Level Monte-Carlo method for Uncertainty Quantification in Turbulent Compressible Aerodynamics Problems modeled by RANS</i>, MATHICSE Technical Report 10.2017</li> </ul>
<b>Book Chapters</b>	<ul style="list-style-type: none"> <li>• R. Schmidt, M. Voigt, M. Piaroni, F. Nobile, P. Leyland, J. P. Prats, G. Bugeada, <i>General Introduction to Monte-Carlo and Multi-Level Monte-Carlo Methods</i>, UMRIDA: Uncertainty Management and Quantification for Robust Industrial Design in Aeronautics, Notes on Numerical Fluid Mechanics and Multidisciplinary Design, Springer, 2018</li> <li>• M. Piaroni, F. Nobile and P. Leyland, <i>Continuation Multi-Level Monte-Carlo</i>, UMRIDA: Uncertainty Management and Quantification for Robust Industrial Design in Aeronautics, Notes on Numerical Fluid Mechanics and Multidisciplinary Design, Springer, 2018</li> <li>• M. Piaroni, F. Nobile and P. Leyland, <i>Robust design with Multi-Level Monte-Carlo</i>, UMRIDA: Uncertainty Management and Quantification for Robust Industrial Design in Aeronautics, Notes on Numerical Fluid Mechanics and Multidisciplinary Design, Springer, 2018</li> </ul>
<b>Recent Conference Talks</b>	<hr/> <ul style="list-style-type: none"> <li>• M. Piaroni, <i>A Multilevel Monte Carlo Evolutionary Algorithm for Uncertainty Quantification and Robust Multi Objective Shape Optimization</i>, AVT-252 Stochastic Design Optimization for Naval and Aero Military Vehicles, NATO 40th AVT Panel Business Meeting Week, Utrecht, Netherlands, 9-13 October 2017.</li> <li>• M. Piaroni, <i>A Multilevel Monte Carlo Algorithm for Robust Multi Objective Aerodynamic Shape Optimization</i>, MDO-03, MDO: Aerodynamic Shape Optimization II, 18th AIAA/ISSMO Multidisciplinary Analysis and Optimization Conference, 2017 AIAA Aviation and Aeronautics Forum and Exposition, Denver USA, 5-9 June 2017.</li> <li>• M. Piaroni, <i>A Multilevel Monte Carlo Algorithm for Robust Multi Objective Shape Optimization</i>, Invited Session 126 - Deterministic and Stochastic Simulation-based Design Analysis and Optimization in Marine Engineering, VII International Conference on Computational Methods in Marine Engineering (ECCOMAS Thematic Conference Marine 2017), Nantes, France, 15-17 May 2017.</li> <li>• M. Piaroni, <i>Continuation Multi Level Monte Carlo for Uncertainty Quantification in Compressible Aerodynamics</i>, Minsymposium lecture, Computational Uncertainty Quantification of Hyperbolic Problems, 2016 SIAM Conference on Uncertainty Quantification, Lausanne, Switzerland, 5-8 April 2016.</li> </ul>
<b>Other Experiences</b>	<hr/> <ul style="list-style-type: none"> <li>• Participation and contribution to the Working Group <i>Deterrence and Defence</i> NATO Young Professionals, part of the NATO Transformation Seminar, Budapest, 21 March 2017</li> </ul> <hr/>

